

CRANFIELD UNIVERSITY

SCHOOL OF ENGINEERING

PhD THESIS

Benjamin P. Graziano

Computational Modelling of Aerodynamic Disturbances on Spacecraft within a  
Concurrent Engineering Framework

Supervisor: Peter C. E. Roberts

September 2007

© Cranfield University 2007. All rights reserved. No part of this publication may be reproduced without the written permission of the copyright owner.



## **ABSTRACT**

This research was motivated by the need to perform an accurate aerodynamic analysis of the drag deorbit device concept under development within the Space Research Centre, Cranfield University. Its purpose is to deorbit satellites from low Earth orbit at the end of the useful lives, in order to help reduce the growing problem of space debris.

It has been found that existing spacecraft aerodynamic analysis tools do not adequately support concurrent engineering. Furthermore, use of concurrent engineering in the space industry is currently limited to Phase A (preliminary design studies). To remedy this, the Spacecraft Engineering, Design, and Analysis Tools (SEDAT) Concept has been proposed.

Inspired by the approach employed by enterprise applications, it proposes that all the computer tools used on a spacecraft project should be incorporated into one system as separate modules, presented via a single client, and connected to a centralised Relational Database Management System. To demonstrate the concept and assess its potential a SEDAT System and accompanying Free Molecular Flow (FMF) spacecraft aerodynamic analysis module have been developed.

The FMF Module is explicitly designed to facilitate concurrent engineering and make use of the maximum variety of Gas-Surface Interaction Models (GSIMs) and their associated data. It also incorporates a new Hybrid method of FMF analysis that combines the Ray-Tracing Panel (RTP) and Test-Particle Monte Carlo (TPMC) methods, enabling it to analyse complex geometries that are subject to surface shielding and multiple molecular reflections.

Studies have been performed using a Hybrid version of the Schaaf and Chambre GSIM. One of these studies analysed a drag deorbit device design using a range of accommodation coefficients, including the latest empirically based incidence-dependent coefficients. Based on this analysis, recommendations have been made regarding the material selection and structural design of the device.



For my Parents



# I CONTENTS

I	Contents..	i
I.i	List of Figures .....	v
I.ii	List of Tables .....	x
II	Acknowledgements .....	xiii
III	Notation.....	xv
III.i	Symbols.....	xv
III.ii	Acronyms .....	xix
III.iii	Software Providers .....	xxii
1	Introduction.....	1
1.1	Background .....	1
1.2	Evolution of Ideas .....	3
1.3	Rationale .....	5
1.4	Objectives .....	5
1.5	Approach.....	6
1.6	Scope.....	7
1.6.1	Spacecraft Aerodynamics .....	8
1.6.2	Concurrent Engineering.....	8
1.6.3	Systems Engineering.....	9
1.6.4	Computing.....	9
1.7	Summary .....	9
2	Spacecraft Aerodynamics .....	11
2.1	The Neutral Earth Atmosphere .....	12
2.1.1	Atmospheric Model .....	12
2.1.2	Characteristics.....	13
2.2	Free Molecular Flow .....	18
2.2.1	Regime Definition.....	18
2.2.2	Characteristics in Low Earth Orbit .....	22
2.2.3	Hyperthermal and Sub-Hyperthermal Flow.....	26
2.2.4	Gas-Surface Interactions .....	29
2.3	Aerodynamic Coefficients .....	29
2.4	Aerodynamic Forces and Moments on a Body .....	31
2.5	Analytical Analysis Methods.....	32
2.5.1	Empirical Methods.....	32
2.5.2	Geometric Analysis Methods.....	33
2.6	Computational Analysis Methods.....	33
2.6.1	Panel Method .....	34
2.6.2	RTP Method.....	36
2.6.3	TPMC Method .....	37

2.6.4	DSMC Method.....	39
2.6.5	Flow Regime Bridging Methods.....	41
2.6.6	CFD Method .....	42
2.7	Analysis Studies and Tools.....	42
2.8	Verification of Analyses .....	45
2.9	Summary .....	46
3	Gas-Surface Interaction Models .....	49
3.1	Newtonian Model.....	50
3.1.1	Original Model.....	51
3.1.2	Modified Newtonian Model.....	51
3.2	Maxwellian Model .....	52
3.2.1	Original Model.....	52
3.2.2	Schaaf and Chambre's Improved Model .....	53
3.2.3	Hyperthermal and Sub-Hyperthermal Flow.....	59
3.3	Accommodation Coefficients .....	63
3.3.1	Environmental Factors .....	63
3.3.2	Determination by Experiment.....	65
3.3.3	Determination by Orbital Observations .....	66
3.3.4	Determination by Onboard Experiment.....	68
3.4	Other Models .....	71
3.5	Future Directions .....	72
3.6	Summary .....	72
4	Spacecraft Concurrent Engineering .....	75
4.1	Current Approaches .....	77
4.1.1	Pre-Phase A and Phase A.....	77
4.1.2	Phases B, C, and D.....	79
4.2	Information Technology Challenges.....	80
4.2.1	Increasing Number of Tools .....	81
4.2.2	Data Continuity .....	82
4.3	Information Technology Solutions to other Business Challenges .....	84
4.4	Summary .....	85
5	The SEDAT System.....	87
5.1	Concept .....	87
5.2	Scope.....	90
5.3	Architecture.....	91
5.4	Technologies .....	92
5.5	The Database.....	92
5.5.1	Design .....	93
5.5.2	Implementation .....	94
5.5.3	Key Features .....	96



5.5.4	Detailed Examples of the Database Design .....	97
5.6	The Client.....	99
5.6.1	Approach.....	99
5.6.2	Key Features .....	101
5.6.3	Programming Strategy .....	105
5.6.4	Adding Module Components and Screens.....	107
5.7	The Help System.....	107
5.8	Testing.....	108
5.9	Installation.....	108
5.10	Summary .....	110
6	The Free Molecular Flow Module .....	111
6.1	Prototype .....	111
6.1.1	Description.....	111
6.1.2	Lessons Learnt .....	112
6.2	The Hybrid Method.....	114
6.2.1	Overview .....	114
6.2.2	Shielding .....	115
6.2.3	Multiple Reflections.....	116
6.2.4	Surface Mesh Density .....	118
6.2.5	Comparison with Other Methods.....	118
6.3	The SEDAT Ray-Tracer .....	120
6.3.1	Geometry-Dependent Panel Properties.....	122
6.3.2	Intersecting a Ray and a Panel.....	123
6.3.3	Bounding Boxes.....	126
6.3.4	Finding the Closest Panel.....	129
6.3.5	Shadowing.....	130
6.3.6	Computational Performance .....	132
6.4	Implementation .....	133
6.4.1	Database.....	134
6.4.2	Client.....	134
6.4.3	Analysis Set-Up via GUI .....	135
6.4.4	Analysis Set-Up via an Interface .....	136
6.4.5	Analysis Process .....	136
6.5	Key Features .....	141
6.5.1	Geometry Modelling and Transformation .....	141
6.5.2	Aerodynamic Damping.....	142
6.5.3	Gas-Flow Modelling .....	144
6.5.4	Surface-Dependent Properties .....	146
6.5.5	Multiple Gas-Surface Interaction Models.....	146
6.5.6	Multiple Atmospheric Models .....	147

6.5.7	Computing and Data Handling Capabilities .....	147
6.6	Summary .....	148
7	Pre-Installed Gas-Surface Interaction Models .....	151
7.1	Newtonian Model.....	151
7.2	Hybrid Schaaf and Chambre Model .....	152
7.2.1	Pressure and Shear Stress.....	153
7.2.2	Accommodation Coefficients .....	155
7.2.3	Scattering Kernel .....	158
7.2.4	Heat Transfer .....	161
7.2.5	Surface Temperature .....	164
7.2.6	Parameters, Bounds, and Attributes.....	165
7.3	Summary .....	168
8	Case Studies .....	169
8.1	Coordinate System and Flow Geometry .....	170
8.2	Simple Convex Shapes .....	173
8.2.1	Different Accommodation Coefficient Results for a Flat Plate ....	173
8.2.2	Sphere Parametric Analysis .....	176
8.2.3	Detailed Surface Results for a Sphere.....	181
8.2.4	Affect of Surface Temperature Differences.....	183
8.3	Modelling Reflected Flow .....	185
8.4	Drag Deorbit Device .....	188
8.4.1	Comparison with Analytical Newtonian Results .....	191
8.4.2	Comparison of Different Accommodation Coefficient Results....	193
8.4.3	Damping Torques.....	206
8.5	Other Demonstration Studies .....	209
8.5.1	Space Shuttle.....	209
8.6	Summary .....	214
9	Discussion and Conclusions .....	217
9.1	Assessment of the SEDAT Concept .....	217
9.1.1	The SEDAT System.....	217
9.1.2	The FMF Module.....	218
9.1.3	Future Prospects.....	219
9.2	Conclusions.....	220
9.3	Summary of Contributions.....	225
9.4	Suggestions for Further Work.....	226
10	References.....	231
11	Bibliography .....	241
A1	Appendix 1 - Digital Information .....	243
A2	Appendix 2 - FMF Module Technical Implementation.....	245
A2.1	Database Tables .....	245

A2.2 Client Object Model.....	247
A2.2.1 Aurora.Engineering.ThreeD.VectorSpace .....	248
A2.2.2 Aurora.Engineering.ThreeD.WorkSpace.....	250
A2.2.3 Aurora.Engineering.ThreeD.WorkSpace.RayTracer .....	251
A2.2.4 Aurora.Engineering.Aerodynamics .....	253
A2.2.5 Aurora.Engineering.Aerodynamics.Flow .....	253
A2.2.6 Aurora.Engineering.Aerodynamics.FMF.RayTracer.....	254
A2.2.7 Aurora.Engineering.Aerodynamics.FMF.RayTracer.GSI .....	257
A2.2.8 Aurora.SEDAT.Data.....	259
A3 Appendix 3 - FMF Module Analysis Set-Up via an Interface.....	261

## I.i List of Figures

Figure 1-1 - Collapsing Drag Sail.....	2
Figure 1-2 - Skynet 5 Military Communications Satellites .....	4
Figure 1-3 - Thesis Roadmap.....	7
Figure 2-1 - Comparison of the Main Disturbing Accelerations on Spacecraft in Low Earth Orbit .....	11
Figure 2-2 - Variation of Satellite Drag Coefficients with Altitude .....	13
Figure 2-3 - The Neutral Earth Atmosphere .....	14
Figure 2-4 - Variation of the Earth's Atmospheric Temperature with Altitude for Low, Mean, and High Solar Activity Levels.....	15
Figure 2-5 - Variation of the Earth's Atmospheric Density with Altitude for Low, Mean, and High Solar Activity Levels .....	15
Figure 2-6 - Variation of the Earth's Atmospheric Composition with Altitude.....	16
Figure 2-7 - Structure and Trends in the Earth's Atmosphere .....	17
Figure 2-8 - Molecular Mean Free Path ( $\lambda$ ).....	18
Figure 2-9 - Classification of Rarefied Flow Regimes Using Knudsen Number .....	19
Figure 2-10 - Free Stream Knudsen Number versus Altitude Trend for Selected Spacecraft Dimensions .....	20
Figure 2-11 - Selected Aerodynamic Parameters versus Altitude based on the Number Density Weighted Average (Mean) of the Gas Species .....	23
Figure 2-12 - Hypersonic Flow ( $s \rightarrow \infty$ ).....	27
Figure 2-13 - Sub-Hypersonic Flow ( $s << \infty$ ).....	27
Figure 2-14 - Molecular Mach Angle ( $\eta$ ).....	28
Figure 2-15 - Flow Geometry .....	31
Figure 2-16 - Comparison of Existing Computational Approaches to Spacecraft Aerodynamics in Low Earth Orbit .....	34
Figure 2-17 - The GRACE Satellites .....	36

Figure 2-18 - Schematic of the Test-Particle Monte Carlo (TPMC) Method.....	38
Figure 2-19 - DMSC Software Screenshot .....	40
Figure 2-20 - Screen Shot of the RAMSES Software.....	44
Figure 3-1 - Newton's Gas-Surface Interaction Model .....	51
Figure 3-2 - Schematic of the Maxwellian Gas-Surface Interaction Model.....	53
Figure 3-3 - Elemental Area Flow Geometry .....	55
Figure 3-4 - Error Function ( $erf(x)$ ) .....	57
Figure 3-5 - Newtonian Pressure Distribution on a Flat Plate using the Schaaf and Chambre Gas-Surface Interaction Model .....	58
Figure 3-6 - Pressure and Shear Stress Coefficients on a Flat Plate Using the Schaaf and Chambre Gas-Surface Interaction Model - Fully Diffuse Reflection.....	59
Figure 3-7 - Pressure and Shear Stress Coefficients on a Flat Plate Using the Schaaf and Chambre Gas-Surface Interaction Model - Fully Specular Reflection.....	60
Figure 3-8 - Pressure and Shear Stress Coefficients on a Flat Plate Using the Schaaf and Chambre Gas-Surface Interaction Model - Fully Diffuse Reflection - Hot Surface.....	62
Figure 3-9 - Variation of Spherical Satellite Drag Coefficient with Altitude Showing Variation Due to Specular and Diffuse Reemissions .....	63
Figure 3-10 - Schematic of the Main Environmental Factors Affecting Accommodation Coefficients in Low Earth Orbit.....	64
Figure 3-11 - Incidence-Dependent Accommodation Coefficients for the Schaaf and Chambre Gas-Surface Interaction Model .....	68
Figure 3-12 - BREMSAT.....	69
Figure 3-13 - Space Shuttle Experiment to Determine the Angular Distribution of Reflected Atomic Oxygen Flux .....	70
Figure 3-14 - Spacecraft Glow.....	70
Figure 3-15 - Schematic of the Cercigani-Lampis-Lord (CLL) and Nocilla Gas- Surface Interaction Models.....	71
Figure 4-1 - Typical Spacecraft Engineering Project Phases.....	75
Figure 4-2 - The Concurrent Design Facility (CDF) at ESTEC .....	77
Figure 4-3 - ESA Concurrent Design Facility (CDF) Floor Layout.....	78
Figure 4-4 - ESA Concurrent Design Facility Integrated Design Model Graphical Representation .....	79
Figure 4-5 - A Typical Spacecraft Systems Engineering Project Today .....	83
Figure 4-6 - Real-Time Collaborative Review of a Part and its Related Data using a CAD Interface Embedded in an Enterprise Application .....	85
Figure 5-1 - The SEDAT Concept.....	88
Figure 5-2 - SEDAT Client-Server Architecture .....	91

Figure 5-3 - SEDAT Database High-Level Design .....	94
Figure 5-4 - SEDAT Database Table Relationships (Schema).....	95
Figure 5-5 - SEDAT Database Relationships Displayed via the SEDAT Client.....	96
Figure 5-6 - SEDAT Database Grid Computing Schematic .....	97
Figure 5-7 - SEDAT Database Relationships: Selected Spacecraft Tables .....	98
Figure 5-8 - SEDAT Database Relationships: Solar System Body Tables.....	99
Figure 5-9 - The SEDAT Client: Screen shot showing the application's tree view component and table maintenance and navigation functionality .....	100
Figure 5-10 - The Latest Microsoft Outlook and SAP Clients .....	101
Figure 5-11 - SEDAT Help System .....	107
Figure 5-12 - Testing Phases.....	108
Figure 5-13 - The SEDAT Setup Program .....	109
Figure 6-1 - TerraSAR-L .....	113
Figure 6-2 - Surface Shielding .....	115
Figure 6-3 - Apparent Similarity of Different Concave Surfaces when Reflected Flow is not considered .....	116
Figure 6-4 - Modelling Reflected Flow using the Hybrid Method.....	117
Figure 6-5 - Comparison of the Hybrid Method with Existing Computational Approaches to Spacecraft Aerodynamics in Low Earth Orbit .....	119
Figure 6-6 - A Ray-Traced Scene from the 1986 Film Luxo Junior.....	121
Figure 6-7 - Triangular Panel Geometry.....	122
Figure 6-8 - The Parametric Equation of a Ray .....	123
Figure 6-9 - The Panel Intersection Sum of Angles Calculation Method.....	125
Figure 6-10 - The Panel Intersection Scaling Calculation Method.....	125
Figure 6-11 - Bounding Boxes.....	127
Figure 6-12 - Finding the Closest Panel .....	129
Figure 6-13 - Pseudo-Code to Find the Closest Panel .....	130
Figure 6-14 - Pseudo-Code to Calculate $t$ for a Panel.....	130
Figure 6-15 - Geometry of Projection Shadowing.....	131
Figure 6-16 - Geometry of Line-of-Sight Shadowing .....	131
Figure 6-17 - Pseudo-Code to Determine which Panels are Shadowed .....	132
Figure 6-18 - Analysis Program Flow .....	137
Figure 6-19 - Impact Procedure .....	138
Figure 6-20 - Impact Event Handlers.....	139
Figure 6-21 - Gas-Surface Interaction Event Handlers.....	140
Figure 6-22 - Aerodynamic Damping.....	143
Figure 6-23 - Selected Aerodynamic Parameters versus Altitude based on the Dominant Gas Species.....	145
Figure 7-1 - Hybrid Schaaf and Chambre GSIM.....	152
Figure 7-2 - Hybrid Schaaf and Chambre GSIM Program Flow .....	153

Figure 7-3 - Maxwellian Diffuse Reemission Scattering Geometry.....	158
Figure 7-4 - Specular Reemission Geometry .....	160
Figure 7-5 - Accommodation Coefficients versus Incidence Angle Using the Knechtel & Pitts Curve-Fit Parameters .....	166
Figure 7-6 - Accommodation Coefficients versus Incidence Angle Using the Mazanek Curve-Fit Parameters .....	167
Figure 8-1 - Definition of Angles of Attack $\alpha$ and Sideslip $\beta$ .....	171
Figure 8-2 - Nominal Spacecraft Body-Fixed Coordinate System and Lift ( $L$ ), Drag ( $D$ ), and Side ( $S$ ) Force Directions .....	172
Figure 8-3 - Flat Plate Analysis: Configuration.....	173
Figure 8-4 - Flat Plate Analysis: Comparison of Pressure and Shear Stress versus Incidence for Different Accommodation Coefficients .....	174
Figure 8-5 - Flat Plate Analysis: Drag and Lift Forces versus Angle of Attack.....	175
Figure 8-6 - Drag Coefficient versus Altitude for a Spherical Satellite in Low Earth Orbit Assuming Diffuse Reemission with $T_w/T_\infty = 1$ .....	176
Figure 8-7 - Comparison of Drag Coefficient versus Altitude for a Spherical Satellite in Low Earth Orbit for Different Accommodation Coefficients... ..	178
Figure 8-8 - Molecular Number Density Flux ( $N_i$ ) on a Sphere .....	181
Figure 8-9 - Pressure Distribution ( $C_p$ ) on a Sphere .....	182
Figure 8-10 - Shear Stress Distribution ( $C_\tau$ ) on a Sphere .....	182
Figure 8-11 - Heat Transfer Rate Distribution ( $C_H$ ) on a Sphere.....	183
Figure 8-12 - Corner Plate Analysis: Pressure Distribution and Reflected Test Particle Paths for Specular (left) and Diffuse (right) Accommodation Coefficients.....	186
Figure 8-13 - Drag Sail Concept.....	189
Figure 8-14 - Drag Deorbit Device Analysis: Cone Geometry, Body-Fixed Force ( $F$ ) and Torque ( $T$ ) Definitions, and Drag ( $D$ ) and Lift ( $L$ ) Directions .....	189
Figure 8-15 - Drag Deorbit Device Analysis: Coarse Surface Mesh (Left), Refined Surface Mesh (Right).....	191
Figure 8-16 - Drag Deorbit Device Analysis: Newtonian Results Compared with Analytical Calculations.....	192
Figure 8-17 - Drag Deorbit Device Analysis: Force and Torque versus Angle of Attack for Coarse and Refined Surface Meshes, using a Newtonian GSIM .....	192
Figure 8-18 - Drag Deorbit Device Analysis: Ray-Tracer Renderings for Angles of Attack $75^\circ$ , $90^\circ$ , and $180^\circ$ showing Side and Rear Views.....	193
Figure 8-19 - Drag Deorbit Device Analysis: Body-Fixed Force and Torque Coefficients versus Angle of Attack, assuming Specular Reflection ..	194

Figure 8-20 - Drag Deorbit Device Analysis: Pressure Coefficient ( $C_p$ ) Distribution assuming Specular Reflection for Angles of Attack 105°, 120°, 135°, 150°, 165°, and 180° .....	196
Figure 8-21 - Drag Deorbit Device Analysis: Body-Fixed Force and Torque Coefficients versus Angle of Attack, assuming Diffuse Reflection ....	197
Figure 8-22 - Drag Deorbit Device Analysis: Diffusely Reflected Test Particle Paths for Angle of Attack $\alpha = 180^\circ$ .....	197
Figure 8-23 - Drag Deorbit Device Analysis: Body-Fixed Force and Torque Coefficients versus Angle of Attack, assuming Knechtel & Pitts (K & P) Accommodation Coefficients .....	198
Figure 8-24 - Drag Deorbit Device Analysis: Body-Fixed Force and Torque Coefficients versus Angle of Attack, assuming Mazanek Accommodation Coefficients .....	199
Figure 8-25 - Drag Deorbit Device Analysis: Body-Fixed Force and Torque Coefficients versus Angle of Attack, assuming Quasi-Specular “50-50” Reemission.....	199
Figure 8-26 - Drag Deorbit Device Analysis: Pressure ( $C_p$ ), Shear Stress ( $C_\tau$ ), and Heat Transfer ( $C_h$ ) Coefficient distributions assuming Mazanek Accommodation Coefficients for Angles of Attack 30° and 60° .....	200
Figure 8-27 - Drag Deorbit Device Analysis: Pressure ( $C_p$ ), Shear Stress ( $C_\tau$ ), and Heat Transfer ( $C_h$ ) Coefficient distributions assuming Mazanek Accommodation Coefficients for Angles of Attack 120° and 150° ....	201
Figure 8-28 - Drag Deorbit Device Analysis: Body-Fixed Force and Torque Coefficients versus Angle of Attack for Different GSIMs and Accommodation Coefficients .....	203
Figure 8-29 - Drag Deorbit Device Analysis: Lift and Drag Coefficients versus Angle of Attack for Different GSIMs and Accommodation Coefficients.....	204
Figure 8-30 - Drag Deorbit Device Analysis: Damping Contribution to Torque Coefficient ( $C_{T(y)}$ ) as a function of Angle of Attack for Different GSIMs and Accommodation Coefficients .....	207
Figure 8-31 - Drag Deorbit Device Analysis: Angular Velocity Component Directions for Attacking Panels at Angles of Attack 0° and 180° .....	208
Figure 8-32 - The Space Shuttle Endeavour Docked to the Destiny Laboratory of the International Space Station .....	210
Figure 8-33 - Space Shuttle Analysis: Surface Mesh .....	210
Figure 8-34 - Space Shuttle Analysis: Ray-Tracer Rendering (rear view) .....	211
Figure 8-35 - Space Shuttle Analysis: Pressure ( $C_p$ ) Distribution .....	212
Figure 8-36 - Space Shuttle Analysis: Shear Stress ( $C_\tau$ ) Distribution .....	213
Figure 8-37 - Space Shuttle Analysis: Heat Transfer ( $C_h$ ) Distribution .....	213

Figure 9-1 - Bolt-On Aerodynamics Package for Low Earth Orbit.....	229
Figure A2-1 - Vector Class Structure .....	249
Figure A2-2 - <i>Aurora.Engineering.ThreeD.WorkSpace</i> Inheritance Hierarchy .....	251
Figure A2-3 - Gas Class Inheritance Hierarchy of the <i>Aurora.Engineering.Aerodynamics.Flow</i> Namespace .....	254
Figure A2-4 - Inheritance Hierarchy and Implementation Structure for the <i>Aurora.Engineering.Aerodynamics.FMF.RayTracer</i> Namespace .....	256
Figure A2-5 - End-to-End Line of Inheritance for the Panel Classes .....	257
Figure A2-6 - SEDAT Database Relationships: Gas-Surface Interaction Model (GSIM) Tables .....	259
Figure A3-1 - Example COM Callable Interface to Perform a FMF Analysis in Microsoft Excel .....	261
Figure A3-2 - <i>GetForceCoefficient</i> Function Executable Code .....	262
Figure A3-3 - Example Code to Perform a Simple FMF Analysis in Microsoft Excel using the Example COM Callable Interface .....	263

## I.ii List of Tables

Table III.I - Definition of Symbols .....	xv
Table III.II - Definition of Subscripts .....	xviii
Table III.III - Definition of Superscripts, Prefixes, and other Symbols.....	xix
Table III.IV - Definition of Acronyms .....	xix
Table III.V - Software Providers .....	xxii
Table 2-1 - Definition of Flow Regimes.....	21
Table 2-2 - Software Tools for the Analysis of Aerodynamic Disturbances on Spacecraft in Free Molecular Flow.....	42
Table 2-3 - Key Elements of Software Systems for the Analysis of Environmental Disturbances on Spacecraft.....	44
Table 4-1 - Some Typical Project Tasks and Information Technologies .....	81
Table 5-1 - Selected Bespoke GUI Components .....	102
Table 6-1 - Advantages and Disadvantages of the Hybrid Method over the RTP and TPMC Methods .....	120
Table 6-2 - Panel Intersection Calculation Methods.....	124
Table 7-1 - Nominal Hybrid Schaaf and Chambre GSIM Parameters .....	166
Table 7-2 - Hybrid Schaaf and Chambre GSIM Bounds .....	168
Table 7-3 - Hybrid Schaaf and Chambre GSIM Attributes .....	168
Table 8-1 - Sphere Analysis: Summary of Inputs.....	177
Table 8-2 - Uniform versus Hot and Cold Temperature Distribution for a Spherical Spacecraft .....	184
Table 8-3 - Corner Plate Analysis: Drag Coefficient.....	187



Table A2-1 - The Database Tables of the FMF Module.....	245
Table A2-2 - The Main Aurora.Engineering.ThreeD.VectorSpace Classes.....	248
Table A2-3 - The Main Aurora.Engineering.ThreeD.WorkSpace Classes.....	250
Table A2-4 - The Main Aurora.Engineering.ThreeD.WorkSpace.RayTracer Classes.....	252
Table A2-5 - The Main Aurora.Engineering.Aerodynamics.Flow Classes.....	253
Table A2-6 - The Main Aurora.Engineering.Aerodynamics.FMF.RayTracer Classes.....	255
Table A2-7 - The Main Aurora.Engineering.Aerodynamics.FMF.RayTracer.GSI Classes....	257
Table A2-8 - FMF Module's Data Access Layer .....	260
Table A3-1 - Example COM Callable Interface: Required References.....	263



## II ACKNOWLEDGEMENTS

When I first decided I wanted to study space engineering I applied to several institutions. However, it was my meeting with Dr Stephen Hobbs in August 2002 that convinced me to pursue my studies at the Space Research Centre at Cranfield University. Dr Hobbs gave me the opportunity to enrol on an MSc by Research in Space Engineering, which later turned into this PhD. For this, I remain very grateful.

I would also like to take this opportunity to thank the two referees who supported my application to Cranfield: Dr Varnavas Serghides of Imperial College, London, who supervised my MEng thesis in aerospace vehicle design and encouraged me to go to Cranfield, where he completed his own doctorate; and Mathea Beck, who took time out of her busy schedule managing the implementation of big IT systems in companies all over Europe to write an embarrassingly nice referral letter for me.

For the contents of this thesis, I have to thank my supervisor Dr Peter Roberts for giving me the freedom I wanted and encouraging my creativity. We had many long, wide-ranging conversations about space, physics, and engineering that were driven by a common curiosity and a desire to do things better. I thoroughly enjoyed these exchanges and thank him for them.

One of the main references dotted throughout this thesis relates to the PhD thesis of Dr Patrick Harkness, who completed his studies at the Space Research Centre in 2006. We relied on one another to validate each other's results and I cannot tell him how grateful I am that they matched!

I would like to thank Dr Yasin Kassim, a good and generous friend, who helped and encouraged me all the way. He understood better than anyone the tedious battle I fought with programming bugs, and thanklessly proof read the first drafts of this thesis.

I would sincerely like to thank all my other friends, relatives, and acquaintances for their encouragement and their commendable attempts at feigning interest these last few years.

Finally, but most importantly, I would like to thank my wife, Martine, for her unwavering support and encouragement, especially during the hard times, slumped in front of my laptop, facing yet another bug.

Ben Graziano  
London, September 2007



### III NOTATION

#### III.i Symbols

**Table III.I - Definition of Symbols**

Symbol	Description
$a$	Speed of sound ( $\text{m s}^{-1}$ ), or plane equation constant
$A$	Area ( $\text{m}^2$ ), or accommodation coefficient curve-fit parameter
$B, C$	Accommodation coefficient curve-fit parameters
$b, c, d$	Plane equation constants
$A_p$	Projected area ( $\text{m}^2$ )
$A_{ref}$	Characteristic area of a body ( $\text{m}^2$ )
$\bar{c}$	Centroid (m)
$c$	Number of constituents in a gas mixture
$C_D$	Drag coefficient
$C_F$	Force coefficient
$C_h$	Heat transfer coefficient
$C_M$	Moment (Torque) coefficient
$C_p$	Pressure coefficient
$C_T$	Torque (Moment) coefficient
$C_\tau$	Shear stress coefficient
$D$	Drag (N)
$d_{avg}$	Mean molecular collision diameter (m)
$E, e$	Energy (J or eV, where 1 eV is equivalent to $1.60 \times 10^{-19}$ J)
$E_A$	Collision activation energy (eV)
$erf$	Error function
$exp$	Exponential ( $e^x$ )
$F_e$	Electromagnetic radiation pressure force (N)
$F$	Force (N)
$f()$	Bridging function, or number density probability distribution function
$g$	Acceleration due to gravity near Earth ( $9.81 \text{ m s}^{-2}$ )
$h$	Height (m)
$\hat{i}$	Incident direction (a unit vector)
$J$	Total number of incident test particles
$k$	Boltzmann constant ( $1.3807 \times 10^{-23} \text{ J K}^{-1}$ ), or panel intersection calculation length factor

$Kn$	Knudsen number
$l$	Length (m), or parametric length
$L$	Lift (N)
$\ln$	Natural log ( $\log_e$ )
$l_{ref}$	Characteristic length of the body (m)
$\dot{m}$	Mass flow rate ( $\text{kg s}^{-1}$ )
$M$	Mach number, or Moment (N m)
$m$	Molar mass ( $\text{kg kmol}^{-1}$ )
$m'$	Molecular mass (kg)
$M_d$	User-defined number of diffusely reemitted test particles
$\hat{n}$	Unit normal direction for a surface or panel (a unit vector)
$n$	Number density (molecules per $\text{m}^3$ ), or number of surface mesh panels
$N$	Molecular number flux (number of molecules per second)
$N'$	Number of real molecules represented by a test particle
$N_A$	Avogadro's constant ( $6.02 \times 10^{26} \text{ kmol}^{-1}$ )
$\bar{p}$	Normal momentum ( $\text{kg m s}^{-1}$ ), or Point of intersection between a ray and a plane (m)
$\hat{p}$	Pressure direction
$p$	Pressure ( $\text{N m}^{-2}$ )
$P()$	Probability function
$P_e$	Electromagnetic radiation pressure ( $\text{N m}^{-2}$ )
$p_o$	Stagnation pressure ( $\text{N m}^{-2}$ )
$q$	Dynamic pressure of a gas flow ( $\text{N m}^{-2}$ )
$Q$	Heat (J)
$r$	Radius (m), or vector from a chosen reference point to the centroid of an elemental area (m)
$\hat{r}$	Reemission direction (a unit vector)
$R$	Universal gas constant ( $8,314 \text{ J kmol}^{-1} \text{ K}^{-1}$ )
$R_1, R_2, R_3$	Panel reemission coordinate system
$Re$	Reynolds number
$R_F$	Computer generated random fraction
$R_{sp}$	Specific gas constant ( $\text{J kg}^{-1} \text{ K}^{-1}$ )
$\hat{s}$	Electromagnetic radiation direction (a unit vector)
$s$	Molecular speed ratio
$S$	Side Force (N), or a body's surface
$\hat{t}$	Tangential direction (a unit vector)
$T$	Temperature ( $^\circ \text{K}$ ), or Torque (N m)

$t$	Parametric length of a ray, time (s)
$T_w$	Surface temperature ( $^{\circ}$ K)
$V, v$	Speed or velocity ( $\text{m s}^{-1}$ ), vertex position (m), or panel direction
$V_a$	Thermal speed, equivalent to the most probable molecular speed of an equilibrium gas with a Maxwellian distribution of velocities ( $\text{m s}^{-1}$ )
$V_b$	Bulk flow speed ( $\text{m s}^{-1}$ )
$V_{cir}$	Circular orbital speed ( $\text{m s}^{-1}$ )
$V_o$	Orbital speed ( $\text{m s}^{-1}$ )
$\omega$	Angular speed or velocity ( $\text{radian s}^{-1}$ )
$x, y, z$	Cartesian axes in physical space
$\hat{Z}$	Direction vector ( $[0, 0, -1]^T$ )
$\vartheta$	Number of internal degrees of freedom of a gas molecule
$\Omega$	Fraction of incident molecules adsorbed
$\alpha$	Angle of attack
$\beta$	Inverse thermal speed ( $1/V_a$ ), or angle of sideslip
$\delta$	Angle of incidence between the incident flow and the surface or panel normal direction
$\epsilon_d, \epsilon_s$	Fractions of incident molecules diffusely reflected, and specularly reflected respectively in the Maxwellian GSIM
$\phi$	Angle that subtends the vector between vertices 1 and 2 and the vector between vertices 1 and 3, or the azimuth angle of a diffusely reemitted test particle
$\gamma$	Ratio of specific heats
$\lambda$	Mean-free path between molecules (m)
$\eta$	Molecular Mach angle
$\mu$	Dynamic viscosity coefficient ( $\text{kg s}^{-1} \text{m}^{-1}$ )
$\mu_{Earth}$	Earth's gravitational constant ( $3.986 \times 10^{14} \text{ m}^3 \text{ s}^{-2}$ )
$\pi$	Pie
$\theta$	Angle of elevation between the flow and the plane of the surface or panel
$\theta_1, \theta_2, \theta_3$	Angles that subtend the vectors that connect the point of intersection between a ray and a plane and a panel's vertices
$\rho$	Density ( $\text{kg m}^{-3}$ )
$\rho_d, \rho_s$	Fractions of incident molecules diffusely reflected, and specularly reflected respectively in the Schaaf and Chambre GSIM
$\sigma_a$	Thermal accommodation coefficient
$\sigma_N$	Normal momentum accommodation coefficient
$\sigma_T$	Tangential momentum accommodation coefficient
$\hat{\tau}$	Shear stress direction (a unit vector)
$\tau$	Shear stress ( $\text{N m}^{-2}$ )

$\bar{\tau}$	Shear momentum (kg m s <sup>-1</sup> )
$\xi_a, \xi_{r_d}, \xi_{r_s}$	Fractions of impinging photons absorbed, diffusely reflected, and specularly reflected respectively
$\psi$	Angle that subtends the vector that connects the point of intersection between a ray and a plane and the vector between the vertices 1 and 2
$\zeta$	Number of degrees of freedom of a gas molecule

**Table III.II - Definition of Subscripts**

Subscript	Represents
$0$	Origin value
$1, 2, 3$	Vertex numbers, position numbers, velocity numbers, or length numbers
$\infty$	A free stream value
$A$	Thermal value
$A, B$	Panel designation
<i>Actual</i>	Actual value
<i>avg</i>	Average value
$b$	Bulk flow value
<i>cir</i>	Circular orbit value
<i>CON</i>	Continuum flow conditions
$D$	Drag value
$d$	Diffusely reemitted flow value
<i>Earth</i>	Earth value
$F$	Force value
<i>FMF</i>	Free molecular flow conditions
<i>Hyper</i>	Hyperthermal value
$i$	Incident value, or integer value (molecule number, gas species number, or panel number)
<i>int</i>	Internal value (relates to energy)
$j$	Integer value (incident test particle number)
$k.e$	Kinetic energy value
$L$	Lift value
$m$	Integer value (diffusely reemitted test particle number)
<i>max</i>	Maximum value
<i>min</i>	Minimum value
<i>mol</i>	Molar value
$M$	Moment value
$N$	Normal momentum value



$O$	Stagnation point value, or orbital value
$p$	Projected value
$Q$	Heat value
$r$	Reflected flow value
$ref$	Reference value
$S$	Side force value
$s$	Specularly reemitted flow value
$s/c$	Spacecraft body-fixed coordinate system
$T$	Tangential momentum value, or torque value
$Total$	Total value
$trans$	Translational value (relates to kinetic energy)
$w$	Surface (wall) value
$x$	Component in the x direction
$y$	Component in the y direction
$z$	Component in the z direction
$\omega$	Angular velocity component

**Table III.III - Definition of Superscripts, Prefixes, and other Symbols**

Symbol	Represents
$\bar{x}$	Mean value, or vector
$\hat{x}$	Unit vector
$\Delta x$	A small change, or elemental quantity
$x'$	A test-particle quantity (except in the case of molecular mass)
$ x $	A normalised vector quantity
$\dot{x}$	Flow rate
$\rightarrow x$	In the direction of

### III.ii Acronyms

**Table III.IV - Definition of Acronyms**

Acronym	Description
3D	Three-Dimensional
3NF	Third Normal Form (Database Design Standard)
API	Application Programming Interface

BNSC	British National Space Centre
CAD	Computer-Aided Design
CAM	Computer-Aided Manufacture
CD	Compact Disc
CDF	Concurrent Design Facility (ESA)
CE	Concurrent Engineering
CEW	Concurrent Engineering Workshop (ESA)
CFD	Computational Fluid Dynamics
CLL	Cercignani-Lampis-Lord (Gas-Surface Interaction Model)
CLR	Common Language Runtime (Microsoft .Net technology)
CNES	French Space Agency (Centre National d'Etudes spatiale)
CODE	COncurrent Development Environment (of Alenia Spazio <sup>1</sup> )
COM	Component Object Model
CRM	Customer Relationship Management
DAL	Data Access Layer
DLL	Dynamic Link Library (file)
DSMC	Direct Simulation Monte Carlo (Method)
EOL	End-Of-Life
ERP	Enterprise Resource Planning
ESA	European Space Agency
ESTEC	European Space Technology and Research Centre
FA	Financial Accounting
FK	Foreign Key
FMF	Free Molecular Flow
GFR	Gas Flow Ray
GG	Gravity Gradient
GSI	Gas-Surface Interaction
GSIM	Gas-Surface Interaction Model
GUI	Graphical User Interface
GUID	Globally Unique Identifier
H-SC	Hybrid Schaaf and Chambre (GSIM)
HTML	Hypertext Markup Language
IADC	Inter-Agency Space Debris Coordination Committee
IDM	Integrated Design Model (ESA CDF)
ISES	International Space Environment Service

---

<sup>1</sup> Alenia Spazio: [www.alespazio.it](http://www.alespazio.it)

ISO	International Standards Organisation
ISS	International Space Station
IT	Information Technology
K & P	Knechtel and Pitts
KBE	Knowledge Based Engineering
LEO	Low Earth Orbit
MD	Molecular Dynamics
MDO	Multidisciplinary Design Optimisation
MSISE	Mass Spectrometer and Incoherent Scatter Radar (Earth atmospheric model, where the E indicates that it extends from the ground to space)
NASA	National Aeronautics and Space Administration (USA)
OCDS	Open Concurrent Design Server (ESA CDF)
ODBMS	Object (orientated) Database Management System
OMS	Orbital Manoeuvring System (of the Space Shuttle)
OOP	Object-Orientated Programming
PDC	Project Design Centre (NASA)
PhD	Philosophy Doctorate
PK	Primary Key
PLM	Product Lifecycle Management
POA	Precise Orbital Analysis
PPRL	Processing, Presentation, and Reporting Layer
RDBMS	Relational Database Management System
RT	Real-Time
RTP	Ray-Tracing Panel (method)
SAR	Synthetic Aperture Radar
SC	Schaaf and Chambre
SCM	Supply Chain Management
SDO	Satellite Design Office (of EADS Astrium <sup>2</sup> )
SEDAT	Spacecraft Engineering, Design, and Analysis Tools
SEE	Single Event Effect
SFR	Shadow Feeler Ray
SLR	Satellite Laser Ranging
SQL	Structured Query Language
SRC	Space Research Centre (Cranfield University)
SRP	Solar Radiation Pressure
STEP	STandard for the Exchange of Product model data

---

<sup>2</sup> EADS Astrium: [www.space.eads.net](http://www.space.eads.net)

TLE	Two-Line Elements
TPMC	Test-Particle Monte Carlo
U{x}	Unique Key {x}
UAT	User Acceptance Testing
UI	User Interface
UK	United Kingdom
UML	Unified Modelling Language
USA	United States of America
USAF	United States Air Force
VB	Visual Basic
VBA	Visual Basic for Applications
VR	Virtual Reality
XML	Extensible Mark-up Language

### III.iii Software Providers

**Table III.V - Software Providers**

Name	Provider
Satellite Tool Kit (STK)	Analytical Graphics ( <a href="http://www.stk.com">www.stk.com</a> )
AutoCAD	AutoDesk ( <a href="http://www.autodesk.com">www.autodesk.com</a> )
Crystal Reports	Business Objects ( <a href="http://www.businessobjects.com">www.businessobjects.com</a> )
Autovue	Cimmetry ( <a href="http://www.cimmetry.com">www.cimmetry.com</a> )
.Net, Access, Excel, SQL Server, Visual Studio .Net, DirectX, Visual Basic .Net (VB.Net), ActiveX Data Objects (ADO.Net), Windows XP	Microsoft ( <a href="http://www.microsoft.com">www.microsoft.com</a> )
Oracle Business Suite, Oracle Database	Oracle ( <a href="http://www.oracle.com">www.oracle.com</a> )
SAP	SAP ( <a href="http://www.sap.com">www.sap.com</a> )
MATLAB	The Mathworks ( <a href="http://www.mathworks.com">www.mathworks.com</a> )

# 1 INTRODUCTION

This chapter provides the background and evolution of ideas behind the work and explains the rationale for it. It describes the reasons for picking the two main themes of the research: spacecraft aerodynamics and concurrent engineering. It then describes the objectives of the work in relation to the themes.

A summary of the approach taken to meet the objectives is also presented, along with a chapter road map to assist with navigating the thesis. Finally, an indication is given of the scope of the work undertaken and the scope of the thesis.

## 1.1 Background

There are a number of research areas currently being investigated within the Space Research Centre (SRC) at Cranfield University. One of the areas is space debris mitigation.

In this context, space debris refers to man-made debris, consisting of the remnants of rockets, satellites, and other man-made orbital objects that no longer serve any useful purpose. Mitigation refers to the removal of these objects from orbits in which they risk affecting an ongoing spacecraft mission. According to the United Nations Technical Report on Space Debris [1]:

*“... the implementation of some debris mitigation measures today is a prudent step towards preserving space for future generations. In some cases, technical work remains to be done to determine the most effective and cost-efficient solutions”*

The Inter-Agency Space Debris Coordination Committee (IADC) provides a set of guidelines for space debris mitigation and describes the different mitigation strategies available [2]. The guidelines are based on a number of studies including the ESA Handbook on Space Debris [3]. One of the guidelines, which has been widely adopted by most major national and international space agencies, states that satellites in orbits up to an altitude of 2000 km should have their post-operational lifetime limited to 25 years.

Prior to the start of this research project, the SRC had been researching several mitigation methods that would address this requirement. One of these was the use of a bolt-on spacecraft component, known as a drag deorbit device [4].

The idea behind the device is that when activated at the end of the satellite's useful life it deploys a drag sail. At altitudes below approximately 1000km, the large area of the sail would increase the aerodynamic drag of the satellite and therefore reduce its orbital energy.

There are currently 418 operational satellites in low Earth orbit and 324 of these operate below approximately 1000 km [5]. Therefore, it was foreseen that a significant reduction in space debris could be achieved if future low altitude missions employed such a device.

Preliminary calculations indicated that the sail would gradually lower the satellite's orbit until it collapsed under increased aerothermodynamic loading, as shown in Figure 1-1, and both the satellite and the device would then burn-up on re-entry [6][7]. It was estimated that an effective design could produce enough drag to deorbit a spacecraft in as little as two to three months, instead of two years [8].

The drag deorbit device concept was not an entirely novel idea since other studies had proposed similar solutions [9][10], and it was latterly found that the French Space Agency (CNES) had been developing a similar device for their MYRIADE family of spacecraft, one of which is due to launch in 2010 [11].

However, in 2002, at the start of this research project, a detailed engineering analysis of the technological feasibility of using a device of this kind had not been published. In addition, ongoing work within the SRC suggested that more research was necessary to validate the aerodynamic calculations that under-pinned the concept. This was not only because the design of the device was uncertain, but also because the concept behind the device is that it should be capable of functioning when coupled to a wide variety of spacecraft with differing shapes, characteristics, and mission profiles.



**Figure 1-1 - Collapsing Drag Sail**

**Image credit Harkness [12], background credit Google Earth. Image shows the fully deployed drag sail collapsing during re-entry.**

At the time, the aerodynamic analysis methods that had been used within the SRC were restricted to simple two-dimensional convex shapes, using a simplified atmospheric model. Therefore, some means of analysing the aerodynamic response of any spacecraft, of arbitrary three-dimensional shape, in low Earth orbit, using an

accurate model of the neutral Earth atmosphere was required. This was the starting point for the research described in this thesis into spacecraft aerodynamics, and specifically spacecraft aerodynamic analysis tools.

## 1.2 Evolution of Ideas

During the first year of research, an extensive literature survey was conducted into spacecraft aerodynamics and the tools used to perform analyses of spacecraft in the low Earth orbit regime of spaceflight. Limitations identified in these tools, their immediate availability, and the need to understand more about the underlying physics of the problem led to the development of a prototype spacecraft aerodynamic analysis tool.

Patrick Harkness joined the SRC in 2003 to begin research into the systems engineering aspects of the concept and demonstrate its applicability [12]. His complementary work effort enabled this research to take an even more detailed look at spacecraft aerodynamic analysis methods and address some related issues.

In early 2004, a three-month period of paid internship for the spacecraft prime contractor EADS Astrium<sup>1</sup>, based in Portsmouth, provided first-hand experience of spacecraft engineering.

Assigned to the Skynet 5 military communications satellite project, as part of the project management team reporting to the programme director (Patrick Wood), project-wide access was granted. This led to a better understanding of both the project management and information systems' challenges of spacecraft engineering. Two of the three planned Skynet 5 satellites are illustrated in Figure 1-2.

The Skynet 5 role involved development of a strategy for developing and maintaining an intellectual property rights register for the complete system. One of the major challenges of the role was identifying a reliable and appropriate system breakdown structure for both the space and ground segment. Multiple independent system breakdown structures existed for different purposes, but none of them provided the complete picture, nor were they connected in any way.

Anecdotal evidence from discussions with colleagues suggested that issues such as duplication of work effort, the use of multiple redundant information systems, and the lack of data continuity between information systems are common to most spacecraft engineering projects. However, earlier experiences operating as a professional freelance information technology consultant for several years suggested an integrated information systems approach as a solution to these issues.

Around the time of the paid internship, funding issues forced a temporary suspension of registration while six months of paid contract work was carried out

---

<sup>1</sup> EADS Astrium: [www.space.eads.net](http://www.space.eads.net)

(spread over nine months with the internship in-between). After this period, continued funding concerns prompted a short two-month period of study for the qualification of Microsoft Certified Professional in Developing Windows-Based Applications. The combined eleven-month pause in work during 2003-2004 created an opportunity to evaluate the direction the research was taking.



**Figure 1-2 - Skynet 5 Military Communications Satellites**  
Image credit Paradigm Secure Communications<sup>1</sup>.

The multi-disciplinary dependencies of aerodynamic analysis and the large amounts of data involved indicated that the prototype tool could be significantly enhanced by improving its underlying relational database management system. It was also discovered that some existing spacecraft aerodynamic analysis tools had more advanced features than the prototype tool, such as the capability to model multiple flow reflections. As a better understanding of spacecraft aerodynamics developed, it was realised that these features, as well as some other unique features would be needed to perform a comprehensive analysis of the drag deorbit device concept.

There were continued uncertainties over the device's design, concerns regarding the as yet unquantified effect of aerodynamic damping, as well as inherent uncertainties over the types of satellite the device might be attached to, and the flight scenario that the device might encounter. This later uncertainty became an increasing concern because a detailed review of rarefied gas dynamics revealed that different types of gas-surface interaction models and associated input parameters exist for different spaceflight scenarios.

---

<sup>1</sup> Paradigm Secure Communications: [www.paradigmsecure.com](http://www.paradigmsecure.com)



It was realised that a state-of-the-art spacecraft aerodynamic analysis tool must be able to handle large amounts of data, calculate aerodynamic damping terms, model multiple flow reflections, and incorporate multiple different gas-surface interaction models.

In October 2004, the first Concurrent Engineering for Space Applications Workshop (CEW) took place at ESA's ESTEC facility. The embryonic nature of the workshop, previous professional experiences, the work that had been completed, the knowledge acquired from the internship, and the Microsoft qualification all suggested a new tool could also be used to demonstrate how the entire spacecraft development process could be expedited via the use of concurrent engineering principles facilitated by modern information systems methodologies.

This view was further reinforced by attendance of the Eighth International Workshop on Simulation for European Space Programmes (SESP) in October 2004. The workshop galvanised the idea that the client-server model exemplified by enterprise applications, which incorporates multiple integrated modules presented via a single GUI connected to a centralised relational database management system, could be applied to the entire spacecraft design and development lifecycle.

Two years of work followed to develop the idea and create the SEDAT System and FMF Module. The former demonstrating the application of concurrent engineering principles and modern information systems methodologies. The latter providing a practical demonstration of concept, in the form of a feature-rich state-of-the-art free molecular flow spacecraft analysis tool.

### **1.3 Rationale**

The original motivation for the research project was to analyse the aerodynamics of the drag deorbit device that had been proposed by the SRC for mitigating space debris in low Earth orbit. However, as described in the previous section, numerous factors combined to present a novel method for achieving this. A method that incorporated new aerodynamic analysis techniques whilst simultaneously providing a platform for demonstrating an innovative approach to implementing concurrent engineering across the spacecraft development lifecycle.

### **1.4 Objectives**

Based upon the background, evolution of ideas, and rationale described above, the objectives of this research are:

1. To develop a desktop computing tool that can be used by any appropriately trained systems engineer to perform aerodynamic calculations on spacecraft operating in the free-molecular flow regime.

2. To use the tool to perform the required aerodynamic analyses of the drag deorbit device currently under development within the SRC.
3. To use the tool to demonstrate how the client-server model successfully employed by enterprise applications, which incorporates a centralised relational database management system, can be used to facilitate concurrent engineering across the entire spacecraft development lifecycle.
4. To ensure that future developers and investigators can easily modify the tool and add functionality to it.

## **1.5 Approach**

The thesis roadmap, shown in Figure 1-3, illustrates the relationships between each chapter. It also describes the main topics of each chapter and how they are related to spacecraft aerodynamics and concurrent engineering, which are the two main themes of the thesis.

As Figure 1-3 illustrates, Chapters 2, 3, and 4 begin by introducing these themes. They present contemporary research into spacecraft aerodynamics and concurrent engineering and identify some of the challenges presented by them.

Chapter 5 suggests a solution to some of the concurrent engineering challenges identified. Chapters 6 and 7 provide a practical demonstration of this solution that addresses the aerodynamic analysis requirements of the thesis.

Chapter 8 presents the results of several aerodynamic analyses and provides a detailed discussion of them.

Chapter 9 assesses the concurrent engineering solution proposed, and provides overall conclusions and suggestions for further work.

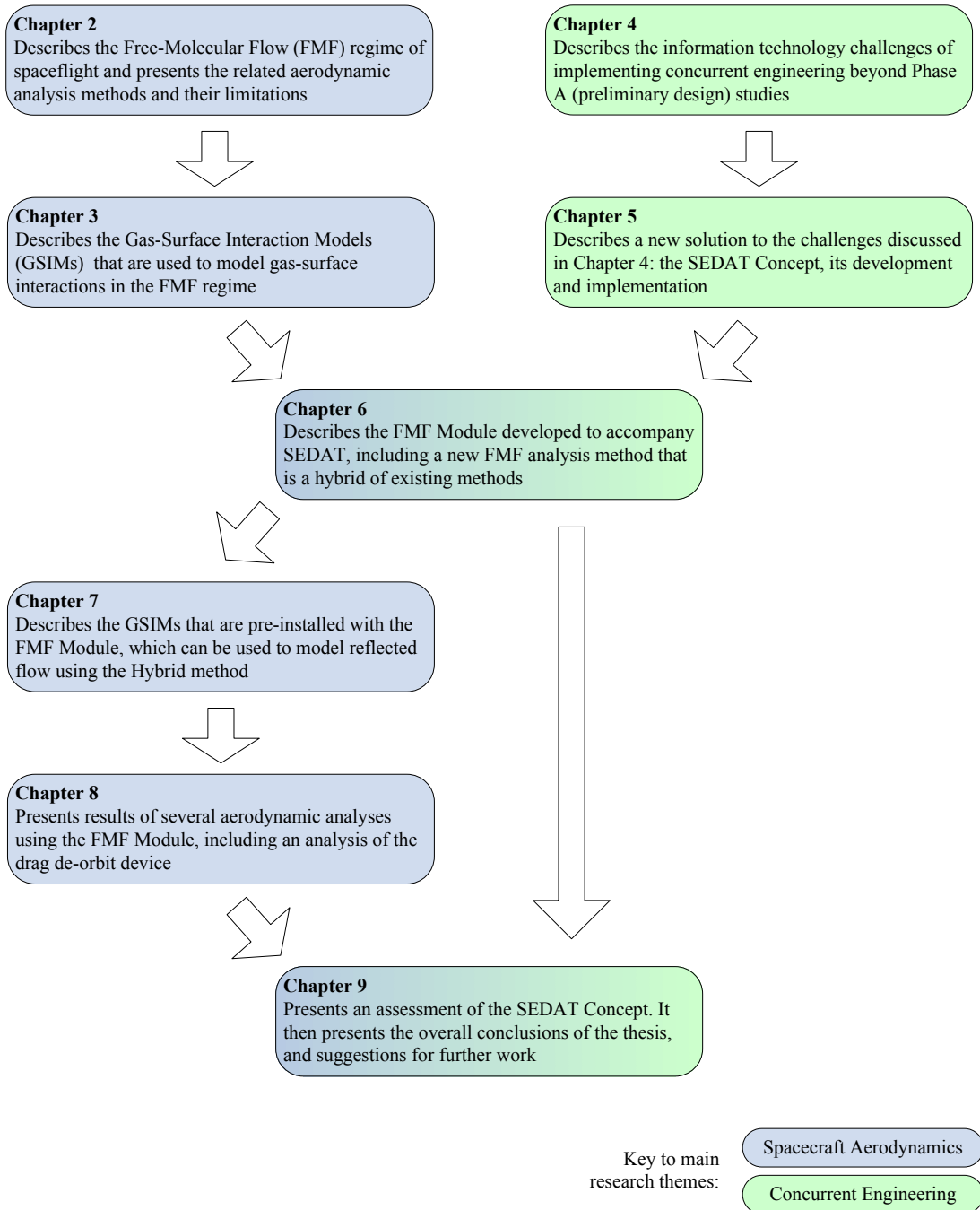


**Figure 1-3 - Thesis Roadmap**

## 1.6 Scope

The lifetime and resources of a PhD project are finite. In order to meet the objectives of the research it was not possible to explore every avenue of investigation or present every aspect of the work carried-out. This section describes, in broad terms, the boundaries of the project and the thesis.

For further detailed information regarding areas of investigation that are directly related to the current study, but out of scope, please refer to the suggestions for further work outlined in Section 9.4.

### 1.6.1 Spacecraft Aerodynamics

The current study concentrates on those aspects of rarefied gas dynamics that are relevant to spacecraft flight in the neutral free-molecular flow regime of low Earth orbit. This excludes subsonic and hypersonic launch phases, re-entry analysis, ablation of surface materials, aspects related to other planetary atmospheres, the effects of plumes, out-gassing, ionized gas flows (plasma), chemically reacting flows, and other neutral atmosphere effects (for example, sputtering, and atomic oxygen attack) except where related to gas-surface interactions (for example, the effect of atomic oxygen attack on gas-surface interaction model parameters, such as accommodation coefficients).

### 1.6.2 Concurrent Engineering

Concurrent engineering is a broad and relatively mature subject. However, for a variety of reasons it is just recently that the space industry has started to investigate it: the first Concurrent Engineering for Space Applications Workshop (CEW) only took place at ESA's ESTEC facility as recently as 2004. The majority of speakers and attendees at this workshop, as well as the second workshop held in 2006 were representatives from industry; indicating the practical nature of the topic.

Therefore, the thesis concentrates on the application of concurrent engineering principles within the space industry. Emphasis is placed on what can be learnt from other industries and business sectors that were directly encountered by the author in a professional capacity.

The thesis does not look in detail at concurrent engineering facilities used for conceptual design studies (Phase A and Pre-Phase A studies), such as ESA's Concurrent Design Facility (CDF). There are two reasons for this:

1. Unlike a small number of other universities and organisations, the SRC does not have its own CDF-type facility from which to draw direct knowledge or experience.
2. The emphasis of this work is on the application of concurrent engineering principles across the entire spacecraft design and development lifecycle (*i.e.*, *beyond Phase A*).

Further restrictions on the scope of the concurrent engineering methodologies employed to achieve the objectives of the research are discussed in Section 5.2.

### **1.6.3 Systems Engineering**

The thesis investigates those aspects of systems engineering that are directly related to the implementation of concurrent engineering and the development of SEDAT and the FMF Module. For example, it does not look in detail at those aspects of spacecraft dynamics and control that could utilise the results generated by the FMF Module. Those aspects have been thoroughly investigated within the SRC by the related research of Harkness [12] in his analysis and design of the drag deorbit device.

### **1.6.4 Computing**

The many computational aspects of the research have required the use of multiple new information technologies that have significantly contributed to meeting the overall objectives. However, the individual technologies themselves, and the details of their use, have only been considered relevant to the study if they enhanced the features of the SEDAT System or FMF Module in a novel way that specifically meets the objectives. For example, the features of the graphics engine, the reporting functionality, or the GUI components are not described in detail, despite their many unique aspects.

For specific information regarding a particular technology, please refer to the relevant links and references in the text, or the help documentation that accompanies the SEDAT System, which is provided in digital format in the *Help* folder in Appendix 1.

## **1.7 Summary**

This chapter has provided the background to the thesis and explained the origin and evolution of the ideas behind it. It has provided the rationale for the thesis and defined its objectives. It has also outlined the approach that will be taken to explain the main ideas of the thesis. The scope of the thesis has also been described in some detail in order to provide some rationale for the boundaries of the thesis.

As explained in Section 1.1, the initial motivation for this work was to perform an aerodynamic analysis of the Drag Deorbit Device concept. For this reason, the following chapter (Chapter 2) provides a review of contemporary spacecraft aerodynamics.



## 2 SPACECRAFT AERODYNAMICS

The relative magnitudes of the main forces acting on a spacecraft in Low Earth Orbit (LEO) are shown in Figure 2-1. As illustrated in the figure, spacecraft aerodynamic forces can be significant at low orbital altitudes. This is because they are directly proportional to atmospheric density, which increases exponentially with decreasing altitude.

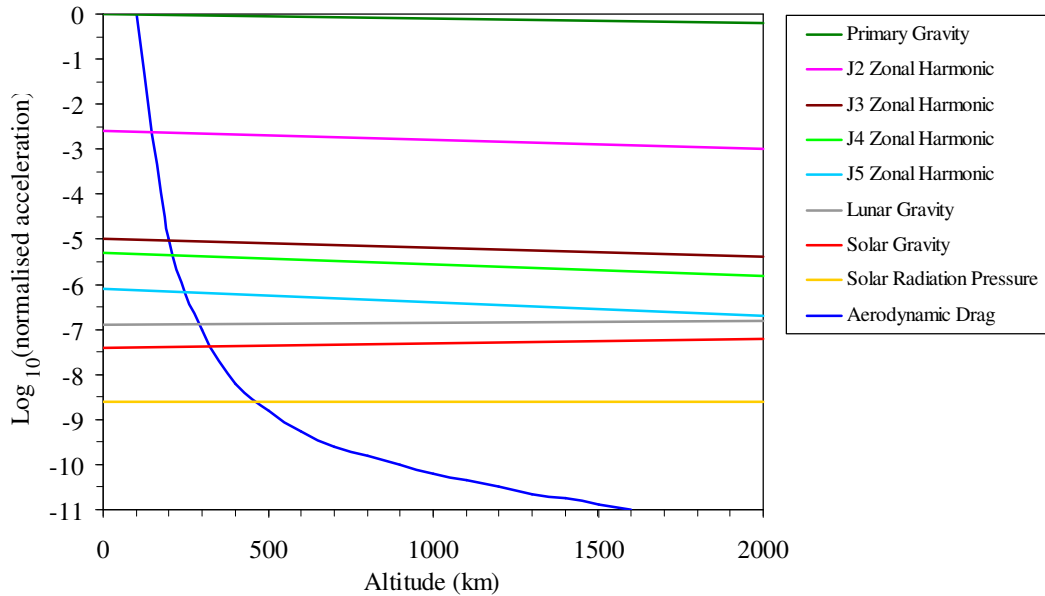


**Figure 2-1 - Comparison of the Main Disturbing Accelerations on Spacecraft in Low Earth Orbit**

Reproduced from [13]. Accelerations are normalised by primary gravity at ground level.

Aerodynamic drag, in particular, can have a significant effect on spacecraft in LEO. The effects of aerodynamic drag are to reduce orbital energy, and circularise and lower a satellite's orbit [14].

These effects are used advantageously by the SRC's drag deorbit device concept [12]. However, operational satellites in LEO often need to have their orbits routinely boosted to counter these effects. The frequency of these manoeuvres varies according to operational requirements and atmospheric conditions. All such manoeuvres utilise fuel and, as a result, drag correction manoeuvres are often the determining factor for satellite operational lifetime in LEO.

In addition to drag, transverse aerodynamic forces, usually referred to as lift and side force, can affect a spacecraft's orbit. Furthermore, the aerodynamic torques that result from lift, drag, and side force can affect spacecraft attitude and have a significant bearing on operational performance.

This chapter describes the atmospheric conditions of low Earth orbit spaceflight and highlights some of the aspects of the neutral Earth atmosphere that must be considered during aerodynamic analysis. It then describes the flow regime of Earth spaceflight and introduces some of the important aerodynamic parameters of this regime. The different aerodynamic analysis methods that can be applied to this regime of spaceflight are reviewed and contrasted. Finally, some of the existing aerodynamic analysis tools are described and evaluated.

## **2.1 The Neutral Earth Atmosphere**

This section describes the atmospheric model that has been selected for this study. It then details some of the main features of the neutral Earth atmosphere that are relevant to spacecraft aerodynamics.

### **2.1.1 Atmospheric Model**

The Earth's atmosphere is constantly changing under the influence of multiple phenomena. Consequently, spacecraft aerodynamicists are reliant upon aeronomists for an accurate model of the atmosphere. Reciprocally, aeronomists are equally reliant upon spacecraft aerodynamicists to help them understand the satellite measurements that enable them to build their models.

Numerous models have been developed from a variety of data sources. Some of them use accelerometer, pressure gauge, and mass-spectrometer measurements taken onboard satellites and sounding rockets (see, for example, [15]). Others use ground-based observation of satellite and rocket trajectories. From these data, smoothed density models are calculated across a range of altitudes assuming a constant drag coefficient of 2.2.

The value of 2.2 was based upon early estimates of the drag coefficient for a spherically shaped satellite [16]. However, later studies indicated that the actual value may be as low as 1.68 [17]. Today, it is acknowledged that accurate determination of drag coefficients depends on a number of factors, many of which are described throughout this thesis. In particular, improvements in the understanding and calculation of satellite drag coefficients have demonstrated that the underlying assumption that a satellite will have the same coefficient of drag at all altitudes is incorrect, as illustrated by Figure 2-2.

The Earth atmospheric model used throughout this paper is the MSISE-90 model, currently recommended by ESA [18]. It has been reported that this model overestimates air density by up to 15% at some altitudes because of the constant drag coefficient assumption [19]. Other authors, who have applied methods to correct for the constant drag coefficient assumption during aerodynamic analysis, corroborate the finding that the MSISE-90 model overestimates density [20].



Through a process of iteratively feeding-back improved estimates of drag coefficients into atmospheric models, some of these inaccuracies should diminish in future using the recently developed technique of atmospheric model density calibration [21]. However, at present, the MSISE-90 model, like other atmospheric models, should be used with caution.

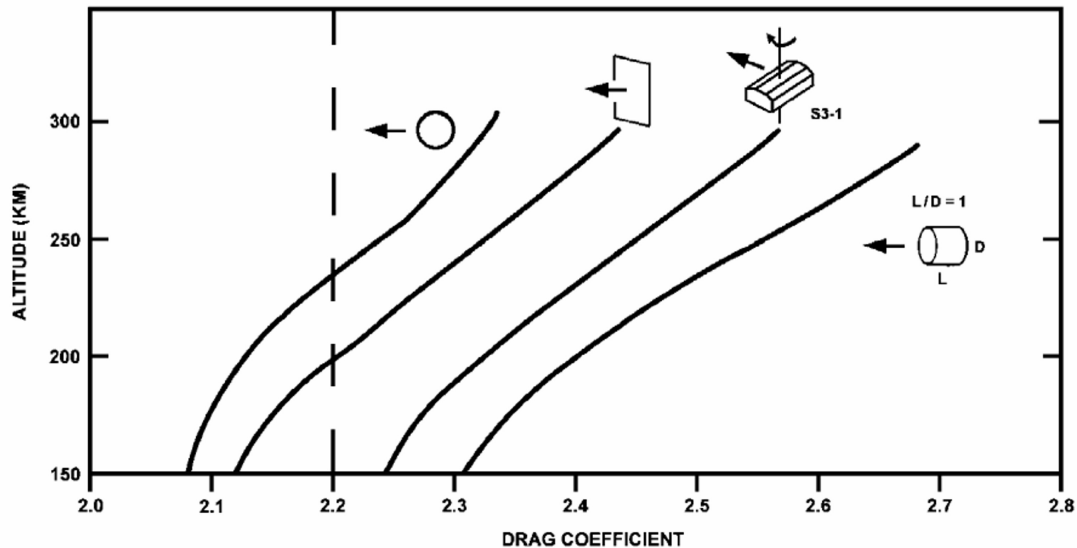


**Figure 2-2 - Variation of Satellite Drag Coefficients with Altitude**

**Image Credit [19]. Assumes diffuse reemission of incident molecules and atmospheric conditions of low solar activity. The trend lines from left to right are for a spherical satellite, a flat plate with normal incident flow, a spinning satellite, and a short cylindrical satellite with its flat front-face normal to the incident flow.**

### 2.1.2 Characteristics

Below approximately 85-120 km, satellites cannot maintain orbit and will enter a re-entry flight trajectory due to the increased aerodynamic drag they experience. Therefore, the neutral atmospheric regions of interest to this study are the high-altitude heterospheric regions that exist above 85 km, comprised of the thermosphere and the exosphere. These regions are illustrated in Figure 2-3.

The heterospheric regions are defined by their temperature profiles. The thermosphere absorbs the most ultra-violet energy from the Sun (predominantly due to the atomic oxygen in this region). As a result, its temperature increases exponentially with altitude between the homopause and the thermopause. In contrast, the exospheric temperature remains constant with altitude (at the asymptotic limit of the thermospheric temperature), due to the infrequency of intermolecular collisions that occur in this more rarefied region.

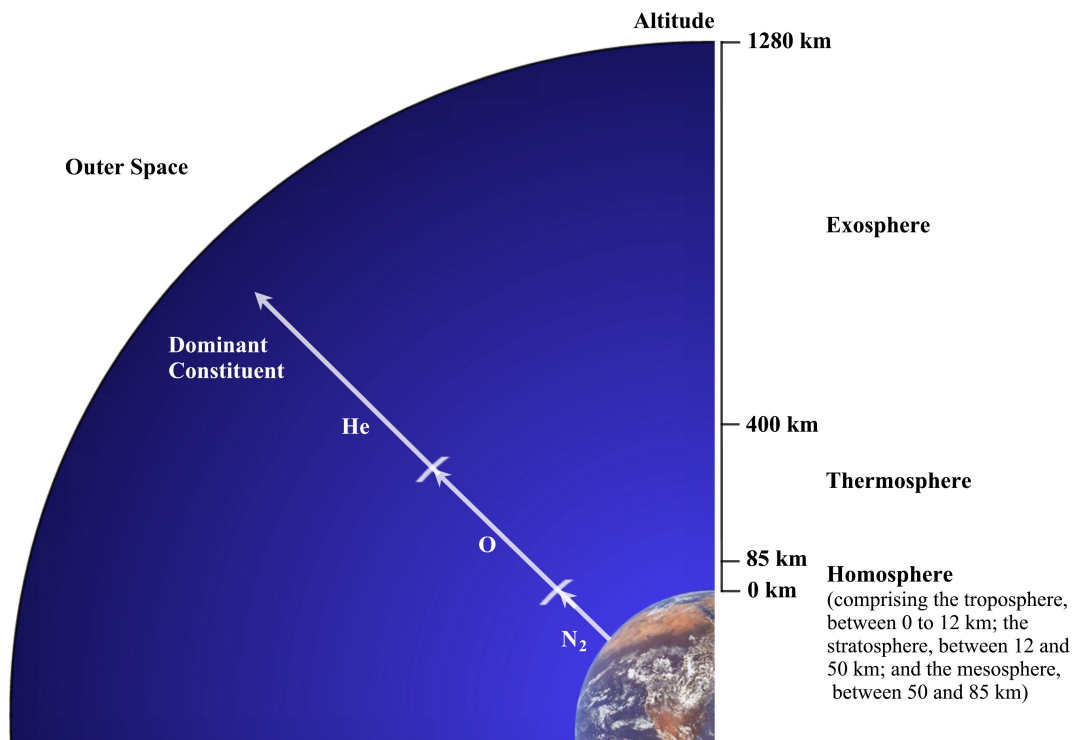


**Figure 2-3 - The Neutral Earth Atmosphere**

Scales assume mean solar conditions, based on the MSISE-90 atmospheric model [18]. The Earth is not drawn to scale. Earth image credit NASA.

The altitude and dominant constituent scales illustrated in Figure 2-3 are approximately accurate for a mean solar activity level. However, solar activity levels vary over an eleven-year cycle. Variation in the heterospheric temperature profiles described previously for low, mean, and high levels of solar activity over this cycle, as defined by [18], are illustrated in Figure 2-4.

As Figure 2-5 illustrates, at the orbital altitude of the International Space Station (approximately 340 km), atmospheric density varies by up to almost two orders of magnitude across a single solar cycle. It is this effect on atmospheric density, caused by the solar cycle, which is the dominant factor affecting spacecraft aerodynamic performance [22]. One well-known consequence of this is that during periods of high solar activity, satellites in low Earth orbit deorbit quicker and have their operational lifetimes reduced as a result.

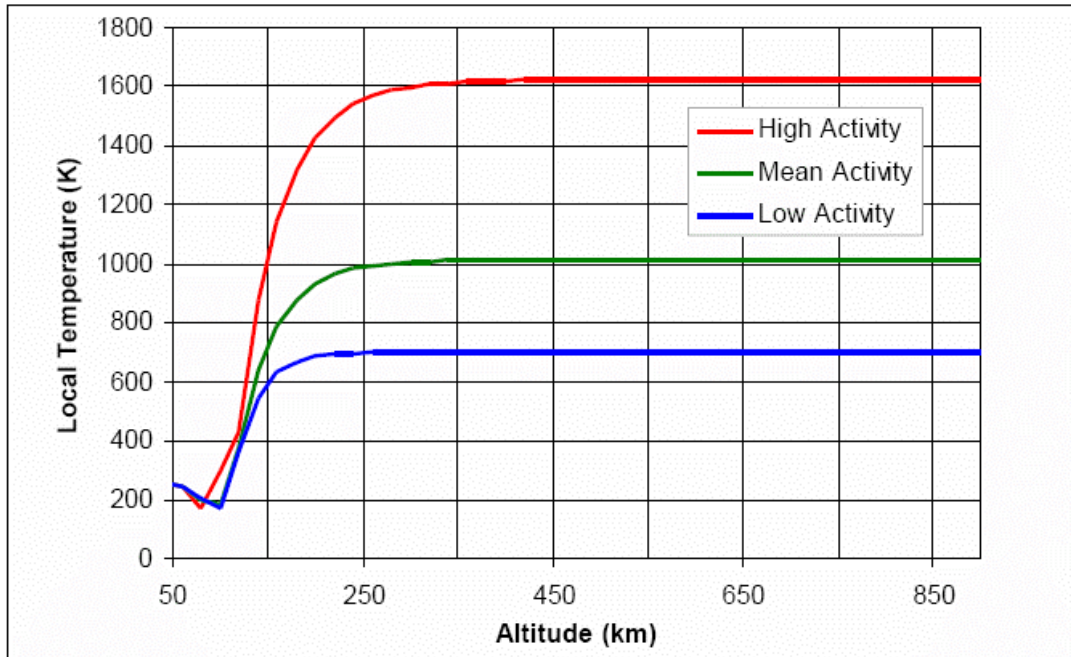


**Figure 2-4 - Variation of the Earth's Atmospheric Temperature with Altitude for Low, Mean, and High Solar Activity Levels**  
Image credit [18]

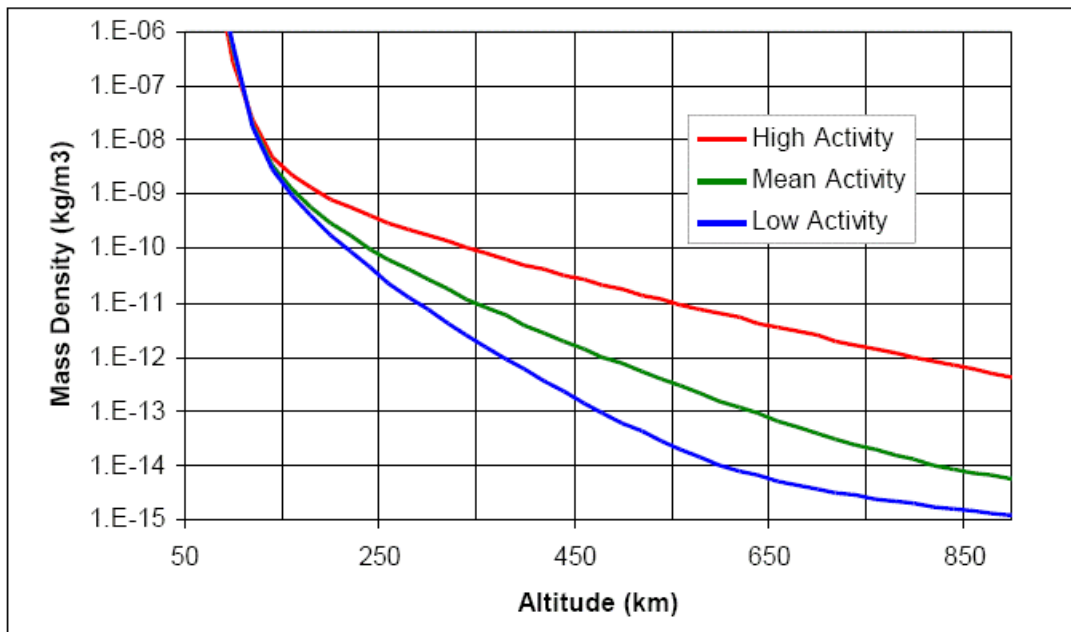


**Figure 2-5 - Variation of the Earth's Atmospheric Density with Altitude for Low, Mean, and High Solar Activity Levels**  
Image credit [18]

The composition of the atmospheric gas mixture varies with altitude, as illustrated in Figure 2-6. These variations are due to gravity acting more strongly on

molecules with higher mass, as well as because chemical reactions and ultra-violet energy from the Sun cause molecular bonds to break at higher altitudes.

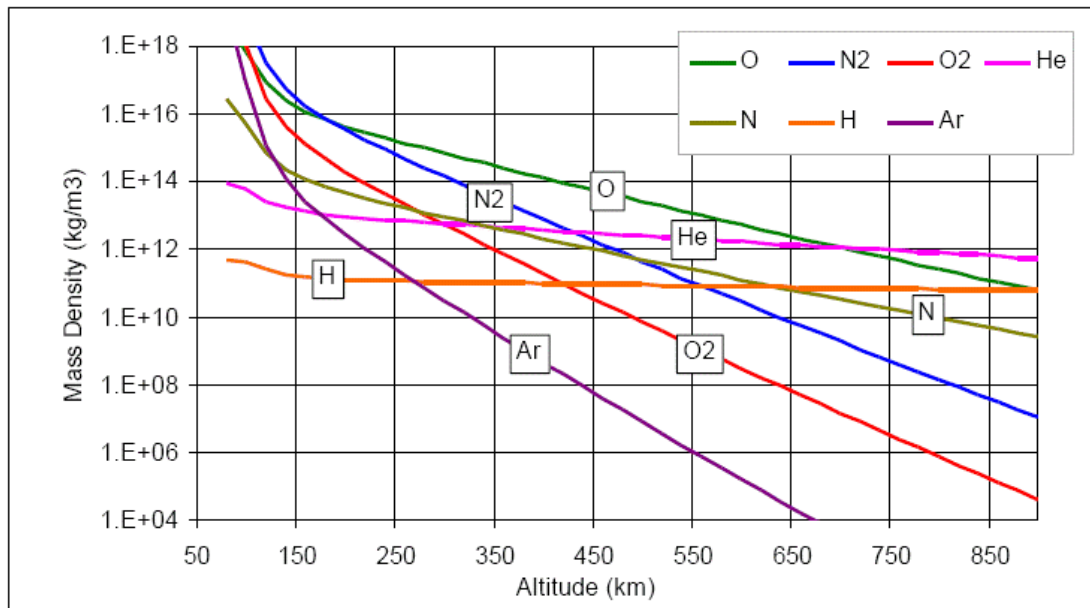


**Figure 2-6 - Variation of the Earth's Atmospheric Composition with Altitude**  
Image credit [18]

In addition to these variations, atmospheric composition will fluctuate as the atmosphere expands and contracts under the influence of the solar cycle. Such that a spacecraft orbiting at a constant altitude over the period of a single solar cycle will not only experience an increase in density and temperature as the solar activity level rises, but may also experience a change in dominant gas species.

If variations in atmospheric composition are not taken into account during spacecraft aerodynamic calculations then significant errors will arise due to the varying molar mass and ratio of specific heats of the gas mixture.

Besides the effects of the solar cycle, more transient and localised effects due to diurnal, seasonal, longitudinal, and latitudinal variations in atmospheric conditions, as well as the effects of winds (caused primarily by the Earth's rotation and the Coriolis effect), may need to be accounted for in the aerodynamic analysis of a specific mission. Overall, their effects on aerodynamic performance are less significant than solar-cycle variations in atmospheric density and composition. However, they can be important over shorter timescales and because of the periodic excitations that they may cause over repeated orbits.

For example, winds, acting predominantly in the local horizontal plane, can reach speeds of up to  $500 \text{ m s}^{-1}$  or more in Polar Regions during nightfall [23]. Furthermore, diurnal variations in atmospheric density (a variation of approximately 10-20%, depending on solar activity, at the orbital altitude of the International Space

Station) have been shown to alter the predicted deorbit times of satellites coupled to a drag deorbit device [12].

Geomagnetic fluctuations caused by solar storms, which occur more frequently during periods of peak solar activity, have been shown to increase thermospheric density by up to a factor of five [24]. However, such events are unpredictable, short-lived, and of varying magnitude. In addition, they have been shown to have little long-term effect on satellite lifetime [22]. Therefore, they are generally not worth specific aerodynamic consideration.

In 1860, the Victorian art critic John Ruskin said that the sky is “*Sometimes gentle, sometimes capricious, sometimes awful, never the same for two moments together; almost human in its passions...*” [25]. Recently, new evidence has suggested that the upper atmosphere is cooling because of rising levels of anthropogenic greenhouse gases [26]. This cooling is contracting the atmosphere and has already resulted in a 2-3% lowering of thermospheric density per decade over the past few decades. The cooling trend of the upper atmosphere, as well as the warming trend of the lower atmosphere, are illustrated in Figure 2-7.

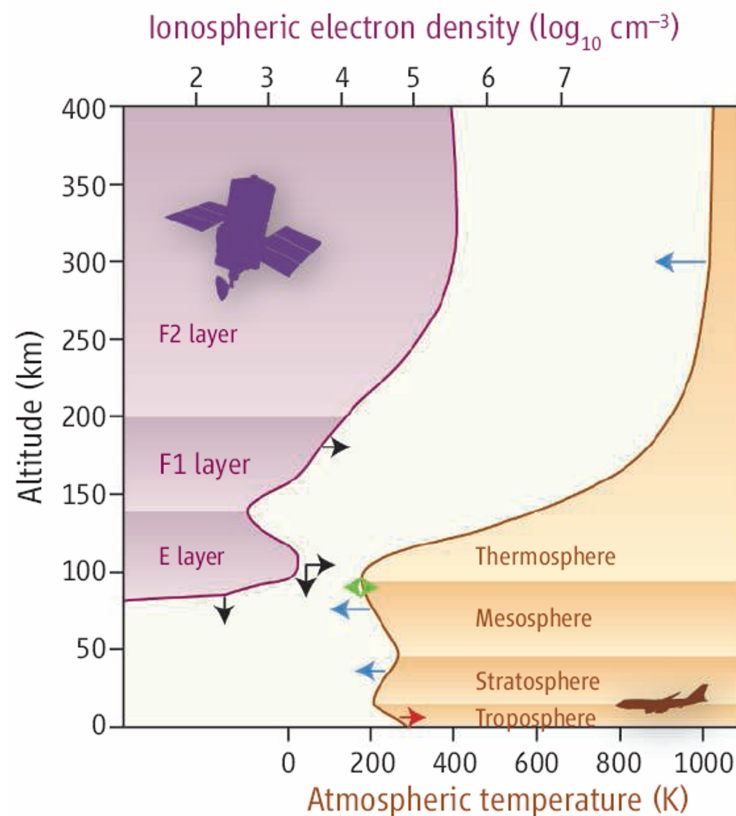


**Figure 2-7 - Structure and Trends in the Earth's Atmosphere**

“Atmospheric layers (orange, right) are defined by the temperature profile. Ionospheric layers (purple, left) are defined by the electron density profile (shown here at midnight at the equator). Arrows denote the direction of observed changes in the past 3 to 4 decades: Red, warming; blue, cooling; green, no temperature change; black, changes in maximum electron density (horizontal) and the height of ionospheric layers (vertical).” Image and caption credit [26].

Humanity's influence on the upper atmosphere will benefit some spacecraft missions. For example, low Earth orbiting satellites will require fewer aerodynamic drag correction manoeuvres and have an increased lifespan.

Unfortunately, the anthropogenic effects on the upper atmosphere will also cause post-operational spacecraft debris to remain in orbit longer. Thus strengthening the case for all future low Earth orbit satellites to incorporate some means of eliminating their own debris threat over shorter timescales than today's spacecraft.

## 2.2 Free Molecular Flow

The highly rarefied atmosphere of low Earth orbit requires a different approach to aerodynamics than that employed in the continuum regime that exists at aircraft flight altitudes and below. The following sections will define the regime of low Earth orbit spaceflight and then provide details of the various characteristics and mathematical parameters of the regime that are of interest to the spacecraft aerodynamicist.

### 2.2.1 Regime Definition

The flow regime of low Earth orbit spaceflight is commonly described as free molecular. This means that the mean-free path between atmospheric gas molecules (the mean distance between consecutive collisions), which is illustrated in Figure 2-8, is many times greater than the characteristic dimension of a body immersed in the flow. Therefore, collisions between molecules are extremely rare in the flow field around the body, such that the flow can be assumed collisionless.

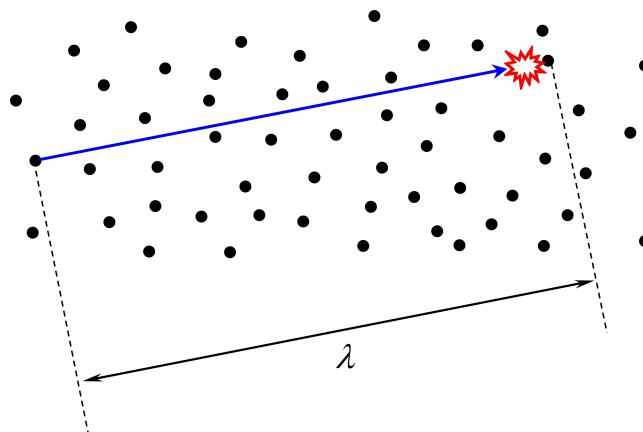


**Figure 2-8 - Molecular Mean Free Path ( $\lambda$ )**

A non-dimensional parameter known as a Knudsen number ( $Kn$ ), given by Equation 2-1, is commonly used to define low-density flow regimes. It indicates the

degree of rarefaction and hence the difference between continuum and non-continuum flow.

$$Kn = \frac{\lambda}{l_{ref}} \quad 2-1$$

The term  $l_{ref}$  is the characteristic dimension of the spacecraft and the mean-free path  $\lambda$  can be approximated in rarefied flow by the semi-empirical Equation 2-2 [18].

$$\lambda = \frac{kT}{\sqrt{2}\pi d_{avg}^2 p} \quad 2-2$$

The term  $k$  is the Boltzmann constant ( $1.3807 \times 10^{-23} \text{ J K}^{-1}$ ),  $T$  is the kinetic gas temperature (in Kelvin),  $d_{avg}$  is the mean collision diameter, and  $p$  is the ambient pressure (in  $\text{N m}^{-2}$ ).

A high  $Kn$  indicates that the flow is particulate in nature (i.e. free molecular) and that the collisionless Boltzmann equation should be employed, a low  $Kn$  indicates that the flow is continuum in nature and should be analysed using the Navier-Stokes equations. Figure 2-9 illustrates how Knudsen number can be used to describe rarefied flow regimes.

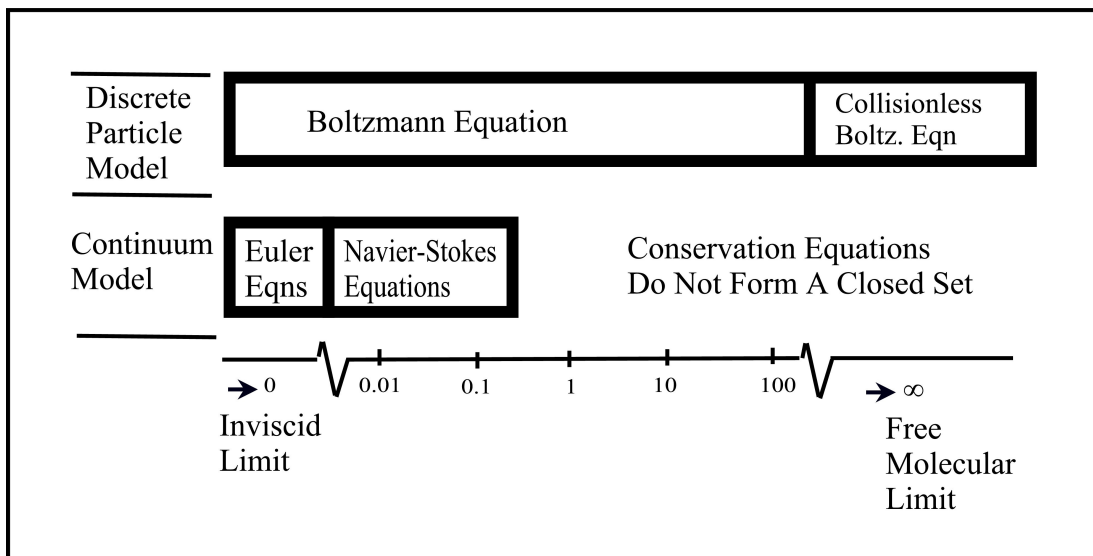


**Figure 2-9 - Classification of Rarefied Flow Regimes Using Knudsen Number**  
Reproduced from [27]

Figure 2-10 shows the trend of free stream Knudsen number ( $Kn_\infty$ ) with altitude for some selected spacecraft dimensions. The graph illustrates how spacecraft size determines the applicability of the free-molecular flow assumption at lower altitudes.

Insufficient gas species data is available to calculate an average molecular mean collision diameter  $d_{avg}$  for the atmospheric gas mixture. Therefore, the  $Kn_{\infty}$  values plotted in Figure 2-10 assume  $d_{avg}$  is equivalent to that for  $N_2$  ( $3.62 \times 10^{-10}$  m), which is the dominant constituent at lower altitudes, where  $Kn$  is most relevant. This approach is also used by authors of the ESA standard atmospheric model [18].

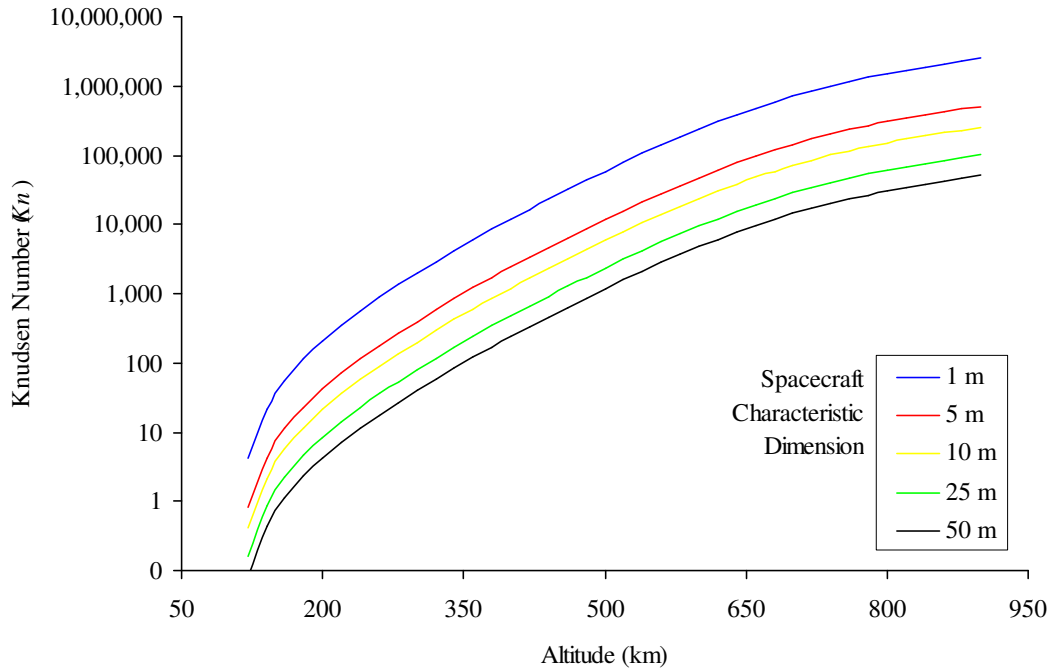


**Figure 2-10 - Free Stream Knudsen Number versus Altitude Trend for Selected Spacecraft Dimensions**

Based on Equations 2-1, 2-2, and data from the MSISE-90 Atmospheric Model [18]. Assumes mean solar conditions (as defined by [18]). Calculation of mean free path ( $\lambda$ ) assumes  $d_{avg}$  is equivalent to that for  $N_2$  ( $3.62 \times 10^{-10}$  m). Because atmospheric composition varies with altitude and solar activity, this assumption is only valid for illustrating the general trend of Knudsen number with altitude.

It is generally assumed in most rarefied gas dynamics literature that the free molecular flow assumption is valid for  $Kn_{\infty} \geq 10$  (see, for example [28]). However, for complex geometries at low free stream Knudsen numbers multiple reflections between gas molecules and surfaces can lead to increases in local density. These increases decrease the local mean free path between molecular collisions, such that local Knudsen numbers may be lower than the free stream Knudsen number.

Therefore, at free stream Knudsen numbers below approximately 100 (the cut-off point illustrated in Figure 2-9), the free molecular flow assumption should be treated with caution, particularly if the spacecraft geometry is complex and contains significant concave regions exposed to the free stream flow.

It follows that the transition regime between the free molecular flow regime and the continuum regime can only be very loosely defined. In the lower transitional



regime in particular, the mean free path can vary widely from one point to another across a spacecraft's flow field, such that a corrected mean free path is often used to account for variations in local density [29]. In addition, the choice of characteristic dimension in the calculation of Knudsen numbers becomes less straightforward and may depend upon the properties of the flow field (for example, boundary layer thickness).

The previous discussion highlights the limited utility of attempting to classify regimes definitively. At one end of the scale some texts choose to use  $Kn_\infty > 1$  as the definition of free molecular flow (see, for example [18]), whilst at the other end  $Kn_\infty > 100$  is used (for example, see [27]). The definitions that will be used in the current study are provided in Table 2-1.

**Table 2-1 - Definition of Flow Regimes**

Mach Number (M) / Reynolds Number (Re)	Knudsen Number (Kn)	Flow Regime
$M/Re > 3$	$Kn > 10$	Free molecular
$3 > M/Re > 0.01$	$0.01 < Kn < 10$	Transitional
$M/Re < 0.01$	$Kn < 0.01$	Continuum

Table 2-1 includes an alternative description of rarefied flow regimes, based on the ratio of Mach number  $M$  to Reynolds number  $Re$  [18]. These dimensionless aerodynamic numbers, which may be more familiar to a continuum aerodynamicist, are provided as Equations 2-3 and 2-4 respectively.

$$M = \frac{V}{a} \quad 2-3$$

The term  $V$  is the flow velocity and  $a$  is the speed of sound, given by Equation 2-6 in the following section.

$$Re = \frac{\rho V l_{ref}}{\mu} \quad 2-4$$

The term  $\rho$  is the density ( $\text{kg m}^{-3}$ ),  $V$  is the flow velocity,  $l_{ref}$  is the characteristic dimension of the body (or the flow field), and  $\mu$  is the dynamic viscosity coefficient (in  $\text{kg s}^{-1} \text{m}^{-1}$ ) given by the Equation 2-5, which is a semi-empirical relation that is appropriate to rarefied flow [18].

$$\mu = \frac{2}{3} \lambda \rho a \sqrt{\frac{2}{\pi \gamma}} \quad 2-5$$

It should be noted that Reynolds number is more commonly used in the continuum and transition regimes rather than the free molecular flow regime. This is

because the very large free mean path of free molecular flow ensures that a boundary layer does not form at the surface of the body, such that  $Re < 1$  in most scenarios of interest (for example, above an altitude of 180 km, assuming a circular Earth orbit in which  $V$  is equivalent to the orbital velocity,  $L = 5\text{m}$ , and using the MSISE-90 atmospheric model [18]). This is in contrast to flow in the continuum regime in which Reynolds number may approach tens of thousands.

## 2.2.2 Characteristics in Low Earth Orbit

Figure 2-11 illustrates the trend lines for several macroscopic flow properties with altitude in Earth's upper atmosphere. These properties and their underlying equations are described in the following paragraphs.

Rarefied neutral gas, such as that found in the free molecular flow regime of low Earth orbit spaceflight, can accurately be assumed to behave like a perfect gas [18][27]. The so-called speed of sound in a perfect gas is a function of temperature ( $T$  in Kelvin) given by Equation 2-6.

$$a = \sqrt{\gamma R_{sp} T} \quad 2-6$$

The term  $R_{sp}$  is the specific gas constant in  $\text{J kg}^{-1} \text{K}^{-1}$  and  $\gamma$  is the ratio of specific heats of the gas. A plot of the variation of the speed of sound with altitude in the Earth's upper atmosphere is illustrated in Figure 2-11. The figure shows that the speed of sound increases with increasing temperature in the thermosphere and increasing specific gas constant in the exosphere.

The specific gas constant and the ratio of specific heats of the gas are dependent upon the composition of the gas mixture. They are given by Equations 2-7 and 2-10 respectively.

$$R_{sp} = \frac{R}{m} \quad 2-7$$

The term  $R$  is the universal gas constant ( $8,314 \text{ J kmol}^{-1} \text{K}^{-1}$ ) and  $m$  is the molar mass of the gas in  $\text{kg kmol}^{-1}$ . Note that the value of  $m$  in  $\text{kg kmol}^{-1}$  is numerically equal to the molecular mass  $m'$  of the gas in units of unified atomic mass ( $u$ ). This is because  $m'$  is given by Equation 2-8, where  $N_A$  is Avogadro's constant ( $6.02 \times 10^{26}$ ) in units of  $\text{kmol}^{-1}$ . For example, the molar mass of atomic oxygen is  $16 \text{ kg kmol}^{-1}$  and its molecular mass  $m'$  is  $16 u$ , which equals  $2.6569 \times 10^{-26} \text{ kg}$ .

$$m' = \frac{m}{N_A} \quad 2-8$$

By definition, the mean molar mass  $\bar{m}$  of a gas mixture composed of  $c$  individual constituents is equivalent to the number density weighted average of the molar masses of the individual species, as defined by Equation 2-9 [18].

$$\bar{m} = \frac{\sum_{i=1}^c (n_i m_i)}{\sum_{i=1}^c (n_i)} \tag{2-9}$$

The terms  $n_i$  and  $m_i$  are the number density (molecules per unit volume) and molar mass of the  $i^{th}$  species respectively. Comparison of the trend line for  $\bar{m}$  in Figure 2-11 with the variation of atmospheric constituents with altitude, illustrated in Figure 2-6, indicates the effect of gravity on the higher mass molecules and explains the trend of  $R_{sp}$  with altitude.

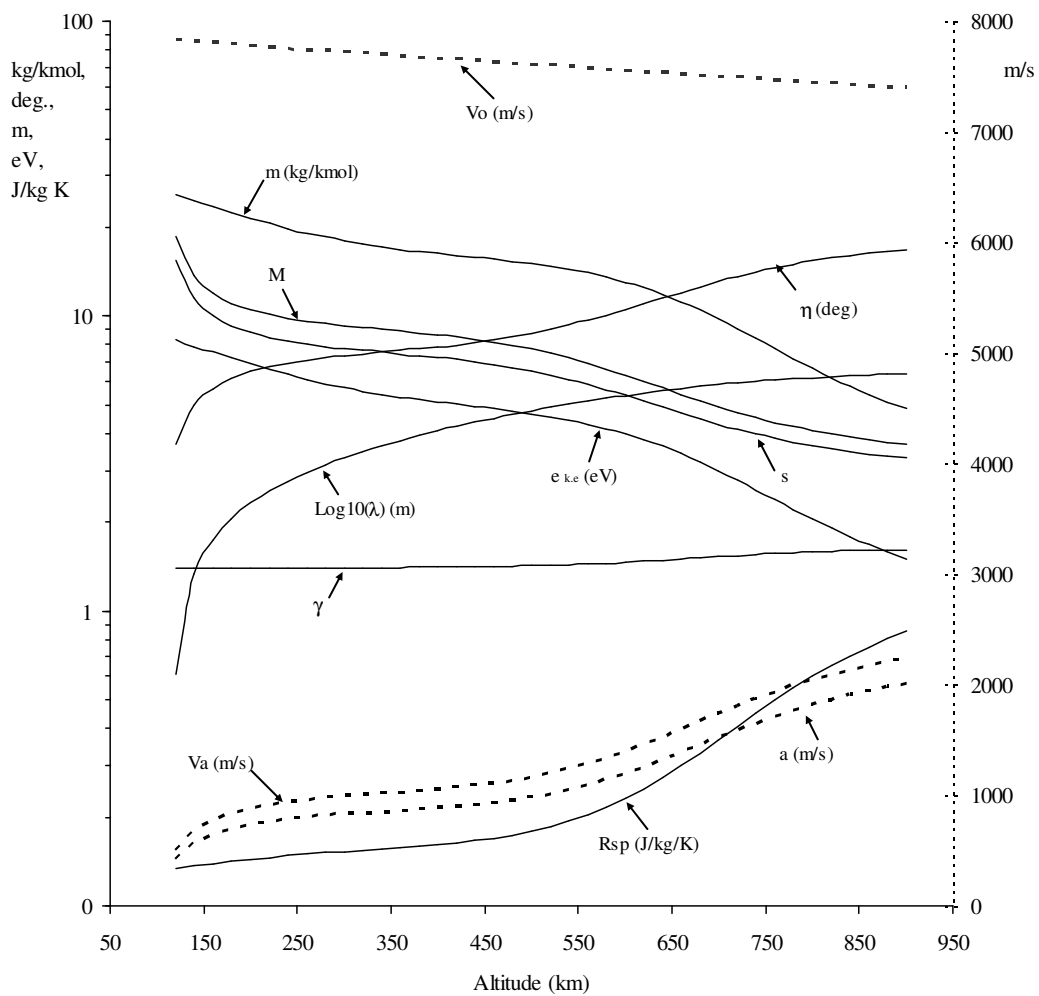


**Figure 2-11 - Selected Aerodynamic Parameters versus Altitude based on the Number Density Weighted Average (Mean) of the Gas Species**  
 Solid trend lines relate to the left vertical axis, dashed trend lines relate to the right vertical axis. Based on Equations 2-1 to 2-3, 2-6 to 2-18, and data from the MSISE-90 Atmospheric Model [18]. Assumes mean solar conditions (as defined by [18]) and number density weighted average (mean) values of  $\gamma$ ,  $m$ , and  $\zeta$  ( $\bar{\gamma}$ ,  $\bar{m}$ , and  $\bar{\zeta}$ ). Calculation of mean free path ( $\lambda$ ) assumes a molecular mean collision diameter equivalent to that for  $N_2$  ( $d_{avg} = 3.62 \times 10^{-10}$  m).

The number density weighted average ratio of specific heats  $\bar{\gamma}$  for a gas mixture with  $c$  constituent species is given by Equation 2-10.

$$\bar{\gamma} = \frac{\sum_{i=1}^c (n_i \gamma_i)}{\sum_{i=1}^c (n_i)} \quad 2-10$$

This definition of the mean ratio of specific heats may not accurately represent multi-component planetary atmospheres and can introduce errors of up to 0.4% [30]. However, as Figure 2-11 illustrates, in low Earth orbit, the mean ratio of specific heats varies very little with altitude. It therefore has little effect on its dependencies. For example, mean free path is more dependent on temperature (in the thermosphere) and density.

It can be shown, using the kinetic theory of gases and the Boltzmann equation, that for an equilibrium gas, with a Maxwellian distribution of velocities, the most probable molecular speed of the gas is given by Equation 2-11 [27].

$$V_a = \sqrt{2R_{sp}T} \quad 2-11$$

This velocity term is usually called the thermal speed of the gas and defines temperature as a measure of the most probable molecular speed of a gas (moving in a reference frame with the gas at its bulk velocity,  $V_b$ ).

Given this definition, it is worth noting that although the temperature of the atmosphere in the free molecular flow regime of low Earth orbit spaceflight is high owing to the high thermal velocities of its constituents, its very low density means that very little heat is transferred to objects in the flow.

Therefore, in contrast to our terrestrial experiences, an Earth-orbiting object, such as an astronaut on a spacewalk, experiences surface temperatures between approximately  $\pm 120^\circ\text{C}$  (depending on solar illumination and surface properties), rather than the temperature of the surrounding atmosphere, which may be several hundred degrees Celsius.

Equation 2-11 is analogous to the definition of the speed of sound (Equation 2-6), and for this reason follows a similar trend with altitude, as shown in Figure 2-11. However, the speed of sound is a measure of the speed of propagation of a disturbance via intermolecular collisions. Therefore, it depends upon the ratio of specific heats of the gas and is lower than the thermal speed.

Consequently, thermal speed more accurately reflects the speed of propagation of a disturbance in a collisionless gas flow than the speed of sound. For this reason,  $a$  is usually referred to as the “continuum” speed of sound. In addition, a dimensionless number, known as the molecular speed ratio  $s$ , given by Equation 2-12 [27], is often used in place of Mach number in rarefied flow.

$$s = \frac{V}{V_a} \quad 2-12$$

The molecular speed ratio will be discussed in more detail in the next section, along with the related parameter  $\eta$  the molecular Mach angle, which is also plotted on the graph illustrated in Figure 2-11.

Both the Mach number and the molecular speed ratio plotted in Figure 2-11 assume a free stream flow velocity  $V_\infty$  that is equivalent to the circular orbital speed  $V_{cir}$  at the given altitude, which can be calculated using Equation 2-13 [13]. This assumption ignores the effects of atmospheric winds, but provides an accurate indication of the general trends with altitude [19].

$$V_{cir} = \sqrt{\frac{\mu_{earth}}{r_{cir}}} \quad 2-13$$

The term  $\mu_{Earth}$  is the Earth's gravitational constant ( $3.986 \times 10^{14} \text{ m}^3 \text{ s}^{-2}$ ) and  $r_{cir}$  is the radius of the orbit, which can be calculated given that the radius of the Earth is approximately 6,378 km.

It is possible to calculate the kinetic energy of a mole of gas  $e_{k.e(mol)}$  with temperature  $T$  and molar mass  $m$  moving with bulk velocity  $V_b$  relative to a satellite using Equation 2-14 (stated in similar form by Harrison and Swinerd [31]).

$$e_{k.e(mol)} = \frac{1}{2}(mV_b^2 + \zeta RT) \quad 2-14$$

The second term in Equation 2-14 is due to the kinetic energy that the gas would have at rest (zero bulk velocity, such that  $V_b = 0$ ) because of the random thermal motion of its molecules. It is a statement of the equipartition theorem and can be derived from the Maxwell-Boltzmann distribution function from consideration of the degrees of freedom of the gas (see, for example, [32]).

The term  $\zeta$  denotes the number of degrees of freedom of the gas. For a monatomic gas, there are three translational degrees of freedom. For a diatomic gas, there are five or more degrees of freedom: three translational, one rotational, and one or more vibrational. For polyatomic gases, there may be more degrees of freedom. However, the main atmospheric constituents of the upper atmosphere are all either monatomic or diatomic (the two diatomic constituents  $\text{N}_2$  and  $\text{O}_2$ , both have five degrees of freedom [27]).

The mean number of degrees of freedom  $\bar{\zeta}$  of a gas mixture with  $c$  constituent species can be approximated using a number density weighted average, as defined by Equation 2-15.

$$\bar{\zeta} = \frac{\sum_{i=1}^c (n_i \zeta_i)}{\sum_{i=1}^c (n_i)} \quad 2-15$$

To calculate the kinetic energy of a single molecule of gas  $e_{k.e}$  the result of Equation 2-14 in  $\text{kmol}^{-1} \text{ J}$  must be divided by Avogadro's constant  $N_A$  ( $6.02 \times 10^{26} \text{ kmol}^{-1}$ ). Avogadro's constant, the Boltzmann constant  $k$  ( $1.3807 \times 10^{-23} \text{ J K}^{-1}$ ), and the universal gas constant  $R$  ( $8,314 \text{ J kmol}^{-1} \text{ K}^{-1}$ ) are related by Equation 2-16.

$$k = \frac{R}{N_A} \quad 2-16$$

Therefore, dividing Equation 2-14 by  $N_A$ , and noting the definitions provided by Equations 2-8 and 2-16, results in Equation 2-17. Such small energies are normally quoted in electron Volts (eV), where one eV is equivalent to  $1.60 \times 10^{-19}$  Joules.

$$e_{k.e} = \frac{1}{2} (m' V_b^2 + \bar{\zeta} k T) \quad 2-17$$

The trend of  $e_{k.e}$  against altitude, assuming  $V_b = V_\infty = V_{cir}$ , is plotted in Figure 2-11. The graph illustrates that  $e_{k.e}$  is mostly comprised of the bulk kinetic energy, represented by the first term, because of the very high orbital velocities

The thermal kinetic energy of the gas, represented by the temperature term in Equation 2-14, is small, but increases as a proportion of total kinetic energy from approximately 1% to just under 9% between 120 and 900 km. This is because temperature increases with altitude, while bulk kinetic energy decreases with altitude.

The bulk kinetic energy is most strongly influenced by the molar mass term, rather than the squared velocity term. This is because circular orbital velocity decreases by just 5.5% between 120 and 900 km, whereas  $m$  decreases by over 80%. This further emphasises the importance of properly accounting for the change in atmospheric gas composition with altitude when performing aerodynamic calculations.

### 2.2.3 Hyperthermal and Sub-Hyperthermal Flow

At low altitudes, in the thermosphere, temperature decreases exponentially towards the homopause. Correspondingly, the thermal velocity ( $V_a$ ) of the atmosphere tends towards zero, such that the molecular speed ratio tends towards infinity. In this scenario ( $V_a \rightarrow 0, s \rightarrow \infty$ ), the flow is described as hyperthermal.

The term “*hyper*” in the definition of hyperthermal flow refers to the fact that the bulk velocity of the gas is many times greater than the thermal velocity of the

gas. This is analogous to the definition of hypersonic flow based on Mach number and the speed of sound.

In hyperthermal flow, the low random thermal motion of the atmospheric gas constituents means that the free stream gas flow can be treated as a collimated beam of molecules, all travelling at the free stream velocity  $V_\infty$ , as illustrated in Figure 2-12.

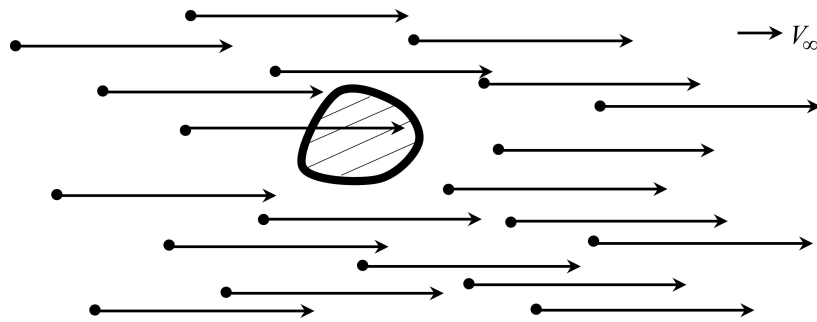


**Figure 2-12 - Hyperthermal Flow ( $s \rightarrow \infty$ )**

**Molecules move relative to the body at the bulk (free stream) velocity of the flow ( $V_\infty$ ) in a continuous parallel stream.**

At higher altitudes, the thermal velocity of the atmosphere increases with temperature towards the thermopause, and then continues to increase with altitude through the exosphere as mean molar mass decreases. In this scenario, thermal speed increases such that the molecular speed ratio decreases ( $s \ll \infty$ ) and the flow may be described as “*sub-hyperthermal*<sup>1</sup>,” as illustrated in Figure 2-13.

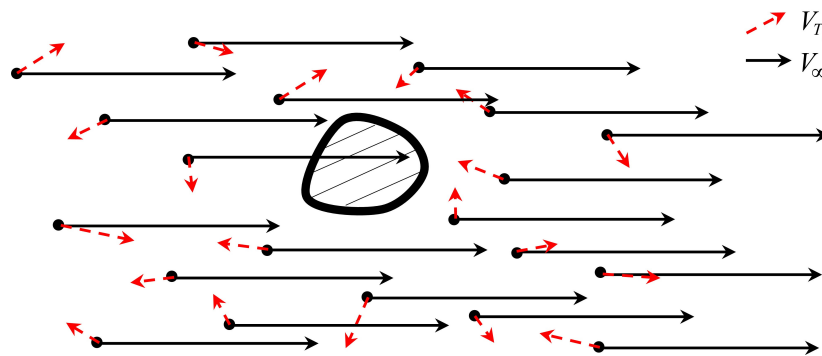


**Figure 2-13 - Sub-Hyperthermal Flow ( $s \ll \infty$ )**

**Molecules move relative to the body with a velocity composed of the bulk (free stream) velocity of the flow ( $V_\infty$ ) plus their random thermal velocity ( $V_{T_i}$ , where  $i$  represents the  $i^{\text{th}}$  molecule).**

<sup>1</sup> Continuing the analogy with Mach number it is also possible to split sub-hyperthermal flow into “*transthermal*” or “*superthermal*” flow where  $1 < s \ll \infty$ , and “*hypothermal*” or “*subthermal*” flow where  $s < 1$ . The terms “*sub-hyperthermal*,” “*transthermal*,” “*superthermal*,” “*hypothermal*” and “*subthermal*” are introduced in this thesis, but not seen elsewhere.

In sub-hyperthermal flow, the high random thermal motion of the atmospheric gas constituents means that the free stream gas flow cannot be treated as collimated beam of molecules. Instead, as illustrated in Figure 2-13, each molecule will have a velocity composed of the free stream velocity  $V_\infty$  plus its random thermal velocity ( $V_{T_i}$ , where  $i$  represents the  $i^{\text{th}}$  molecule).

The molecular speed ratio  $s$  is therefore an important parameter because it provides an indication of the extent to which the flow behaves like a collimated beam of molecules (hyperthermal flow) or a chaotic drifting Maxwellian flow (sub-hyperthermal flow). An alternative way of viewing this relationship is to use the concept of a molecular Mach angle,  $\eta$ , defined by Equation 2-18 [33].

$$\eta = \tan^{-1}\left(\frac{1}{s}\right) \quad 2-18$$

The molecular Mach angle represents the extent to which the molecular flux deviates from the bulk velocity vector of the gas flow, as illustrated in Figure 2-14.

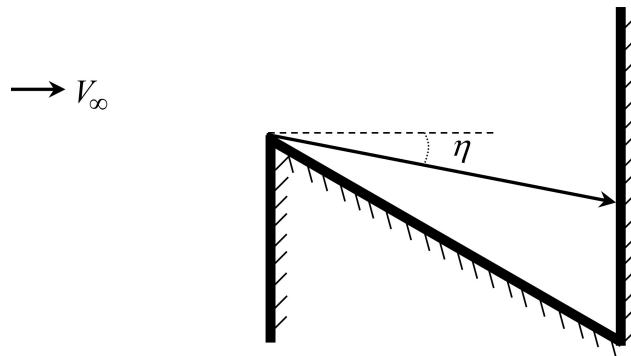


**Figure 2-14 - Molecular Mach Angle ( $\eta$ )**

The higher  $\eta$  is, the less valid the assumption of hyperthermal flow becomes. The lower  $\eta$  is, the more the flow can be treated like a collimated beam of molecules. The variations of both  $\eta$  and  $s$  with altitude, in mean solar conditions, assuming a circular orbit for which  $V_\infty = V_{cir}$ , are illustrated in Figure 2-11.

It is generally assumed in most texts that the hyperthermal flow assumption is valid for  $s > 5$ , such that the molecular Mach angle is less than  $11^\circ$  (see, for example, [16][34]).

In sub-hyperthermal flow ( $s < 5$ ), all surfaces may be impinged by molecules due to their random thermal motion regardless of whether they are forward facing or shielded. In practice, most molecules arrive at forward facing, unshielded surfaces, and only a small amount of momentum is imparted to aft facing or shielded surfaces due to the random thermal motion of molecules.



The consequences of sub-hyperthermal flow for aerodynamic analysis are discussed further in Sections 2.5 and 2.6. In addition, the effects of accounting for a finite value of  $s$ , rather than assuming hyperthermal flow ( $s \rightarrow \infty$ ), in Gas-Surface Interaction Models (GSIMs) are described in section 3.2.3.

#### 2.2.4 Gas-Surface Interactions

In the free molecular flow regime, collisions between molecules are extremely rare, even between incident and reflected particles. Consequently, a body will have a negligible influence on its upstream flow field. Therefore, the transfer of energy and momentum to a body in free molecular flow is dominated by the nature of the Gas-Surface Interactions (GSIs) that take place.

Sections 2.5.1 and 2.6 describe some of the different analyses methods available for calculating aerodynamic quantities in rarefied flow. All of them rely upon mathematical models of gas-surface interactions. The variety, complexity, and multiplicity of Gas-Surface Interaction Models (GSIMs) requires that they be treated as a subject in their own right. Chapter 3 will deal with the subject of GSIMs in more detail.

### 2.3 Aerodynamic Coefficients

Aerodynamic coefficients are dimensionless numbers that can be used to relate aerodynamic properties between different vehicle and flow scenarios. They provide a macroscopic description of the effects of the microscopic flow field on the body's surface. Consequently, one of the main goals of a spacecraft aerodynamicist is to determine the aerodynamic coefficients of a spacecraft in multiple flight scenarios and attitudes.

Definitions of the aerodynamic coefficients for forces  $F$ , moments  $M$ , and pressures  $p$  (including shear stresses) are provided in Equations 2-19 to 2-21 respectively.

$$C_F = \frac{F}{q_\infty A_{ref}} \quad 2-19$$

$$C_M = \frac{M}{q_\infty A_{ref} l_{ref}} \quad 2-20$$

$$C_p = \frac{\Delta p}{q_\infty} \quad 2-21$$

The term  $q_\infty$  is known as the dynamic pressure and is provided by Equation 2-22,  $A_{ref}$  is a characteristic area of the body, and  $l_{ref}$  is a characteristic length of the body.

$$q_\infty = \frac{1}{2} \rho_\infty V_\infty^2 \quad 2-22$$

The term  $\rho_\infty$  is the flow density and  $V_\infty$  is the flow velocity. The subscript  $\infty$  indicates that the properties relate to free stream conditions.

Given the definitions provided by Equations 2-19 to 2-21, it is possible to calculate the actual forces, moments, and pressures if the coefficients themselves are known. For example, given a coefficient of drag  $C_D$ , for a particular spacecraft flight scenario, the actual drag force can be calculated if the free stream conditions, described by  $q_\infty$ , are known along with the reference area  $A_{ref}$ .

Aerodynamic coefficients are traditionally used in continuum aerodynamics to relate the results of wind tunnel tests to actual flight scenarios. To ensure similarity between the two different scales, the Reynolds number and Mach number of the wind tunnel flow are adjusted so that they are equal to the actual flight values of the scenario being tested. The aerodynamic coefficients measured in the wind tunnel can then be used to predict the actual forces, moments, and pressures in flight.

As explained in Section 3.3.3, it is currently not possible to perform accurate wind tunnel tests on scale models of satellites under orbital conditions. Therefore, spacecraft aerodynamic coefficients can only be determined using analytical or computational methods pre-launch.

Unlike aircraft, which have a well-defined flight direction and many comparable dimensions, satellites come in all shapes and sizes and can “fly” in a multitude of different attitudes. In addition, as discussed in section 2.1, atmospheric conditions vary significantly over a range of satellite orbital altitudes and with satellite lifetime. The surface properties of a satellite also affect the aerodynamic coefficients, and may also vary over the course of a satellite’s lifetime (see Chapter 3 for a more detailed discussion of these effects).

Therefore, direct comparison of the aerodynamic coefficients of two different satellites, or even the same satellite at two different altitudes or in two different mission phases, is often not that helpful and can sometimes be misleading. Moe [19] provides a detailed and contemporary summary of the erroneous nature of comparing spacecraft aerodynamic coefficients without a proper understanding of the issues involved.

Because spacecraft aerodynamic coefficients are calculated using analytical or computational methods, as opposed to wind tunnel tests, the choice of characteristic dimensions is largely subjective. However, in general,  $A_{ref}$  is usually chosen to be the cross-sectional area of the body in the nominal spacecraft attitude (see, for example, [19][31]). For asymmetrical bodies that require analysis at

multiple attitudes the area of one of the dominant exterior surface features is sometimes chosen (for example, for the analysis of ERS-1, one author has used the area of the solar panels [34]). Note also, that some authors choose to use the projected area of the body in the spacecraft attitude being analysed [35].

The longest length of the spacecraft is usually chosen for the characteristic length  $l_{ref}$ .

## 2.4 Aerodynamic Forces and Moments on a Body

The aerodynamic forces and moments on a body are a consequence only of the pressure and shear stress distribution over it. Therefore, the force and moment coefficients can be calculated by integrating the pressure and shear stress distribution over the body's surface.

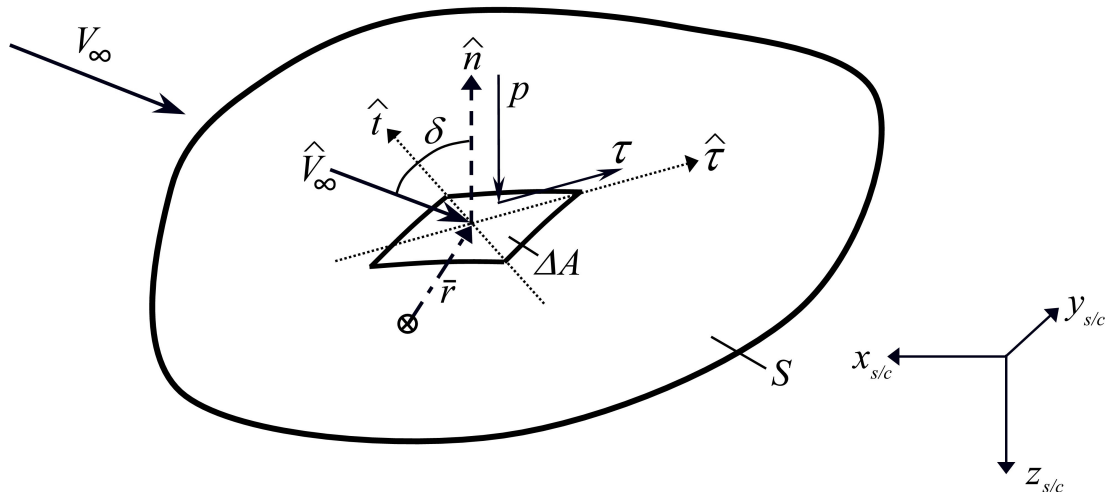


Figure 2-15 - Flow Geometry

Figure 2-15 illustrates a body immersed in a free stream flow, which is moving with velocity  $V_\infty$ . The pressure  $p$  on an elemental area  $\Delta A$  of the body's surface  $S$  acts along the negative unit normal  $-\hat{n}$  of the elemental area. The shear stress  $\tau$  acts parallel to the surface, in the same plane as the unit normal and the incident unit vector of the free stream flow  $\hat{V}_\infty$ , which acts at an angle  $\delta$  to the unit normal. Given these definitions, and assuming a right-handed coordinate system, it follows that the unit shear stress direction  $\hat{\tau}$  can be described using Equation 2-23.

$$\hat{\tau} = \hat{t} \times \hat{n} = (\hat{n} \times \hat{V}_\infty) \times \hat{n} \quad 2-23$$

The term  $\hat{t}$  is the tangential unit vector that is parallel to the surface and perpendicular to both  $\hat{n}$  and  $\hat{\tau}$ .

From Equations 2-18 and 2-21, the coefficient of force on the body  $C_F$ , in terms of the coefficients of pressure  $C_p$  and shear stress  $C_\tau$ , is then given by Equation 2-24.

$$C_F = \frac{F}{q_\infty A_{ref}} = -\iint_S C_p \hat{n} \Delta A + \iint_S C_\tau \hat{\tau} \Delta A = \iint_S [C_\tau \hat{\tau} - C_p \hat{n}] \Delta A \quad 2-24$$

The moment coefficient, given by Equation 2-25, follows from Equation 2-20 in a similar fashion.

$$C_M = \frac{M}{q_\infty A_{ref} l_{ref}} = \iint_S \{ \bar{r} \times [C_\tau \hat{\tau} - C_p \hat{n}] \} \Delta A \quad 2-25$$

The term  $\bar{r}$  is the vector from a chosen reference point to the centroid of the elemental area.

Consequently, the primary challenge of aerodynamics is to calculate  $C_p$  and  $C_\tau$  over the entire surface of the body. All of the complexity of the aerodynamic flow field is hidden behind  $C_p$  and  $C_\tau$ .

The forces and moments calculated using Equations 2-24 and 2-25 relate to the body fixed spacecraft coordinate system illustrated in Figure 2-15 and denoted by the subscript  $s/c$ .

## 2.5 Analytical Analysis Methods

Since it is not possible to calculate spacecraft aerodynamic coefficients or other macroscopic aerodynamic quantities using wind tunnel tests, there are only two non-computational methods for evaluating the aerodynamic performance of a spacecraft. The first is to use direct observation of operational spacecraft to develop empirical models, the second is to use geometric analysis and Gas-Surface Interaction Models (GSIMs).

### 2.5.1 Empirical Methods

Direct comparison between different spacecraft is difficult due to the inherent uniqueness of spacecraft missions and changing atmospheric conditions. In spite of this, one investigator made significant strides in the area over two decades ago. King-Hele's definitive work [14] provides an empirical analysis of the orbital histories of spacecraft from direct ground-based telescope observation.

From the data gathered, King-Hele derived a method for calculating the aerodynamic drag coefficient of a satellite. However, his method has some limitations. It is difficult to apply, only accurate for common satellite configurations, and requires the use of a number of look-up tables.

### 2.5.2 Geometric Analysis Methods

Numerous investigators have developed analytical methods for calculating the aerodynamic forces and moments on a simple convex body in free molecular flow. All of them make use of the fact that intermolecular collisions can be neglected in free molecular flow, such that a body has no influence on the upstream flow.

The forces on a body can then be calculated by integrating the pressure distribution over the surface area using some form of Equation 2-24. Where pressure and shear stress coefficients can be determined using a Gas-Surface Interaction Model (GSIM).

So long as there is no surface shielding, simple convex shapes such as spheres, cylinders, flat plates, and closed-end circular cones can all be analysed analytically in both hyperthermal and sub-hyperthermal flow.

The simplest analytical case to solve is that of so-called Newtonian flow, which uses Newton's GSIM (described in Section 3.1). However, more complex GSIMs, which take account of shear stresses, partial momentum accommodation, and a finite molecular speed ratio, can also be used to determine the pressure distribution over simple convex shapes (see, for example, Cook [16] and Pike [36]). Numerous other references to standard results are listed by Schaaf and Chambre [37]. In addition, Storch [38] provides analytical methods for some simple convex shapes and provides a detailed discussion of the consequences of using a GSIM that assumes hyperthermal flow, as well as the effects of a rotating spacecraft.

All of the published analytical results are for simple convex bodies. However, within the SRC, Harkness [12] has deduced analytical results for flow into the concave end of a circular cone. Harkness's technique accounts for surface shielding, but not reflections, and also assumes a simple Newtonian GSIM.

## 2.6 Computational Analysis Methods

There are four main computational methods for analysing the aerodynamics of a body in free molecular flow. They are compared in Figure 2-16, along with the Computational Fluid Dynamics (CFD) method that is used in continuum flow.

The right-hand axes of Figure 2-16 represents both the free stream molecular speed ratio  $s_\infty$  and free stream Knudsen number  $Kn_\infty$ . The Knudsen number is based on a spacecraft with a characteristic dimension of 5 m. The different regimes of rarefied flow are indicated using the Knudsen number scale. The hyperthermal and sub-hyperthermal flow regions are indicated based on the definitions provided in Section 2.2.3.

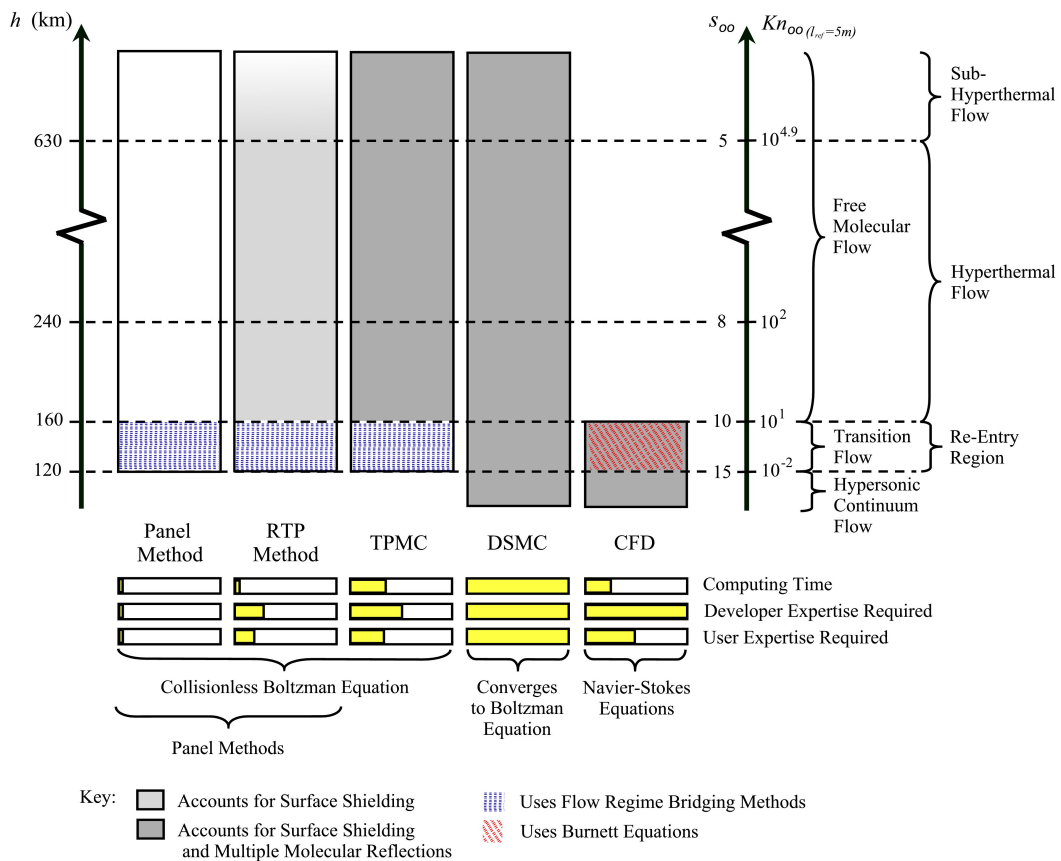


**Figure 2-16 - Comparison of Existing Computational Approaches to Spacecraft Aerodynamics in Low Earth Orbit**

Assumes mean solar conditions (as defined by [18]) and a free stream Knudsen number ( $Kn_\infty$ ) based upon a spacecraft characteristic dimension of 5 m. The term  $h$  refers to Earth altitude and  $s_\infty$  refers to the free stream molecular speed ratio. The Computing Time, Developer Expertise Required, and User Expertise Required scales are based upon a qualitative survey of numerous rarefied gas dynamics texts (see, for example, [27]). They are provided as a “rule of thumb,” without quantitative explanations save those given in the following sections and chapters.

Other aspects of Figure 2-16, including the different terms and various computational analysis methods depicted, will be described in more detail in the following sections.

### 2.6.1 Panel Method

As explained in previous sections, in free molecular flow, intermolecular collisions can be neglected, such that a body may be seen as having no influence on its upstream flow field.

Therefore, a body may be idealised as being made up of a number of discrete panels that can each be modelled as a flat plate subject to a chosen Gas-Surface

Interaction Model (GSIM). The coefficients of pressure and shear stress can then be calculated using the chosen GSIM, for each forward facing panel.

A forward facing panel satisfies the condition that the angle,  $\delta$ , between the incoming free stream flow, defined by the unit free stream velocity vector  $\hat{V}_\infty$  and the panel outward unit normal  $\hat{n}$  is less than or equal to  $90^\circ$ . This condition is described in vector terms by Equation 2-26.

$$\hat{n} \cdot \hat{V}_\infty \geq 0 \quad 2-26$$

For a meshed body with  $n$  panels the total aerodynamic force and torque coefficients that result from the distribution of pressure and shear stress over its external surfaces are given by Equations 2-27 and 2-28, which can be derived from Equations 2-24 and 2-25 [29].

$$C_F = \frac{F}{q_\infty A_{ref}} = \sum_{i=1}^n \left\{ C_{P_i} (-\hat{n}_i) + C_{\tau_i} \left[ \hat{n}_i \times (\hat{V}_\infty \times \hat{n}_i) \right] \right\} A_i \quad 2-27$$

$$C_M = \frac{M}{q_\infty A_{ref} l_{ref}} = \sum_{i=1}^n \left[ \bar{r}_i \times \left\{ C_{P_i} (-\hat{n}_i) + C_{\tau_i} \left[ \hat{n}_i \times (\hat{V}_\infty \times \hat{n}_i) \right] \right\} \right] A_i \quad 2-28$$

The term  $\bar{r}_i$  is the vector from the moment reference point to the centroid of the  $i^{th}$  panel and  $A_i$  is the area of the  $i^{th}$  panel.

The flow is treated as a collimated beam of molecules in both the hyperthermal and sub-hyperthermal flow regimes. The random thermal motion of molecules in the sub-hyperthermal regime can be accounted for by the inclusion of a finite molecular speed ratio in the gas-surface interaction model (for further explanation of this see Section 3.2.3).

This approach to sub-hyperthermal flow assumes that all panels may be impacted regardless of whether they are forward facing or not ( $0^\circ \leq \delta \leq 180^\circ$ ). This is because the molecules move with a velocity composed of their random thermal motion plus the bulk flow velocity. However, in practice, very few molecules will arrive at aft facing surfaces (again, see section 3.2.3 for further explanation of this).

The panel method is only applicable for convex shapes. More complex shapes that have regions of concavity, or areas that are shielded to the flow cannot be modelled realistically. Fortunately, however, many low Earth-orbiting satellites have simple convex shapes.

For example, the panel method was used to perform pre-launch aerodynamic analyses of the GRACE satellites, illustrated in Figure 2-17, which were launched in March 2002 [20]. As illustrated, the two GRACE satellites have a simple convex shape, composed of an elongated trapezoid.

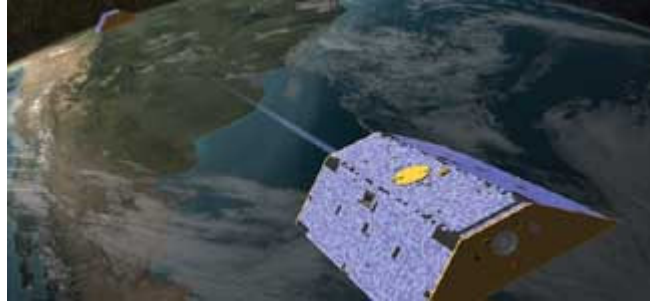


**Figure 2-17 - The GRACE Satellites**

**Image credit Centre for Space Research, University of Texas, USA.**

The aim of the GRACE mission is to map the Earth's gravitational field. The GRACE satellites fly in a near-polar circular orbit at an altitude of approximately 500 km, with an along-track separation of 220 km. To determine the effect of gravity, the separation distance is measured to within microns using a K-Band microwave ranging system.

The aerodynamic disturbances on the spacecraft had to be predicted with considerable accuracy for a number of reasons. These included, predicting spacecraft orbital lifetime, evaluating attitude control requirements, and calculating drag-correction manoeuvre frequency. This latter calculation was critical to mission success. This is because, although the spacecraft are geometrically identical, they experience different drag forces because of their opposing orientations (the trailing satellite faces in the opposite direction to the leading satellite) and slightly different attitudes, which are necessary for aligning the microwave ranging system.

The use of the panel method for calculating the aerodynamic disturbances on the GRACE spacecraft demonstrates the trustworthiness with which its predictions are regarded for certain applications.

## **2.6.2 RTP Method**

The Ray-Tracing Panel (RTP) method improves upon the panel method described in the previous section because it considers the shielding of spacecraft surfaces from the incident free stream flow by upstream components. It can therefore be used to analyse more complex geometrical configurations.

The method assumes that the free stream flow behaves as a collimated beam of particles. This beam is analogous to a beam of light, such that areas that are shielded to the incident free stream flow (i.e. in "shadow") can be determined using ray-tracing techniques. In this way, only unshielded forward facing panels can be impacted by the incident free stream flow. Shielded and aft facing panels are excluded from the integration of forces and moments. In order to account accurately for surface shielding, the surface mesh density must be correspondingly high in regions prone to shielding.



The assumption that the flow travels as a collimated beam of molecules is only valid under hyperthermal conditions ( $s > 5$ ,  $\eta < 11^\circ$ ). When modelling convex bodies with no shielded surfaces in sub-hyperthermal flow this is inconsequential because the random thermal motion of molecules can be accounted for at the panel level in the GSIM (for further explanation of this see section 3.2.3). However, when modelling complex, concave bodies with shielded surfaces in sub-hyperthermal flow, the RTP method loses its accuracy. This is indicated in Figure 2-16 by the fading grey region at the top of the RTP box, above about 630 km.

The accuracy of the RTP method for complex configurations is not only limited by the hyperthermal assumption, but also because it cannot account for the effects of multiple reflections (the reflection of a molecule from one surface, such that it impinges upon another surface).

Consequently, the RTP box illustrated in Figure 2-16 is coloured a light shade of grey to indicate that it can account for surface shielding, but not the effects of multiple reflections.

TPMC, described in the following section, can account for multiple reflections. For this reason, many investigators have compared the results of RTP and TPMC analyses of complex spacecraft geometries at lower altitudes to investigate the effects of multiple reflections:

- In 1990, Crowther [33] compared the RTP and TPMC methods in his orbital analysis of the ANS-1 satellite. Crowther concluded by cautioning against the use of the RTP method for complex vehicles.
- In 1995, Klinkrad, Koppenweller, Johannsmeier, Ivanov, and Kashkovsky [39] developed the RAMSES program under ESA contract. It incorporates both the TPMC and RTP methods.
- In 1998, Kinkrad and Fritsch [23] used ESA's ANGARA software, which implements both RTP and TPMC, to model the ERS-1 and ENVISAT satellites.

### 2.6.3 TPMC Method

The Test-Particle Monte Carlo (TPMC) method was first proposed by Davis in 1961 [40]. In TPMC, the model is surrounded by a control tube into which a number of representative particles are sequentially fired. Each particle represents many thousands of real molecules. These test-particles - or simulated molecules - can be emitted from all sides of the control tube to mimic the characteristics of the real flow, as illustrated in Figure 2-18.

Each simulated molecule is initially fired with a velocity composed of the free stream velocity  $V_\infty$  plus a component due to its thermal velocity  $V_{T_i}$  (where  $i$

represents the  $i^{\text{th}}$  molecule), which is determined probabilistically. Therefore, the particles may all enter from one direction as a collimated beam (hyperthermal flow), or represent a drifting Maxwellian flow (sub-hyperthermal flow). Consequently, unlike the RTP box illustrated in Figure 2-16, the TPMC box has a fully grey region above about 630 km.

The particles can reflect off the surfaces of the model, but do not interact with one another (as is the case in DSMC). Therefore, TPMC can be used to model the effects of multiple reflections. Consequently, the TPMC box illustrated in Figure 2-16 is coloured a dark shade of grey to indicate that it can account for surface shielding and the effects of multiple reflections.

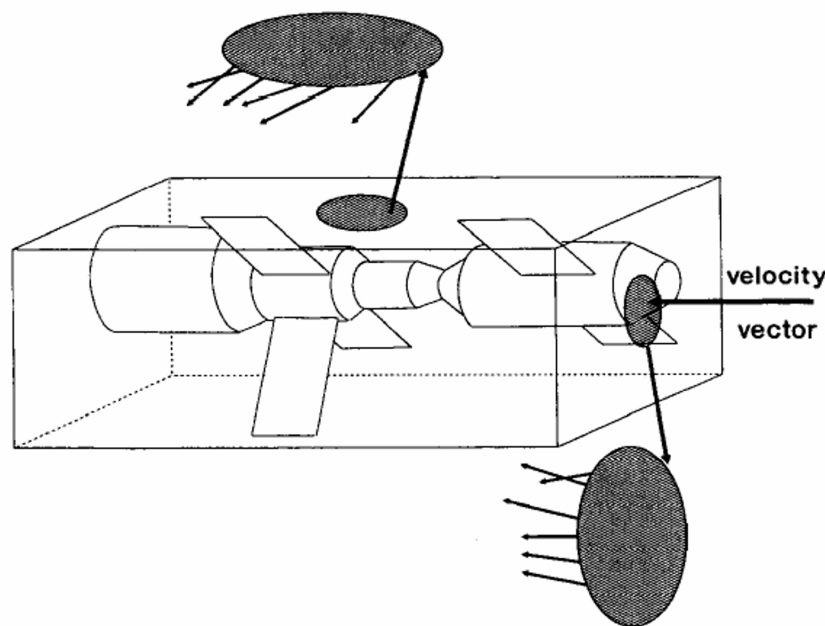


**Figure 2-18 - Schematic of the Test-Particle Monte Carlo (TPMC) Method**  
Image credit [41]. The spacecraft represented is the Salyut 7 space station that re-entered the Earth's atmosphere in 1991.

The total number density of all simulated molecules fired into the control tube during the simulation is the same as the total number density of molecules that would pass into an equivalent volume in the real gas over unit time. Therefore, the energy and momentum transferred to a surface over the course of a simulation (over unit time) due to all gas-surface interactions can be summed to give the related fluxes.

The pressures and shear stresses can be calculated from the momentum flux using the chosen Gas-Surface Interaction Model (GSIM). The forces on the body can then be calculated using Equation 2-24 (or Equation 2-27, if the model is represented by a surface mesh consisting of discrete flat panels). The GSIM also determines the

trajectories of reflected simulated molecules and their related energy and momentum states.

The main disadvantage of the TPMC method is that its computing time is proportional to the number of simulated molecules. Consequently, it is considerably slower than the RTP method [33][39]. Furthermore, in addition to a surface mesh, the TPMC method also requires the test-particle initial conditions to be defined across the boundaries of the control tube in three-dimensional space. This is in contrast to the RTP method, in which the flow is defined by a single vector.

Nevertheless, TPMC remains a powerful alternative to the RTP method. It provides a realistic and conceptually simple model of flow around complex, concave bodies in both hyperthermal and sub-hyperthermal free molecular flow.

#### 2.6.4 DSMC Method

The Direct Simulation Monte Carlo (DSMC) was originally proposed by Graeme Bird [27], and has been assiduously pioneered by him for over 44 years. Professor Bird's programs are still widely used today, and can be downloaded from [42]. A screenshot of his two-dimensional analysis software is provided in Figure 2-19.

As its name suggests, the DSMC method directly simulates molecules. Each simulated molecule represents  $10^{12}$  to  $10^{20}$  real molecules. Unlike in TPMC, the simulated molecules can collide with one another. Collision samples and collision pairs are determined in a probabilistic manner. However, the movements of the molecules are deterministic and uncoupled from the collisions. Gas-surface interactions are handled using Gas-Surface Interaction Models (GSIMs).

The body is typically represented by a surface mesh and, in a similar manner to TPMC, the model and the flow field are enclosed by a flow tube. In order to reduce the collision sample size the flow field enclosed by the flow tube is usually divided into cells, which may or may not be fixed over the duration of a simulation.

The simulation time period depends on the gas's relaxation rate (the rate at which the gas returns to equilibrium conditions after a disturbance), and hence Knudsen number. Macroscopic quantities, such as temperature and pressure, can be calculated at each time step and then averaged to determine steady-state values.

The DSMC method provides a realistic and intuitive model of flow at the particulate level, which is amenable to multiple adaptations. For instance, it can be used to model multidimensional flow travelling through electromagnetic and gravitational fields, as well as flow composed of ionized gas and chemically reacting molecules.

It has become the de facto method for modelling rarefied flow in the transition regime and is able to accurately model both the flow field and gas-surface interactions from the highly rarefied free molecular flow regime ( $Kn > 10$ ), right

down to the continuum limit ( $Kn = 0.001$ ). DSMC simulation results have also been proven to converge towards the Boltzmann equation [43]. Therefore, in theory, DSMC could be used to model flow in the continuum regime too.

However, its computational load is directly proportional to the density of the gas. In the lower transition regime and continuum regime, this makes it prohibitively expensive in computational terms at the current time, especially for complex three-dimensional bodies.

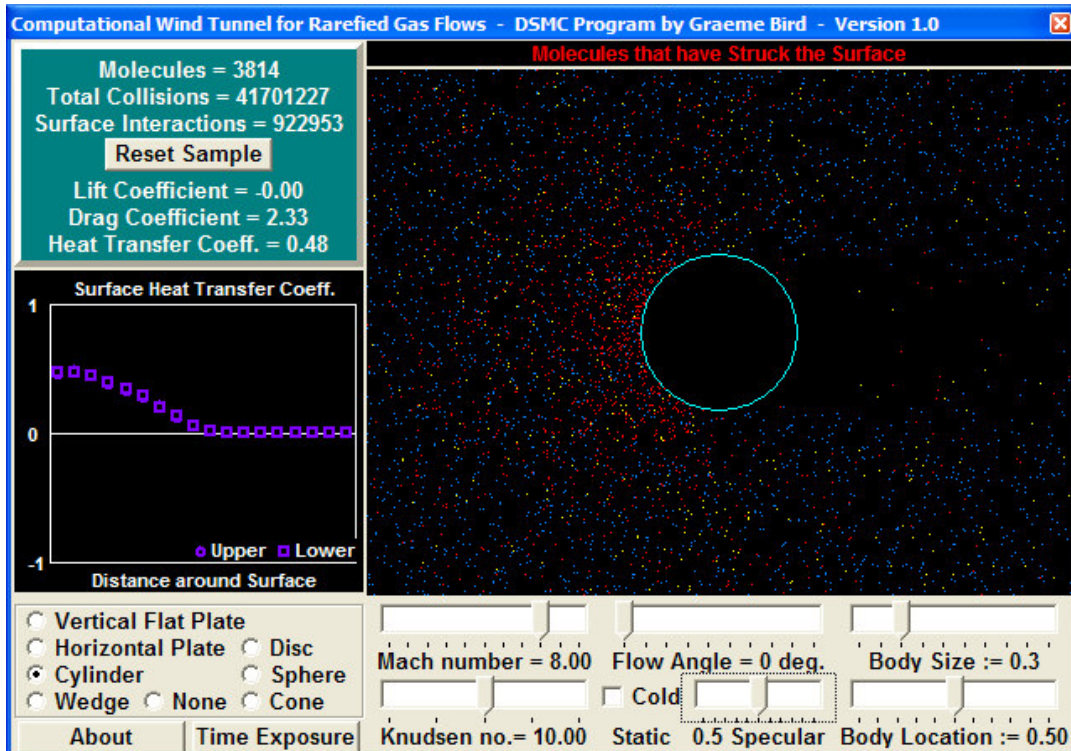


**Figure 2-19 - DSMC Software Screenshot**

Image credit [42]. The different types of simulated molecule are represented by different colours in the visualisation screen. Red indicates that the molecule has struck the surface, yellow indicates that the molecule has been involved in an intermolecular collision, blue indicates that the molecule has not been involved in a collision of any type.

In the free molecular flow regime, gas-surface interactions dominate the flow and little benefit is gained by modelling the limited number of gas-gas interactions unless detail of the flow field is required. Therefore, if modelling of free molecular flow is required using DSMC, the so-called Collisionless DSMC method is most commonly used.

Collisionless DSMC is similar to standard DSMC, but with the intermolecular collision routine turned off. It is used to model unsteady rarefied flows [27]. However, it has been shown that collisionless DSMC does not provide greater accuracy than panel methods or the TPMC method in the free molecular flow regime [28][44][45].

DSMC therefore has little appeal to most spacecraft design engineers wishing to perform analyses in the free molecular flow regime because it provides no greater accuracy than other methods, yet it requires extensive knowledge of rarefied gas dynamics and requires access to a suitable DSMC code.

### 2.6.5 Flow Regime Bridging Methods

Below free stream Knudsen numbers of about ten, complex bodies with regions of concavity may induce areas of higher density to develop, such that local Knudsen numbers may be lower than free stream Knudsen numbers (as described in Section 2.2.1). Therefore, computational analysis methods that neglect intermolecular collisions (those based on the collisionless Boltzmann equation), lose their applicability.

However, bridging methods can be used to extend the panel methods and TPMC through the transition regime to the limits of the continuum regime, where conventional CFD modelling using the Navier-Stokes equations can be utilised.

Knudsen number dependent bridging formula for drag and lift coefficients are provided in Equations 2-29 and 2-30 respectively [18], where the subscripts *CON* and *F<sub>MF</sub>* denote continuum and free molecular flow respectively.

$$f_D(Kn) = \frac{C_D - C_{D_{CON}}}{C_{D_{F_{MF}}} - C_{D_{CON}}} \quad 2-29$$

$$f_L(Kn) = \frac{C_L - C_{L_{CON}}}{C_{L_{F_{MF}}} - C_{L_{CON}}} \quad 2-30$$

Given free molecular and continuum values of the coefficients, Equations 2-29 and 2-30 can be rearranged to determine the transition coefficients if a suitable bridging function  $f_i$  can be derived. Equation 2-31 defines a typical bridging function for drag ( $f_D$ ) [46], where the term  $g$  is the acceleration due to gravity on Earth ( $9.81 \text{ m s}^{-2}$ ).

$$f_D(Kn) = \sin^3[\pi(0.5 + 0.25gKn)] \quad 2-31$$

Similar expressions can be defined for pressure and shear stress coefficients [47]. Therefore, if a suitable database of free molecular and continuum flow coefficients is available, bridging functions can be used within Gas-Surface Interaction Models (GSIMs).

Transition regime bridging methods, though not as accurate, are simpler, easier to use, and quicker than the DSMC method. They are also relatively easy to integrate into panel method codes. Therefore, they are often preferred by investigators wishing to perform analyses of vehicle re-entry and break-up (see, for example [44][45][47][48][49][50]).

### 2.6.6 CFD Method

As indicated in Figure 2-16, some attempts have been made to extend Computational Fluid Dynamics (CFD) techniques into the rarefied transitional flow regime using the Burnett equations (see, for example [51]).

However, for some, these efforts are incongruous and direct resources away from what are believed might be more fruitful avenues of research, such as DSMC. According to Bird [43], *“there is a clear reluctance on the part of many workers to let go of the traditional CFD methods. Evidence for this is provided by the heroic efforts that are still being made to solve the Burnett equations for problems that can and have been readily solved by DSMC.”*

## 2.7 Analysis Studies and Tools

Numerous studies have analysed the effects of aerodynamic disturbances on a spacecraft. Many of these studies used bespoke software tools, others re-used and if necessary adapted and updated existing software tools to perform the required analyses. Some of the most frequently cited tools are compared in Table 2-2.

The methods used by the tools (for example, the panel, RTP, TPMC, and DSMC methods), which are referred to throughout Table 2-2, are described in detail in Section 2.6. In addition, where relevant, further references are made to a number of the tools and studies in the chapters that follow.

**Table 2-2 - Software Tools for the Analysis of Aerodynamic Disturbances on Spacecraft in Free Molecular Flow**

Study	Software	Software Notes	Year	Software Availability
[52]	MOLFLUX	A free molecular flux program developed by NASA that can be used to calculate forces and torques using secondary software. It runs on the UNIX operating system.	?	Only available to US citizens resident within the US.
[53] [54] [55]	SYSTEMA (incorporating PLUME)	A suite of software tools developed over many years by EADS Astrium <sup>1</sup> to assist with spacecraft systems engineering analysis and design. PLUME is the free molecular flux module.	?	Available to academics under certain conditions.
[34]	FREEMAC	Originally developed by Pennsylvania State University. Uses the RTP method. Updated to include rotating parts for the study of ERS-1.	1991	Unknown

<sup>1</sup> EADS Astrium: [www.space.eads.net](http://www.space.eads.net)

[56] [39] [50]	RAMSES	Originally created by Professor M. S. Ivanov, of the Institute of Theoretical and Applied Mechanics, Russia. It incorporates both the RTP and TPMC methods.	1995	Available to academics under certain conditions. Available commercially from HTG HSE <sup>1</sup> .
[47]	SCARAB	Produced under contract for ESA's European Space Operations Centre (ESOC). It incorporates both the RTP and TPMC methods.	1997	Available as part of a consultancy package.
[44] [45]	DACFREE	A NASA program. It uses the RTP method.	1997	Not available.
[23]	ANGARA	Produced under contract for ESA's European Space Operations Centre (ESOC). It incorporates both the RTP and TPMC methods.	1998	Available as part of a consultancy package.
[20]	FREEMOL	Produced under contract for NASA GRACE Mission. Only applicable to convex bodies. Does not account for individual surface properties or thermal distribution. Uses simple panel method.	2000	Available as part of a consultancy package.
[28]	Collisionless DSMC	NASA X-Vehicle aerothermodynamic study. Uses a collisionless version of NASA's in-house DSMC program DAC.	2001	Not available.
[57] [58]	ESABASE	According to ESA, "ESABASE is an engineering tool supporting the harmonisation / standardisation of spacecraft analysis modelling and space related analysis." The software incorporates a new module that uses the RTP method with multiple reflections. The new module replaced the previous ATOMOX module in 2004. It runs on the UNIX operating system.	2004	Available under one year lease from Alstom Power Technology Centre <sup>2</sup> for £5500. Educational discount available.
[35]	GOPAS	Developed by GMV <sup>3</sup> . Used to perform aerodynamic analyses of the low Earth orbit Synthetic Aperture Radar (SAR) satellite, TerraSAR-L, which was due for launch in 2009/2010, but is now scrapped. Uses the panel method.	2005	Available as part of a consultancy package.

A sample screen shot of the RAMSES software listed in Table 2-2 is provided in Figure 2-20.

<sup>1</sup> HTG HSE: [www.htg-hst.de](http://www.htg-hst.de)

<sup>2</sup> Alstom Power Technology Centre: [www.techcentreuk.power.alstom.com](http://www.techcentreuk.power.alstom.com)

<sup>3</sup> GMV: [www.gmv.com](http://www.gmv.com)

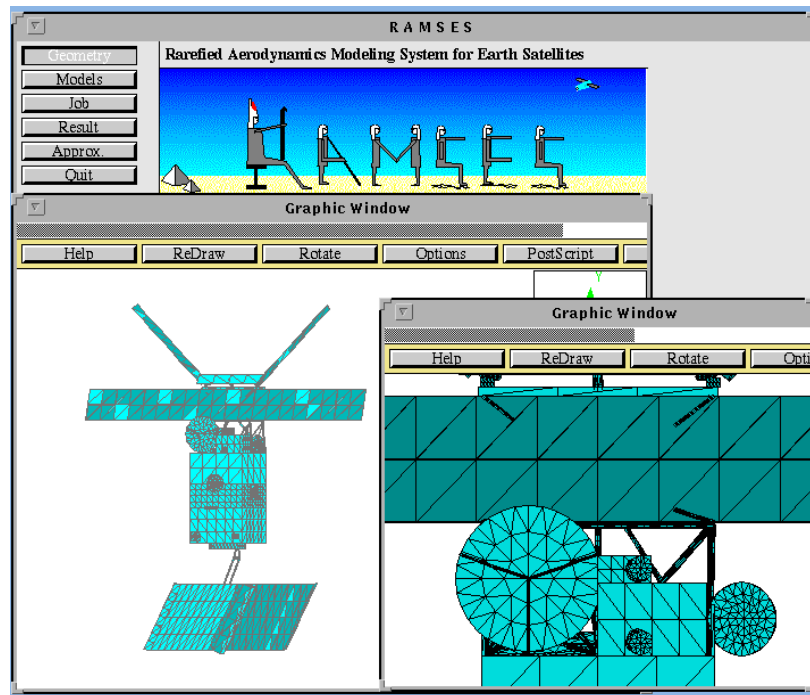


**Figure 2-20 - Screen Shot of the RAMSES Software**  
Image credit [56]

The authors of the studies and the software developers made numerous recommendations describing the improvements that the various software systems would benefit from. In addition, some common capabilities and limitations were also identified from the software descriptions available. These are all summarised in Table 2-3.

**Table 2-3 - Key Elements of Software Systems for the Analysis of Environmental Disturbances on Spacecraft**

Improvements Recommended by Different Authors	<ul style="list-style-type: none"> <li>• Capability to incorporate multiple Gas-Surface Interaction Models (GSIMs)</li> <li>• Capability to incorporate surface-dependent material properties</li> <li>• Capability to incorporate surface-dependent temperatures</li> <li>• Capability to calculate damping forces due to rotating body or body parts</li> <li>• Algorithms to handle flow shielding (shadowing)</li> <li>• Algorithms to handle multiple reflections (concave bodies)</li> <li>• Data transfer and system integration capabilities</li> <li>• Greater adoption of concurrent engineering principles</li> <li>• Capability to incorporate multiple atmospheric models</li> </ul>
Common Capabilities	<ul style="list-style-type: none"> <li>• Graphical User Interface (GUI)</li> <li>• Graphical visualisation tools</li> </ul>



<b>Common Limitations</b>	<ul style="list-style-type: none"> <li>• Limited data import, export, interfacing, and manipulation capabilities</li> <li>• File-based data-storage system, as opposed to a Relational Database Management (RDBMS) storage system</li> <li>• Platform / operating system dependency</li> <li>• Many of the systems are old (10 years or more) and have been modified, rather than designed, to incorporate changes in information technology capabilities, advances in the field of rarefied gas dynamics and the demanding new requirements of modern Earth observation missions</li> <li>• Use of obsolete information technology</li> <li>• Programming language dependency</li> <li>• Use of obsolete software development strategies (for example, linear programming as oppose to object-orientated programming).</li> <li>• Inadequate implementation of concurrent engineering principles due to hybrid nature of developments, which were spread over a number of years</li> <li>• Require users to be trained (as oppose to self-taught using help documentation)</li> </ul>
---------------------------	--

A detailed appraisal of each software system would not be possible with the resources available to this study. However, it is worth briefly mentioning one example that is most relevant to a European-based study such as this, because it highlights the main limitations identified in Table 2-3. Namely, that the software systems were not designed to facilitate concurrent engineering, which, as discussed in Chapter 1, is a relatively recent approach to spacecraft systems engineering.

The example is provided by the work of some of the leading European protagonists in the field of spacecraft aerodynamic analysis. In 2006, Koppenweller, Fritsche, and Lips combined RAMSES (illustrated in Figure 2-20) with SCARAB and ANGARA [50]. This combination of a number of legacy analysis tools is marketed as a suite of multi-disciplinary analysis tools for orbit and re-entry.

This new terminology is in keeping with the modern drive towards concurrent engineering methods. However, RAMSES, SCARAB, and ANGARA were developed separately under ESA contract, commissioned by Dr H. Klinkrad, over a period of 14 years. They were not specifically designed to work together in a multi-disciplinary context, nor were they expressly intended to work with other engineering tools within a collaborative concurrent engineering context.

Furthermore, as will be shown in Chapter 3, any modern FMF analysis tool must be able to incorporate the increasing number of GSIMs and their associated data. The suite of tools commissioned by Klinkrad were not explicitly designed to do this and have no obvious mechanism for dealing with large quantities of data.

## 2.8 Verification of Analyses

Analysis of operational flight data for comparison with analytical and computational aerodynamic calculations is not straightforward. Even if all sources of attitude and orbital perturbation can be accounted for (using, for example, onboard accelerometers); the complete history of the spacecraft's local atmospheric

conditions is required over multiple orbits. Collecting such information presents a formidable task and requires access to comprehensive and often proprietary datasets. As a result, very few notable studies have been performed.

Some work has been carried out at Aston University, in the United Kingdom. In 1985, Boulton [59] analysed the orbit of the 1964-52B satellite. As part of a comprehensive analysis of the various perturbations on the satellite, he calculated the effects of aerodynamic drag using a variety of techniques, including King-Hele's [14].

At the same university in 1997, Moore and Ehler [60] compared the altitude differences between the near-identical ERS-1 and ERS-2 satellites, which orbited on the same repeated ground track with a separation of 32 minutes. From this they were able to eliminate the effects of Earth's gravity (and its localised geographic perturbations), as well as the effects of solar gravity. They were left with the residual forces on the satellites due to aerodynamic drag and lunar gravity, from which they planned to extract the aerodynamic drag data (the published results of this work have not been located).

Between 1990 and 1995, Harrison and Swinerd [31] performed a number of comprehensive Precise Orbital Analysis (POA) studies at the Department of Astronautics and Aeronautics at Southampton University. These analyses used King-Hele's methods in conjunction with Satellite Laser Ranging (SLR) data to verify aerodynamic calculations of the low Earth orbit satellites ERS-1, STARLETTE, and STELLA. Harrison and Swinerd's POA method appears to be a reliable and reproducible way of validating analytical and computational analyses.

A recent study by Moe [19], lists a small number of alternative methods for performing verification studies that have been published during the course of this PhD. These studies use the United States Air Force (USAF) High-Accuracy Satellite Drag Model (HASDM) program, which employs an energy dissipation rate method to process orbital data related to pairs of satellites operating at similar perigee altitudes.

## **2.9 Summary**

This chapter has provided an overview of spacecraft aerodynamics in the free molecular flow regime of low Earth orbit spaceflight and identified some of the main challenges of modelling aerodynamic disturbances in this regime. It has compared and contrasted the main aerodynamic analysis methods, and described some existing computational analysis tools.

It has been shown that in the free molecular flow regime, Gas-Surface Interactions (GSIs) dominate the flow. Gas-Surface Interaction Models (GSIMs) are the subject of Chapter 3.

Comparison of the existing computational analysis tools, identified a number of common capabilities, limitations, and recommended improvements. One of the main issues identified is that existing analysis tools are not designed with concurrent engineering in mind from the outset. The challenges of implementing concurrent engineering within a spacecraft-engineering context are described in Chapter 4.

This chapter has also laid the foundations for describing the detailed implementation of a new method that has been implemented in the FMF Module, which is a hybrid between the RTP and TPMC methods. The Hybrid method and other key features of the FMF Module are described in Chapter 6.



### 3 GAS-SURFACE INTERACTION MODELS

In the free-molecular flow regime of low Earth orbit spaceflight, a negligible number of intermolecular collisions occur, such that the flow field is characterised by the gas-surface interactions that take place.

Therefore, aerodynamic analysis in the free molecular flow regime is only as accurate as the Gas-Surface Interaction Models (GSIMs) that are employed. Even in the slightly denser transitional regime, *“predictions of aerothermodynamic behaviour are subject to the same uncertainties as those in the gas-surface interaction model itself”* [61].

However, the numerous varieties of all possible gas-surface interactions, means that despite extensive research and many experimental studies no single generic GSIM yet exists.

In simple terms, the challenge of developing a successful GSIM is to model the exchange of energy and momentum between molecules and surfaces due to impact and reemission. In practice, this means that in rarefied flow at satellite speeds a number of factors must be considered, including:

- Gas properties (chemical composition, molar mass, ratio of specific heats, number of degrees of freedom, density, temperature, bulk speed)
- Surface properties (chemical composition, roughness, cleanness, and temperature)
- Angle of incidence between the flow vector and the surface

A contemporary review of progress in gas surface interaction studies was presented by Borisov [62] at the twenty-fourth International Rarefied Gas Symposium, in July 2004. His paper demonstrates that a comprehensive GSIM would need to consider the effects of quantum physics and other physics at the leading edge of science and beyond. However, for the accuracy required for analysis of spacecraft in low Earth orbit, only classical models have been employed to date.

Classical gas-surface interaction models evolved from consideration of the kinetic theory of gases developed by Daniel Bernoulli in 1738, and subsequently James Clerk Maxwell in 1859. In 1872, Boltzmann’s work generalised Maxwell’s findings. The result is that most GSIMs are based on some form of the Maxwell-Boltzmann distribution function, which can be used to describe the probability distribution of various properties of a gas (e.g. molecular velocities, number density).

The Maxwell-Boltzmann distribution function is used in the models to describe the nature of the impinging gas and sometimes (as in the case of the Maxwellian model and other drifting Maxwellian models) the reflected gas.

However, newer models also employ more complex distribution functions to describe the nature of the reflected gas. These functions, often described as scattering kernels, can be quite complex but they are considered to provide a better description of the reemitted gas and hence the interaction itself.

One additional feature that arises from Maxwell's work is that gas-surface interaction models should ideally satisfy the condition of reciprocity [63]. That is, for equilibrium, the relationship between the probability of a gas-surface interaction with one set of incident and reflected velocities and the probability of the inverse interaction should satisfy the condition given by Equation 3-1.

$$v_r \cdot \hat{n} P(-v_r, -v_i) \exp\left(\frac{-e_r}{kT_w}\right) = -v_i \cdot \hat{n} P(v_i, v_r) \exp\left(\frac{-e_i}{kT_w}\right) \quad 3-1$$

The terms  $v$  and  $e$  refer to molecular velocity and energy respectively. The subscripts  $i$  and  $r$  refer to the incident and reflected molecules. The function  $P(v_1, v_2)$  is the probability that an incident molecule with velocity  $v_1$  leaves the surface with velocity  $v_2$ . The remaining terms are consistent with previous notation, such that  $\hat{n}$  is the surface unit normal (outwards),  $k$  is the Boltzmann constant ( $1.3807 \times 10^{-23} \text{ J K}^{-1}$ ), and  $T_w$  is the temperature of the surface.

There are so many models and variations on models that it would not be practical or sensible to describe them all within the context of this work. This chapter looks at two of the most popular GSIMs used by spacecraft aerodynamicists: the Newtonian model and the Maxwellian model. The characteristic input parameters of the Maxwellian model are then discussed. For comparison, several alternative GSIMs are briefly listed. Finally, some future directions of gas-surface interaction modelling are summarised.

### 3.1 Newtonian Model

Newton published the first ever gas-surface interaction model, as part of his *Philosophiae Naturalis Principia Mathematica* in 1687 [64]. He assumed that:

1. Gas flow can be represented by a continuous stream of parallel particles, with no component of random motion.
2. Gas molecules lose all normal momentum upon impact with a surface, but maintain their tangential momentum and so slide across the surface after impact.

This situation is illustrated in Figure 3-1.

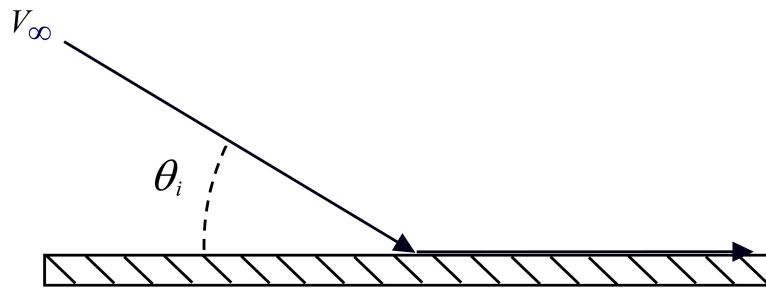


**Figure 3-1 - Newton's Gas-Surface Interaction Model**

### 3.1.1 Original Model

Newton's original Gas-Surface Interaction Model (GSIM) results in a coefficient of pressure for a flat plate, inclined at an incident angle  $\theta_i$  to the flow, given by Equation 3-2.

$$C_p = 2 \sin^2 \theta_i \quad 3-2$$

Newton incorrectly believed that this GSIM was valid in all flow regimes. We now know that his underlying assumptions were not valid. However, his sine-squared law, which assumes total normal accommodation of momentum, is still in use today. This is because it provides a good rough estimate of the pressure distribution over a blunt body in transitional and free molecular flows, and an initial benchmark by which other results can be compared (see, for example, [44]).

Newton's model does not account for the transfer of energy, nor does it accurately simulate the reemitted molecules. It also does not satisfy the condition of reciprocity.

### 3.1.2 Modified Newtonian Model

A modified form of Newton's GSIM can be used to provide a more accurate estimate of the pressure distribution over a blunt body in hypersonic flow. This is achieved by replacing the numerical value 2 in Equation 3-2, with an estimation of the maximum pressure coefficient ( $C_{p,\max}$ ) that would occur at the stagnation point behind the normal shockwave that formed in front of the blunt body. An expression for the maximum pressure coefficient is provided as Equation 3-3 [65].

$$C_{p,\max} = \frac{p_o - p_\infty}{q_\infty} \quad 3-3$$

The term  $p_o$  represents the stagnation pressure behind the normal shockwave, given by Equation 3-4.

$$p_o = p_\infty \left( \frac{1 - \gamma + 2\gamma M_\infty^2}{\gamma + 1} \right) \left( \frac{(\gamma + 1)^2 M_\infty^2}{4\gamma M_\infty^2 - 2(\gamma - 1)} \right)^{\gamma/(\gamma-1)} \quad 3-4$$

The benefit of the modified Newtonian method is immediately apparent from this very simple relation between the free stream and stagnation pressures; it is dependent only on the ratio of specific heats  $\gamma$  and the free stream Mach number  $M_\infty$ .

## 3.2 Maxwellian Model

The Maxwellian model is the most popular gas-surface interaction model for analysing spacecraft in the free molecular flow regime [66]. The majority of the tools listed in Table 2-2, which are concerned with the analysis of spacecraft aerodynamic drag and torque, incorporate some form of the Maxwellian model.

It is the reduction of the highly complex gas-surface interaction to apparently simple parameters that underpins the popularity of the Maxwellian model in the fields of both theoretical analysis and experiment. It is presented in various forms in [20][29][67][68][69][70][71] and elsewhere.

Although the model satisfies the condition of reciprocity, the scattering kernel it employs is not physically realistic. Therefore, the calculation of energy and momentum transferred to the surface by the reemitted molecules is implicitly incorrect and leads to inaccuracies in the prediction of surface pressures and shear stresses.

The unrealistic reemission model becomes even more problematic in scenarios where multiple reflections need to be simulated (for example using TPMC or DSMC). Numerous investigators have developed more sophisticated models for predicting the reflected flow field, some of which are detailed in Section 3.4.

### 3.2.1 Original Model

In 1879, James Clerk Maxwell developed a GSIM in which he postulated that a fraction  $\varepsilon_d$  of incident molecules may be assumed to reflect diffusely, and a fraction  $\varepsilon_s (= 1 - \varepsilon_d)$  specularly, as illustrated in Figure 3-2.

In this scenario, the collision between the specularly reflected molecules and the surface is assumed perfectly elastic. Such that the specularly reflected molecules experience a full reversal of their normal component of momentum relative to the surface, whilst their tangential component<sup>1</sup> remains unchanged. In a perfectly elastic

---

<sup>1</sup> Tangential component: should more accurately be described as the shear component in keeping with the definition provided in Section 2.4. However, most GSIM texts use the term tangential. For consistency with these texts, the term tangential will be used whenever referring to this GSIM.



collision (incident speed equals reemitted speed), the molecules therefore impart twice their normal momentum to the surface, but no tangential momentum or energy.

Maxwell assumed that the collision between the remaining molecules and the surface is inelastic and that the molecules impart all of their incident normal and tangential (shear) momentum to the surface. The molecules lose all knowledge of their incoming direction and are then reemitted with a Maxwellian velocity distribution as if having issued from a fictitious stationary gas behind the surface (the gas having no bulk velocity relative to the surface). Maxwell did not assume that the diffusely reemitted molecules would be in thermal equilibrium with the surface.

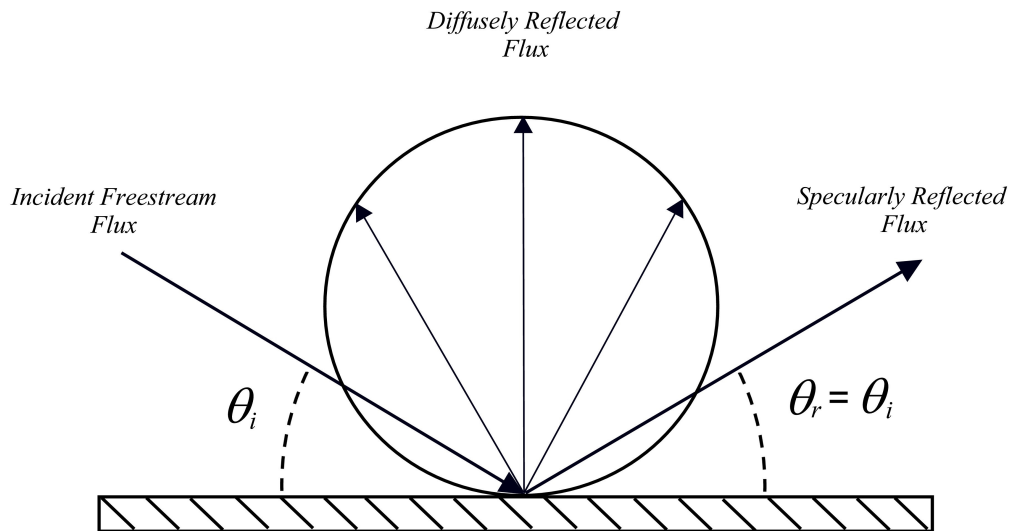


**Figure 3-2 - Schematic of the Maxwellian Gas-Surface Interaction Model**

A gas with a Maxwellian distribution of velocities contains molecules that are moving randomly due to their thermal energy, such that all possible thermal velocities of an individual molecule are equally likely. Therefore, Maxwell's diffusely reemitted molecules do not impart a shear stress to the surface as they leave, but they do impart the equal and opposite of their normal momentum to it.

### 3.2.2 Schaaf and Chambre's Improved Model

Shortly after Maxwell published his work, Smoluchowski [72] postulated that the extent of energy transfer to a surface by an incident molecular flux can be described by the thermal accommodation coefficient  $\sigma_a$ , given by Equation 3-5.

$$\sigma_a = \frac{\Delta E_i - \Delta E_r}{\Delta E_i - \Delta E_w} \quad 3-5$$

The terms  $\Delta E_i$  and  $\Delta E_r$  are the incident and reflected energy fluxes respectively. The term  $\Delta E_w$  is the energy flux that would be carried away if all the molecules were reemitted with a Maxwellian distribution in thermal equilibrium with the surface, such that they have the same temperature as the surface  $T_w$ .

In 1958, Schaaf and Chambre [37] introduced two analogous coefficients to Maxwell's GSIM to describe the extent of normal and tangential momentum transfer to the surface. Their phenomenological coefficients, provided by Equations 3-6 and 3-7 respectively, improve upon Maxwell's model because they separate the effects of incomplete normal and tangential momentum transfer.

$$\sigma_N = \frac{p_i - p_r}{p_i - p_w} \quad 3-6$$

$$\sigma_T = \frac{\tau_i - \tau_r}{\tau_i - \tau_w} = \frac{\tau_i - \tau_r}{\tau_i} \quad (\tau_w = 0) \quad 3-7$$

The term  $\sigma_N$  is usually referred to as the normal momentum accommodation coefficient and  $\sigma_T$  as the tangential momentum accommodation coefficient. The subscripts  $i$  and  $r$  refer to incident and reflected flux respectively.

As a corollary to the definition of thermal accommodation coefficient, Schaaf and Chambre also assumed that some of the reemitted molecules might leave in thermal equilibrium with the surface. Therefore, as before, the subscript  $w$  refers to the molecules that are reemitted with a Maxwellian distribution of velocities corresponding to the temperature of the surface  $T_w$ .

Consequently, for complete specular reflection with no energy exchange (elastic collision)  $\sigma_a = \sigma_N = \sigma_T = 0$ . Whereas, for complete diffuse reflection, in which the energy of the molecules completely accommodates to the surface,  $\sigma_a = \sigma_N = \sigma_T = 1$ .

Having lost all their momentum and energy to the surface, diffusely reemitted molecules only leave with a component of thermal velocity (Equation 2-11, with  $T$  equal to the temperature of the surface  $T_w$ ). They therefore have significantly lower velocities than specularly reemitted molecules and correspondingly less of an impact on subsequent surfaces in the case of multiple reflections.

Although all three coefficients are defined independently of one another, it would be physically impossible for  $\sigma_N = \sigma_T = 1$ , whilst  $\sigma_a = 0$ . This is because if all of the flux is reflected diffusely, some of its energy must have accommodated to the surface during the process of thermal equilibration.

Conversely, if  $\sigma_N = \sigma_T = 0$  and all of the flow is reflected specularly, then  $\sigma_a$  may be non-zero. In this scenario,  $\sigma_a$  describes the elasticity of the specular interaction and hence the energy of the reflected flux as a proportion of the incident

flux ( $\Delta E_r = (1 - \sigma_a)\Delta E_i$ ). However, it is most often assumed that  $\sigma_a = 0$  in the case of specular reflection, such that interactions are perfectly elastic and there is vanishing energy exchange (incident speed equals reemitted speed) [38].

Equations 3-6 and 3-7 can be rearranged to give expressions for the pressure and shear stress on the surface due to the reflected flux, as given by Equations 3-8 and 3-9 respectively.

$$p_r = (1 - \sigma_N)p_i + \sigma_N p_w \quad 3-8$$

$$\tau_r = (1 - \sigma_T)\tau_i \quad 3-9$$

Given these definitions, Schaaf and Chambre were able to formulate expressions for the pressure and shear stress on the surface from consideration of the momentum flux imparted to the surface by both incident and reflected molecules. A schematic of the situation is provided in Figure 3-3.

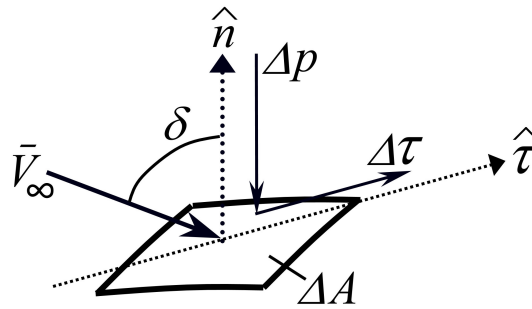


**Figure 3-3 - Elemental Area Flow Geometry**

The vectors  $\hat{n}$ ,  $\hat{\tau}$ , and  $\bar{V}_\infty$  are coplanar and represent the element unit normal direction (outwards), the unit shear stress direction (defined by Equation 2-23), and the incident flow vector respectively. The term  $\delta$  is the angle between the incident flow vector and the element unit normal (note that  $\delta = (90^\circ - \theta_i)$ , where  $\theta_i$  is the angle of elevation of the incident flow defined in Figure 3-2, such that  $\cos\delta = \sin\theta_i$ ).

From Figure 3-3, it is possible to write expressions for the net pressure and shear stress acting on the surface in terms of the incident and reflected flux. Substituting Equations 3-8 and 3-9, one then obtains these expressions in terms of the momentum accommodation coefficients, as illustrated by Equations 3-10 and 3-11.

$$\Delta p = p_i + p_r = (2 - \sigma_N)p_i + \sigma_N p_w \quad 3-10$$

$$\Delta \tau = \tau_i - \tau_r = \sigma_T \tau_i \quad 3-11$$

The term  $p_w$  is the pressure exerted by the molecules leaving the surface as if having all issued from the fictitious Maxwellian gas under steady-state conditions. This pressure is simply a function of the average normal momentum component imparted by the molecules as they are emitted from the surface area in unit time, as described by Equation 3-12 [37].

$$p_w = \frac{1}{2} m' \sqrt{2\pi R_{sp} T_w} N_i \quad 3-12$$

The term  $N_i$  is the number of molecules that are incident upon the element (with area  $\Delta A$ ) per unit time, as defined by Equation 3-13 [37], which under steady state conditions is equal to the number of molecules reemitted diffusely ( $N_w$ ). The remaining terms are consistent with previous notation, such that  $m'$  is the molecular mass of the gas and  $R_{sp}$  is the specific gas constant.

$$N_i = \frac{\rho_\infty}{m'} \sqrt{\frac{R_{sp} T_\infty}{2\pi}} \left\{ \exp(-s_\infty^2 \cos^2 \delta) + \sqrt{\pi} s_\infty \cos \delta [1 + \operatorname{erf}(s_\infty \cos \delta)] \right\} \Delta A \quad 3-13$$

As before, the terms  $\rho_\infty$  and  $T_\infty$  refer to the free stream density and temperature of the gas respectively. Gas density is defined by Equation 3-14 [18].

$$\rho = \frac{nm}{N_A} = nm' \quad 3-14$$

The terms  $n$ ,  $m$ ,  $m'$ , and  $N_A$  are the number density (molecules / m<sup>3</sup>), molar mass (in kg kmol<sup>-1</sup>), molecular mass (in kg), and Avogadro's constant (6.02 × 10<sup>26</sup> kmol<sup>-1</sup>) respectively.

From the definition of density provided by Equation 3-14 and the definition of thermal speed  $V_a$  provided by Equation 2-11, it is possible to write Equation 3-13 in the form provided by Equation 3-15.

$$N_i = \frac{n_\infty V_a}{2\sqrt{\pi}} \left\{ \exp(-s_\infty^2 \cos^2 \delta) + \sqrt{\pi} s_\infty \cos \delta [1 + \operatorname{erf}(s_\infty \cos \delta)] \right\} \Delta A \quad 3-15$$

The molecular speed ratio  $s_\infty$  is sometimes written in terms of  $\beta_\infty$ , which is equivalent to the inverse of the gas's thermal speed  $V_a$ . This is illustrated by Equation 3-16.

$$s_\infty = V_\infty \beta_\infty = \frac{V_\infty}{\sqrt{2R_{sp} T_\infty}} = \frac{V_\infty}{V_a} \quad 3-16$$

The expression  $\operatorname{erf}()$  is the error function defined by Equation 3-17. Its magnitude for some value  $x$  is illustrated in Figure 3-4 and can be computed using standard series expansions, or approximations (see, for example, [27][29]).

$$\operatorname{erf}(x) = \frac{2}{\sqrt{\pi}} \int_0^x \exp(-U^2) dU \quad 3-17$$

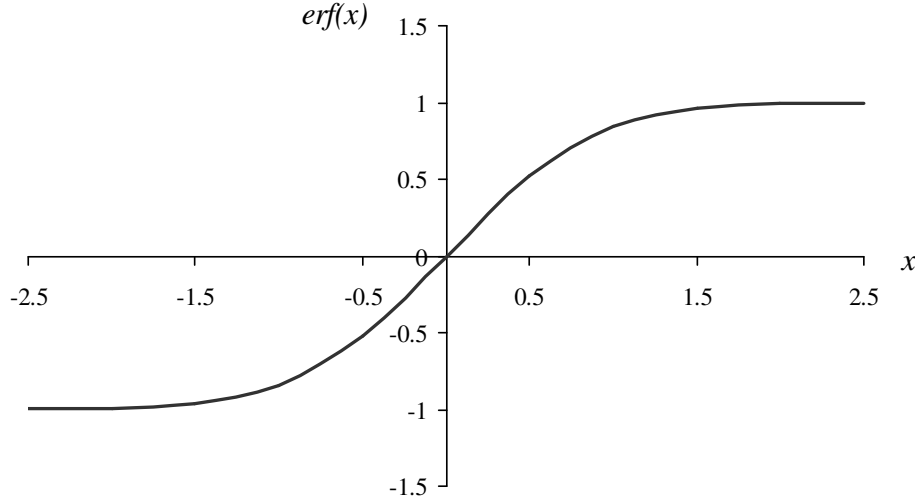


**Figure 3-4 - Error Function ( $\operatorname{erf}(x)$ )**

The error function results from integration of the number density probability distribution function ( $f$ ) across the range of all possible incident velocities. Note that for a Maxwellian gas,  $f$  describes the number density of molecules per unit volume of phase space of the incident gas moving relative to the surface, such that each molecule moves with a velocity composed of the bulk velocity plus its own random thermal velocity.

Similar expressions to Equation 3-13 can be derived for  $p_i$  and  $\tau_i$  from consideration of the momentum fluxes in these directions, again assuming a Maxwellian distribution of number density [37]. Combining these expressions for  $p_i$  and  $\tau_i$  with Equations 2-21, 3-10, 3-11, 3-12, and 3-13, the coefficients of pressure and shear stress acting on the elemental area can be derived [37], as given by Equations 3-18 and 3-19 respectively.

$$C_p = \frac{\Delta p}{q_\infty} = \frac{1}{s_\infty^2} \left\{ \left[ \frac{(2 - \sigma_N)}{\sqrt{\pi}} s_\infty \cos \delta + \frac{\sigma_N}{2} \left( \frac{T_w}{T_\infty} \right)^{1/2} \right] \exp(-s_\infty^2 \cos^2 \delta) + \left[ (2 - \sigma_N) \left( \frac{1}{2} + s_\infty^2 \cos^2 \delta \right) + \frac{\sigma_N}{2} \left( \frac{T_w}{T_\infty} \right)^{1/2} \sqrt{\pi} s_\infty \cos \delta \right] [1 + \operatorname{erf}(s_\infty \cos \delta)] \right\} \quad 3-18$$

$$C_\tau = \frac{\Delta\tau}{q_\infty} = \frac{\sigma_T \sin \delta}{s_\infty \sqrt{\pi}} \left\{ \exp(-s_\infty^2 \cos^2 \delta) + \sqrt{\pi} s_\infty \cos \delta [1 + \operatorname{erf}(s_\infty \cos \delta)] \right\} \quad 3-19$$

An equation for the coefficient of convective heat transfer ( $C_h$ ) to the surface under steady and uniform free molecular flow in terms of the thermal accommodation coefficient can be derived in a similar manner and is provided by Equation 3-20.

$$C_h = \frac{\Delta Q}{q_\infty V_\infty \Delta A} = \frac{\sigma_a}{2s_\infty^3 \sqrt{\pi}} \left\{ \left[ s_\infty^2 + \frac{\gamma}{\gamma-1} - \frac{\gamma+1}{2(\gamma-1)} \left( \frac{T_w}{T_\infty} \right) \right] \right. \\ \times \left[ \frac{1}{\exp(s_\infty^2 \cos^2 \delta)} + \sqrt{\pi} s_\infty \cos \delta [1 + \operatorname{erf}(s_\infty \cos \delta)] \right] \\ \left. - \frac{1}{2 \exp(s_\infty^2 \cos^2 \delta)} \right\} \quad 3-20$$

The term  $\Delta Q$  in Equation 3-20 represents the convective heat flux to the surface (heat transfer per second).

It is interesting to note that Equation 3-18 can be used to calculate a Newtonian pressure distribution ( $C_p = 2 \cos^2 \delta$ , as described by Equation 3-2) [29]. This is achieved by setting  $s_\infty = \infty$ ,  $\sigma_N = 1$ ,  $\sigma_T = 0$  and  $T_w/T_\infty = 1$ . In this case,  $C_\tau = 0$ , as illustrated in Figure 3-5.

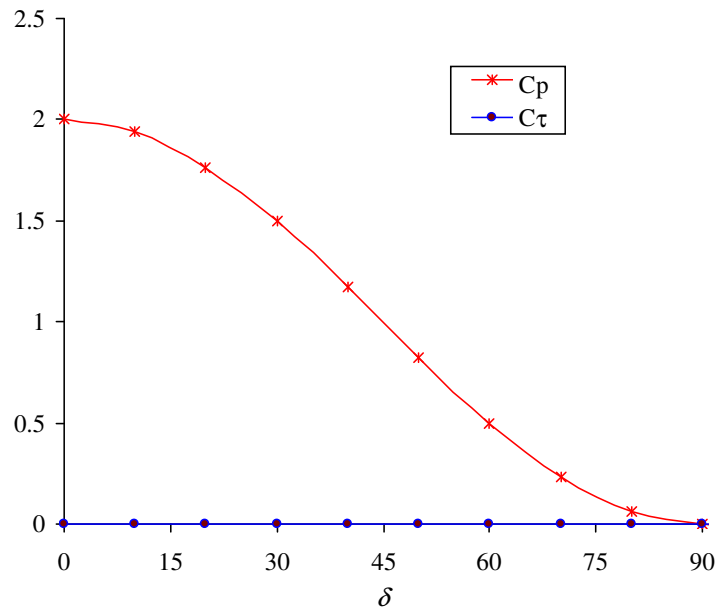


**Figure 3-5 - Newtonian Pressure Distribution on a Flat Plate using the Schaaf and Chambre Gas-Surface Interaction Model**

Uses Equations 3-18 and 3-19, with  $s_\infty = \infty$ ,  $T_w/T_\infty = 1$ ,  $\gamma = 1.4$ ,  $\sigma_N = 1$ ,  $\sigma_T = 0$ .  $\delta$  is the angle of incidence between the incoming flow and the surface normal.

### 3.2.3 Hyperthermal and Sub-Hyperthermal Flow

Equations 3-18 and 3-19 are plotted in Figure 3-6 for a range of molecular speed ratios under the assumption of complete diffuse reflection ( $\sigma_N = \sigma_T = 1$ ).

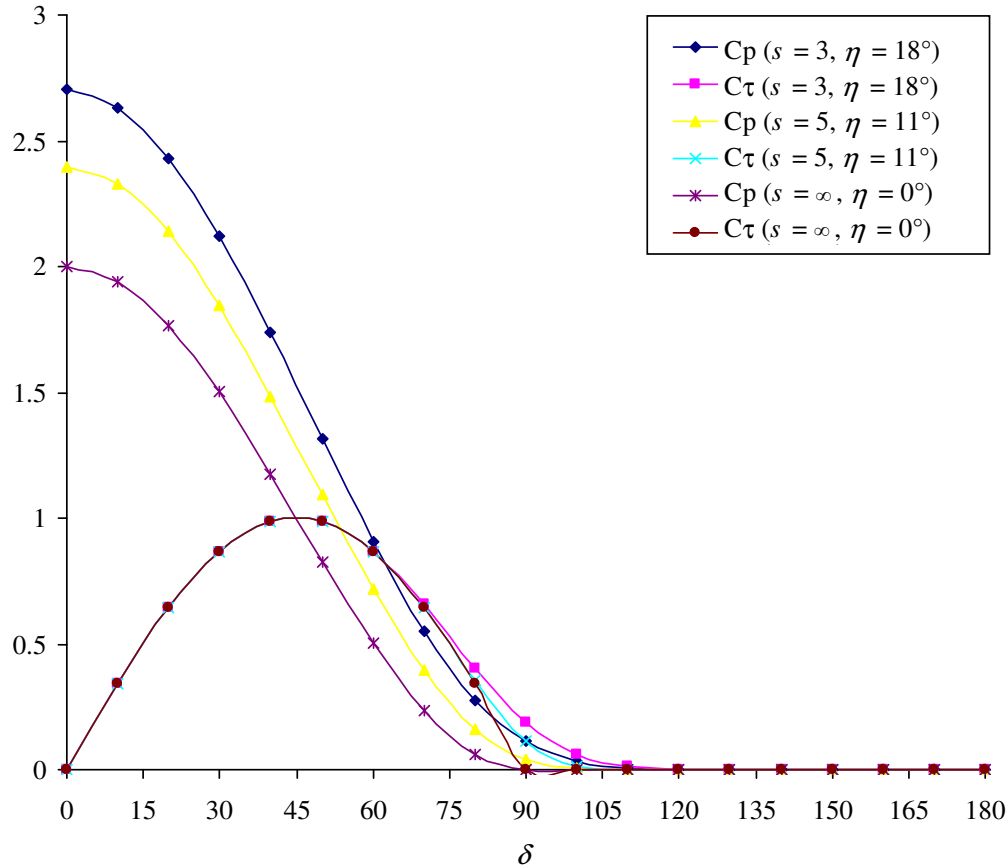


**Figure 3-6 - Pressure and Shear Stress Coefficients on a Flat Plate Using the Schaaf and Chambre Gas-Surface Interaction Model - Fully Diffuse Reflection**

Uses Equations 3-18 and 3-19, with  $T_w/T_\infty = 1$ ,  $\gamma = 1.4$ ,  $\sigma_N = \sigma_T = 1$ .  $\eta$  is the molecular Mach angle defined by Equation 2-18 and  $\delta$  is the angle of incidence between the incoming flow and the surface normal.

It is notable from Figure 3-6 and its underlying equations that there is no restriction on the angle of incidence  $\delta$ . Consequently, it may take values greater than  $90^\circ$ . In this scenario, the surface is aft facing. However, it may still be impacted by molecules that have large lateral thermal velocities in comparison to the bulk velocity vector.

The lower the molecular speed ratio  $s_\infty$ , the higher the possible lateral thermal velocities of individual molecules, and hence the higher the molecular Mach angle  $\eta$  (defined by Equation 2-18). Consequently, as the molecular speed ratio decreases the extent to which the flow can reach around the body increases. It is for

this reason that the pressure and shear stress remain non-negligible until approximately  $\delta = (90^\circ + \eta)$ .

Therefore, both the forward facing and aft facing surfaces of a convex body immersed in sub-hypersonic flow with a finite molecular speed ratio, can be modelled using Equations 3-18 and 3-19.

Figure 3-6 also illustrates that in hypersonic flow ( $s_\infty \rightarrow \infty, \eta \rightarrow 0$ ), the surface has zero pressure and shear stress for  $\delta > 90^\circ$ , as would be expected. In addition, the definition, first stated in Section 2.2.3, that when  $s_\infty > 5$  the flow can be described as hypersonic, appears to be justified.

For comparison, Equations 3-18 and 3-19 are plotted in Figure 3-7, under the assumption of complete specular reflection ( $\sigma_N = \sigma_T = 0$ ). In this scenario, the shear stress is zero in all cases, and the pressure increases by a factor of approximately 1.5 to 2 at lower incidences.

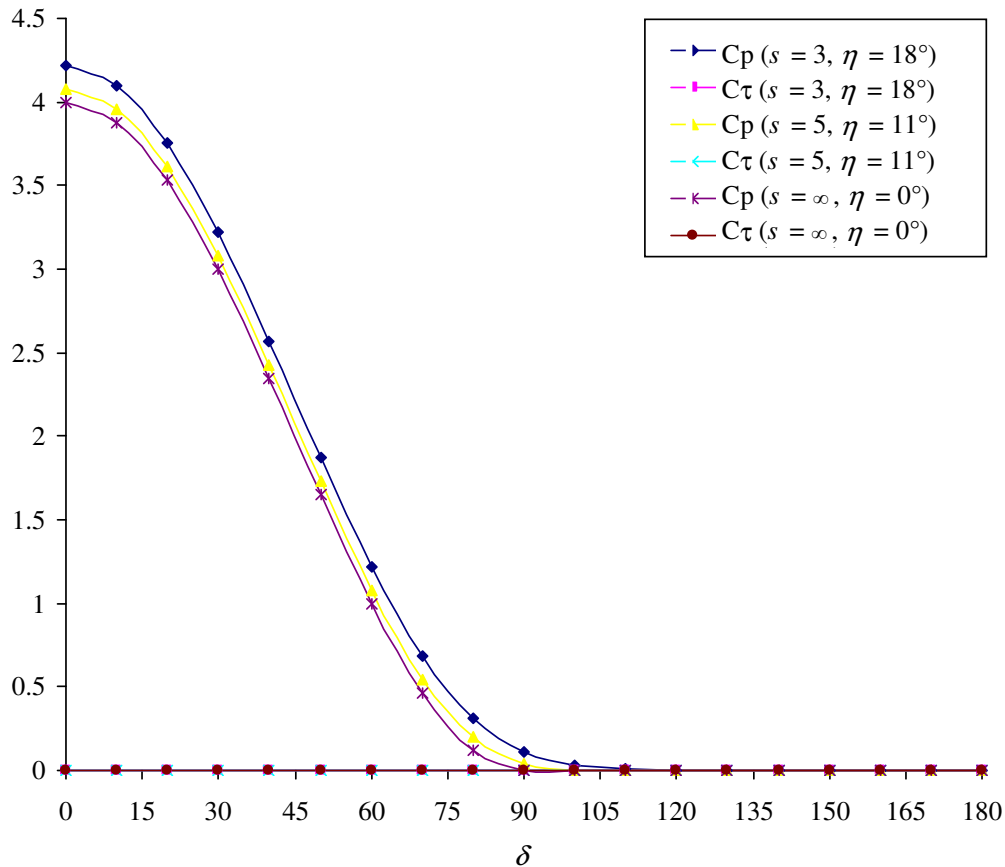


**Figure 3-7 - Pressure and Shear Stress Coefficients on a Flat Plate Using the Schaaf and Chambre Gas-Surface Interaction Model - Fully Specular Reflection**

Uses Equations 3-18 and 3-19, with  $T_w/T_\infty = 1, \gamma = 1.4, \sigma_N = \sigma_T = 0$ .  $\eta$  is the molecular Mach angle defined by Equation 2-18 and  $\delta$  is the angle of incidence between the incoming flow and the surface normal.



As illustrated in Figure 3-7, the hyperthermal specular pressure coefficient results have approximately twice the magnitude of the Newtonian results illustrated in Figure 3-5 across all incidences. This is because in the hyperthermal specular case the molecules impart momentum as they are reemitted, whereas, as described in Section 3.1, in the Newtonian model the molecules are not reemitted.

The surface still experiences some pressure for  $\delta > 90^\circ$  in sub-hyperthermal flow under the assumption of complete specular reflection. However, the pressure is lower than the fully diffuse case by a factor of approximately 75%. This is to be expected because if  $\sigma_N = 0$ , the temperature-related terms in Equation 3-19, which correspond to the diffusely reflected Maxwellian flow, are nullified.

This is consistent with Maxwell, Schaaf, and Chambre's concept of diffuse flow better representing the gas-surface interaction under conditions of non-zero energy transfer (i.e. accounting for the thermal states of the gas and the surface).

Moreover, it is to be expected that in sub-hyperthermal flow, under the assumption of complete diffuse reflection, as  $T_w/T_\infty$  increases, the pressure exerted on the surface increases. This scenario is demonstrated by comparison of Figure 3-6 with Figure 3-8. The latter, based on a temperature ratio three times higher than the former, illustrates correspondingly higher pressures for the sub-hyperthermal cases.

Equations 3-18 and 3-19 may be applied to the individual species of a gas mixture. Because the thermal speed is inversely proportional to the square of molar mass (Equations 2-7 and 2-11), heavier species will have higher molecular speed ratios and will therefore have a greater effect on surfaces where  $\delta < 90^\circ$  [73].

Note that under hyperthermal flow conditions the number of molecules incident upon an element  $\Delta A$  per unit time, as defined by Equation 3-13, reduces to the form provided by Equation 3-21.

$$N_i|_{Hyper} = \frac{\rho_\infty V_\infty}{m'} \Delta A_p \quad 3-21$$

The term  $\Delta A_p$  is the projected area of the surface element in the flow direction (the surface area of the element when projected onto a plane that is perpendicular to the flow direction), given by Equation 3-22.

$$\Delta A_p = \Delta A \cos \delta \quad 3-22$$

From the definition of density provided by Equation 3-14, it is possible to write Equation 3-21 in terms of number density, as provided by Equation 3-25.

$$N_i|_{Hyper} = n_\infty V_\infty \Delta A_p \quad 3-23$$

The incident mass flow  $\dot{m}_i$  under hyperthermal conditions can be calculated by multiplying  $N_i|_{Hyper}$  by the molecular mass  $m'$  of the gas, and is given by Equation 3-24.

$$\dot{m}_i|_{Hyper} = \rho_\infty V_\infty \Delta A_P \tag{3-24}$$

Equation 3-24 should be familiar to continuum aerodynamicists as the algebraic expression used in the mass continuity equation for steady flow.

Hyperthermal mass flow per unit area (mass flux) and molecular flow per unit area (molecular flux) can be derived by dividing Equations 3-23 and 3-24 respectively by  $\Delta A_P$ . These hyperthermal fluxes may be considered the “bulk” fluxes of the flow in sub-hyperthermal conditions.

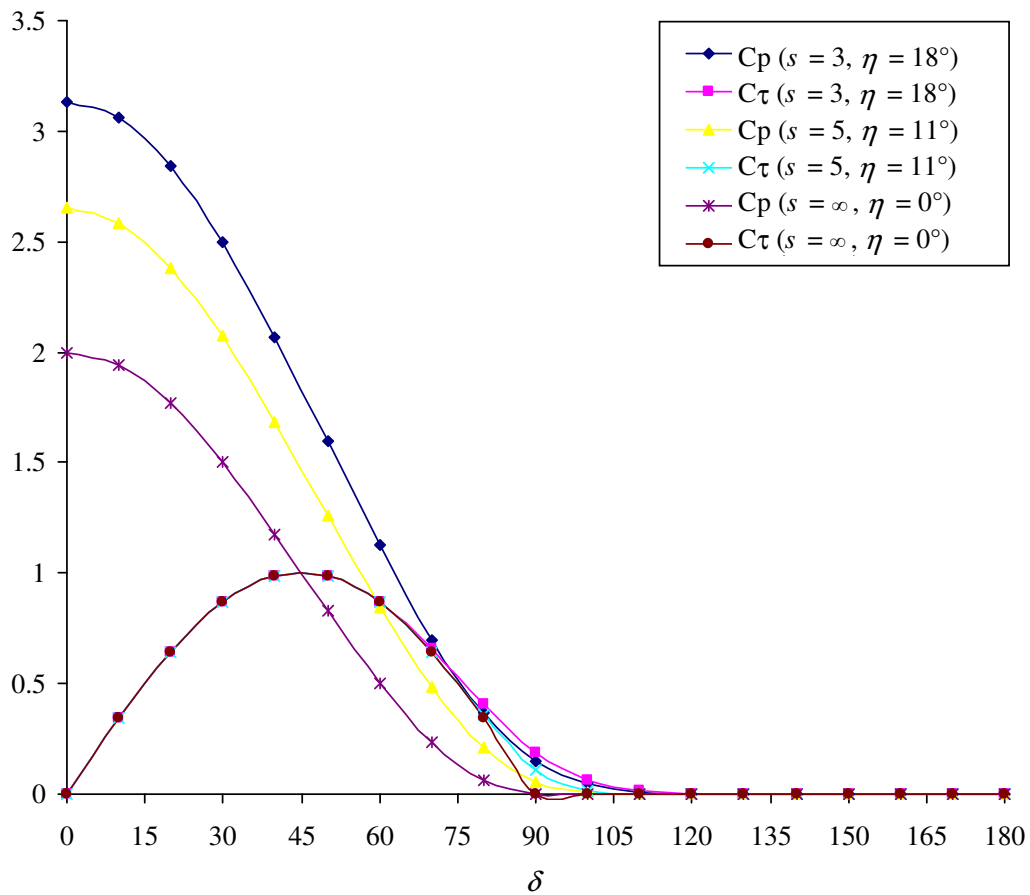


**Figure 3-8 - Pressure and Shear Stress Coefficients on a Flat Plate Using the Schaaf and Chambre Gas-Surface Interaction Model - Fully Diffuse Reflection - Hot Surface**

Uses Equations 3-18 and 3-19, with  $T_w/T_\infty = 3$ ,  $\gamma = 1.4$ ,  $\sigma_N = \sigma_T = 1$ .  $\eta$  is the molecular Mach angle defined by Equation 2-18 and  $\delta$  is the angle of incidence between the incoming flow and the surface normal.

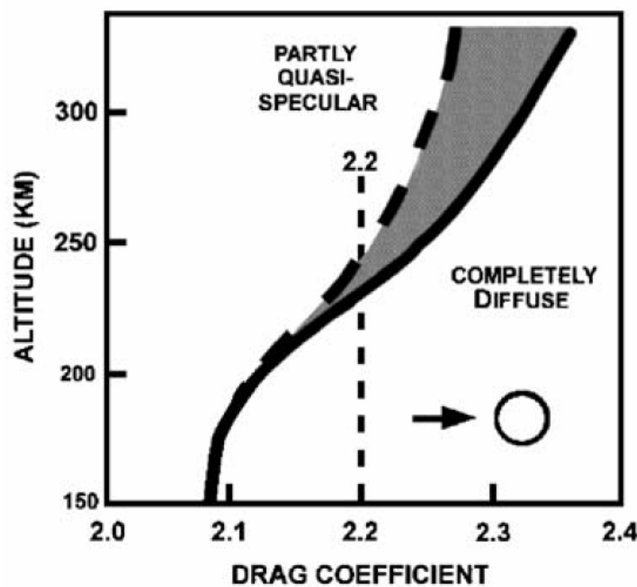
### 3.3 Accommodation Coefficients

Accurate determination of the accommodation coefficients for any given scenario requires an understanding of the material properties and microscopic geometry of the surface as well as the nature of the free stream gas.

This section examines some of the environmental factors that affect the accommodation coefficients. It also describes some of the methods that can be used to determine them.

#### 3.3.1 Environmental Factors

In practice, the accommodation coefficients have magnitudes that create a reemission pattern somewhere between the two extremes of specular and diffuse. Figure 3-9 illustrates that variations in the possible extent of quasi-specular versus diffuse reemission create uncertainties in the prediction of satellite drag coefficient.



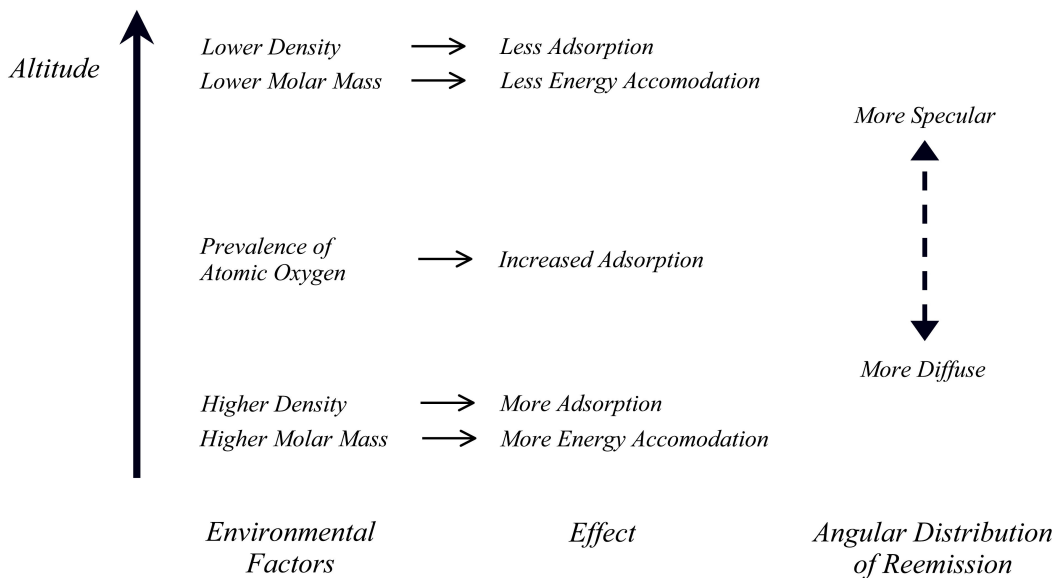
**Figure 3-9 - Variation of Spherical Satellite Drag Coefficient with Altitude Showing Variation Due to Specular and Diffuse Reemissions**

Image Credit [19]. Uses the Sentman Gas-Surface Interaction Model and assumes low solar activity.

The two main environmental factors that affect the angular distribution of reemitted molecules are the molar mass of the incident gas and a process known as adsorption. The effects of these factors vary with altitude due to changes in atmospheric composition and, in the case of adsorption, changes in density. Figure 3-10 provides broad rules of thumb to indicate how the angular distribution of reemission varies with altitude because of these effects.

Laboratory experiments have shown that heavier molecules with a higher kinetic energy experience greater accommodation of momentum and energy than lighter molecules [17][19]. Therefore, heavier molecules are reemitted more diffusely. Consequently, the effect of increased molar mass at lower altitudes is to increase the extent of diffuse reflection.

Adsorption describes the process by which satellite surfaces in low Earth orbit become covered by atmospheric molecules that are trapped close to the surface [19]. The surface contamination caused by adsorption leads to an increase in energy accommodation (more energy is lost to the contaminated surface by incident molecules on impact). Therefore, the effect of adsorption is a broader angular distribution of reemitted molecules, which is closer to the diffuse case.



**Figure 3-10 - Schematic of the Main Environmental Factors Affecting Accommodation Coefficients in Low Earth Orbit**

Furthermore, laboratory experiments have demonstrated that in general, clean, smooth surfaces produce a more specular distribution of reemitted molecules than rough, or contaminated surfaces, especially at higher incidences [17][74]. It is also worth noting that some authors have found that specular reemission is more likely with increasing surface temperature [15].

The effects of adsorption are more pronounced at some altitudes. There are two main reasons for this. Firstly, at higher altitudes, where the atmosphere is more rarefied, surface interaction is less frequent, such that fewer molecules are likely to be adsorbed. Secondly, atmospheric composition varies with altitude and some atmospheric constituents are more likely to be adsorbed than others.

Atomic oxygen is particularly likely to be adsorbed. This is because it is highly reactive with a wide variety of materials, causing corrosion by oxidation and

general erosion [75]. Spacecraft surfaces are generally chosen for their thermal characteristics and low mass rather than their resistance to atomic oxygen. Therefore, they are particularly susceptible to atomic oxygen attack [76].

In addition, the volatile molecules produced during the chemical reaction between atomic oxygen and a reactant surface can themselves become adsorbed [19]. Therefore, surface contamination due to adsorption is particularly significant at altitudes where atomic oxygen is prevalent (between approximately 200 and 700 km in mean solar conditions from Figure 2-6).

It seems reasonable to suggest that the cumulative effects of atomic oxygen attack, general surface erosion, and contamination might cause changes to the accommodation coefficients over the course of a satellite's lifetime. However, some authors have cautioned against making this assumption [33].

### 3.3.2 Determination by Experiment

Since the beginning of the space age, numerous experiments have been conducted to understand the nature of gas-surface interactions in the free molecular flow regime of spaceflight.

It would not be feasible to describe all the experiments here. However, details of many of them can be found amongst the twenty-five bi-annual symposiums that have to date been held on the subject of rarefied gas dynamics currently published by The American Institute of Physics<sup>1</sup>. Two papers from these symposia that, respectively, provide historical background and future directions for experimental research germane to this study are [62] and [77].

Many of the investigators that carried out experiments with spaceflight in mind used the Maxwellian and Schaaf-Chambre gas-surface interaction models to correlate their results with others and improve upon estimates of the accommodation coefficients.

In 1973, Knechtel and Pitts conducted pioneering laboratory experiments, which demonstrated that the Schaaf and Chambre accommodation coefficients depend upon the angle at which the gas hits the surface [17].

They used ion beam apparatus, a vacuum chamber, and a microbalance to calculate the forces exerted on surfaces by a collimated beam of low-energy incident ions. They presented electrodynamic calculations that demonstrated that the effects of ionisation could be neglected. Therefore, their results are equivalent to the results that would be expected for neutral molecules with similar energies.

Through a process of curve fitting, they were able to derive empirical expressions for the accommodation coefficients as a function of incidence angle. These expressions are provided by Equations 3-25 and 3-26.

---

<sup>1</sup> The American Institute of Physics (AIP): [www.aip.org](http://www.aip.org)

$$\sigma_N = A_n - B_n \exp(-C_n E_A \cos^2 \delta) \quad 3-25$$

$$\sigma_T = A_t - B_t \exp(-C_t E_A \sin^{\frac{3}{4}} \delta) \quad 3-26$$

The terms  $A_n$ ,  $B_n$ ,  $C_n$ ,  $A_t$ ,  $B_t$ , and  $C_t$  are constant curve fit parameters and, as before,  $\delta$  is the angle between the local surface normal and the incident flow. The term  $E_A$  is the collision activation energy in electron volts (eV). It is equivalent to the kinetic energy of a neutral impinging gas molecule  $e_{k.e.}$ , described by Equation 2-17. By setting  $B_n$  and  $B_t$  equal to zero,  $A_n$  and  $A_t$  represent the original accommodation coefficients defined by Schaaf and Chambre.

From their experiment, Knechtel and Pitts calculated values for their curve fitting parameters for diatomic nitrogen ( $N_2$ ) impacting a smooth commercial grade sheet of chemically clean aluminium. The targets were not atomically cleaned and were therefore coated in a small layer of gas despite the near-vacuum conditions (a scenario similar to that experienced by satellite surfaces in low Earth orbit).

They determined the curve fitting parameters for incidence angles in the range  $15^\circ$  to  $75^\circ$ , and ion energies between 5 and 39.5 eV. They then extrapolated these results across the full range of incidences. They calculated that for  $0^\circ \leq \delta \leq 90^\circ$  and  $5 \leq E_A \leq 39.5$  eV,  $A_n = 1.0$ ,  $B_n = 0.9$ ,  $C_n = 0.28$ ,  $A_t = 0.9$ ,  $B_t = 1.2$ , and  $C_t = 0.147$ .

The range of energies covered by Knechtel and Pitts's results includes most scenarios of interest below about 500 km (in mean solar conditions). Above this altitude, incident molecular energies fall below 5 eV because of the very low mean molar mass of the atmospheric gas mixture, as illustrated in Figure 2-11.

Knechtel and Pitts calculated that their curve fitting parameters predicted the coefficient of drag for a sphere to be up to 23% less than the generally assumed value of 2.2 used by most atmospheric models (see Section 2.1.1 for a discussion of the reciprocal relationship between atmospheric models and the prediction of drag coefficient).

### 3.3.3 Determination by Orbital Observations

Ground based experiment is limited by the fact that it is currently not possible to accurately recreate the near-vacuum atmospheric conditions that may be experienced in low Earth orbit [15][19]. A particular challenge is achieving the very low molecular energies required, especially for some atmospheric gas species such as atomic oxygen [78].

Given this dearth of data, it is not unsurprising that attempts have been made to improve upon experimental measurements of accommodation coefficients by direct observation of satellite orbits.

In 2000, Mazanek, Kumar, Qu, and Seywald [20] proposed a solution to account for the discrepancy that Knechtel and Pitts discovered between their calculated coefficient of drag for a sphere and the value of 2.2. They suggested that Knechtel and Pitts's tangential curve fitting parameters be modified in order to provide results that match actual satellite data.

Modification of the tangential rather than the normal accommodation coefficient was chosen because the authors concluded that the apparatus used by Knechtel and Pitts was not well suited to measuring the tangential coefficients. In addition, they found that this modification correlated well with empirical results based on orbital decay.

The curve for their modified tangential accommodation coefficient, which uses the parameters  $A_t = 1.67$ ,  $B_t = 1.67$ , and  $C_t = 0.147$ , is shown in Figure 3-11. The results illustrated are applicable for aluminium surfaces in a circular orbit at an altitude of approximately 500 km. At this altitude, in mean solar conditions, atomic oxygen is the major atmospheric constituent with a kinetic energy of approximately 5 eV.

The expressions describing the normal and tangential forces exerted on a flat plate used by Mazanek et al assume hyperthermal conditions ( $s_\infty = \infty$ ) and assume the surface temperature to be equal to the temperature of the free stream gas ( $T_w/T_\infty = 1$ ).

Pressure and shear stress coefficients can be derived from Equations 3-18 and 3-19 under these assumptions and by setting  $1/s_\infty^2 \rightarrow 0$ . The resulting expressions, given by Equations 3-27 and 3-28 respectively are identical to those that can be derived from Mazanek et al's normal and tangential force expressions.

$$C_p = 2(2 - \sigma_N) \cos^2 \delta + \sigma_N \frac{\sqrt{\pi}}{s_\infty} \cos \delta \quad 3-27$$

$$C_\tau = 2\sigma_T \sin \delta \cos \delta \quad 3-28$$

In order to compare Equations 3-27 and 3-28 with Mazanek et al's normal and tangential force equations it should be noted that the variable ( $V_b$  in their notation) that they use to define the mean velocity of the diffusely reemitted molecules is equal to  $(\sqrt{\pi}/2)V_a$  [27], where  $V_a$  is the most probable velocity of diffusely reemitted molecules given by Equation 2-11.

Prior to Mazanek et al's work [20], Crowther and Stark [79] of Southampton University in the United Kingdom proposed incident-dependent accommodation coefficients that they suggested are more robust than the Knechtel and Pitts coefficients, especially at low incidences. Later analysis from observation of the ANS-1 satellite using Crowther and Stark's accommodation coefficients was inconclusive [33].

However, at the same university, several years after Crowther and Stark's work, Harrison and Swinerd [31] used Satellite Laser Ranging (SLR) data and Precise Orbital Analysis (POA) of the ERS-1 satellite to compare several gas-surface interaction models and accommodation coefficients. They found that an earlier model developed by Stark produced the closest match to observations. However, no other citations of the use of this model for predictive aerodynamic analysis studies have been found.

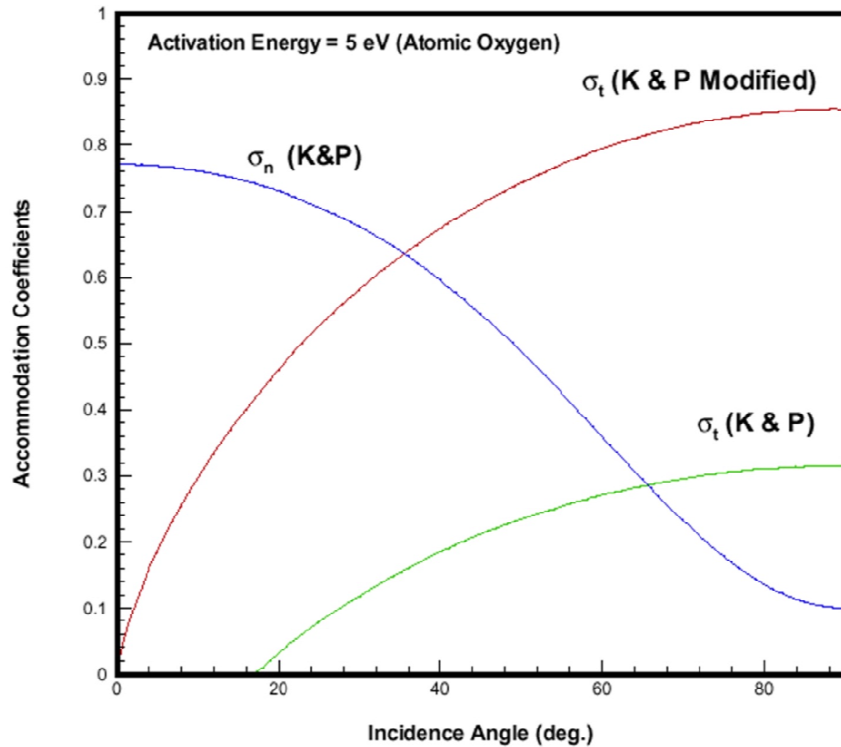


**Figure 3-11 - Incidence-Dependent Accommodation Coefficients for the Schaaf and Chambre Gas-Surface Interaction Model**

Image credit [20]. K & P refers to Knechtel and Pitts [17].  $\sigma_N$  (K&P) is defined by Equation 3-25, with  $A_n = 1.0$ ,  $B_n = 0.9$ , and  $C_n = 0.28$ .  $\sigma_T$  is defined by Equation 3-26, with  $A_t = 1.67$ ,  $B_t = 1.67$ , and  $C_t = 0.147$ , in order to produce  $C_D = 2.2$  for a spherical satellite.

### 3.3.4 Determination by Onboard Experiment

The ideal place to investigate gas-surface interactions in low Earth orbit conditions is obviously low Earth orbit itself. However, onboard experiments are expensive. Despite this, a small number of them have been conducted to measure the flux of incident atmospheric molecules in low Earth orbit. Two examples are provided in the following paragraphs.

The University of Bremen, in Germany, developed the BREMSAT satellite, illustrated in Figure 3-12 [58]. BREMSAT was launched from Space Shuttle flight



STS-60 in February 1994 into a near-circular orbit at an altitude of 160 km. One of the instruments onboard was an atomic oxygen sensor for measuring atomic oxygen flux. One of the mission objectives was to measure the exchange of momentum and energy between the molecular flow and the rotating satellite. BREMSAT deorbited approximately one year after its launch, in February 1995.

NASA have also conducted their own atomic flux experiments during Space Shuttle flights. One such experiment is illustrated in Figure 3-13. The experiment illustrated was flown on the six-day NASA Space Shuttle flight STS-8, launched in 1983. It was used to measure the angular distribution of atomic oxygen flux scattered onto silver-coated detection plates by a polished vitreous carbon target inclined at  $55^\circ$  to the incoming flow vector. One of the other objectives of the mission was to determine the cause of the glow, illustrated in Figure 3-14, which occurs around spacecraft at night<sup>1</sup>.

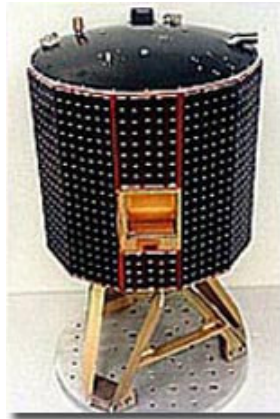


**Figure 3-12 - BREMSAT**  
Image Credit OHB-System<sup>2</sup>.

These experiments only provide details of atomic oxygen flux, but not the flux of other gas species. Nor do they directly measure the surface forces experienced. In addition, the experiments only provide data for a limited number of altitudes, atmospheric states, and surface material types and temperatures. Consequently, it is difficult to correlate their data with other scenarios of interest and derive useful accommodation coefficients.

With the projected rise in low Earth orbit satellite missions over the short term [80], there appears to be a significant case for further onboard experiments in

---

<sup>1</sup> Spacecraft glow is still not well understood, but it is known to be caused by the presence of the neutral Earth atmosphere. However, it is interesting to note that surface materials that are susceptible to atomic oxygen attack are not susceptible to glow [106].

<sup>2</sup> OHB-System: [www.OHB-System.de](http://www.OHB-System.de)

the very near future. Future experiments would ideally be capable of capturing gas-surface interaction data for all gas species and multiple surface types, at different altitudes. If possible, they should also include some means of measuring molecular flux and surface forces due to both primary and secondary interactions (reflections).

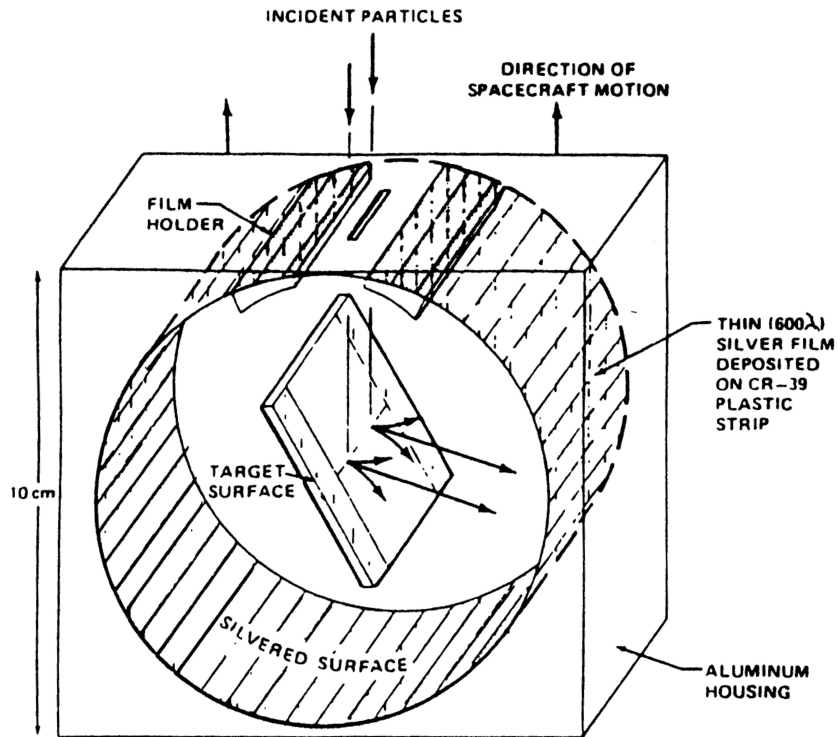


**Figure 3-13 - Space Shuttle Experiment to Determine the Angular Distribution of Reflected Atomic Oxygen Flux**

Image Credit [77]. The experiment was flown on NASA shuttle flight STS-8 launched in 1983.



**Figure 3-14 - Spacecraft Glow**

Image Credit NASA. Image shows glow surrounding the vertical stabiliser and the Orbital Manoeuvring System (OMS) pods of the Space Shuttle Columbia.

### 3.4 Other Models

Several alternative gas-surface interaction models have been applied to spacecraft surfaces with varying degrees of success. Two of the most popular models, which account for non-diffuse scattering of the reemitted molecules, are illustrated in Figure 3-15.

The Cercignani-Lampis-Lord (CLL) model [63], represented by Figure 3-15 satisfies the condition of reciprocity, and has been shown to produce similar pressure and shear stress distribution results to the Maxwellian model [61].

It provides a more physically realistic model of the angular distribution of reflected flux from clean surfaces at high incidences (low  $\theta_i$ ). It is therefore of particular interest for DSMC and TPMC simulations. However, very little data exists for the type of gas-surface interactions that are encountered during these simulations [43]. Furthermore, because the state of the reflected flux is not always relevant and the CLL model is more complex than the Maxwellian model, it is not widely used for free molecular flow analysis.

The empirical Nocilla model, also represented by Figure 3-15, does not satisfy the condition of reciprocity [66]. Despite this, it has been shown to accurately simulate non-diffuse scattering at high incidences (low  $\theta_i$ ) [74]. However, it is not frequently used to perform aerodynamic calculations of satellites in the free molecular flow regime. Therefore, citations of its use for this purpose are limited (see, for example, [31][81]).

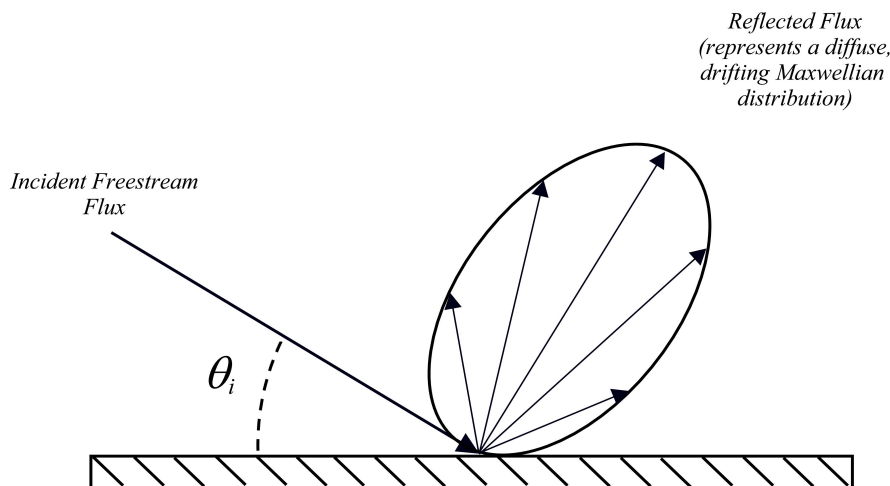


**Figure 3-15 - Schematic of the Cercignani-Lampis-Lord (CLL) and Nocilla Gas-Surface Interaction Models**

**Both models account for non-diffuse quasi-specular scattering by representing the reemitted molecules by a drifting Maxwellian distribution. However, only the CLL model satisfies the condition of reciprocity (Equation 3-1).**

There are multiple variations on the Maxwellian, CLL, and Nocilla models. Notable models have been developed by Epstein (Maxwell / Lord), Sentman (Maxwell), Schamberg (Maxwell), Goodman (Maxwell), Cook (Maxwell), Karr (Maxwell / Nocilla), Stark (Maxwell / Nocilla), and Stark and Crowther (Maxwell). It should be noted that many of the derivative Maxwellian and Nocilla models differ only in their expressions for the respective accommodation coefficients and these expressions are often empirically derived.

### **3.5 Future Directions**

The previous sections have described the difficulties involved in conducting ground-based experiments, the cost involved in conducting in-orbit experiments, the complexity of deriving useful aerodynamic data from direct observation of satellites, the multiplicity of gas-surface interaction models and their derivatives, and the enormous number of relevant gas-surface interaction scenarios that exist.

In light of these difficulties, some investigators have attempted to analyse the nature of gas-surface interactions using computer simulations [62]. In a similar manner to the DSMC method detailed in Section 2.6.4, individual molecules can be simulated impacting on microscopically simulated surfaces. When individual molecular movements are simulated in this way, the approach is known as Molecular Dynamics (MD) simulation.

Some work has recently been undertaken to develop a new GSIM from the results of MD gas-surface interaction simulations [66]. The emphasis of this work has been to combine simple phenomenological models, such as the Maxwell, CLL, and Nocilla models, with detailed scattering data, which can be directly correlated to the nature of the incidence flux.

This type of work holds some promise for the future direction of gas-surface interaction modelling. However, the vast array of data that is produced during MD simulations, as well as the numerous permutations of gas-surface interactions, indicates that any resulting model would need to be coupled to a very large database of input parameters and bounds.

Databases have already been employed by some DSMC investigators in order to provide look-up tables to GSIM parameters, which account for chemical reactions during collisions [43].

### **3.6 Summary**

This chapter has detailed three of the main Gas-Surface Interaction Models (GSIMs) used by spacecraft aerodynamics and systems engineers: the Newtonian model, the Maxwellian model, and the Schaaf and Chambre model. It has discussed some of the physical phenomena that they reveal, their limitations, and their input

parameters. It has described the accommodation coefficients (the phenomenological input parameters that describe the extent of energy and momentum transfer to the surface in the Maxwellian and Schaaf and Chambre GSIMs).

It has described how the accommodation coefficients are affected by environmental phenomena, as well as how they can be determined from ground-based experiment, direct satellite observation, and onboard experiment. It has also summarised details of alternative GSIMs, as well as future directions for gas-surface interaction modelling.

The chapter indicates that there are continued uncertainties surrounding our knowledge of gas-surface interactions. It demonstrates that no single gas-surface interaction model hitherto developed is accompanied by enough proven data to be sufficiently accurate for all scenarios of interest.

This poses questions as to how the variety of different GSIMs and their numerous input parameters can be incorporated into a practical aerodynamic analysis tool in order to enable modelling of the widest range of scenarios possible using existing data. By implication, this indicates that an ideal aerodynamic analysis tool would also need to be able to incorporate future GSIMs and all their associated data.

The challenges of storing, retrieving, and manipulating large amounts of engineering data are dealt with in Chapter 5. The challenge of incorporating multiple gas-surface interaction models and their associated data into a spacecraft aerodynamic analysis tool is dealt with in Chapters 6 and 1.



## 4 SPACECRAFT CONCURRENT ENGINEERING

The preceding chapters have focussed mainly on the scientific aspects of performing spacecraft aerodynamic analysis. However, engineering is a practical subject and the motivation for investigating these aspects has been to apply it to real-world engineering problems. Therefore, the question is what is the best way of developing a spacecraft aerodynamic analysis tool for use on a modern spacecraft development project?

The traditional phased approach to spacecraft design and development is shown in Figure 4-1. Although not illustrated in the figure, prior to the conceptual design phase, there may also be some Pre-Phase A (Phase 0) conceptual work carried out by the commissioning agency (customer or customers) to perform trade-off studies.

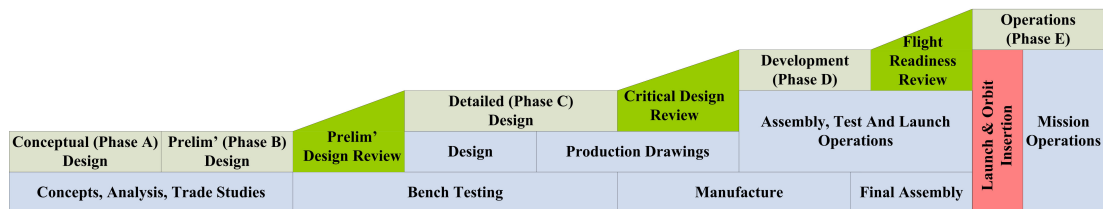


**Figure 4-1 - Typical Spacecraft Engineering Project Phases**

Based on diagrams and explanations from [82] and [83]. The project timeline runs from left to right. The height of the elements has no meaning.

After each design phase, there is normally a design review, as illustrated by the green blocks in Figure 4-1. The design reviews represent both schedule and engineering milestones, and additionally serve several other purposes. For example, they assist with feeding-back changes into the design specifications, communicating engineering data across the project, and managing risks. Furthermore, they provide a forum for the project's progress to be assessed by all of the project's internal and external customers.

Within each phase a host of activities take place. Some of these activities are shown in blue in the Figure 4-1. As illustrated, many of these activities are carried-out sequentially, but they may also overlap across phases and be performed simultaneously via close collaboration between interested parties.

Over time, greater understanding of the spacecraft development process has led to more overlap and simultaneous collaboration. This, in turn, has caused earlier consideration of downstream engineering and product lifecycle issues. In addition, new computer tools have accelerated these trends by facilitating greater utilisation of resources and dissemination of information within and across phases.

Concurrent Engineering (CE) may be seen merely as recognition of these trends, and a formalised attempt to speed them up and manage them in a more directed and intelligent way.

According to ESA's Concurrent Design Facility (CDF), which manages CE activities at ESTEC [84], *"Concurrent Engineering is a systematic approach to integrated product development that emphasises the response to customer expectations. It embodies team values of co-operation, trust and sharing in such a manner that decision making is by consensus, involving all perspectives in parallel, from the beginning of the product life-cycle."*

The key word in this definition is the term "systematic." As alluded previously, it is likely that many of these working methods would evolve anyway over the course of time. Therefore, it must be emphasised that concurrent engineering is a "systematic" attempt to improve the systems engineering process. Systematic improvement not only requires an understanding of the process, but also a well-defined objective.

However, a single goal is something that many advocates of concurrent engineering are unable to communicate to their organisations. Values such as collaboration, trust, and sharing cannot be disagreed with, but they also cannot be measured easily. This leaves many in an organisation wondering what the practical benefits of concurrent engineering are.

In a modern workplace, the cultural shift towards working in a collaborative, co-operative, and sharing way to meet customer expectations will only be achieved if the Information Technology (IT) infrastructure supports it. Therefore, one single measurable goal that can be defined is to design IT infrastructure to facilitate concurrent engineering rather than hinder it. Success can then be measured by how well the IT infrastructure supports the systems engineering process and product lifecycle.

Consequently, the emphasis of this chapter lies less on the cultural goals of concurrent engineering and more on the practical mechanisms for achieving these goals through the use of information technology.

Concurrent engineering is a relatively new concept in the space industry. As stated in Section 1.6.2, the first Concurrent Engineering Workshop (CEW) only took place at ESA's ESTEC facility as recently as 2004. In addition, similar to business administration, concurrent engineering is a practical field that relies on first-hand experience. Because of these factors, very little academic reference material exists.

Given this background, much of the current chapter is based upon the author's first-hand professional experiences. As described in Section 1.2, these experiences include working for numerous companies as an information technology consultant as well as working for a short period as part of the programme management team of a large spacecraft project.



This chapter first describes some of the current approaches to implementing concurrent engineering in the space industry. It then discusses some of the information technology challenges of implementing concurrent engineering. Finally, it draws comparisons between these challenges and the information technology challenges posed by other business areas.

## 4.1 Current Approaches

This section describes some of the approaches to concurrent engineering currently employed in the space industry. The first Concurrent Engineering Workshop (CEW) for spacecraft applications held at ESA's ESTEC facility in 2004 provides much of the reference material for this section. However, it should be noted that none of papers presented at the conference were specifically related to the application of concurrent engineering in Phases B, C, and D.

### 4.1.1 Pre-Phase A and Phase A

Most attempts at applying concurrent engineering principles to the spacecraft development process have largely been limited to tackling Pre-Phase A (Phase 0) and Phase A (conceptual design) studies.

These studies require fewer systems engineers than other phases as well as fewer and generally simpler tools. Therefore, all required resources, including support, can be co-located to enable real-time communication and decision making.

ESA's Concurrent Engineering Facility (CDF) at ESTEC in the Netherlands, illustrated in Figure 4-2, and NASA's Project Design Centre (PDC) at the Jet Propulsion Laboratory in California, are excellent examples of this approach.

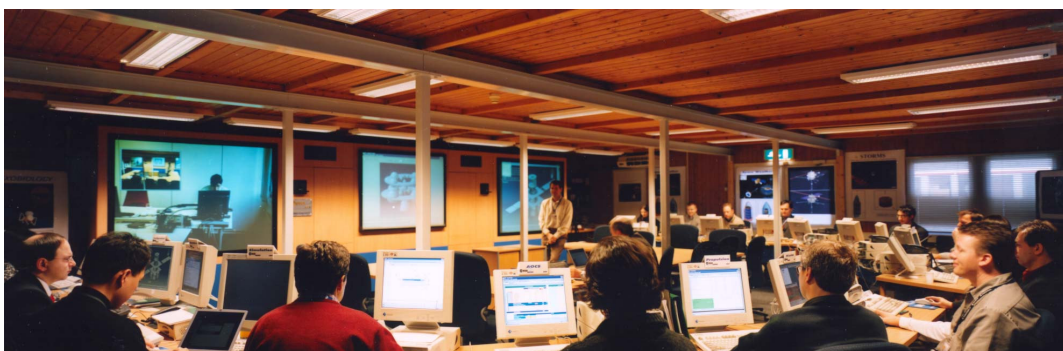


**Figure 4-2 - The Concurrent Design Facility (CDF) at ESTEC**

Image credit ESA. The facility is used for Pre-Phase A and Phase A conceptual design studies.

Figure 4-3 shows the CDF floor layout. It illustrates how all the different engineering disciplines and other interested parties are arranged to facilitate the

collaborative and simultaneous concurrent engineering process. The NASA PDC and other concurrent engineering facilities have similar layouts.

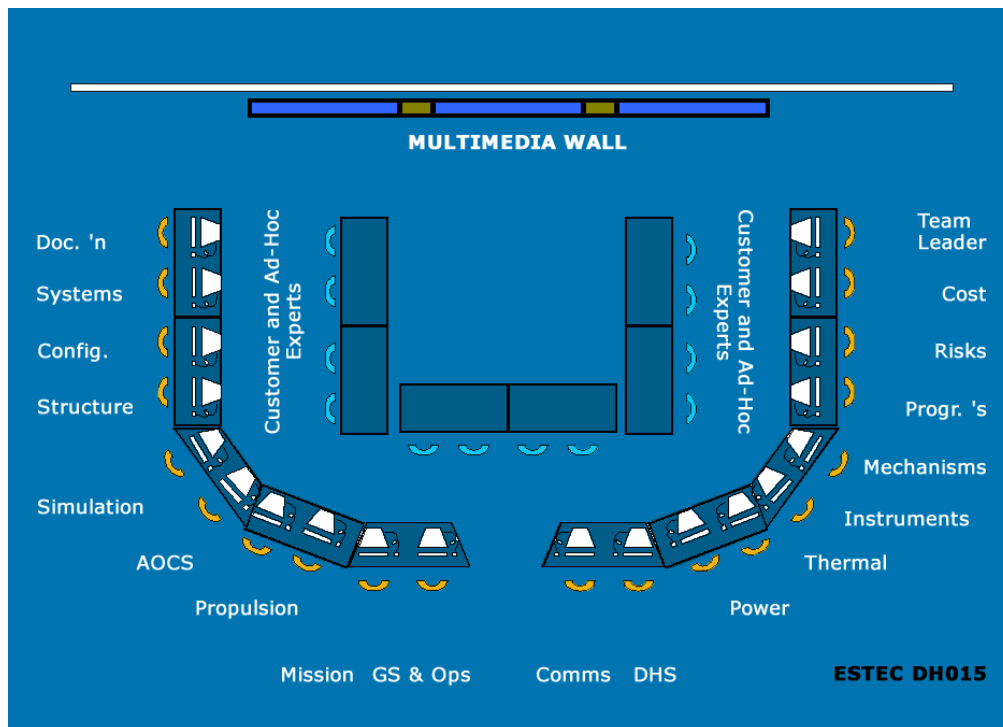


**Figure 4-3 - ESA Concurrent Design Facility (CDF) Floor Layout**  
Image Credit [85].

The ESA CDF uses an Integrated Design Model (IDM), based on an Excel<sup>1</sup> data environment, as illustrated in Figure 4-4 [86]. The Excel workbooks of each different engineering discipline are linked to a single data exchange workbook. The data exchange workbook is used to control design changes using manual switches (Excel cell drop-downs). If changes are accepted, they are stored in the data exchange workbook. Therefore, at any given time, the data exchange workbook provides details of all the design parameters of the current design iteration.

In 2004 the NASA PDC proposed a radical re-design of its information systems architecture with a move towards a centralised database system, similar to the IDM, for all its tools to connect to [87]. This proposal was aimed at improving data mining capabilities, real-time data exchange, and more efficient re-use of tools.

Many spacecraft companies have very similar facilities to the CDF and PDC that use comparable information technology strategies. For example, EADS Astrium<sup>2</sup>

<sup>1</sup> Software application providers are listed in Section III.iii.

<sup>2</sup> EADS Astrium: [www.space.eads.net](http://www.space.eads.net)

has a Satellite Design Office (SDO) [88] and Alenia Spazio<sup>1</sup> has a Concurrent Development Environment (CODE) [89].

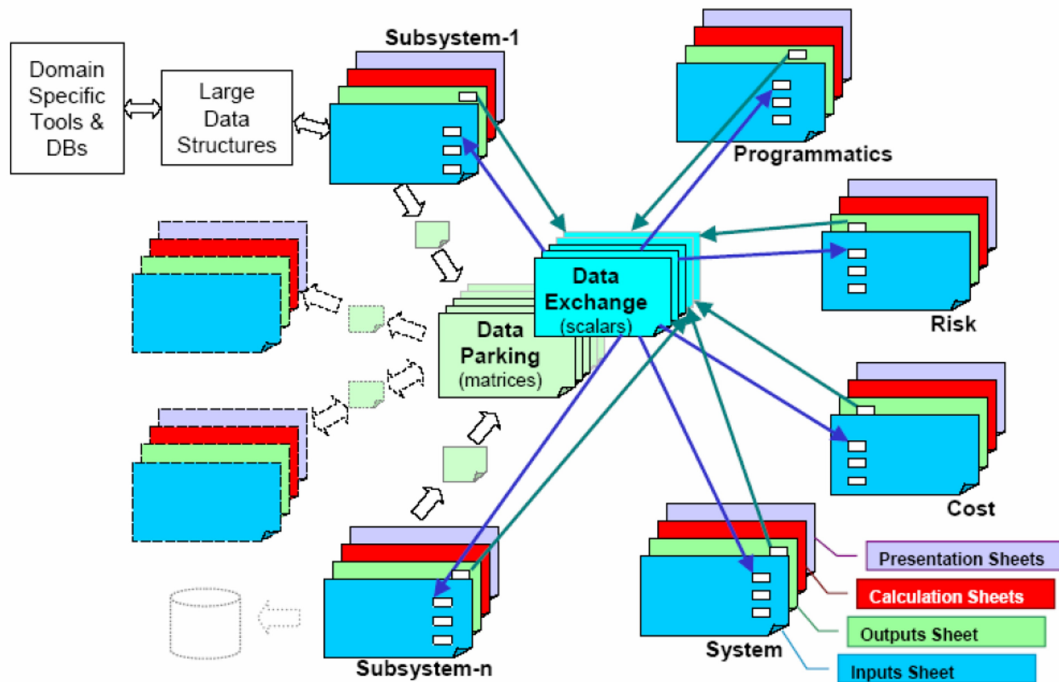


**Figure 4-4 - ESA Concurrent Design Facility Integrated Design Model  
Graphical Representation**

Image Credit [86].

#### 4.1.2 Phases B, C, and D

Beyond Phase A, the number of systems engineers and tools involved means that collocation of all resources would not be feasible. In addition, an Excel-based data-environment such as that used currently by ESA's CDF and NASA's PDC would not be practicable at these scales.

However, the challenge remains. It is how to bring together all interested parties to work in a collaborative way to improve both the development process and hence the product through earlier consideration of downstream product lifecycle issues. With a large number of geographically dispersed resources, this inevitably means employing a considerable amount of information technology infrastructure.

For an organisation to design, develop, and implement such an infrastructure would require substantial investment and cause a lot of disruption. It therefore represents a considerable business risk.

<sup>1</sup> Alenia Spazio: [www.alespazio.it](http://www.alespazio.it)

Furthermore, the management team of a spacecraft development project has a different set of priorities to anyone wishing to implement cross-organisational initiatives. This is because a typical project is schedule-driven, with very tight deadlines and limited resources. Consequently, any utilisation of these resources for non-project work is difficult for a project manager to sanction.

Given the business risk, as well as the conflicting priorities of the various stakeholders within an organisation, concurrent engineering advocates have hitherto had difficulty constructing an adequate business case for re-designing all information technology infrastructures to meet their goals. Consequently, they have often been forced to implement less than ideal solutions beyond Phase A.

One approach has been to attempt to bring ownership of all analysis tools under the control of a single multi-disciplinary organisation-wide support team, and create a collaboration portal [90]. The purpose of the portal is to link together and hierarchically organise the remaining disparate information systems and resources through a single user interface.

An advantage of this approach is that it promotes communication and collaboration. It provides a forum for engineers to voice concerns, post messages, cooperate with each other, and share knowledge in a systematic way.

Such solutions are a vital first step towards implementing concurrent engineering. However, they are only ever able to provide a high-level presentation layer to project-wide information systems and, as such, they are by-passed by users who know where to find the information system they use regularly.

Furthermore, based on the author's own professional experiences, such solutions do little to re-engineer and rationalise systems engineering processes, change working habits, or improve data continuity. They do not inherently eliminate duplicate systematic work effort, or shift the emphasis towards early consideration of downstream product lifecycle considerations, early analysis and testing, and greater iterative feedback throughout the development process.

## 4.2 Information Technology Challenges

According to Massimo Bandecchi, head of ESA's Concurrent Design Facility (CDF), "*Concurrent engineering is a state of mind - you can help to put it in place, with tools [and] facilities*" [91].

The concurrent engineering "*state of mind*" described by Massimo Bandecchi can be greatly facilitated during Phase A through the co-location of resources, as described in Section 4.1.1. However, as highlighted in Section 4.1.2, the co-location of resources is no longer feasible beyond Phase A.

Therefore, as described in the introduction to this chapter, the facilitation of concurrent engineering and its promotion as a state of mind becomes predominantly an information technology challenge in Phases B, C, and D.

This challenge manifests itself in two main ways: the increasing number of computer tools used by a spacecraft development project, and the related issue of data continuity. These topics are discussed in more detail in the following sections.

#### 4.2.1 Increasing Number of Tools

The spacecraft development process requires the use of a large number of computer tools. These tools take many different forms and are used for multiple purposes, from engineering analysis to project control. The quantity and complexity of tools is growing as spacecraft become ever more sophisticated and development schedules become shorter.

A single tool may be used for any number and type of tasks. It may have originated entirely in-house, be a highly tailored third party system, such as a document management system, or represent a model within an off-the-shelf system, such as a spreadsheet or MATLAB<sup>1</sup> model. Table 4-1 lists some typical project tasks and examples of the types of information technology used to handle them.

**Table 4-1 - Some Typical Project Tasks and Information Technologies**

Typical Project Task	Example Information Technology
Mass Budget Control	Microsoft Excel Spreadsheet
Attitude Modelling	MATLAB
Verification and Validation Tracking	Microsoft Access Database
Document Management	Bespoke in-house tool (e.g. SPRINT used by EADS Astrium <sup>2</sup> )
Thermal Analysis	ESATAN [92]
Project Resource Scheduling	Microsoft Project
Project Information Dissemination	Group Ware Tools (e.g. email and intranet-portals)
Sub-System Procurement	External Business Systems (e.g. procurement systems, such as the SAP Supply Chain Management (SCM) module)

There are some instances when the development or procurement of new tools is essential. For example, when a genuinely new or unique design or process is developed, the results of earlier engineering analyses need to be verified independently, or the information technology used by existing tools is outdated.

However, engineers and other project resources often consider it necessary to develop or procure new tools even when existing ones could be adapted. This is

<sup>1</sup> Software providers are listed in Section III.iii.

<sup>2</sup> EADS Astrium: [www.space.eads.net](http://www.space.eads.net)

either because they are not aware of the existence of such tools or because the tools are inadequately maintained and documented.

This may be a result of project time pressures, a general lack of resources, or because the original developers and users considered the tools to be one-offs. The consequence of this is that multiple, parallel, overlapping, and duplicate tools may be developed across, and occasionally within, projects [90].

Another factor that leads to the creation of an increasing number of tools is the long duration of spacecraft development projects. If a large system is implemented at the beginning of a project, but later on, because of changing project circumstances, external influences, or technological deficiencies, it no longer performs its function adequately, it may not be worthwhile replacing or upgrading within the remaining project timeframe. The result is that new tools need to be implemented and manual processes need to be put in place to provide the missing functionality or circumvent problems.

This increasingly large and complex mixture and usage of tools, and their overlapping roles, complicates the engineering process. It therefore makes applying concurrent engineering principles across the whole spectrum of a project very difficult.

According to Michael Schreuble of EADS Astrium, *“The point is that you do not let the tool impact the process, you have the process and you use the tool to implement it”* [91]. In other words, to facilitate concurrent engineering, any new tool must be developed to fit within the overall systems engineering process.

#### **4.2.2 Data Continuity**

As early as 1991, with the nascent use of personal computers, advocates of multi-disciplinary optimisation and concurrent engineering estimated that within the aircraft industry up to 50-80% of a system design engineer’s time was spent organizing and exchanging data between different tools [93]. It is likely that this proportion has decreased. However, systematic, timely, reliable, and efficient data exchange between tools remains one of the challenges of systems engineering.

To meet this challenge, a great deal of effort has been put in to developing industry-wide file specifications for transferring data from one analysis tool to another [94]. Yet, data transfer between analysis and design tools is not the only area where data continuity is an issue. As described in the previous section, a modern spacecraft development project will utilise multiple other tools, such as those used for project management, risk assessment, and document management.

Many of these tools and systems will have their own databases. However, they may not necessarily interface with one another automatically. Therefore, frequent and numerous different manual interventions are often required to maintain the concurrency of information across these systems.

Figure 4-5 illustrates this situation. It demonstrates a scenario where, for example, a change note issued on a part may require multiple updates to different documents within a document management system, as well as several formal communications to other interested parties. These parties may then need to convene to agree an appropriate course of action.

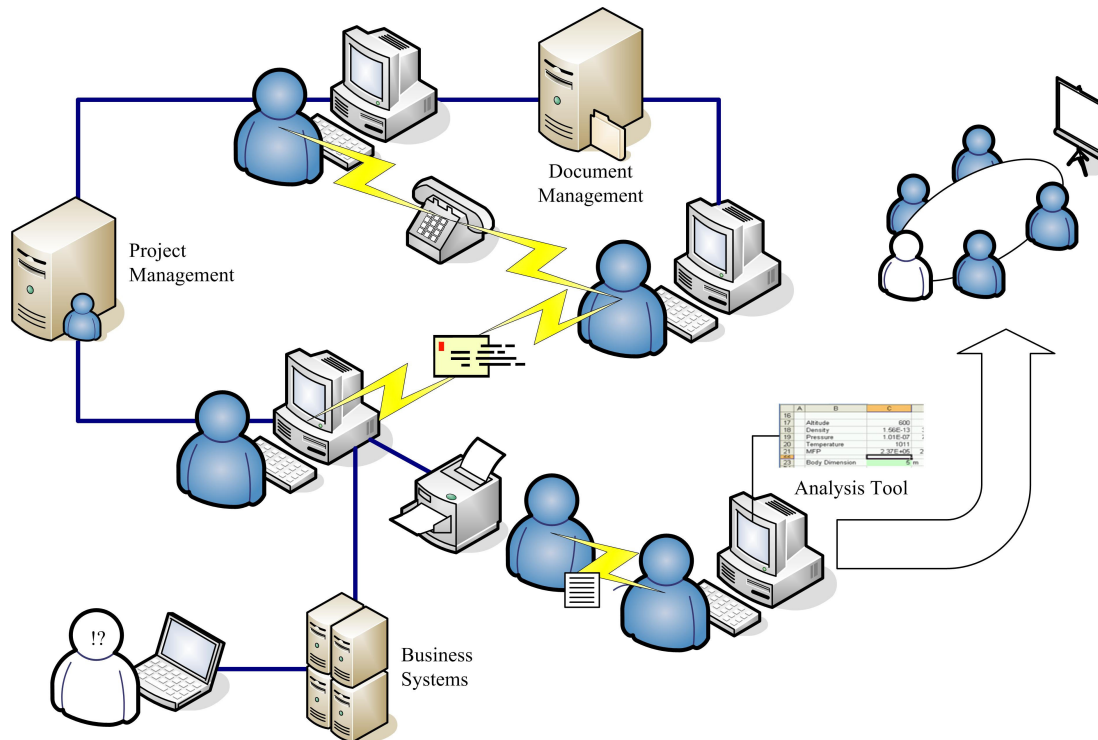


**Figure 4-5 - A Typical Spacecraft Systems Engineering Project Today**

All too often, manual processes rely heavily on individual experience and knowledge of who needs to be notified or contacted instead of procedural best practice and company expertise [90]. In addition, manual processes can be slow, are frequently unreliable, and often rely on smaller tools, such as spreadsheets and emails, which are hard to keep track of and understand within the overall context of a project.

These factors make manual processes very difficult to control, hindering efficient project management and leading to frustration, confusion, and conflict between project management and systems engineers. Unless procedures are in place and they are followed, some changes and updates may lead to data loss, corruption, duplication, or inadequate data conversion.

These effects can have potentially serious consequences that go beyond schedule and budget considerations. For example, the NASA Mars Climate Orbiter mission failure in 1999 was thought to be the result two teams working on the same navigation software failing to convert between metric and English units.

Following the failure, the Mars Climate Orbiter Mishap Investigation Board observed that *“most mission failures and serious errors can be traced to a breakdown in existing communication channels, or failure to follow existing processes - in other words, a failure in execution”* [95].

### **4.3 Information Technology Solutions to other Business Challenges**

It is possible to draw comparisons between the information technology challenges of implementing concurrent engineering and the information technology challenges of other business areas. This poses the question, how are the information technology challenges of other business areas handled in a modern organisation?

In the business environment, enterprise applications, such as SAP<sup>1</sup> and Oracle Business Suite, have evolved over the last decade to address the issues of data continuity and the increasing number of information systems used in different business areas.

Enterprise applications are software applications that provide an integrated system to manage processes across all aspects of business. They have a client-server architecture consisting of multiple different modules. Each module supports a different business area, such as, Supply Chain Management (SCM), Customer Relationship Management (CRM), Enterprise Resource Planning (ERP), or Financial Accounting (FA).

The modules are designed to support best-practice business processes, but can also be configured to meet the individual needs of an organisation. Within each module are multiple sub-modules for each of the different business processes of the business area.

All of the modules that an organisation requires are presented to the user via a single Graphical User Interface (GUI). In addition, all of the modules are connected to a single centralised Relational Database Management System (RDBMS). The centralised database is used to store both static and dynamic (real-time) business data as well as data relating to the enterprise application's configuration. In addition to the RDBMS, enterprise applications usually also incorporate a centralised document server that enables them to provide centralised document management functionality.

Enterprise applications typically also include a range of powerful tools specifically for manufacturing companies. These tools are usually bundled together to form a Product Lifecycle Management (PLM) module. A typical PLM module incorporates interfaces to Computer Aided Design/Computer Aided Manufacture (CAD/CAM) software in addition to Product Data Management (PDM) tools. These

---

<sup>1</sup> Software providers are listed in Section III.iii.



features facilitate collaborative real-time viewing and editing of information related to selected engineering parts and sub-systems.

Extra PLM add-ons provide real-time user interfaces to third party software. This software appears to the user to be embedded in the enterprise application's client. Figure 4-6 illustrates an example. It shows a CAD drawing and its related data and documents being viewed, edited, annotated, and shared in real-time via a third party CAD add-on embedded in the SAP client.

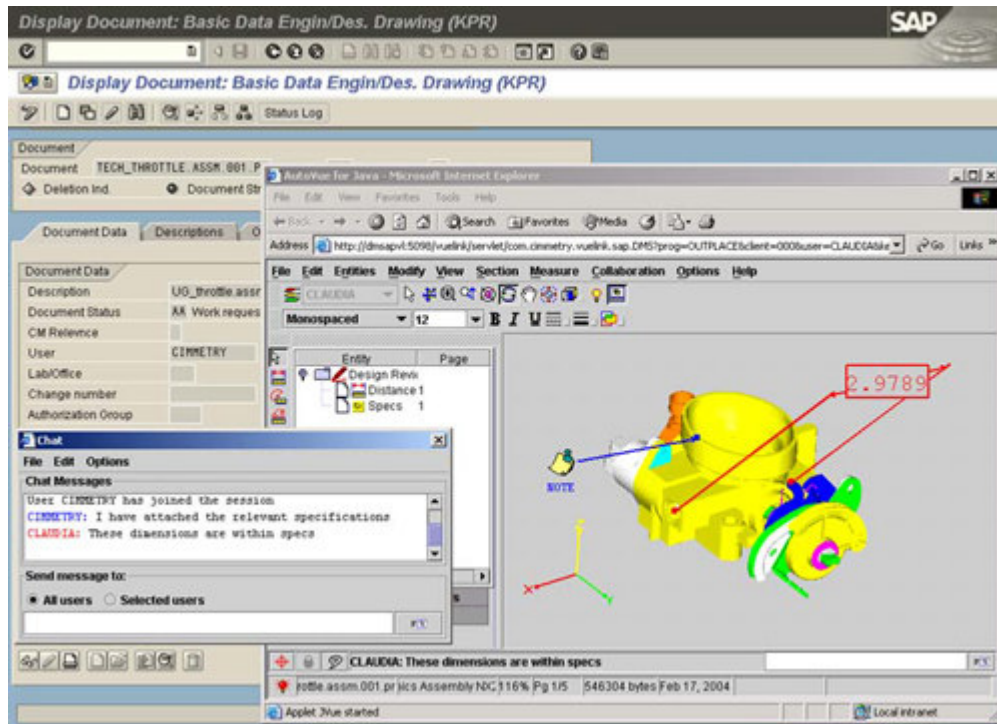


**Figure 4-6 - Real-Time Collaborative Review of a Part and its Related Data using a CAD Interface Embedded in an Enterprise Application**

Image Credit Cimmetry<sup>1</sup>. Image shows a part being viewed and modified by multiple users. The Enterprise Application is SAP, the CAD viewer is AutoVue by Cimmetry.

## 4.4 Summary

This chapter has shown that the development of an analysis tool for a spacecraft development program requires an understanding of the engineering environment that the tool will be used in. It has described how some members of the spacecraft industry have recently begun to try and systematically improve the spacecraft development process with the implementation of concurrent engineering principles.

<sup>1</sup> Software providers are listed in Section III.iii.

It has outlined how concurrent engineering has been successfully employed in Phase A and Pre-Phase A conceptual design studies. In addition, it has highlighted how little has so far been done to implement concurrent engineering beyond Phase A.

The chapter has shown that the challenge of implementing concurrent engineering beyond Phase A is predominantly an information technology one, which is manifested in two main ways: the increasing number of computer tools used and the related problem of maintaining data continuity among these tools.

The chapter has demonstrated that lessons can be learnt from the information technology solutions employed by organisations to tackle similar challenges in other business areas.

An information technology strategy for implementing concurrent engineering beyond Phase A that takes heed of these lessons is proposed in Chapter 5, in the form of the SEDAT Concept. A practical implementation of this concept has been built that incorporates a spacecraft aerodynamic analysis module. This module is described in Chapter 6.

## **5 THE SEDAT SYSTEM**

SEDAT stands for Spacecraft Engineering, Design, and Analysis Tools. The SEDAT System is a software system, which can be installed on any personal computer that runs the Microsoft Windows operating system.

This chapter describes the SEDAT Concept and outlines the scope of the SEDAT software system that has been developed as part of this PhD project. It describes the architecture and technologies used to implement the system. It then explains the design, implementation, and testing of the database and client components and outlines the accompanying help system. Finally, it provides details of how to obtain and install the SEDAT software system that has been developed.

### **5.1 Concept**

The SEDAT Concept is an attempt to apply the enterprise application model, described in Section 4.3, to the entire spacecraft development process in order to facilitate concurrent engineering.

As shown in Figure 4-5 in the previous chapter, a typical spacecraft development project has multiple separate information systems, or computer “tools,” each with its own database, for performing the many systems engineering functions on a project. These tools are rarely connected to each other or external business systems. The concept behind SEDAT is that all of these tools should be incorporated into one client-server domain, as illustrated in Figure 5-1.

The separate tools, or groups of tools, are represented within SEDAT as individual modules. The design of these modules should be such that, like enterprise applications, they promote best practice spacecraft systems engineering methods. Yet they should also be configurable, so that individual organisations can tailor the system to suit their needs and adapt the standard solution. The tailoring may include changes to a Graphical User Interface (GUI), additional reports, or a change to the underlying code of the module.

The representation of all modules in a single system provides a controlled environment for managing changes and controlling new module releases, upgrades, and documentation. Consequently, it addresses the first main information technology challenge of implementing concurrent engineering, as outlined in Section 4.2.1; it facilitates and encourages the re-use of modules (i.e. tools) and individual module components.

There are two types of module: core and non-core. Core modules represent tools that any organisation might need. Non-core modules are highly specialised modules that would not necessarily be required by every organisation. Therefore,

they may be unique to an organisation. The Free Molecular Flow (FMF) Module described in Chapter 6 is a non-core module.

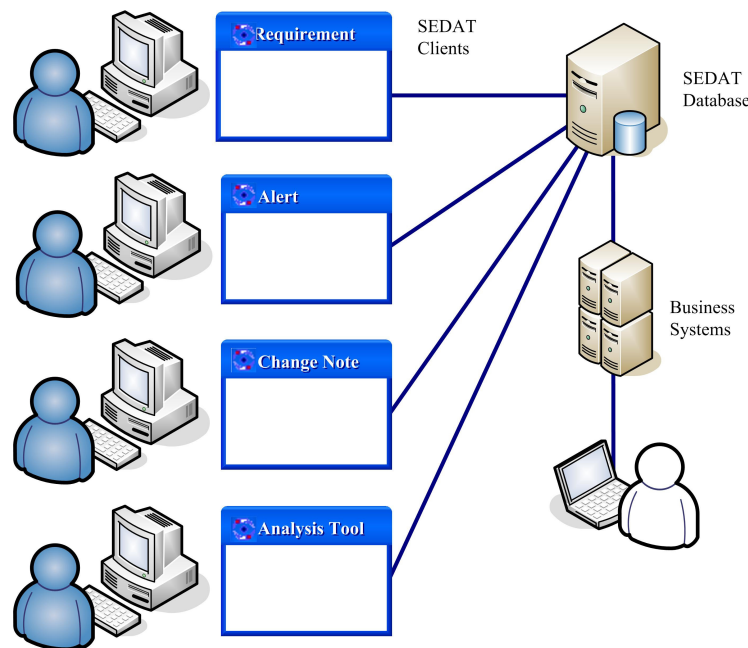


**Figure 5-1 - The SEDAT Concept**

Each SEDAT module is connected to the same centralised repository for all project data: the SEDAT Database, a Relational Database Management System (RDBMS). It may seem that the spacecraft development process is too large and complex to extend ESA's Concurrent Design Facility's (CDF's) Integrated Design Model (IDM), which incorporates a centralised database, beyond Phase A. However, enterprise applications support many large and complicated organisations and their RDBMSs contain tens of thousands of tables.

Besides being able to store and handle large amounts of data, an important feature of RDBMSs is that, properly designed, they eliminate redundant data. A unit of data is stored once and once only. Data-exchange between these unique data units is facilitated via pre-defined relationships and procedures, which manage and propagate changes according to pre-defined rules.

Therefore, a centralised RDBMS addresses the second information technology challenge of implementing concurrent engineering, as outlined in Section 4.2.2. It enables data continuity to be maintained in real time across modules and interfaces to external business systems without the need for manual intervention.

Among other things, a centralised RDBMS would also:

- Provide centralised configuration control: it would enable engineers to quickly view data related to changes without the need to consult multiple

information sources. This would expedite the multidisciplinary decision-making process, leading to earlier systems trade-offs and more optimised designs.

- Enable the chronological history of the development of a system to be built-up. This would provide a vital empirical starting point for future work on similar systems for future missions and a more reliable method for disseminating empirical knowledge across an organisation. Thus reducing over reliance on first hand experience.
- Provide the capability to run Structured Query Language (SQL) queries across multiple related tables. These queries can be used for data processing or presented to the user for reporting purposes.
- Facilitate the storage and processing of data required for interfacing modules with external systems via middleware.
- Make it easier to implement cutting-edge computing methodologies such as distributed grid computing (described in Section 5.5.3) and workflow. Workflow describes how different steps in a process are managed, what rules they are subject to, and whether or not they are performed sequentially or in parallel. For example, enterprise applications typically use workflow to automate processes such as purchase approval, using complex rules to trigger automated events and notify individuals of the need to take action. An analogous systems engineering workflow would facilitate earlier consideration of downstream product lifecycle issues via systematic, knowledge-based, and reliable management of tasks.
- Make it easier to implement advanced concurrent engineering methodologies such as Multidisciplinary Design Optimisation (MDO). This is because a centralised RDBMS would enable data flows and interactions between disciplines to be systematically and efficiently managed.

There are a number of reasons why a centralised RDBMS has been proposed instead of a distributed database system:

- Enterprise applications have demonstrated that a centralised RDBMS can be used to tackle a range of different business aspects and processes.
- Internet technology and modern telecommunications infrastructure enable a centralised RDBMS to be accessed from anywhere in the world. Furthermore, encryption technologies exist that guarantee the security of data transfer over the internet, provided security processes are followed.
- As described previously, centralising the RDBMS enables it to be managed, upgraded, and administrated more effectively by a single co-located and dedicated team of specialists.

- If necessary the entire RDBMS or portions of the RDBMS can be replicated to create disconnected distributed datasets that can be synchronised when needed. For example, a subset of the centralised RDBMS can be replicated to a user's hard drive for use on a portable laptop computer. The local database replica can then be synchronised with the centralised RDBMS when the user reconnects to the network on which the centralised RDBMS resides.

There are two main reasons why a centralised RDBMS has been proposed instead of an Object (orientated) Database Management System (ODBMS) [96]. Firstly, RDBMSs have a proven technological pedigree and are overwhelmingly the most popular solution to the problem of storing, organising, and relating data (all leading commercial enterprise applications use a RDBMS). Secondly, the author has a legacy of using RDBMSs in a professional capacity.

Therefore, it was considered that the effort required to investigate ODBMSs would have diverted resources away from the central objectives of this research. However, it should be noted that ODBMSs present an appealing alternative to RDBMSs, not least because they provide a solution to the problem of marrying object-orientated programming methodologies to object-orientated data modelling strategies. Therefore, they represent an interesting area for further work, as outlined in Section 9.4.

## 5.2 Scope

A practical realisation of the SEDAT Concept has been developed within the framework of this PhD research project. Given this context, the system that has been developed contains a fraction of the functionality of the full SEDAT Concept.

In particular, no attempt has been made to implement advanced concurrent engineering computational methodologies such as change management, data archiving, workflow, or MDO, which, as described in Section 5.1, a centralised RDBMS would facilitate. This is because each of these areas represents a specialised field of study in its own right that would require significant further investigation beyond the scope of this PhD.

For example, although MDO is a mature field of research, to date, very few spacecraft MDO studies have been published and those that have been published relate to Phase A conceptual design studies (see, for example, [97]). Furthermore, even early stage spacecraft conceptual design studies present significant MDO challenges because of the high degree of coupling between disciplines and the large number and complexity of subsystems. Therefore, before attempting to facilitate MDO in a working SEDAT system a considerable amount of leading-edge research

would need to be conducted. Such an undertaking would not be feasible within the time frame of this PhD, especially given that the emphasis of this research is on the implementation of concurrent engineering beyond Phase A.

In addition, no attempt has been made to implement common standards for the management of product related digital data, such as the International Standards Organisation (ISO) Standard for the Exchange of Product model data (STEP) [98], or ESA standards for software engineering [99]. This is because the implementation of standards would have restricted innovation during the embryonic stages of the development of the SEDAT Concept. Furthermore, they would have required a prohibitively high proportion of development time for such a small scale development, but would not necessarily have helped achieve the research objectives.

Despite the limited scope of the system that has been developed, it is fully scalable and has been built using object-orientated principles. Therefore, it provides a good test-bed for assessing the concept and a platform for further work, as outlined in Section 9.4.

### 5.3 Architecture

SEDAT has been implemented with a three-tier client-server system architecture as illustrated in Figure 5-2. This structure provides abstraction between the database and the processing, presentation, and reporting functionality. It maximises the modularity, interoperability, scalability, and upgradeability of the system because it enables modules to be developed within the Processing, Presentation, and Reporting Layer, independently from the Data Layer, and vice-versa.

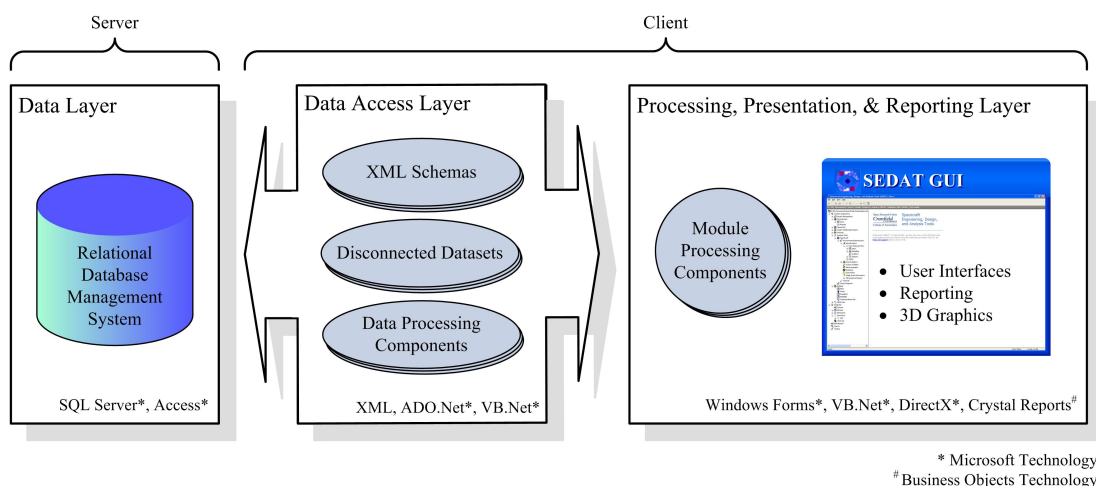


**Figure 5-2 - SEDAT Client-Server Architecture**

For example, the processing component of the Free Molecular Flow (FMF) Module, described in Chapter 6, is an independent collection of components and classes, which can be used by other modules and applications.

The Data Access Layer (DAL) interacts with the two other layers using bespoke data processing components, which populate and manipulate local XML-based representations of the underlying data.

## 5.4 Technologies

There has been a preference for Microsoft technologies over platform-independent technologies, in part, because of the experience of the author, but also because collectively they are mature, easy to use, widespread, highly interoperable, share a common development environment (Microsoft Visual Studio .Net), and are well-supported (both by Microsoft and within organisations).

In addition, they inherently support many of the goals of SEDAT. For example, Microsoft .Net supports managed code, which provides full support for multiple programming languages and object-orientated programming.

With the recent release of Windows XP 64-Bit, Microsoft has also provided an operating system that will enable a single workstation to perform both business functions and high-performance engineering tasks. A significant step forward for concurrent engineering advocates.

The SEDAT Database has been implemented in both Microsoft Access and Microsoft SQL Server. However, its design, and the design of its components (tables and stored procedures) are such that it is database server independent and could be migrated to, for example, an Oracle Database Server.

The SEDAT Client has been implemented as a Microsoft Windows Forms application. It has been developed using predominantly Microsoft .Net<sup>1</sup> technologies, including Visual Basic.Net 1.1, ADO.Net 1.1, and DirectX 9.0 (for 3D graphics).

The SEDAT Help System has been developed using Microsoft HTML Help Workshop 1.3.

## 5.5 The Database

This section describes the conceptual approach used to design the SEDAT database. It then describes the actual database that has been implemented and some of its key features. Finally, it provides some detailed examples of the database design.

---

<sup>1</sup> Software providers are listed in Section III.iii.



### 5.5.1 Design

The purpose of the database is to provide a single data repository for all SEDAT modules. Therefore, the conceptual goal of the database is to model the physical products (the spacecraft and related ground systems), the systems engineering processes, and the product lifecycles in the most accurate, flexible, and configurable way possible.

There are many ways of representing such a complex system in a database. One way is to consider all the entities that need to be modelled as objects [100]. Using this object-orientated methodology, an object, such as a spacecraft, is then represented by multiple inter-related tables in a structure that resembles the actual physical hierarchy of its constituent components.

This object-orientated approach was employed for the design of the SEDAT Database. As well as providing a consistent design methodology, the additional benefit of employing this approach was that the Data Access Layer (DAL), which communicates changes between the client and the database, was much simpler to design. This is because the SEDAT Client's processing code has also been written using object-orientated principles, as described in Section 0.

As stated previously, the concept behind SEDAT is that all the different tools and processes of a spacecraft systems engineering program are represented within one software system by different inter-related modules. Therefore, the database has a modular structure, which is illustrated in Figure 5-3.

As described in Section 5.1, there are two types of module: core and non-core. Core database modules contain groups of tables that can be used by any other module of the database. They represent the tables that any organisation might need. The core database modules, such as the Physical Data and the Geometry modules, are illustrated by the white blocks in Figure 5-3.

The non-core database modules, such as the FMF database module described in Chapter 6, are shown in grey in Figure 5-3. Non-core database modules contain groups of tables that store data related to a specific discipline. The names of all non-core module tables are prefixed with the letter z.

Every organisation and engineering discipline will have a different interpretation of what represents a module and how tables should be grouped into modules. The structure represented by Figure 5-3, represents just one initial interpretation.

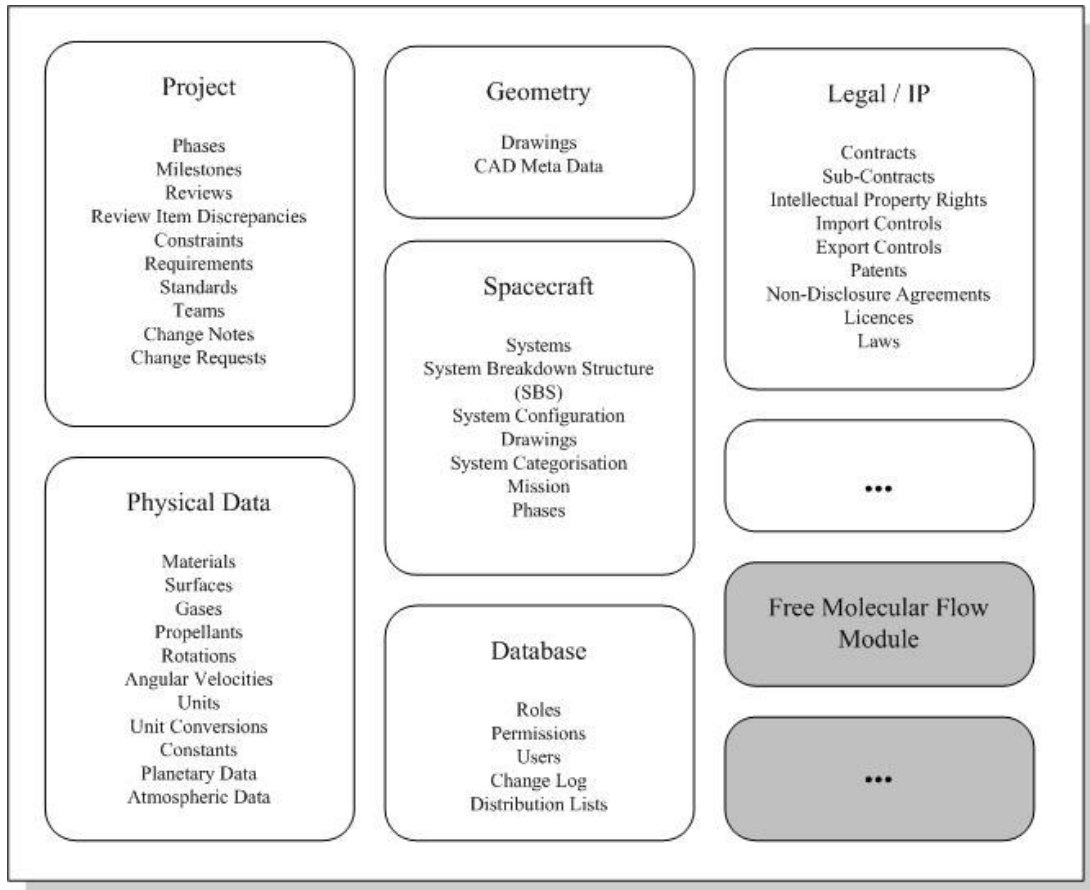


**Figure 5-3 - SEDAT Database High-Level Design**

Image shows some selected core modules (with a white background) and non-core modules (with a grey background). “...” indicates the possibility that additional modules could be added.

### 5.5.2 Implementation

Given the scope of this PhD, emphasis has been placed on developing those aspects of the database necessary to demonstrate the SEDAT Concept. In particular, those aspects necessary to implement the FMF Module.

The final database design was arrived at after multiple comprehensive iterations in addition to numerous smaller adaptations. The final database contains 175 tables. Of these, 52 belong to the FMF Module (their names are prefixed “ZFRT\_” and they are described in Section 6.4.1), 39 core tables are used by the FMF Module, and four tables are used by the client (to configure the GUI and store logon and password information). Therefore, 95 tables directly demonstrate the SEDAT Concept. The remaining 80 tables were developed during the early stages of the project, to assess the feasibility of the SEDAT Concept.

The table relationships that were defined to demonstrate the SEDAT Concept and assess its feasibility are illustrated in Figure 5-4. The figure shows the entire SEDAT Database table relationship diagram (schema). Close-up views of

various portions of the schema are provided and discussed in later sections and chapters.

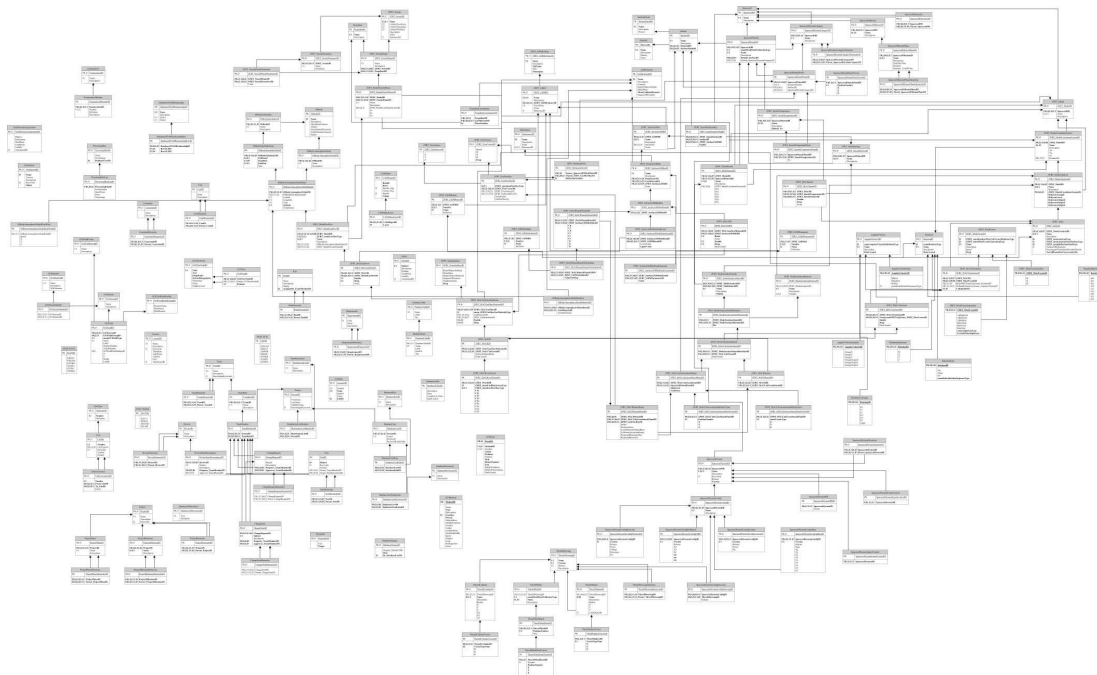


**Figure 5-4 - SEDAT Database Table Relationships (Schema)**

The schema view was generated using the database reverse engineering functionality of Microsoft Visio.

A navigatable and zoom-able view of the entire database schema can be accessed via the SEDAT Client, by selecting the *Database\Schema* node in the tree-view on the left-hand side, as illustrated in Figure 5-5. The same digital version of the schema is also provided in the *Database Schema* folder in Appendix 1.

In addition to all the tables and relationships, the database also contains numerous Structured Query Language (SQL) queries, which are used by the client's Data Access Layer (DAL), described in Section 5.3. Select queries are used by the DAL to retrieve datasets from multiple related tables. Action queries are used by the DAL to append, update, and delete rows of data from tables. Queries can also be run from within the database to perform batch updates or extract large multi-table datasets.



separated by hyphens, for example *BC8C9E50-3705-4998-B136-99344D00BD75*. The benefits of using GUIDs as PKs are that:

- Multiple clients can connect to the database simultaneously and carry out processing threads in parallel without the risk of row-level update conflicts. Simultaneous processing across distributed desktop computers in this way mimics a distributed computing environment, sometimes referred to as a computing grid or just “grid,” as illustrated in Figure 5-6.
- The database and portions of the database can be replicated to additional servers (for load balancing, and back-up and testing purposes), or local machines for mobile use.
- Table-independent relationships can be created between any two records in the database because every row has its own unique GUID.
- The PK duplication problems that can occur when different databases need to be combined is eliminated (this type of problem is common when organisations merge or decide to integrate their database systems).
- GUIDs are effectively future-proof: it is unlikely that any future database table could use-up all possible GUIDs.

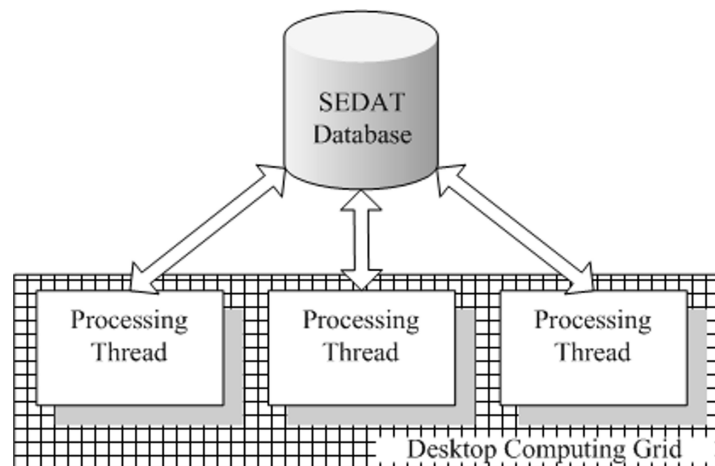


**Figure 5-6 - SEDAT Database Grid Computing Schematic**

#### **5.5.4 Detailed Examples of the Database Design**

Given the complexity of the design and the iterative nature of the development process, a detailed description of every single table and relationship design decision would not be feasible.

In order to provide some insight into the detailed design of the core modules of the database, two examples have been chosen. The examples describe the core tables and relationships used to represent spacecraft and solar system bodies. The

tables involved are directly related to the FMF Module’s tables and constitute the largest inter-related groups of core tables that are used by the module.

The table that represents a spacecraft (*Spacecraft*) is connected to a *SpacecraftHierarchy* table, which enables one spacecraft to be represented as part of another, as illustrated in Figure 5-7. This figure also illustrates how a spacecraft surface mesh is represented in the core tables of the database. This representation is identical in structure to the arrangement of the generic SEDAT classes used to represent three-dimensional geometry described, as described in Section 6.5.1: each surface mesh has a number of panels, and each panel a number of vertices.

Both the surface mesh and the surface mesh’s panels can be associated with different spacecraft system categories. For example, a surface mesh that represents part of the power system category could have some of its panels associated with a solar power system sub-category. The advantage of this is that the system and part data can be grouped logically to provide detailed information at user-defined system and sub-system levels using Structured Query Language (SQL) queries.

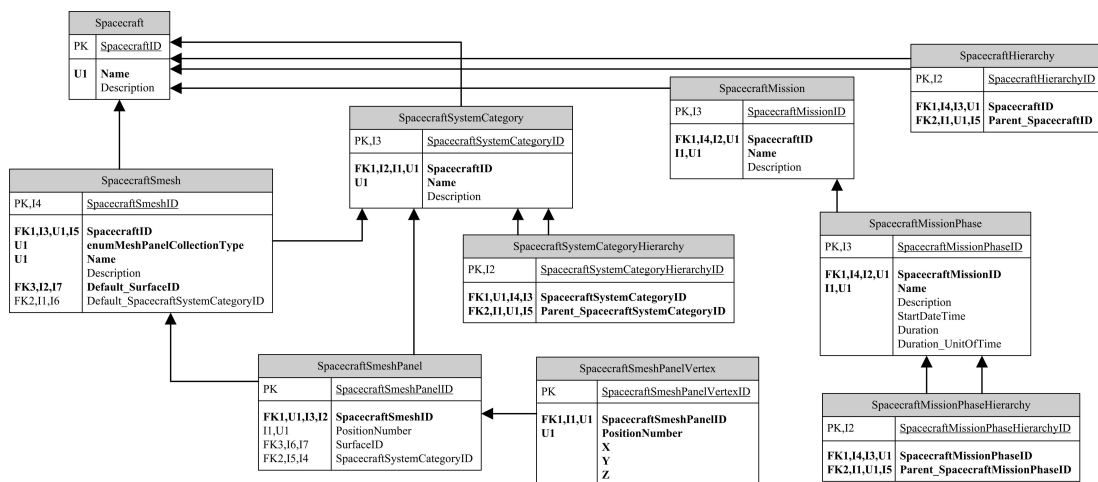


**Figure 5-7 - SEDAT Database Relationships: Selected Spacecraft Tables**

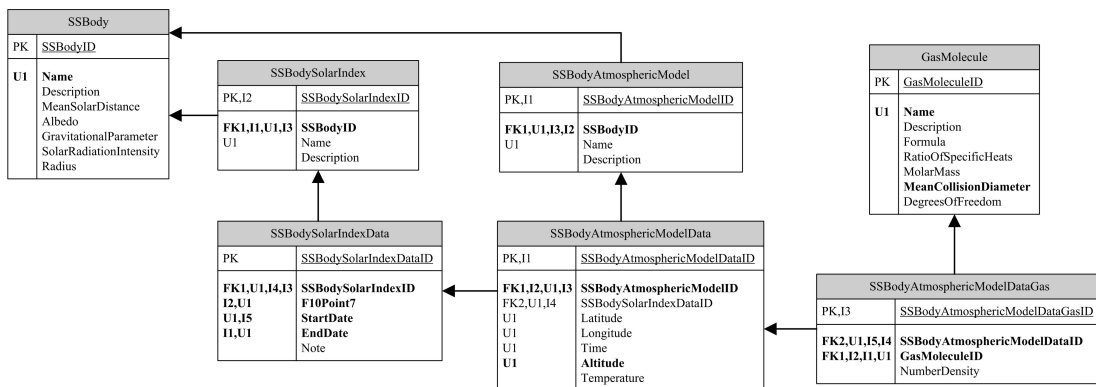
Note that only relationships between displayed tables are shown. Bold field names indicate that the field is part of one the table’s unique keys (e.g. *UI*) or foreign keys (e.g. *FK1*). Primary keys (PKs) are in all cases named *<Table Name>ID*. Arrows indicate the direction of the one-to-many relationship (the arrow points to the “one” side of the relationship).

Figure 5-8 illustrates how solar system bodies, such as the Earth or Mars, are represented within the database. These entities required modelling because of the FMF Module’s requirement to incorporate multiple atmospheric models. They are part of the core database module Physical Data, illustrated in Figure 5-3, rather than the FMF Module. This is because their data is not exclusive to the FMF Module (other modules would likely require access to their data).

The one-to-many relationship between the *SSBody* table and the *SSBodyAtmosphericModel* table, shown in Figure 5-8, enables a single solar system

body, such as Earth, to have multiple atmospheric models associated with it. Each solar system body may also have multiple solar irradiance models connected to it. The solar irradiance models are represented by the related *SolarIndex* tables.

The *SSBodyAtmosphericModelData* table, illustrated in Figure 5-8, provides atmospheric model temperature data for the particular solar conditions defined in the *SSBodySolarIndexData* table at the unique latitude, longitude, altitude, and time defined. The related *SSBodyAtmosphericModelDataGas* table provides the molecular number density for each constituent of the atmospheric gas in these conditions. The constituent's properties are then provided by the related *GasMolecule* table.



**Figure 5-8 - SEDAT Database Relationships: Solar System Body Tables**

Note that only relationships between displayed tables are shown. Bold field names indicate that the field is part of one the table's unique keys (e.g. *U1*) or foreign keys (e.g. *FK1*). Primary keys (*PKs*) are in all cases named *<Table Name>ID*. Arrows indicate the direction of the one-to-many relationship (the arrow points to the "one" side of the relationship).

## 5.6 The Client

This section describes the approach taken to develop the SEDAT Client as well as some of its key features. It then describes the programming strategy employed and how to add modules and module components to the client.

### 5.6.1 Approach

The objective of the SEDAT Client is to provide a single consistent user-interface and processing framework for all SEDAT modules to retrieve, present, and process multiple different types of systems engineering information.

One of the conceptual goals of SEDAT is to maximise the modularity, flexibility, and reusability of modules and their components. To achieve this goal and help meet the objective outlined above, the modules and components of the client were designed using the object-orientated principles of abstraction, encapsulation, and polymorphism. Section 0 describes the Object-Orientated Programming (OOP) strategy employed.

The design of the client Graphical User Interface (GUI) reflects the need to present multiple different types of information to the user via a single flexible and easy to navigate interface.

As illustrated in Figure 5-9, the client GUI has a tree view component in the left-hand pane, which provides users with an overview of where they are in the system and allows them to navigate within and among modules. The tree view also enables the user to view all the database tables and navigate around them (using the *TableMaintenanceNavigator* component described in the following section).

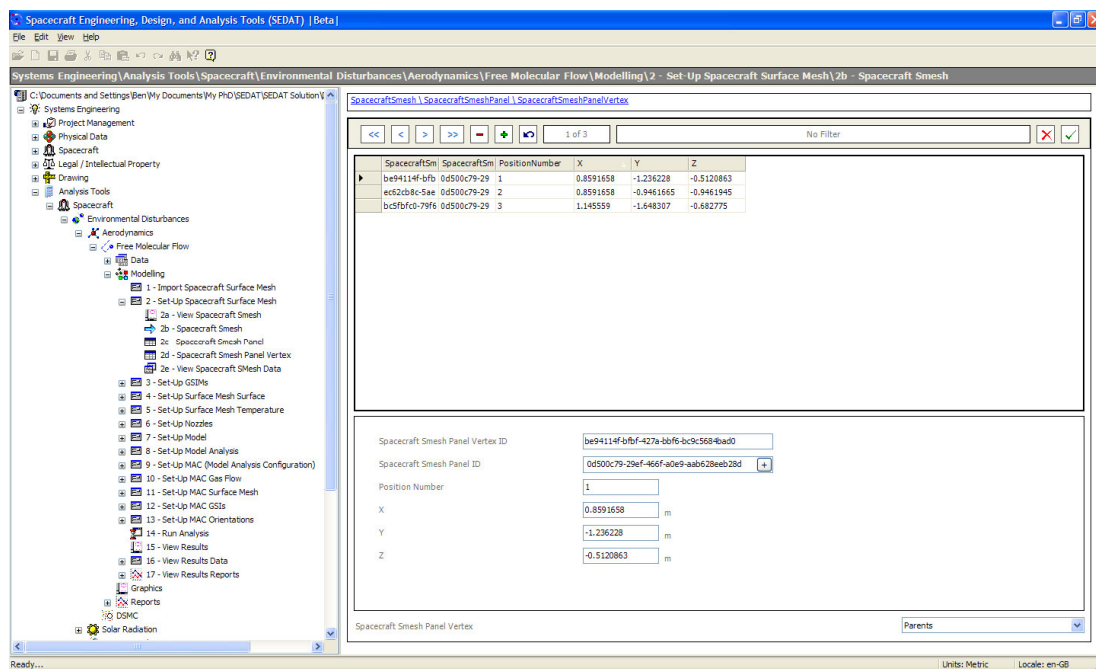


**Figure 5-9 - The SEDAT Client: Screen shot showing the application’s tree view component and table maintenance and navigation functionality**

The screen shot of the SEDAT Client shown in Figure 5-9 also illustrates the simplicity of the GUI design. The client window always displays the main menu, toolbar, and title bar along the top, as well as the tree view component on the left hand-side and the status bar along the bottom.

When the user navigates around the tree view the menu bar, toolbar, title bar, and the right-hand pane are all updated to reflect the user’s selection. Depending on the screen being displayed, the right-hand pane may be composed of multiple smaller panes (this is the case illustrated in Figure 5-9). All of the panes can be re-sized and are scrollable.



The design of the SEDAT Client GUI was inspired by the GUIs of the latest releases of Microsoft Outlook<sup>1</sup> (an email client) and SAP (an enterprise application), which are shown in Figure 5-10. This is because they share a similar objective to the SEDAT Client. They must present large amounts of different types of information to the user in a consistent, structured, navigatable, and easy-to-use way.

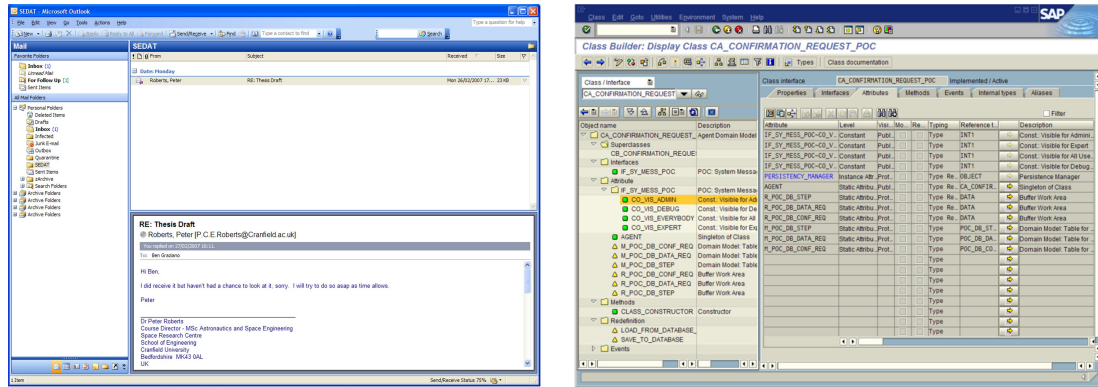


**Figure 5-10 - The Latest Microsoft Outlook and SAP Clients**

The left image illustrates version 11 (2003) of the Microsoft Outlook client and the right image illustrates version 6.4 (2004) of the SAP client.

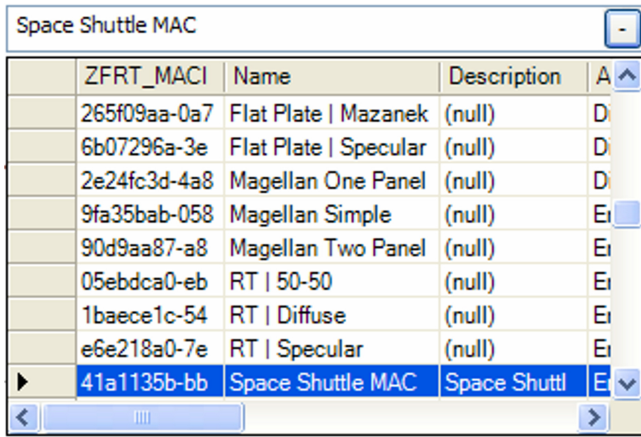
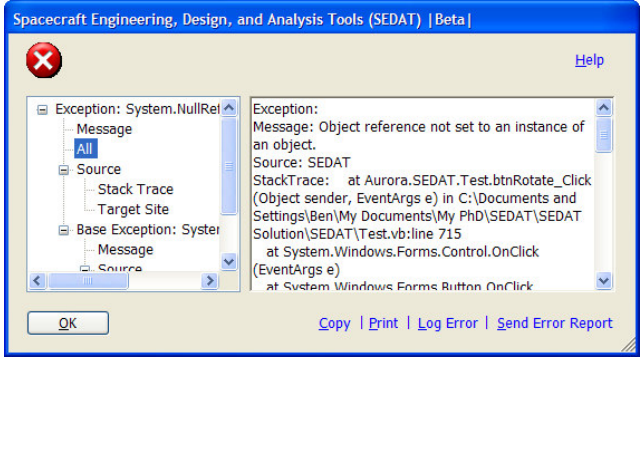
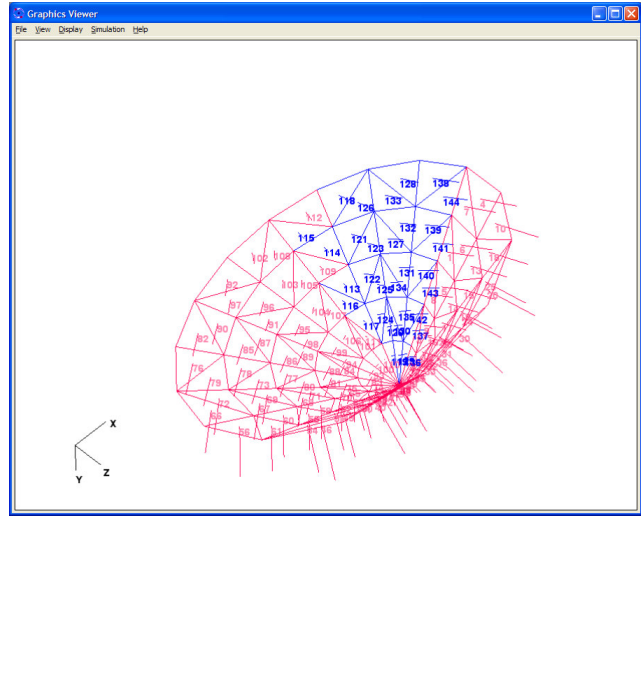
### 5.6.2 Key Features

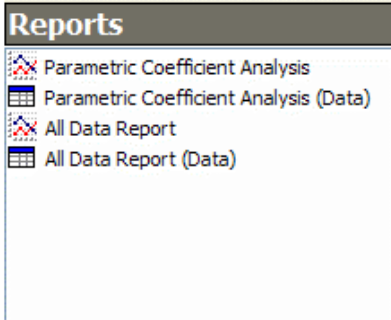
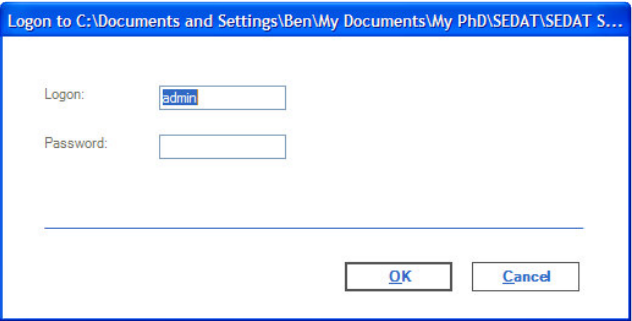
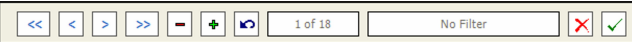
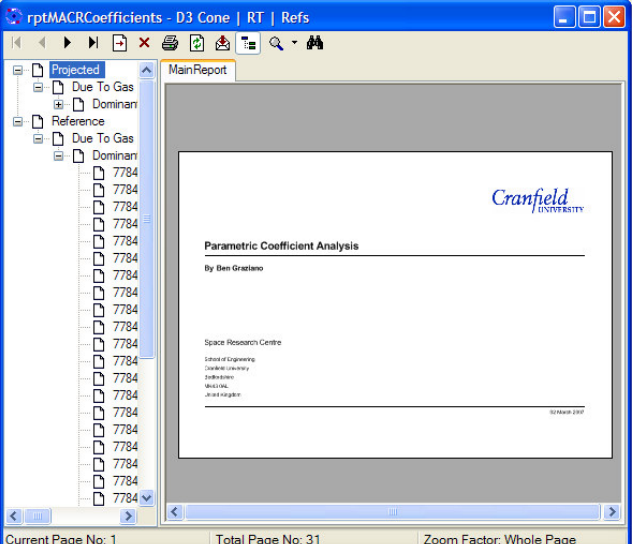
Table 5-1 provides a table listing all of the Graphical User Interface (GUI) components that have been developed specifically for SEDAT. These unique components represent a very labour-intensive aspect of the overall client development.

Nonetheless, their development was deemed crucial for demonstrating the SEDAT Concept effectively because they represent encapsulated objects that can be used anywhere within the application and beyond. This “plug and play” capability was made possible because all of the components were written using Object-Orientated Programming (OOP) methodologies. For more information about the programming strategy, refer to Section 0.

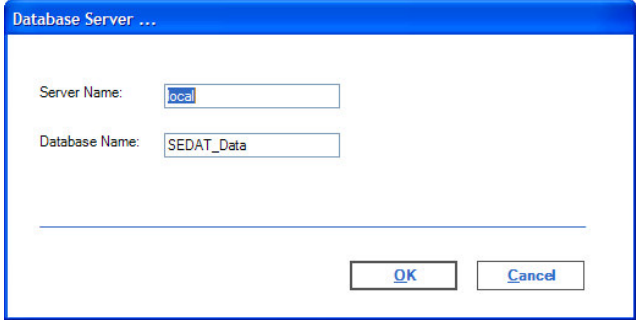
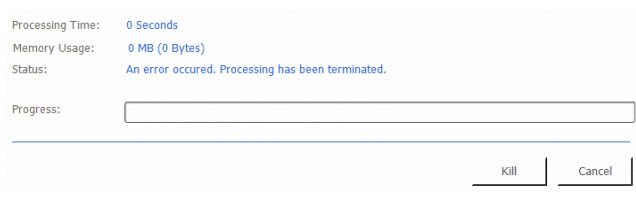
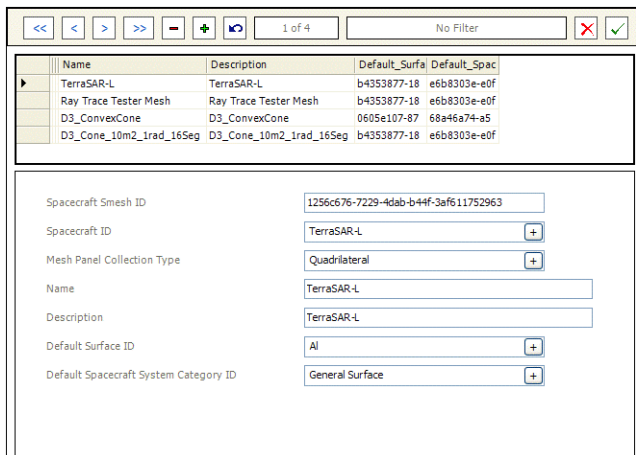
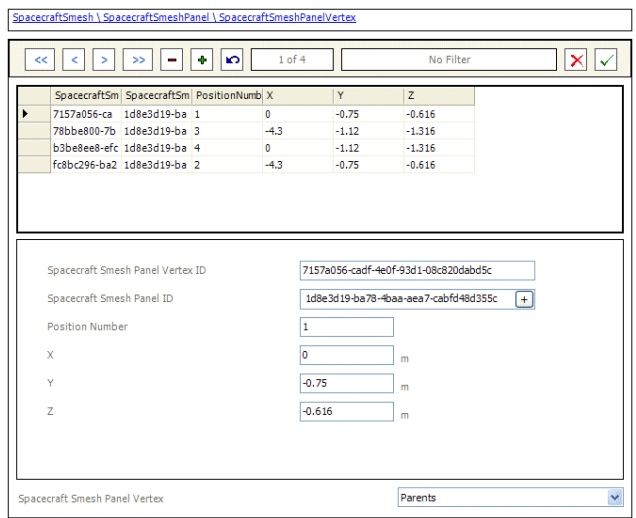
<sup>1</sup> Software providers are listed in Section III.iii.

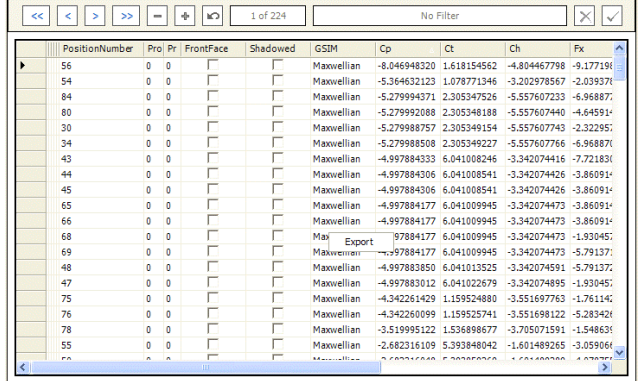
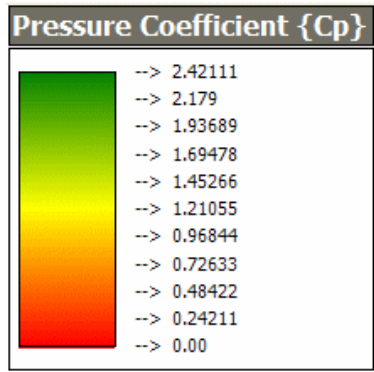
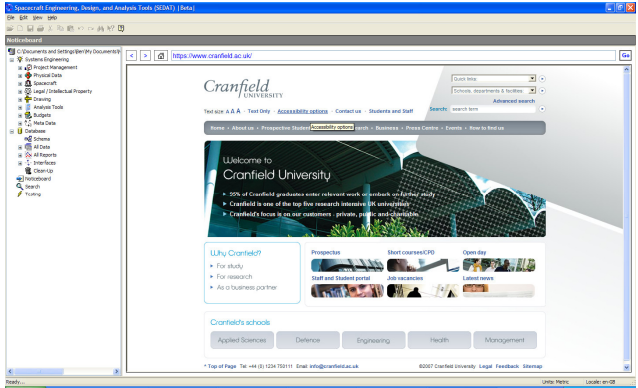
**Table 5-1 - Selected Bespoke GUI Components**

Component	Screen shot
<p><b>DropDown</b></p> <p>Provides the user with access to a drop down list consisting of a table or view (SQL select query), which may have multiple columns and many thousands of rows.</p>	
<p><b>ErrorMessageBox</b></p> <p>A collection of classes and components used to handle errors. The ErrorMessageBox dialog displays the error message, along with details of its origin, stack trace, runtime information, any related or parent errors, and help and error logging options. It can also provide the user with multiple dialog button types and combinations (e.g. <i>Ok</i>, <i>Cancel</i>, <i>Yes</i>, <i>No</i>, <i>Re-Try</i> etc) to control code execution after an error.</p>	
<p><b>GraphicsEngine</b></p> <p>A collection of classes and components used to display 3D graphics. Developed in Microsoft DirectX 9.0 from basic tutorial code [102]. Graphics can be displayed in windows forms controls or stand-alone windows, with a variety of display options. Features include dynamic display sizing, mouse zoom, mouse 3D rotate, left and right-handed coordinate systems, multiple coordinate system display position options, surface normal display, vertex number display, wireframe view, rendered view, back-face culling, background colour selection, and a simple 3D rotation simulation option. Can be used to display <i>SurfaceMesh</i> objects (described in Section A2.2.2).</p>	

<p><b>ListPanel</b></p> <p>Lists items for the user to select.</p>	
<p><b>Logon</b></p> <p>Provides a logon and password prompt dialog.</p>	
<p><b>RecordNavigatorFilter</b></p> <p>Allows the user to navigate a table or view (select query) of data and filter for selected records.</p>	
<p><b>ReportViewer</b></p> <p>Displays bespoke reports designed in Crystal Reports (reporting tool provided by Business Objects<sup>1</sup>)</p>	

<sup>1</sup> Software providers are listed in Section III.iii.

<p><b>SelectDatabaseServer</b></p> <p>Allows the user to select a Microsoft SQL Server.</p>																															
<p><b>StatusPanel</b></p> <p>Displays the progress and memory consumption of long-running processes and provides the user with the option to cancel them or terminate the application.</p>																															
<p><b>TableMaintenance</b></p> <p>Provides the user with a navigatable and filterable display of a table's data, combined with an editable display of the current record's data.</p>	 <table border="1" data-bbox="699 853 1321 949"> <thead> <tr> <th>Name</th> <th>Description</th> <th>Default_Surfa</th> <th>Default_Spac</th> </tr> </thead> <tbody> <tr> <td>TerraSAR-L</td> <td>TerraSAR-L</td> <td>b4353877-18</td> <td>e6b8303e-e0f</td> </tr> <tr> <td>Ray Trace Tester Mesh</td> <td>Ray Trace Tester Mesh</td> <td>b4353877-18</td> <td>e6b8303e-e0f</td> </tr> <tr> <td>D3_ConvexCone</td> <td>D3_ConvexCone</td> <td>0605e107-87</td> <td>68a46a74-a5</td> </tr> <tr> <td>D3_Cone_10m2_1rad_16Seg</td> <td>D3_Cone_10m2_1rad_16Seg</td> <td>b4353877-18</td> <td>e6b8303e-e0f</td> </tr> </tbody> </table>	Name	Description	Default_Surfa	Default_Spac	TerraSAR-L	TerraSAR-L	b4353877-18	e6b8303e-e0f	Ray Trace Tester Mesh	Ray Trace Tester Mesh	b4353877-18	e6b8303e-e0f	D3_ConvexCone	D3_ConvexCone	0605e107-87	68a46a74-a5	D3_Cone_10m2_1rad_16Seg	D3_Cone_10m2_1rad_16Seg	b4353877-18	e6b8303e-e0f										
Name	Description	Default_Surfa	Default_Spac																												
TerraSAR-L	TerraSAR-L	b4353877-18	e6b8303e-e0f																												
Ray Trace Tester Mesh	Ray Trace Tester Mesh	b4353877-18	e6b8303e-e0f																												
D3_ConvexCone	D3_ConvexCone	0605e107-87	68a46a74-a5																												
D3_Cone_10m2_1rad_16Seg	D3_Cone_10m2_1rad_16Seg	b4353877-18	e6b8303e-e0f																												
<p><b>TableMaintenanceNavigator</b></p> <p>Uses the TableMaintenance component and a list of navigatable links to enable navigation amongst linked records in related tables.</p>	 <table border="1" data-bbox="699 1350 1321 1447"> <thead> <tr> <th>SpacecraftSm</th> <th>SpacecraftSm</th> <th>PositionNumb</th> <th>X</th> <th>Y</th> <th>Z</th> </tr> </thead> <tbody> <tr> <td>7157a056-ca</td> <td>1d8e3d19-ba</td> <td>1</td> <td>0</td> <td>-0.75</td> <td>-0.616</td> </tr> <tr> <td>78bbe800-7b</td> <td>1d8e3d19-ba</td> <td>3</td> <td>-4.3</td> <td>-1.12</td> <td>-1.316</td> </tr> <tr> <td>b3be8ee8-efc</td> <td>1d8e3d19-ba</td> <td>4</td> <td>0</td> <td>-1.12</td> <td>-1.316</td> </tr> <tr> <td>fc8bc296-ba2</td> <td>1d8e3d19-ba</td> <td>2</td> <td>-4.3</td> <td>-0.75</td> <td>-0.616</td> </tr> </tbody> </table>	SpacecraftSm	SpacecraftSm	PositionNumb	X	Y	Z	7157a056-ca	1d8e3d19-ba	1	0	-0.75	-0.616	78bbe800-7b	1d8e3d19-ba	3	-4.3	-1.12	-1.316	b3be8ee8-efc	1d8e3d19-ba	4	0	-1.12	-1.316	fc8bc296-ba2	1d8e3d19-ba	2	-4.3	-0.75	-0.616
SpacecraftSm	SpacecraftSm	PositionNumb	X	Y	Z																										
7157a056-ca	1d8e3d19-ba	1	0	-0.75	-0.616																										
78bbe800-7b	1d8e3d19-ba	3	-4.3	-1.12	-1.316																										
b3be8ee8-efc	1d8e3d19-ba	4	0	-1.12	-1.316																										
fc8bc296-ba2	1d8e3d19-ba	2	-4.3	-0.75	-0.616																										

<p><b>TableViewer</b></p> <p>Provides a navigatable view of a table or view (select query) of data. Uses the RecordNavigatorFilter component to enable navigation and filtering of data.</p>	
<p><b>VerticalLevel</b></p> <p>Calculates and presents a colour-coded visual key based on the values passed and the display format chosen.</p>	
<p><b>WebBrowser</b></p> <p>Displays a navigatable view of any Microsoft Internet Explorer 6 compatible document or web page. Includes an address bar and go, backwards, and forwards navigation keys.</p>	

### 5.6.3 Programming Strategy

As described in Section 5.6.1, the client was developed using object-orientated principles. To help achieve this all of the programming code that constitutes the client was written using Object-Orientated Programming (OOP) methods.

In OOP, real-world objects are represented in code by abstract programmatic templates, known as classes. A class provides an encapsulated description of an object, including its properties and its behaviour (in the form of functions, subroutines, and events). Encapsulation is a fundamental principle of OOP. It ensures that all of the data an object requires is contained within the object along with all the functionality required to manipulate that data.

To ensure that class names can be re-used, each class is assigned to a namespace. The namespaces are arranged into a hierarchy in which each branch has a unique namespace path.

Classes can also be inherited. An inherited class shares the features of its parent class, but may also have several additional features. For example, a car class that inherits from a vehicle class would inherit a *Speed* property from the vehicle class, but may also have a property for the number of doors.

In OOP, it is possible to create abstract descriptions to prescribe the behaviour of a group of classes using interfaces. For example, a vehicle class and a house class might both need to provide properties describing their current value. In this case, an interface could be implemented by both classes that forces them both to expose a *CurrentValue* property.

The use of inheritance and interfaces enables different classes to provide different implementations of the same public properties, functions, subroutines, and events. This ability is known as polymorphism and is one of the most useful and powerful features of OOP.

Together, abstraction, encapsulation, and polymorphism increase the interoperability, modularity, and reusability of code. Therefore, the use of OOP was an obvious strategy to employ to develop the SEDAT Client.

The arrangement and structure of objects and the relationships between them is known collectively as an object model. One of the consequences of using OOP is that many more lines of code are required than might typically be expected using linear programming techniques. The client object model is no exception. It is comprised of over 30,000 lines of code, including the FMF Module. In addition to the object model, the client contains numerous XML schemas<sup>1</sup> to represent different data structures.

The client code is documented using comments where appropriate. In addition, a detailed and navigable view of the object model has been generated that can be provided to those wishing to understand the code in more detail or develop it further.

Section 6.4.2 describes the client components of the FMF Module. It also provides a detailed description of the FMF Module's object model via reference to Section A2.2 of Appendix 2.

---

<sup>1</sup> XML schemas are used to describe the data structures of XML documents, which are used to store data.

## 5.6.4 Adding Module Components and Screens

Individual module components and GUI screens can be incorporated into the client using a few table entries within the SEDAT Database (via the *GUITree* and *GUITreeNode* tables). This means that new module components can be developed outside of the main development environment and incorporated into the final client using a few simple data entries at the database level. A similar approach is taken by enterprise applications such as SAP.

## 5.7 The Help System

The SEDAT Help System is installed with the SEDAT Client. It provides context sensitive help throughout the application that can be accessed by pressing *F1* on the keyboard. The help system can also be accessed via the *Help* drop-down in the client's main menu or via a shortcut installed in the start-up menu. A screenshot of the help system is provided in Figure 5-11.

The entire help system, which consists of numerous separate Hypertext Markup Language (HTML) files, incorporating various diagrams and screenshots, is provided in digital format in the *Help* folder in Appendix 1.

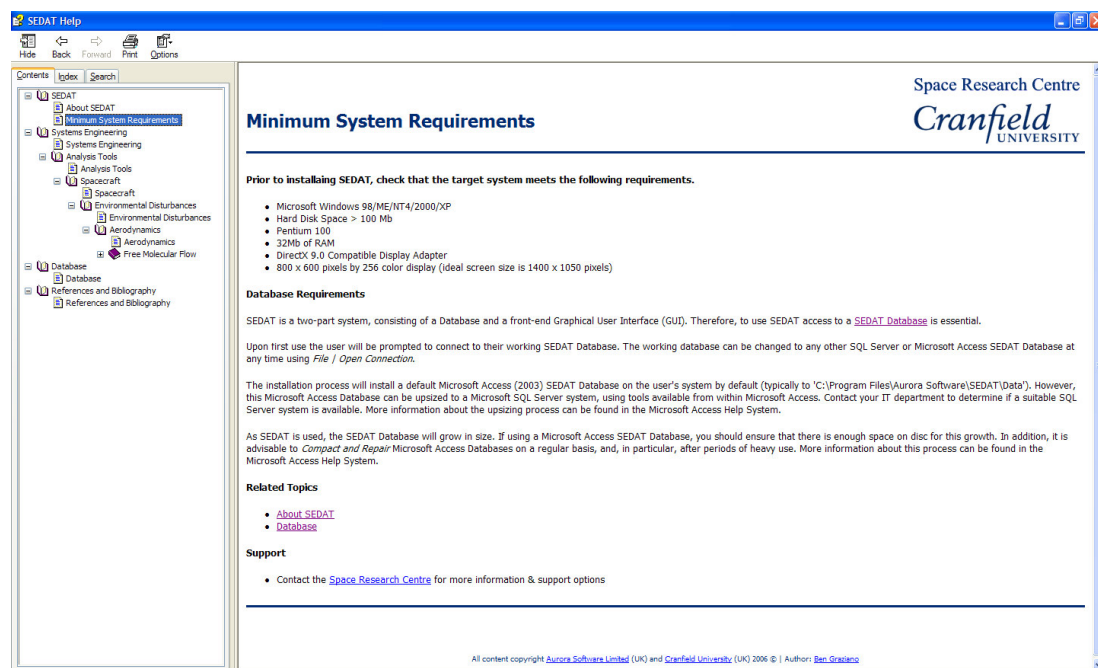


**Figure 5-11 - SEDAT Help System**

## 5.8 Testing

Testing is an integral part of the development cycle and essential for successful application development and implementation. The development process is far from linear and at every stage, feedback from testing will cause iterative changes to the final software application.

In the commercial environment, several different types of testing would be carried out to prove the software. A typical, multi-tier testing strategy is outlined in Figure 5-12.

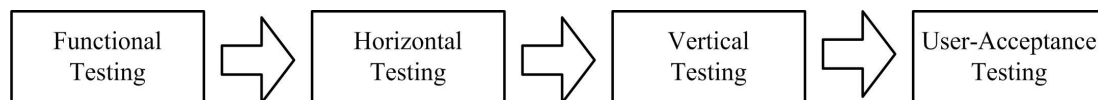


**Figure 5-12 - Testing Phases**

In general, the developer would only be involved at the Functional Testing stage and a dedicated team of testers led by the original specification team would carry out all other tests. Functional testing involves testing that at code level each procedure behaves as expected. Horizontal testing, also known as bench testing, involves testing each separate module of the software. The complete application is tested at the Vertical Test stage. User-Acceptance Testing (UAT) is the final stage.

In the academic research environment, it is not always possible to use separate teams to carry out the different tests. Given the scope of this software development, as outlined in Section 5.2, functional and horizontal testing has been carried out for all components on an ad-hoc basis as they have been developed. However, due to a lack of resources and time constraints, it has not been possible to carry out exhaustive vertical testing or any UAT.

## 5.9 Installation

An installation disc for SEDAT can be obtained, subject to certain terms and conditions, from either the Aurora Software website<sup>1</sup> or the Space Research Centre (SRC), Cranfield University<sup>2</sup>.

SEDAT and the accompanying help files, and example program files as well as a default SEDAT Database can be installed on any computer running the Microsoft Windows operating system (versions 98/ME/NT4/2000/XP/x64) by

<sup>1</sup> Aurora Software: [www.aurorasoftware.co.uk](http://www.aurorasoftware.co.uk)

<sup>2</sup> Space Research Centre, Cranfield University (UK): [www.cranfield.ac.uk/soe/space](http://www.cranfield.ac.uk/soe/space)



running the *setup.exe* setup program on the installation disc. A screenshot of the setup program is illustrated in Figure 5-13.

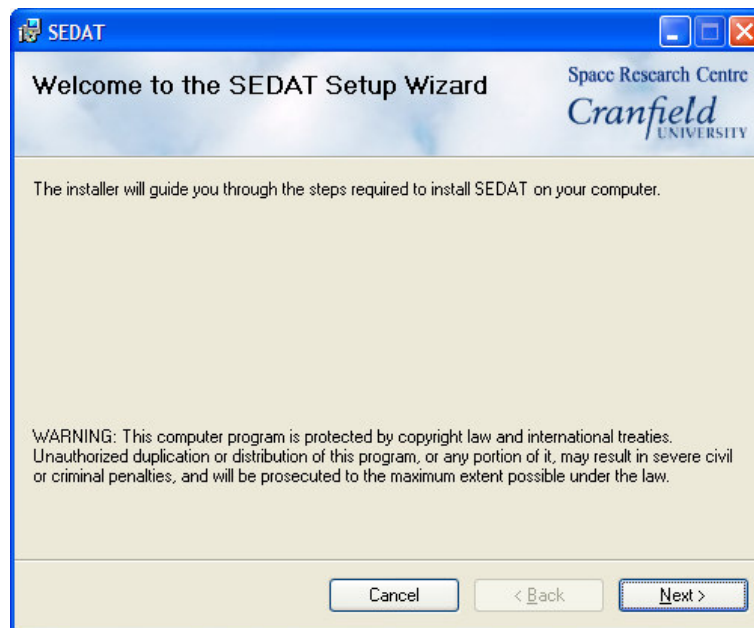


**Figure 5-13 - The SEDAT Setup Program**

The default program directory for the software is *C:\Program Files\Aurora Software\SEDAT*. A shortcut to SEDAT is installed on the user's desktop and in the user's start-up menu, in the *Aurora Software* shortcut folder.

For assistance upon first use of the software, the user is advised to consult the help files that are installed in the program directory (a shortcut to these are also installed in the shortcut folder in the start-up menu).

Owing to the difficulty of deploying a Microsoft SQL Server database and the related installation issues that the user would have to address, the default SEDAT Database installed during setup is a Microsoft Access database system. It is installed in the *Data* folder of the program directory.

The default Microsoft Access database can be upsized to a Microsoft SQL Server database using the Upsizing Wizard provided with Microsoft Access (both this process and the resulting SQL Server database have been tested using Microsoft Access 2003 and SQL Server 2000).

The SEDAT software can be uninstalled in the normal way using the *Add or Remove Programs* utility in the Microsoft Windows *Control Panel*. Note that this process will also remove the default Microsoft Access SEDAT Database file that is installed during setup.

## 5.10 Summary

This chapter has outlined a very ambitious solution to the implementation of concurrent engineering beyond Phase A (conceptual design) of the spacecraft development process. The solution is the SEDAT Concept, which is based upon the enterprise application software model and information technology architecture used in large organisations (described in Section 4.3).

The idea behind SEDAT is that all of the computer tools used on a project should be incorporated into one system as separate modules. All of the modules should be presented via a single GUI and connected to a single centralised RDBMS, which contains all project data.

Within the scope of a PhD, only a limited demonstration of the concept is feasible. This chapter has provided details of the SEDAT software system that has been developed to demonstrate the concept. It has explained both the high-level design and the detailed technical features of the system that has been implemented.

The software system that has been developed was designed to support the objective of developing a spacecraft aerodynamic analysis tool within a concurrent engineering framework. The next chapter (Chapter 6) will outline the FMF Module that has been developed and integrated into SEDAT specifically for this purpose.

## **6 THE FREE MOLECULAR FLOW MODULE**

This thesis represents the result of work spread over a number of years. Early work involved the development of a prototype spacecraft aerodynamic analysis tool, which is described in Section 6.1. Over time, an understanding of the aerodynamic analysis problem, the limitations of the prototype, and the challenges of modern engineering grew. As a result, the SEDAT Concept evolved and was later realised in the form of the SEDAT System, which is described in Chapter 5.

This chapter describes the Free Molecular Flow (FMF) Module and related components that have been implemented as part of the SEDAT System. The purpose of the FMF Module is to enable the aerodynamic analysis of spacecraft operating in FMF. In so doing, it also provides a practical demonstration of the SEDAT Concept and helps fulfil the objectives outlined in Section 1.4.

In order to facilitate efficient analysis of a wide range of spacecraft operating in multiple different scenarios a new method of performing spacecraft aerodynamic analysis has been developed and implemented in the FMF Module. This method is described in Section 6.2.

The method involves the use of ray-tracing techniques. As a result, a bespoke ray-tracer has been developed and implemented. The ray-tracer can be used by other modules within the SEDAT System, but it is nonetheless described in this chapter for clarity. It is described in Section 6.3.

The implementation of the FMF Module and its integration into the SEDAT System is described in Section 6.4. In addition, some of the key features of the module are described in Section 6.5.

### **6.1 Prototype**

Prior to the development of the SEDAT Concept, a free-molecular flow analysis tool was developed during the first nine months of the PhD. This tool has been superseded by the SEDAT System and the FMF Module and it is therefore referred to as the prototype tool. This section describes the prototype and the lessons that were learnt from it.

#### **6.1.1 Description**

The prototype employs the Ray-Tracing Panel (RTP) method described in Section 2.6.2. It implements the Schaaf and Chambre gas-surface interaction model described in Section 3.2.2, along with the empirically based Knechtel and Pitts [17] and Mazanek et al [20] accommodation coefficients described in Sections 3.3.2 and 3.3.3, respectively. It does not account for multiple flow reflections and does not

calculate aerodynamic damping terms (forces and torques caused by the rotation of a body through the surrounding gas). It does not permit surface-dependent properties, such as temperature, to be set. It also does not include an atmospheric model.

The prototype was developed entirely within the desktop Relational Database Management System (RDBMS) Microsoft Access<sup>1</sup> (version 2003). The programming code was written in Microsoft Access's native script, Visual Basic for Applications (VBA). The database application included multiple tables, Structured Query Language (SQL) queries, VBA forms, and reports.

To facilitate the import and export of surface meshes from the desktop Computer-Aided Design (CAD) application AutoCAD, a bespoke interface module was developed using the AutoCAD Application Programming Interface (API). Additional interfaces were built to Microsoft Excel, MATLAB, and Satellite Tool Kit via their respective APIs. These interfaces provided a platform to experiment with different approaches to various aspects of the aerodynamic analysis task.

### 6.1.2 Lessons Learnt

The prototype tool was used to perform preliminary analyses of the TerraSAR-L satellite illustrated in Figure 6-1, which was originally due for launch in 2011 but subsequently abandoned by ESA. Comparison of the TerraSAR-L results with the unpublished results of a study by GMV<sup>2</sup> [35], which was commissioned by ESA, revealed discrepancies. These discrepancies were found to have two causes:

1. The GMV group chose to use the projected area of the body in the attitude being analysed as the reference area when calculating the aerodynamic coefficients for the attitude, rather than a fixed reference area. The projected area is the frontal area of the body at the attitude being analysed, which can be determined by summing the results of Equation 3-22 for each forward facing surface mesh panel.
2. The prototype tool does not include an atmospheric model. For this reason, the dominant atmospheric constituent in mean solar conditions at the altitude being analysed was used. However, over the course of a solar cycle the dominant constituent at this altitude varies. The resultant change in molar mass was not accounted for during calculations of scenarios that deviated from mean solar conditions. This resulted in significant errors.

---

<sup>1</sup> Software providers are listed in Section III.iii.

<sup>2</sup> GMV: [www.gmv.es](http://www.gmv.es)

The first discrepancy was easy to resolve using the prototype tool. By running a Structured Query Language (SQL) query on the result data held in the database, the coefficient values could be modified to use the projected area instead of a fixed reference area. This proved the effectiveness of the RDBMS solution as a means to quickly retrieve and analyse results data. As a result, the FMF Module contains many more SQL queries than the prototype to run post-processing analyses and calculations.

The second discrepancy highlighted the need to expand the database of inputs that could be looked-up automatically by the FMF Module. As described in Section 5.5.4, SEDAT can store multiple atmospheric models. All of these models can be accessed by the FMF Module, thereby eliminating the possibility of a similar error occurring.



**Figure 6-1 - TerraSAR-L**

**Image credit ESA.**

In addition to the TerraSAR-L results discrepancies, it was found that the prototype's ray-tracing algorithm, used for predicting areas of the body shielded to the flow, did not produce consistent results for some geometric shapes. This was found to be due to floating point errors, as well as incorrectly implemented intersection-object ordering and projection methods. It was also found that the bespoke ray-panel intersection method that had been developed was slower than other methods later discovered in published literature (as discussed in Section 6.3.2).

The SEDAT Ray-Tracer, described in Section 6.3, employs a comprehensive strategy to handle floating-point errors, which utilises a global variable to set the floating-point tolerance for the comparison of floating-point numbers. In addition, the SEDAT Ray-Tracer was developed using Object-Orientated Programming (OOP) methodologies, which enabled bugs and errors to be isolated quickly. Consequently, the SEDAT Ray-Tracer has been found to produce consistent results for all geometric shapes that have been tested. Furthermore, multiple strategies were employed to improve the performance of the SEDAT Ray-Tracer, including the use

of bounding-boxes, pre-processing of geometric quantities, and faster panel intersection routines.

The prototype not only provided many lessons, it also highlighted the inadequacy and inflexibility of the analysis method that had been implemented. For example, the prototype cannot calculate aerodynamic damping forces, model reflected flow, or facilitate the incorporation of multiple Gas-Surface Interaction Models (GSIMs).

The FMF Module addresses all of these inadequacies. It combines an innovative analysis method with a number of unique features to provide a flexible and user-friendly solution for the majority of free molecule flow analysis problems encountered during space flight. The remainder of this chapter is used to describe the FMF Module in more detail.

## **6.2 The Hybrid Method**

In 2004, during the course of this PhD, Borde, Renard, Sabbathier, and Drolshagen [60] developed a new spacecraft free-molecular flow analysis tool. Their new tool uses the RTP method described in Section 2.6.2, yet it can account for multiple gas-surface interactions (multiple reflections). The exact method it uses to do this has been difficult to determine from the published literature. However, the tool has been ratified by ESA, who have integrated it into their standard environmental analysis software suite (ESABASE).

Around the same time, and without knowledge of Borde et al's work, a similar method for accounting for multiple reflections using the RTP method was developed and later implemented in the FMF Module. This method, which was developed as part of the current study, is a hybrid of the RTP method and the TPMC method, described in Section 2.6.3.

This section describes the unique Hybrid method that has been developed to model the aerodynamic disturbances on spacecraft operating in the free molecular flow regime. In particular, it describes the two main features of the method: its ability to account for surface shielding and its ability to model reflected flow around complex bodies. At the end of this section, a comparison between the Hybrid method and others methods is also provided.

### **6.2.1 Overview**

The Hybrid method assumes that the free stream flow has a negligible component of thermal velocity, such that it can be simulated by a collimated beam of molecules. Therefore, it uses the RTP method to determine areas of the spacecraft that are shielded to the free stream flow and to calculate the aerodynamic coefficients

due to the direct impact of the free stream flow on each panel of the spacecraft surface mesh (or meshes) using analytical expressions.

Since the incident molecular flux to each panel due to the direct impact of the free stream flow is known, it then uses the TPMC method to simulate the reflected flux from each panel impacting subsequent panels.

The TPMC results are integrated over a unit time step and then added to the RTP results to derive total shear stress, pressure, heat transfer, and molecular flux values for each panel. Equations 2-27 and 2-28 are then used to derive the aerodynamic force and moment coefficients of the spacecraft.

### 6.2.2 Shielding

The RTP method, described in Section 2.6.2, is used to determine which spacecraft surfaces are shielded to the free stream flow or aft facing. The projection shadowing method implemented in the SEDAT Ray-Tracer, described in Section 6.3.5, is used to perform the shielding calculation. Aft facing surfaces are determined using Equation 2-26.

A concave spacecraft with a shape similar to some of the early drag deorbit device designs is illustrated in Figure 6-2. Indicated in the figure are regions of the spacecraft surface that are aft facing, regions that are directly impacted by the free stream flow, and a region that is shielded to the free stream flow.

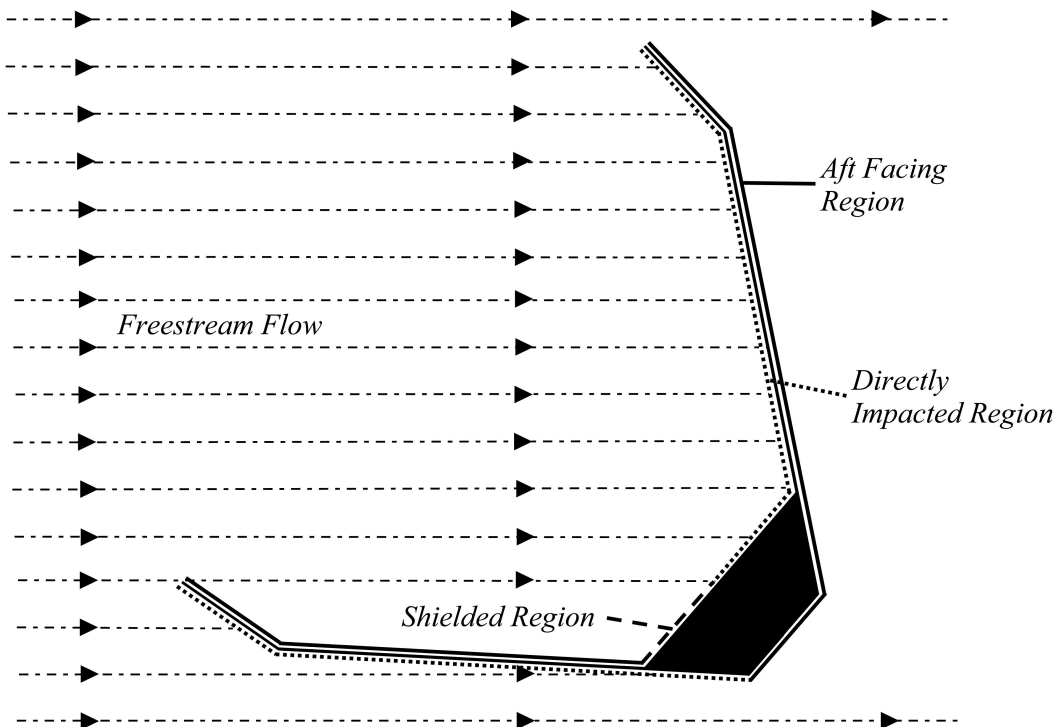
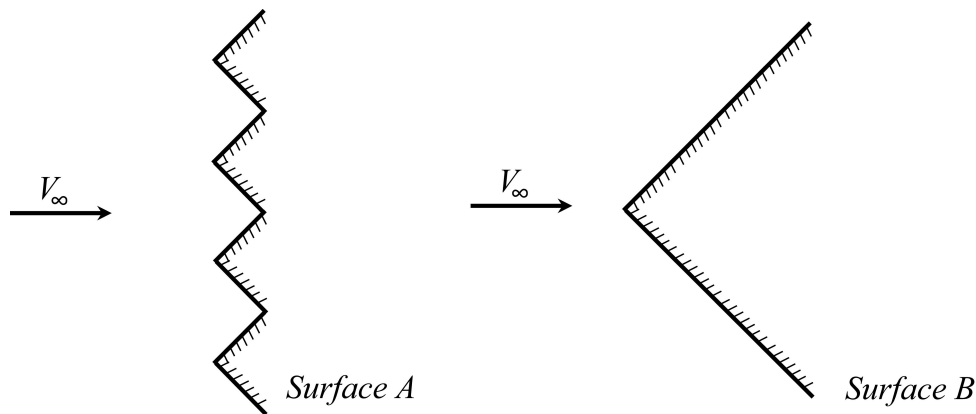


Figure 6-2 - Surface Shielding

### 6.2.3 Multiple Reflections

As described in Section 2.6.2, when gas flow is reemitted from a surface after impact it is said to be reflected. If the spacecraft surface is convex then the reflected flow is highly unlikely to impact another surface and will travel away from the spacecraft. However, if the spacecraft surface is concave then it is possible that some of the reflected flow could impact another part of the spacecraft surface. In this case, multiple reflections are said to have occurred.

The consequences of neglecting the effects of multiple reflections can be visualised with the help of Figure 6-3; the calculation of the force exerted on Surface A would yield the same result as the calculation of the force exerted on Surface B (assuming equivalent surface areas). Yet, in reality, the force exerted on Surface B would be less than the force exerted on Surface A because the surfaces of Surface A would be impacted by reflected flow in addition to free stream flow.



**Figure 6-3 - Apparent Similarity of Different Concave Surfaces when Reflected Flow is not considered**

Like the RTP method described in Section 2.6.2, the Hybrid method uses a Gas-Surface Interaction Model (GSIM) to calculate analytically the pressures and shear stresses exerted on a surface due to the direct impact of the free stream flow.

However, this analytical approach cannot account for the effects of multiple reflections because it is not possible to determine the dynamic pressure ( $q$ ) of the reflected flow that would be incident on a second surface. This is because dynamic pressure is a point property of the flow, which depends upon the phase space relationship between number density, volume, and flow velocity.

To model reflected free molecular flow it is necessary to consider the gas at particulate level. This is the approach employed by the TPMC method, outlined in Section 2.6.3.

The Hybrid method uses a slightly simplified version of TPMC to model the effects of reflected molecules. Instead of firing test-particles into a control volume,



the Hybrid method uses the RTP method to calculate the incident molecular flux to a panel. It then reemits the incident molecular flux as a series of test particles, or simulated molecules over a time period  $\Delta t$ . The Hybrid method for modelling reflected flow is illustrated in Figure 6-4.

The calculation of incident molecular flux and the nature of the reemitted flux (i.e. the number and characteristics of the simulated molecules) is determined by the GSIM chosen. Section 7.2, describes the Hybrid Schaaf and Chambre GSIM that has been pre-installed with the FMF Module, which incorporates a scattering kernel for reemitting simulated molecules.

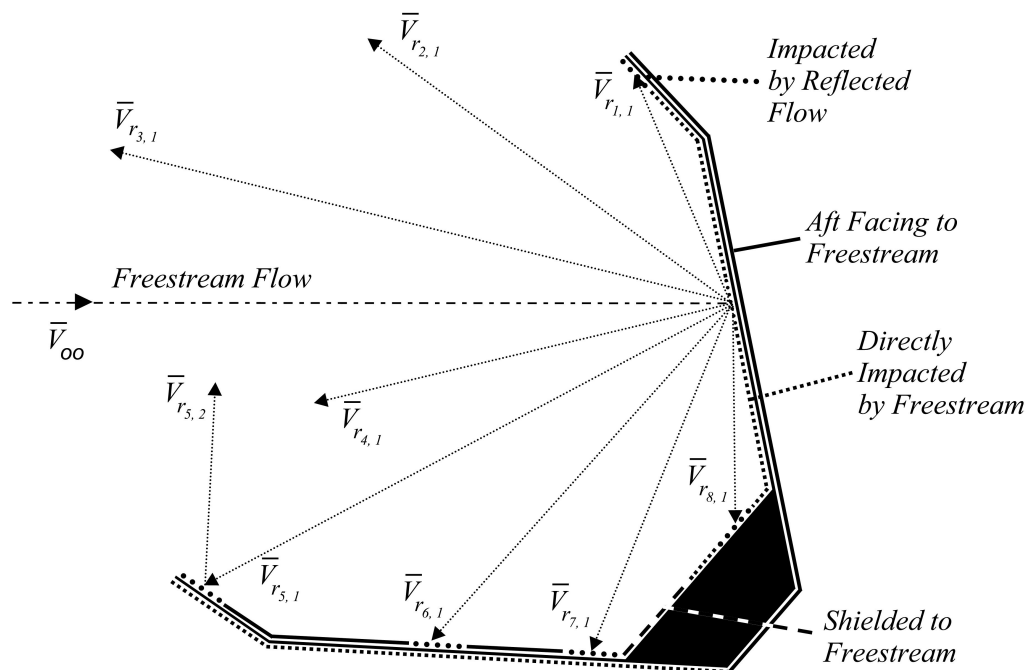


**Figure 6-4 - Modelling Reflected Flow using the Hybrid Method**

Indicated in the figure are regions of the spacecraft surface that are aft facing, regions that are directly impacted by the free stream flow, and a region that is shielded to the free stream flow.

In the example shown, eight simulated molecules (test particles) represent the reflected flow from a single panel. The fifth simulated molecule is also shown reflecting after a secondary gas-surface interaction.

The paths of the simulated molecules are traced using the “closest panel” procedure of the SEDAT Ray-Tracer, described in Section 6.3.4. If a simulated molecule impacts a second surface then it can be reemitted either as a single simulated molecule or as multiple new simulated molecules, depending on the GSIM chosen.

Various constraints can also be applied to determine when to stop the simulation of a particular test particle. For example, the simulation of test particles may be stopped after a certain number of reflections. More information about this

can be found in the *Step 9: Set-Up MAC (Model Analysis Configuration)* page of the SEDAT Help System, described in Section 5.7.

The momentum flux to each panel over the course of the simulation time step  $\Delta t$  can be summed to calculate the total momentum imparted to each panel. For convenience,  $\Delta t$  is set to one second; the total momentum flux then equals the total force imparted, assuming steady flow conditions.

A time step of one second seems reasonable given the typical size of a spacecraft and the very high velocities involved. For example, a gas molecule travelling at a speed ( $V$ ) of over  $100 \text{ m s}^{-1}$  would traverse the span ( $l_{ref}$ ) of the International Space Station (ISS) within one second and the molecules being simulated are travelling much faster than this ( $l_{ref}/V \ll 1$ ).

Once the total force imparted to the panels by the simulated molecules has been calculated, it is a simple matter to calculate the total pressures and shear stresses exerted on each panel due to the reflected flow using the chosen GSIM. Section 7.2.1 describes how the pressure and shear stress coefficients are calculated from the incident momentum fluxes of the simulated molecules using the Hybrid Schaaf and Chambre (H-SC) GSIM that has been pre-installed with the FMF Module.

Since the pressure and shear stress coefficients for both the free stream and reflected flow are normalised using the free stream dynamic pressure, Equations 2-27 and 2-28 can be used to calculate the total aerodynamic forces and moments exerted on the spacecraft.

#### **6.2.4 Surface Mesh Density**

Reflected test particles are reemitted from surface mesh panel centroids. Therefore, surface mesh density must be increased in concave regions that are prone to multiple reflections. In addition, as discussed in Section 2.6.2, surface mesh density must be increased in regions that are susceptible to shielding.

Consequently, iterative refinement of surface mesh density may be required to ensure consistent results. For the reasons outlined in Section 2.2.1, the maximum dimension of a single panel should also be less than approximately one hundredth of the size of the free stream mean free path.

#### **6.2.5 Comparison with Other Methods**

The Hybrid method combines the most useful feature of TPMC, its ability to model reflected gas molecules, with the simplicity, ease-of-use, and computation speed of the RTP method. For comparison purposes, Figure 2-16 is redrawn in Figure 6-5 with the Hybrid method inserted between the RTP and TPMC methods. The Computational Fluid Dynamics (CFD) method has been removed from the comparison diagram for the reasons outlined in Section 2.6.6.

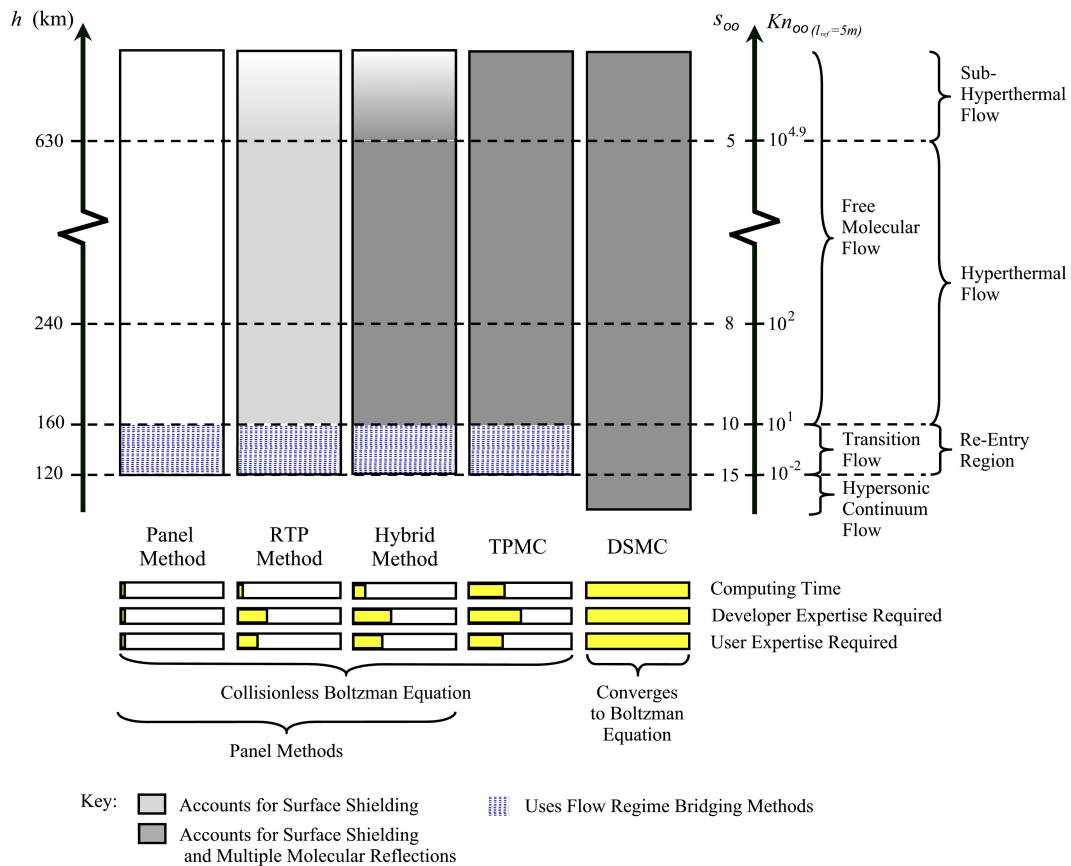


**Figure 6-5 - Comparison of the Hybrid Method with Existing Computational Approaches to Spacecraft Aerodynamics in Low Earth Orbit**

Assumes mean solar conditions (as defined by [18]) and a free stream Knudsen number ( $Kn_\infty$ ) based upon a spacecraft characteristic dimension of 5 m. The term  $h$  refers to Earth altitude and  $s_\infty$  refers to the free stream molecular speed ratio. The Computing Time, Developer Expertise Required, and User Expertise Required scales are based upon a qualitative survey of numerous rarefied gas dynamics texts (see, for example, [27]). They are provided as a “rule of thumb,” without quantitative explanations save those given throughout the thesis.

The advantages and disadvantages of the Hybrid method over the RTP and TPMC methods are listed in Table 6-1.

The main disadvantage of the Hybrid method is that it does not accurately represent sub-hyperthermal flow past a body that is prone to shielding. This is because in sub-hyperthermal flow the free stream flow has a non-negligible thermal velocity component, as described in Section 2.2.3, and cannot be accurately simulated by a collimated beam of molecules.

If the body is concave, but at the orientation being analysed surface shielding does not occur, then the Hybrid method can still be used in sub-hyperthermal flow. This is because the high thermal velocity component and corresponding low molecular speed ratio can be accounted for within the analytical GSIM (for further explanation of this see Section 3.2.3).

In addition, the air is more rarefied at higher altitudes. Therefore, aerodynamic forces are lower and less consequential in the sub-hyperthermal region (see Figure 2-1 for a comparison of the main environmental forces affecting a spacecraft). Therefore, although the Hybrid method is not as versatile as TPMC, it is appropriate for modelling the aerodynamics of the majority of low Earth orbit spaceflight scenarios in which aerodynamic disturbances may be considered significant.

**Table 6-1 - Advantages and Disadvantages of the Hybrid Method over the RTP and TPMC Methods**

Advantages	Disadvantages
<ul style="list-style-type: none"> <li>• Unlike RTP, it can model reflected gas flow.</li> <li>• It is slightly simpler to use than TPMC (only a surface mesh is required, rather than a surface mesh and simulation volume, and it requires fewer boundary conditions, since the flow direction can be described by a single vector).</li> <li>• Like RTP, it can model sub-hyperthermal flow around simple convex bodies, as described in Section 2.6.2 (all panels can be tested for gas-surface interactions not just forward facing unshielded panels).</li> <li>• Aspects of both RTP and TPMC can be turned on or off to optimise the calculation process for a given analysis scenario.</li> <li>• In theory, it should be faster than TPMC.</li> <li>• In theory, it should be as fast as RTP when performing computations using RTP functionality only.</li> <li>• It is slightly simpler to develop than TPMC.</li> </ul>	<ul style="list-style-type: none"> <li>• It does not simulate flow as realistically as TPMC (it assumes the free stream flow has negligible thermal velocity). Therefore, unlike TPMC, it does not accurately represent flow past a body that is prone to shielding in sub-hyperthermal flow (this is illustrated in Figure 6-5 by the faded-grey region at the top of the Hybrid method bar).</li> <li>• It is lightly more complex to develop than RTP.</li> <li>• It is lightly more complex to use than RTP.</li> </ul>

Furthermore, there are a wide variety of interplanetary missions for which the Hybrid method would provide accurate aerodynamic analysis results. For instance, it could be used to perform analyses of the aerobraking performance of spacecraft in hyperthermal flows.

### 6.3 The SEDAT Ray-Tracer

Ray-Tracing evolved during the 1960's with the arrival of high speed computing. Although it is used mainly by artists, animators, and computer game designers for graphics rendering, it is also a useful tool for scientists and engineers. Figure 6-6 illustrates one of the very first animated films to be rendered entirely using ray-tracing.



**Figure 6-6 - A Ray-Traced Scene from the 1986 Film Luxo Junior**  
Image credit Pixar Animation Studios<sup>1</sup>.

One of the core elements of the FMF Module's analysis method is the use of ray-tracing to determine areas of a spacecraft that are shielded to the free stream free molecular flow and to simulate reflected gas molecules.

In general terms, ray-tracing refers to the projection of rays into a scene to determine areas that are shadowed and to calculate the paths of rays as they are reflected from one entity and impact another. A ray is represented by two three-dimensional vectors, one corresponding to an origin and the other to a direction. An entity is any three-dimensional object that can be intersected by a ray. All of the rays and entities being considered at any given time comprise a scene. The terms shielding and shadowing are used interchangeably to describe the phenomenon that occurs when one entity is obscured from a ray by another entity.

The ray-tracer that has been developed is referred to as the SEDAT Ray-Tracer because the ray-tracing classes that have been written are polymorphic and could be used by any module within SEDAT. The Object-Orientated Programming (OOP) object model of the SEDAT Ray-Tracer is outlined in Section A2.2.3 of Appendix 2.

This section describes the fundamentals of ray-tracing, as well as the specific methods implemented by the SEDAT Ray-Tracer. It details the optimisation methods that have been implemented in the SEDAT Ray-Tracer as well as excerpts of pseudo-code to explain the computation process. Finally, it provides details of the computational performance of the SEDAT Ray-Tracer, and the performance enhancements that have been implemented.

---

<sup>1</sup> Pixar Animation Studios: [www.pixar.com](http://www.pixar.com)

### 6.3.1 Geometry-Dependent Panel Properties

The first step when ray-tracing is to determine the geometric characteristics of the entities in the ray-tracing scene. The ray-tracing method that has been implemented uses surface meshes containing triangular and coplanar quadrilateral panels to represent three-dimensional surfaces.

This section describes how to calculate the geometric properties of a triangular panel, as illustrated in Figure 6-7. The geometric properties of a coplanar quadrilateral panel can be found in a similar manner.

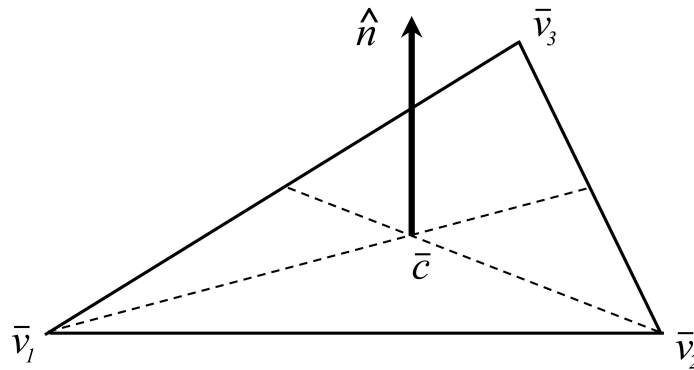


**Figure 6-7 - Triangular Panel Geometry**

Vertices are defined anti-clockwise.

The vectors  $\bar{v}_1$ ,  $\bar{v}_2$ , and  $\bar{v}_3$ , illustrated in Figure 6-7, represent the vertices of the panel. By inspection of the figure, the centroid  $\bar{c}$  of the panel can be found from Equation 6-1.

$$\bar{c} = \bar{v}_1 + \frac{2}{3} \left( \frac{1}{2} (\bar{v}_3 + \bar{v}_2) - \bar{v}_1 \right) \quad 6-1$$

Similarly, the unit normal  $\hat{n}$  of the panel can be found from Equation 6-2.

$$\hat{n} = \frac{(\bar{v}_2 - \bar{v}_1) \times (\bar{v}_3 - \bar{v}_1)}{|(\bar{v}_2 - \bar{v}_1) \times (\bar{v}_3 - \bar{v}_1)|} \quad 6-2$$

As before, the  $\times$  operator represents the vector cross product using a right-handed coordinate system.

By inspection of Figure 6-7, the area of the panel can be found from Equation 6-3.

$$A = \frac{1}{2} |(\bar{v}_2 - \bar{v}_1) \times (\bar{v}_3 - \bar{v}_1)| \quad 6-3$$

### 6.3.2 Intersecting a Ray and a Panel

The most computationally expensive aspect of ray-tracing is determining whether or not a ray intersects an entity in a scene. This section presents the methods that have been employed to determine whether or not a ray intersects a triangular panel. The methods presented are also applicable to a coplanar quadrilateral panel composed of two triangular panels.

The first step is to determine whether or not the ray intersects the panel's plane. To do this it is necessary to combine the equation for a plane with a parametric equation for a line. The equation for a plane is given by Equation 6-4.

$$ax + by + cz + d = 0 \quad 6-4$$

The terms  $a$ ,  $b$ ,  $c$ , and  $d$  are constants for a given plane. The three coefficients  $a$ ,  $b$ , and  $c$  are equivalent to the  $x$ ,  $y$ , and  $z$  components respectively of the plane's unit normal (the plane's unit normal is equivalent to the panel's unit normal provided by Equation 6-2). The constant  $d$  can be found by substituting the values of  $a$ ,  $b$ , and  $c$  back into Equation 6-4 and solving for some arbitrary point on the plane (for example, a panel vertex).

Figure 6-8 illustrates the parametric equation of a ray.

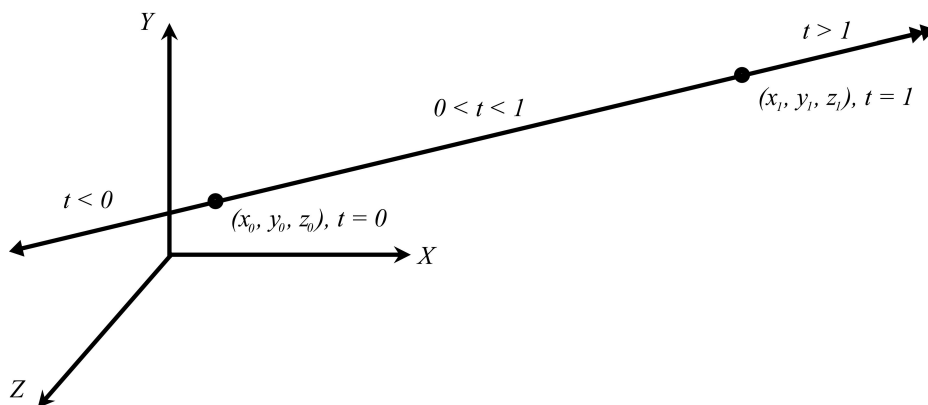


**Figure 6-8 - The Parametric Equation of a Ray**

From inspection of Figure 6-8, the parametric equation of a ray is provided by Equation 6-5.

$$\begin{aligned} x &= x_0 + t\hat{x}_{01} \\ y &= y_0 + t\hat{y}_{01} \\ z &= z_0 + t\hat{z}_{01} \end{aligned} \quad 6-5$$

The term  $t$  is the parameter that is being solved for, and the terms  $\hat{x}_{01}$ ,  $\hat{y}_{01}$ , and  $\hat{z}_{01}$  represent the normalised components of the ray's direction vector.

Substituting the parametric equation for the ray, Equation 6-5, into the equation for a plane, Equation 6-4, and solving for  $t$  results in Equation 6-6.

$$t = -\frac{ax_0 + by_0 + cz_0 + d}{a\hat{x}_{01} + b\hat{y}_{01} + c\hat{z}_{01}} \quad 6-6$$

From a computational viewpoint, it is worth noting that apart from the plane equation constant  $d$ , the terms in Equation 6-6 are the result of two vector dot products; in the numerator between the panel unit normal and the origin of the ray, and in the denominator between the panel unit normal and the direction of the ray.

If the denominator of Equation 6-6 is zero, then the ray is parallel to the plane. If  $t$  is less than zero then the panel is behind the origin of the ray.

If  $t$  is greater than zero then the ray intersects the plane. In this case, substituting the value of  $t$  back into Equation 6-5 will provide the point of intersection between the ray and the plane. All that remains is to determine whether the point of intersection lies within the panel's area.

There are several ways to determine whether the point of intersection lies within the panel's area. The three methods that have been implemented within the panel classes of the SEDAT Ray-Tracer are listed in Table 6-2.

**Table 6-2 - Panel Intersection Calculation Methods**

Method	Description	SEDAT Ray-Tracer Performance (time per million intersections in seconds)	Reference
Sum Of Angles	Uses the fact that the sum of angles from a point in a polygon to the polygon's vertices is $360^\circ$ . Mathematically, this is the simplest method, but computationally it is the slowest.	62	[103]
Scaling	Compares the polygon produced by the intersection point and one of the panel's vertices with the panel's polygon.	51	
Projection Transformation	The polygonal panel surface is projected and transformed into two-dimensional space and then tested for intersections. Mathematically, this is the most complex method, but computationally it is the quickest.	41	[104]

The simplest way of calculating whether or not an intersection point is inside a triangular panel's area is the sum of angles method, illustrated in Figure 6-9.



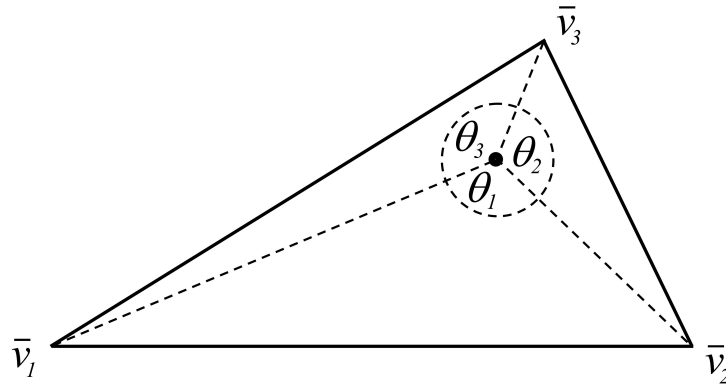


**Figure 6-9 - The Panel Intersection Sum of Angles Calculation Method**

The vectors  $\bar{v}_1$ ,  $\bar{v}_2$ , and  $\bar{v}_3$ , illustrated in Figure 6-9, represent the vertices of the panel. As the figure indicates, if the three angles,  $\theta_1$ ,  $\theta_2$ , and  $\theta_3$  sum to  $360^\circ$  and none of them is greater than  $180^\circ$  then the intersection point lies within the triangular panel's boundaries.

The scaling method listed in Table 6-2 was originally developed as part of this PhD for the prototype tool described in Section 6.1. The geometry of the scaling method is illustrated in Figure 6-10.

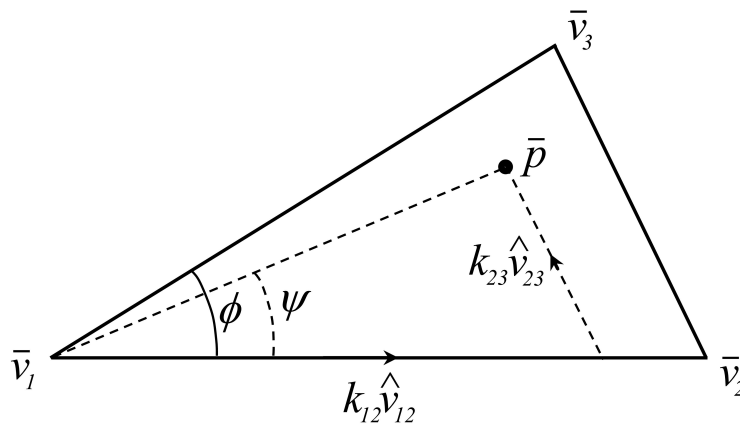


**Figure 6-10 - The Panel Intersection Scaling Calculation Method**

The vectors  $\hat{v}_{12}$  and  $\hat{v}_{23}$  illustrated in Figure 6-10 represent the unit vector directions from vertices one to two and two to three respectively. An expression for the point of intersection  $\bar{p}$  in terms of the products  $k_{12}\hat{v}_{12}$  and  $k_{23}\hat{v}_{23}$  and the vertex coordinate vector  $\bar{v}_1$  can be derived from inspection of Figure 6-10. This expression, which represents a set of three simultaneous equations with two unknowns ( $k_{12}$  and  $k_{23}$ ) in three-dimensional space, is provided as Equation 6-7.

$$\bar{p} = \bar{v}_1 + k_{12}\hat{v}_{12} + k_{23}\hat{v}_{23} \tag{6-7}$$

The point of intersection lies inside the triangular panel's boundaries only if the parameters  $k_{12}$  and  $k_{23}$  are both less than or equal to one, the angle  $\psi$  is less than or equal to  $\phi$ , and all three quantities are greater than or equal to zero, as described by Inequalities 6-8.

$$0 \leq k_{12} \leq 1$$

$$0 \leq k_{23} \leq 1$$

$$0 \leq \psi \leq \phi$$

6-8

Solving Equation 6-7 for  $k_{12}$  and  $k_{23}$  may result in division by zero errors. In this case, the computation will need to be repeated using one of the remaining two vertices  $\bar{v}_2$  or  $\bar{v}_3$  as the starting point.

The scaling method is faster than the sum of angles method because it only requires two angles to be calculated, rather than three. However, in practice, in both methods, only the cosines of the angles, represented by the dot products of the unit direction vectors that form each angle, need to be calculated to perform the required inequality tests.

The final method listed in Table 6-2 was discovered whilst researching optimised ray-tracing methods amongst graphics programming literature for the SEDAT Ray-Tracer. The projection transformation method is a multi-step process, which, despite requiring many more executable lines of code than the other two methods, is very efficient. It is explained in detail by Heiny [104], using several pages of diagrams, pseudo-code, and actual C++ programming code. Therefore, for brevity, it is not described here.

The results of performance tests using the SEDAT Ray-Tracer are indicated in Table 6-2. Based on the results of these tests, the default method used for performing panel intersection calculations in the SEDAT Ray-Tracer is Heiny's projection transformation method.

### 6.3.3 Bounding Boxes

The greatest improvements in ray-tracing computation speed come from reducing the number of intersection calculations that need to be performed. Various methods can be employed to do this. This section outlines the method that has been implemented in the SEDAT Ray-Tracer, which uses bounding boxes (or bounding volumes).

A bounding box is a three-dimensional volume that encloses a number of entities and has its sides aligned parallel to the coordinate system axes. If a ray does not intersect a bounding box, it does not intersect any of the entities that the bounding box encloses. In this case, all of the entities within that bounding box can be skipped saving considerable processing time.

The only multi-component entities implemented in the SEDAT Ray-Tracer are surface meshes. The coordinates of the vertices of a surface mesh's bounding box are easily determined by comparing the maximum and minimum Cartesian values of each vertex of each panel in the surface mesh (i.e.  $x_{min}$ ,  $x_{max}$ ,  $y_{min}$ ,  $y_{max}$ ,  $z_{min}$ ,  $z_{max}$ ).

Figure 6-11 illustrates bounding boxes for each of three surface meshes in a model, as well as the bounding box for the model itself. The ray in Figure 6-11 misses the bounding boxes for surface meshes A and B. Therefore, only the panels of surface mesh C need to be tested for intersections.

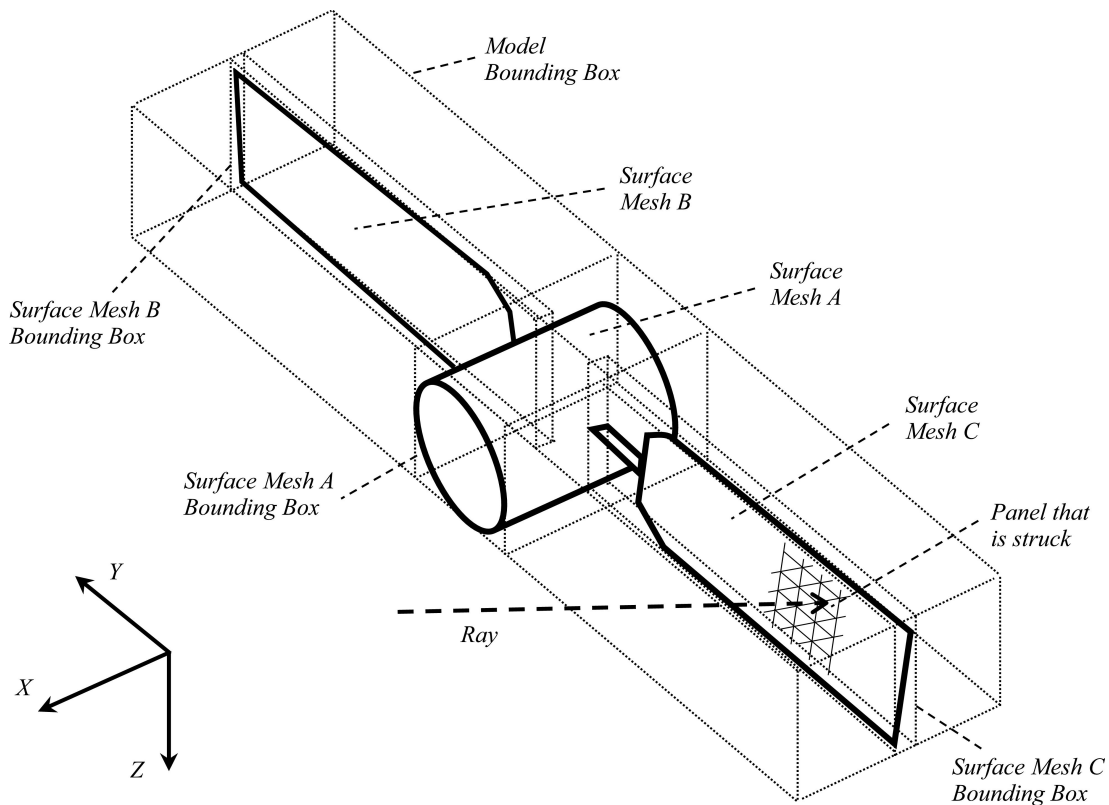


**Figure 6-11 - Bounding Boxes**

The bounding boxes are illustrated by dotted lines.

To determine whether or not a ray intersects a bounding box all that is necessary is to test whether or not the ray intersects any of the bounding box's sides. Because the bounding box's sides are parallel to the coordinate system axes, this process is relatively simple and computationally very fast.

If the ray's direction is parallel to one of the coordinate system axes, then it is straightforward to test whether or not the ray intersects the sides that are aligned with the remaining two axes. For example, if the ray's direction is parallel to the  $x$ -axis, then the ray will only intersect the bounding box if the  $y$  and  $z$  components of the ray's origin lie between the minimum and maximum  $y$  and  $z$  planes of the bounding box.

If the ray's direction is not parallel to one of the coordinate system axes, Equations 6-5 and 6-6 can be used to determine the point of intersection between the ray and each of the planes that extend from the box's sides. The coordinates of each intersection point can then be compared with the coordinates of the bounding box's vertices to determine whether or not the ray intersects any of the sides.

The SEDAT Ray-Tracer implements an optimised calculation routine presented by Heiny [104] that utilises these methods.

The performance gains that can be achieved by using bounding boxes are significant. For example, to determine whether or not each panel in a 30,000 panel surface mesh is shadowed would require up to  $30,000 \times 29,999 = 899,970,000$  intersection calculations to be performed (see Section 6.3.5 for a detailed description of shadowing). Sub-dividing this surface mesh into two smaller surface meshes of 15,000 panels each, and using bounding boxes, would significantly reduce the likely maximum number of intersection calculations required. This is because 15,000 possible intersections can be eliminated simply by checking to see if the shadow feeler ray intersects the bounding box of the other surface mesh.

In general, the greater the number of smaller surface meshes a large surface mesh is divided into the better the performance gain. Therefore, it would be advisable to divide a large surface mesh into a number of smaller surface meshes along and across planes of symmetry, and at junctions between major parts. For example, given a surface mesh representation of the Space Shuttle, the engine nacelles and tail plane could be represented by separate surfaces meshes and the wing-body fuselage could be split along its length into port and starboard sections and then segmented into smaller sections from front to rear.

Besides the use of bounding boxes, there are a small number of more advanced methods for reducing the number of intersection calculations that need to be performed. Three common examples that are applicable to the shadowing or "visible surface" types of ray-tracing problem encountered in this study, include [103] [105]:

- Improved bounding volume definition (calculating bounding volume shapes that more closely match the outlines of the enclosed entities).
- Nested entity hierarchy partitioning (partitioning entities into multiple smaller entities within a hierarchical structure, so that each branch of the hierarchy can be recursively checked for intersections).
- Spatial partitioning (partitioning the scene into multiple sections within a hierarchical structure, so that each branch of the hierarchy can be recursively checked for intersections).

These methods are more complex than the bounding box method and may not necessarily provide any greater performance gain (so long as large surface meshes are subdivided into a reasonable number of smaller logically arranged surface meshes). Therefore, due to time constraints, they have not been investigated further.

### 6.3.4 Finding the Closest Panel

One objective of ray-tracing is to determine whether or not a ray intersects a panel and, if it does, whether or not that panel is the closest to the origin of the ray. For example, one of the requirements of the FMF Module is to determine whether or not reflected gas molecules, represented by test particles carried by gas flow rays, impact other panels, as described in Section 6.2.3.

Figure 6-12 illustrates the geometry of the situation.

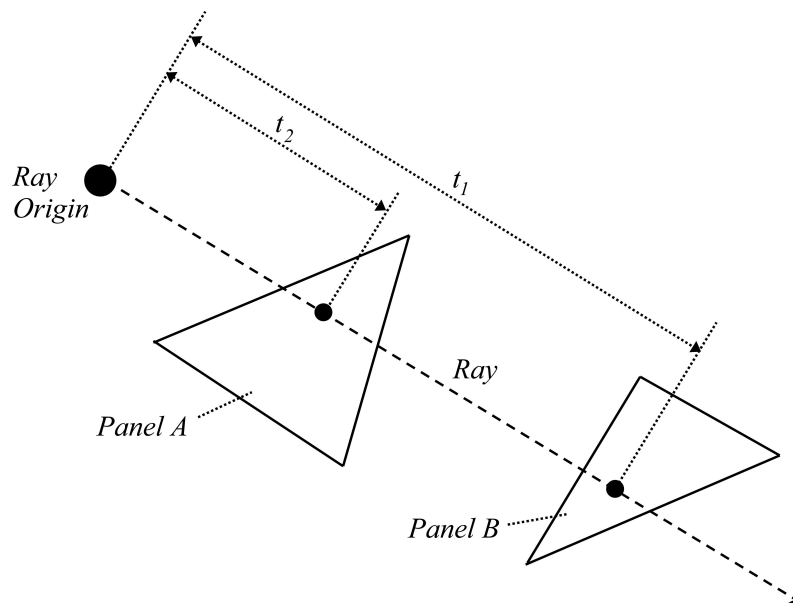


**Figure 6-12 - Finding the Closest Panel**

**The Ray intersects the front of both panels. However, Panel A is the closest to the Ray Origin because  $t_2 < t_1$ . Where the parametric  $t$  values are calculated using Equation 6-6.**

If a ray is found to intersect two panels A and B, then the closest panel can be determined by examining the value of  $t$ , calculated using Equation 6-6, for each panel intersection. In the example shown in Figure 6-12,  $t_2 < t_1$  and  $t_2 > 0$ , therefore, panel A is the closest intersected panel.

The pseudo-code for determining the nearest intersecting panel, which uses bounding boxes for optimisation, is provided in Figure 6-13. If the ray does not intersect any panels in any of the surface meshes then an empty object pointer (i.e. *Nothing*) is returned.

```

tMax = Double.MaxValue
For Each Surface Mesh
    If Ray intersects Bounding Box Then
        For Each Panel of Surface Mesh
            Calculate t for Panel (using pseudo-code in Figure 6-14)
            If t > 0 And t < tMax Then
                tMax = t
                ClosestPanel = Panel
            End If
        Next Panel
    End If
Next Surface Mesh
Return ClosestPanel

```

**Figure 6-13 - Pseudo-Code to Find the Closest Panel**

The pseudo-code to calculate the value of  $t$  for the intersection between a ray and a panel, based on the methods outlined in Section 6.3.2, is provided in Figure 6-14.

```

Calculate t for the intersection of the Ray with the Panel's plane (Equation 6-6)
If t = 0 Then
    ‘ Ray is parallel to the Panel
    Return 0
Elseif t < 0 Then
    ‘ Ray is approaching from behind the Panel
    Return -1
End If
Test to see if the intersection point lies inside the Panel's area using the projection
transformation method outlined in Section 6.3.2
If Panel is intersected Then
    Return t
Else
    Return -1
End If

```

**Figure 6-14 - Pseudo-Code to Calculate  $t$  for a Panel**

### 6.3.5 Shadowing

One of the most powerful features of ray-tracing is that it can be used to determine whether or not one entity or part of an entity is shadowed by another entity or part of an entity. Two types of shadowing have been implemented in the SEDAT Ray-Tracer:

1. Projection Shadowing
2. Line-of-Sight Shadowing

The projection shadowing method is used by the FMF Module to determine which panels are shielded to the free stream gas flow, as described in Section 6.2.2. It assumes that every panel may be struck by a ray travelling parallel to the principal ray, regardless of the origin of the principal ray.

To determine whether or not a particular test panel is shadowed, a Shadow Feeler Ray (SFR) is projected from the centroid of the test panel in the opposite direction to the principal ray and tested for intersection with all other panels. If an intersection is found then the test panel is shadowed. Figure 6-15 illustrates the geometry of the situation.

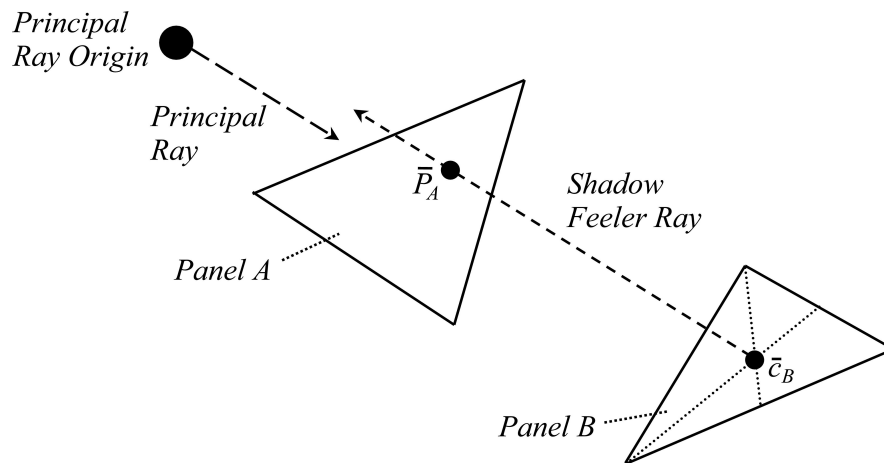


**Figure 6-15 - Geometry of Projection Shadowing**

The *Shadow Feeler Ray* is projected from the centroid of the *Test Panel*, in this case *Panel B*, in the opposite direction to the *Ray* and tested for intersection with all other panels. In this case, the *Shadow Feeler Ray* intersects *Panel A* at point  $\bar{P}_A$ . Therefore, *Panel A* shadows *Panel B*.

The line-of-sight shadowing method is illustrated in Figure 6-16.

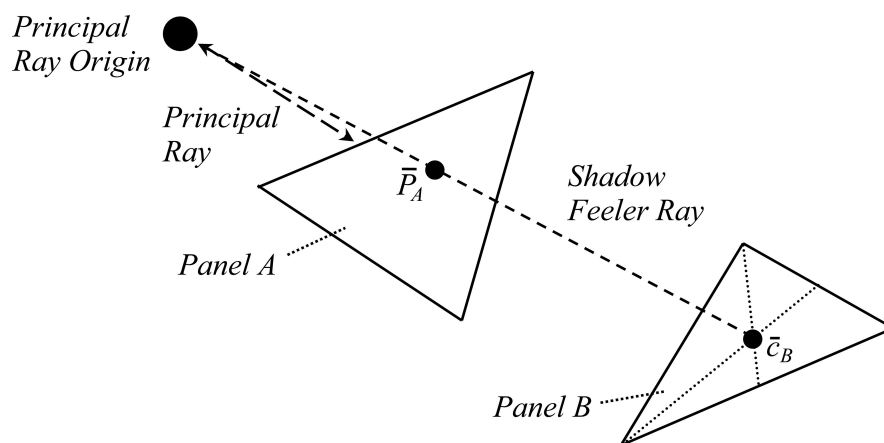


**Figure 6-16 - Geometry of Line-of-Sight Shadowing**

The *Shadow Feeler Ray* is projected from the centroid of the *Test Panel*, in this case *Panel B*, along a vector towards the *Ray Origin* and tested for intersection with all other panels. In this case, the *Shadow Feeler Ray* intersects *Panel A* at point  $\bar{P}_A$ . Therefore, *Panel A* shadows *Panel B*.

The line-of-sight shadowing method, illustrated in Figure 6-16, assumes that every panel may be struck by a ray travelling from the origin of the principal ray to the panel centroid, regardless of the direction of the principal ray. This is the method used by graphics rendering programs to simulate a point source of light and by the FMF Module to determine which panels are impacted by reflected flow.

To determine whether or not a particular test panel is shadowed using the line-of-sight method, a SFR is projected from the centroid of the test panel along a vector towards the principal ray's origin and tested for intersection with all other panels. If an intersection is found then the test panel is shadowed.

Whichever method of shadowing is used, the process for determining whether or not a panel is shadowed is the same. Figure 6-17 provides the pseudo-code to determine which panels in a collection of surface meshes are shadowed, using bounding boxes for optimisation.

```

For Each Test Surface Mesh
  For Each Test Panel of Test Surface Mesh
    Calculate SFR for Test Panel
    For Each Surface Mesh
      If SFR intersects Bounding Box Then
        For Each Panel of Surface Mesh
          If Panel is not Test Panel AndAlso _
            SFR intersects Panel Then
              Test Panel is shadowed
              Go To Continue
          End If
        Next Panel
      End If
    Next Surface Mesh
    Continue:
  Next Test Panel
Next Test Surface Mesh

```

**Figure 6-17 - Pseudo-Code to Determine which Panels are Shadowed**

*SFR* denotes *Shadow Feeler Ray*.

Both types of shadowing rely upon appropriate surface meshing. If a surface mesh region is prone to shadowing, it should be represented by a high density of panels to achieve the desired shadowing contours. Areas less prone to shadowing can be modelled using a coarser surface mesh.

### 6.3.6 Computational Performance

Tests using SEDAT's ray-tracer have shown that calculating and storing panel, surface mesh, and bounding box geometric properties prior to ray-tracing, reduces computation time by up to a factor of twenty. For this reason, the



programmatic objects and classes that represent ray-tracing entities have a common interface that exposes a refresh subroutine, to refresh the geometry-dependent properties of each entity.

For example, after a surface mesh is transformed then rotated, the refresh subroutine can be called to calculate and store the bounding box coordinates of the surface mesh, as well as, among other things, the unit normal, centroid, and area of each panel. Then, during ray-tracing, the stored geometric properties can be accessed instead of having to recalculate them with every call.

In addition to pre-processing geometric quantities, numerous other steps have been taken to improve computational performance. Most of these have involved optimising the code for the functions being performed. Therefore, very few of the equations presented in this section have been used in the exact form presented.

A number of ray-tracing computations require real numbers to be compared. All real numbers are represented in the SEDAT Ray-Tracer using the Microsoft .Net signed 64-bit double-precision floating-point type Double. Tests using the SEDAT Ray-Tracer indicate that a tolerance of  $1 \times 10^{-15}$  can be achieved to compensate for floating-point imprecision. This value is used as the default global tolerance of the SEDAT Ray-Tracer.

When running an analysis using the FMF Module, the user is given the option to increase the ray-tracing tolerance. This option is explained in the *Step 14: Run Analysis* page of the SEDAT Help System, described in Section 5.7.

## 6.4 Implementation

The Hybrid method, described in Section 6.2, combines aspects of various free molecular flow calculation methods to enable the analysis of a wide range of scenarios. It can be used to carry out quick and simple analyses of simple spacecraft shapes, but it can also be used to perform hi-fidelity analyses of complex geometries with a diverse variety of free stream and surface conditions.

To take advantage of the Hybrid method's versatility and meet the objectives outlined in Section 1.4, the FMF Module has been designed to maximise the number of analysis options available using the method. The full range of options is described in Sections 6.4.3 and 6.4.4, which outline the analysis set-up process using either the FMF Module GUI or a programming interface, respectively. The analysis process itself is described in Section 6.4.5.

However, before attempting to describe the analysis set-up process and the analysis process, it is first necessary to describe the main elements of the FMF Module. In keeping with the SEDAT architecture outlined in Section 5.3, the FMF Module comprises two major parts: a database and a client.

The database, which stores all of the data associated with the FMF Module, is described in Section 6.4.1. The client, which provides both a user interface and a set of processing components, is described in Section 6.4.2.

### 6.4.1 Database

The FMF Module's fifty-two database tables represent a separate module in the SEDAT Database, as illustrated in Figure 5-3. Many of the tables are linked to tables of core modules. This arrangement conforms to the design principles outlined in Section 5.5.1.

The relationships between all the SEDAT Database tables (the database schema), including the FMF Module's tables, are described in Section 5.5.2 via reference to a digital version of the schema, which is provided in the *Database Schema* folder in Appendix 1.

High-level explanations of some of the table relationships of core modules are explained in Section 5.5.4. The explanations are deliberately abstract. However, to use such an approach to explain every table and relationship of the FMF Module would be repetitive and not very useful.

Instead, the reader is referred to the *Analysis Process* page of the SEDAT Help System, described in Section 5.7. This page and its associated help pages provide detailed descriptions of every table of the FMF Module as they relate to the analysis set-up process and analysis process itself. They also include practical explanations of every table field (including data type and units), and how to insert, delete, update, and view the data of every table. Individual tables can be searched for using the Help System's built-in search functionality.

To assist with navigating the Help System and the database schema, Section A2.1 in Appendix 2 lists every table of the FMF Module with a high-level description.

Further information about the database design, as it relates to the key features of the module, can be found in Section 6.5.

### 6.4.2 Client

The client is composed of multiple components<sup>1</sup> that fit into the two-tier client architecture of SEDAT, which is illustrated in Figure 5-2. The different components were developed to retrieve, process, and present information to meet the specific requirements of the FMF Module.

---

<sup>1</sup> In this context, a component refers to both a collection of code and, in some cases, one or more XML schemas (an XML schema is an XML representation of a data structure).

The re-use of module components is one of the key principles of the SEDAT Concept, as outlined in Section 5.1. Therefore, all of the components can be used by other modules within SEDAT. This is possible in part because, in keeping with the programming strategy outlined in Section 0, the components were developed using Object-Orientated Programming (OOP) methodologies.

Section 5.1 also describes how the database has been designed using object-orientated principles and indicates some of the advantages of this approach. One advantage is that, to a certain extent, the database design matches the object model of the client. To demonstrate this, Section A2.2.7 of Appendix 2 compares the GSIM table relationships of the FMF Module with the corresponding classes of the FMF Module's client object model.

A further benefit of using OOP is that third party systems can more easily interact with the FMF Module's components via programmatic interfaces. For example, Section 6.4.4 describes how the components of the FMF Module client can be used by third party systems to perform free molecular flow aerodynamic analyses.

Section A2.2 of Appendix 2 explains the FMF Module's object model in detail and provides descriptions of the main classes of the module.

The FMF Module also uses generic code that was written to fulfil some common functions within the SEDAT Client. The namespaces used by the module include *Aurora.Error*, *Aurora.Utilities*, *Aurora.Graphics*, *Aurora.Engineering*, *Maths*. For example, the features associated with the *Aurora.Error* and *Aurora.Graphics* namespaces, which are listed in Table 5-1, are used by the FMF Module to handle errors and display three-dimensional graphics, respectively.

### 6.4.3 Analysis Set-Up via GUI

Once the SEDAT software system has been installed (see Section 5.9 for information regarding installation), a user can set-up numerous analyses for a single spacecraft using the GUI components of the FMF Module's client by following a series of both mandatory and optional steps.

The *Analysis Process* page of the SEDAT Help System, described in Section 5.7, provides an overview of the analysis set-up process, with links to help pages describing each step.

The analysis input parameters and other options are all stored in the FMF Module's database tables. Once all the analysis set-up steps have been completed, the user can perform an analysis. The results of the analysis are also stored in the FMF Module's database tables for post-processing and reporting.

As described in Section 6.5.7, multiple distributed computers can be used to speed up the processing of complex analyses.

#### 6.4.4 Analysis Set-Up via an Interface

It is possible to by-pass the SEDAT Client and access the FMF Module's processing components directly via an interface. This is useful if using a third party software system. For example, to perform real-time analysis of a spacecraft during Phase D simulation testing (for example, using a so-called virtual spacecraft test bed composed of both hardware and software in the loop [106]). Although this is not in keeping with the SEDAT Concept, it is useful to engineers wishing to utilise the FMF Module's code in other programs.

To demonstrate the simplicity and usefulness of interfacing with the FMF Module's components, Appendix 3 provides a detailed example of how to run an FMF analysis of a spacecraft from within Microsoft Excel<sup>1</sup>.

#### 6.4.5 Analysis Process

Once an analysis has been set-up, it can be processed using the *Analyse* subroutine of the analysis class described in Section A2.2.6 of Appendix 2.

The *Step 14: Run Analysis* page of the SEDAT Help System, described in Section 5.7, explains how to process an analysis using the FMF Module's client. In the case of the interface example provided in Section 6.4.4, the *Analyse* subroutine is called by the line containing the code '*myAnalysis.Analyse()*' in Figure A3-2.

If the FMF Module's client is used to set-up an analysis then the input data will be validated prior to processing. Any errors in the input data will be identified and detailed help will be provided to resolve the errors and correct the input data.

If an interface is used to set-up an analysis then the input data is not validated prior to processing. In this case, errors will be handed by the internal error-handling functionality of individual processing components. However, some systematic input data errors may not be caught.

This behaviour is by design. It has been implemented because it places fewer restrictions on an individual component's input data, thereby increasing the abstraction and flexibility of components. This, in turn, ensures that the analysis process can support the widest range of possible inputs and configurations.

The program flow for the analysis process is shown in Figure 6-18. As illustrated in the figure, the ray-tracing methods described in Section 6.3 are used to determine the render state of each panel of each surface mesh. In particular, the projection-shadowing method described in Section 6.3.5 is used to determine if a particular panel is shielded to the free stream gas flow ray. Depending on the exact configuration of the analysis, each forward facing unshielded panel will follow the impact procedure illustrated in Figure 6-19.

---

<sup>1</sup> Software providers are listed in Section III.iii

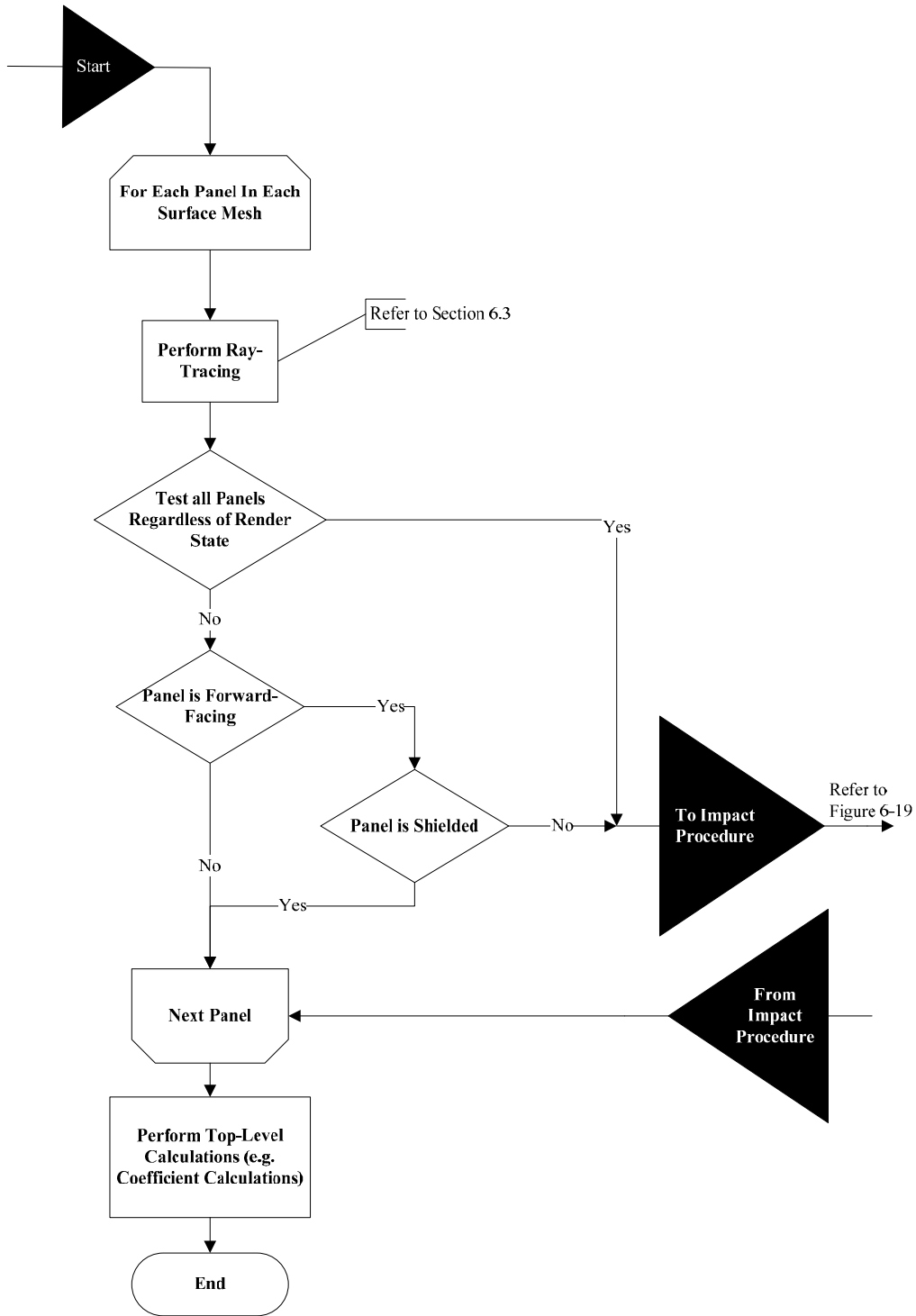


**Figure 6-18 - Analysis Program Flow**

When an impact occurs between a gas flow ray and a panel, an impact object is generated and an impact event is raised. The classes used to represent a gas flow ray and a panel are described in Section A2.2.6. The class used to represent an impact is described in Section of A2.2.7.

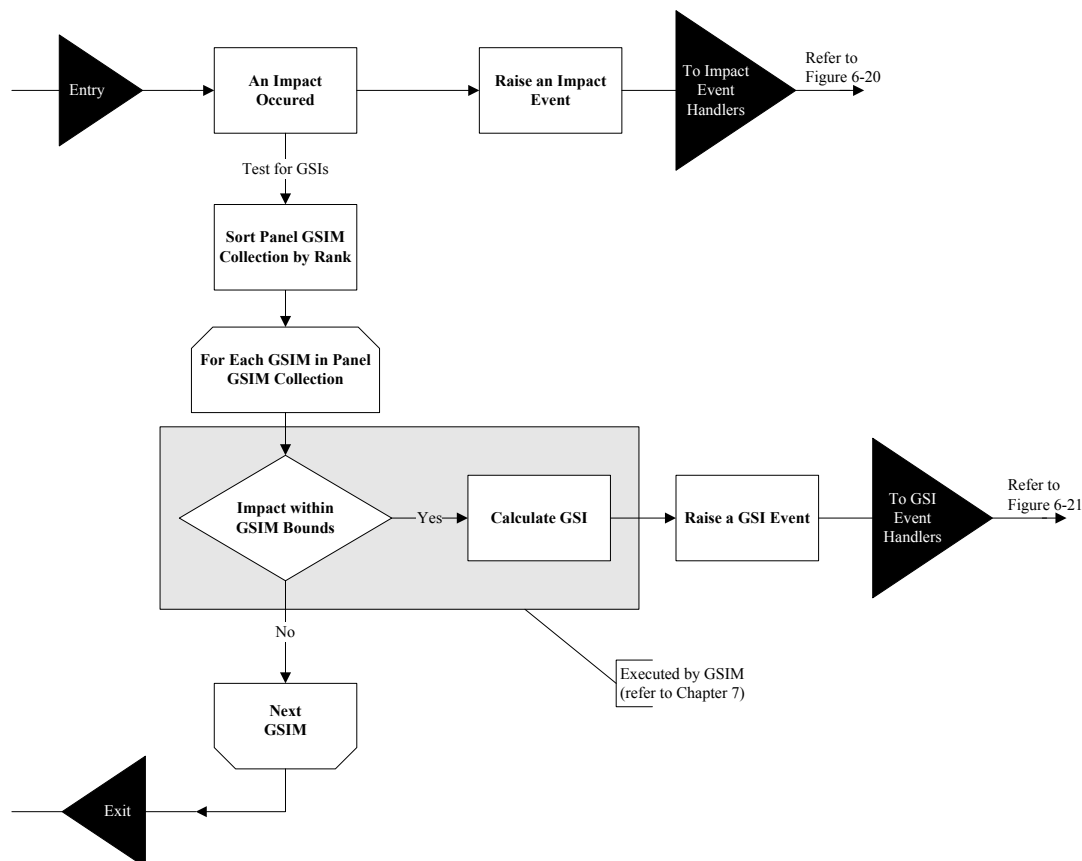


**Figure 6-19 - Impact Procedure**

As illustrated in Figure 6-19, when an impact occurs, the panel is tested for Gas-Surface Interactions (GSIs). The Gas-Surface Interaction Models (GSIMs) associated with each panel can be sorted according to a user-defined rank (GSIMs that can be used with the Hybrid method are described in more detail in Chapter 1). Each GSIM in the panel's GSIM collection is passed the impact object as an input parameter.

If the impact's gas-surface interaction variables lie within a GSIM's bounds then a GSI occurs. For example, if the molecular kinetic energy ( $e_{k.e}$ ) of the gas lies between the upper and lower bounds associated with the empirical data of the GSIM, then the GSIM can be used to handle the GSI. In this case, a GSI object is created and a GSI event is raised. The class that represents a GSI object is described in Section A2.2.7.

If the impact does not lie within the GSIM's bounds then the next highest ranking GSIM is checked. If the impact does not fall within the bounds of any GSIM then no GSI occurs.

The impact event is handled by the impact handlers illustrated in Figure 6-20.

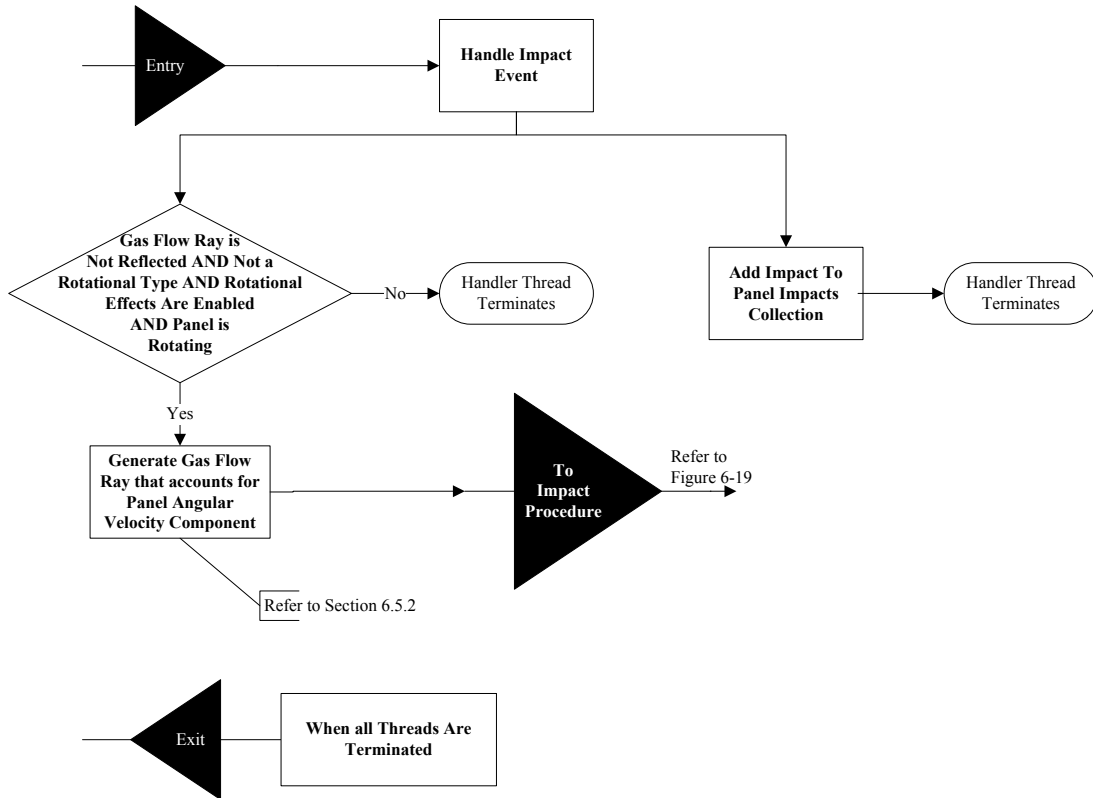


**Figure 6-20 - Impact Event Handlers**

One of the impact event handlers illustrated in Figure 6-20 adds the impact to the panel’s impact collection. The other is used to account for the effect of a panel’s angular velocity to assist with calculating aerodynamic damping forces, as described in Section 6.5.2.

If the analysis is set-up to account for rotational effects then the handler will be invoked so long as the incident gas flow ray represents the free stream flow (i.e. the impact is a primary impact), the incident gas flow ray is not reflected, and the panel has an angular velocity.

In this case, a new incident gas flow ray is generated that accounts for both the free stream flow velocity and the angular velocity of the panel, using the method outlined in Section 6.5.2. This new gas flow ray is passed to the impact procedure illustrated in Figure 6-19, where it is handled like a regular free stream gas flow ray.

At the end of processing, each panel will have results relating to the original free stream gas flow ray and results that relate to the gas flow ray that accounts for both the free stream flow velocity and the panel’s angular velocity component. These two different types of gas flow ray are used because comparing the two sets of results provides insight into the effects of a spacecraft’s angular velocity components.

The GSI handlers invoked by a GSI event in the impact procedure illustrated in Figure 6-19 are shown in Figure 6-21.

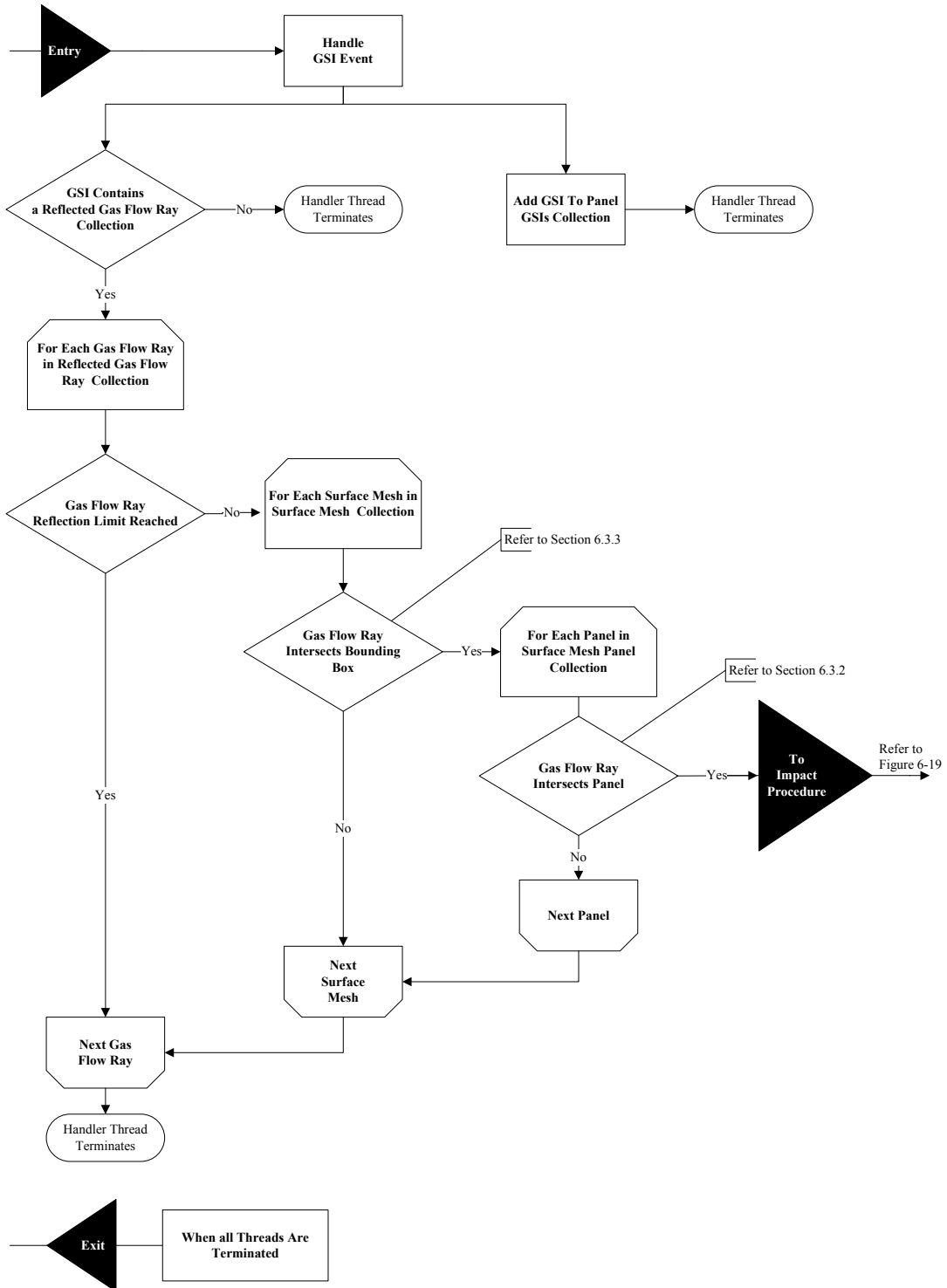


**Figure 6-21 - Gas-Surface Interaction Event Handlers**

One of the GSI event handlers illustrated in Figure 6-21 adds the GSI to the panel’s GSI collection. The other is used to account for the effect reflected flow, as described in Section 6.2.3.



If the GSI generated by the GSIM contains a collection of reflected gas flow rays then the ray-tracing methods described in Section 6.3 can be used to determine the paths of the reflected gas flow rays. Each reflected gas flow ray contains a test particle object that is used to represent a simulated molecule, as defined in Section 6.2.3.

If a reflected gas flow ray is found to intersect a panel then it is passed to the impact procedure illustrated in Figure 6-19. As described in Section 6.2.3, the GSI event handler will trace the paths of reflected gas flow rays (i.e. simulated molecules) until some pre-determined limit is reached (either a number of reflections or a fraction of the incident molecular speed ratio depending on the analysis set-up).

## 6.5 Key Features

This section summarises some of the key features of the FMF Module. In particular, those available via the FMF Module's client. Many of the features address the recommendations made by authors of existing tools as well as the limitations common to most existing tools, as detailed in Section 2.7.

### 6.5.1 Geometry Modelling and Transformation

To enable the implementation of the Hybrid method, spacecraft geometry is represented by surface meshes. A surface mesh may be used to represent a single part or an entire spacecraft. The SEDAT Database tables that are used to store the surface meshes are described in Section 5.5.4.

Functionality is provided for the import of surface meshes from a variety of formats, as explained in the *Step 1: Import Spacecraft Surface Mesh* page of the SEDAT Help System, described in Section 5.7. Surface meshes can also be manually created, as described in the *Step 2: Set-Up Spacecraft Surface Mesh* page of the Help System.

Once imported or manually created, surface meshes can be transformed (translated then rotated) into model analysis space to build a complete model in the spacecraft's body-fixed coordinate system. This process uses the methods associated with the *Vector* class described in Section A2.2.1 of Appendix 2.

The *Step 7: Set-Up Model* and *Step 8: Set-Up Model Analysis* pages of the Help System describe the process and provide links to the *Rotations* page of the Help System. The *Rotations* page details the three-dimensional rotation functionality that has been implemented, which includes the Euler, matrix, axis and angle, and quaternion methods.

## 6.5.2 Aerodynamic Damping

One of the objectives of this PhD (described in Section 1.4) is to calculate the aerodynamic performance of a drag deorbit device. In particular, the analysis of such a device's aerodynamic drag, which depends upon its attitude stability.

Ideally, a drag deorbit device should be passively stable in attitude to enable it to align itself to achieve maximum drag. To accomplish this, the obvious approach to take is to ensure the device is aerodynamically stable in attitude. Its static aerodynamic stability can be determined using the methods already presented. However, to examine its dynamic aerodynamic stability, some additional analysis must be undertaken to determine the aerodynamic damping torques that would arise due to its rotation through a flow.

Preliminary unpublished research within the Space Research Centre (SRC) suggested that aerodynamic damping torques might have a small effect on the stability of a drag deorbit device. Harkness [12] has since found that aerodynamic damping torques are up to four orders of magnitude smaller than static aerodynamic torques for a drag deorbit device (having the geometry of an open-ended circular cone) tumbling at one radian per second.

Significantly, Harkness's analysis found that the effect of the diurnal variation of local atmospheric density in low Earth orbit produced a similar magnitude of rotational damping to static aerodynamic torques. In some scenarios, the diurnal variation even had a convergent effect on rotational stability, causing the spacecraft to tumble. However, Harkness also found that the increase in density experienced during descent had the opposite (stabilising) effect.

Acknowledging Harkness's findings, the modelling of aerodynamic damping torques is no longer considered a vital objective of this PhD.

Nonetheless, at the beginning of this research, the consequences of aerodynamic damping torques were thought to be significant. Therefore, the FMF Module incorporates functionality that enables it to calculate the forces and torques due to the effects of a spinning spacecraft and/or spinning parts.

The situation being considered is illustrated in Figure 6-22. Assuming quasi-static conditions, the relative velocity of the air flow due to the rotation of a spacecraft surface can be added to the free stream velocity to determine the resultant velocity of the flow impacting a surface.

The incident velocity of the flow impinging upon an elemental forward facing and unshielded surface area due to the angular velocity of the spacecraft  $\bar{\omega}$ , is given by Equation 6-9.

$$\bar{V}_i = \bar{V}_\infty - \bar{V}_\omega \quad 6-9$$

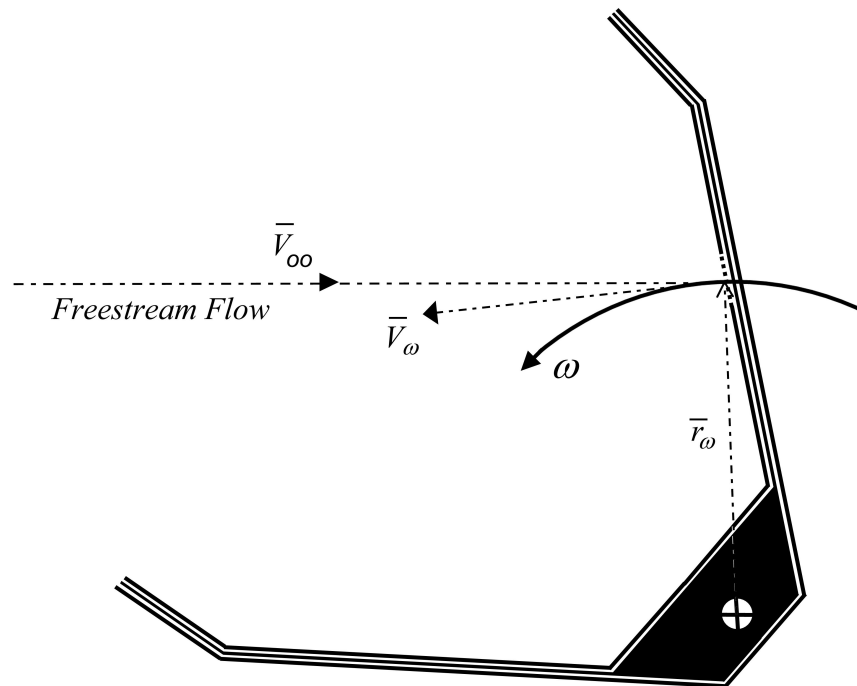


**Figure 6-22 - Aerodynamic Damping**

Assuming a right-handed coordinate system, the angular velocity  $\bar{\omega}$  acts out of the page from the origin of  $\bar{r}_\omega$  and corresponds to a rotation rate  $\omega$ .

The term  $\bar{V}_\infty$  is the component of free stream velocity and  $\bar{V}_\omega$  is the velocity of the elemental surface area due to its angular velocity, which is equal to the vector cross product of  $\bar{\omega}$  and  $\bar{r}_\omega$ . The term  $\bar{r}_\omega$  is the vector from the origin of the angular velocity vector to the centroid of the elemental surface area. The contributions of additional angular velocities can be added to Equation 6-9.

It should be noted that pressure, shear stress, and heat transfer coefficients calculated using the adjusted incident velocity may need to be re-normalised in terms of the free stream dynamic pressure (for example, if using Equation 3-18 to calculate pressure coefficient).

The FMF Module provides the functionality to define angular rotations for both individual surface meshes and models (composed of arrangements of surface meshes). The *Step 8: Set-Up Model Analysis* and *Step 13: Set-Up MAC Orientations* pages of the Help System explain how to do this in detail for surface meshes and models respectively.

As noted previously, Equation 6-9 is applicable to forward facing and unshielded surfaces only. This is because aft facing or shielded panels are effectively moving through a local stationary gas (composed of outgassed molecules and / or reflected flux) and modelling such a scenario is quite different to modelling high-

speed molecules in rarefied flow. Therefore, the shielding calculation of the Hybrid method should be employed if the body contains concave regions.

In general, the modelling of high-speed rarefied gases in concave regions of rotating bodies or parts is extremely difficult due to the complex nature of the reflected flux. The method that has been implemented is strictly only valid for modelling a rotating spacecraft or part that is not susceptible to reflected flow. There are two main reasons for this.

Firstly, the method only accounts for the angular velocity of the first surface impacted by the flow (the primary impact due to the free stream flow). It does not account for the angular velocities of surfaces that are impacted by reflected flow. This is because surface angular velocity components are not added to incident test particle velocities (this is a result of a programming oversight early in the development that was left uncorrected for the reason outlined in the following paragraph).

Secondly, the Hybrid method is not well suited to the analysis of highly dynamic scenarios. This is because it employs analytical expressions that, by definition, use a unit time step. Furthermore, the test particle method it uses also assumes a simulation time period of one second. These factors mean that if the angular rotation rate of the body or a part is too high then the simulation of reflected flow will not be physically realistic. The first surface will have rotated over the time period of the analytical expression and the second surface will have rotated by the time the reflected test particles reach it.

Therefore, in scenarios where a spacecraft is rotating at significant speed and multiple reflections are likely, use of the standard TPMC approach, described in Section 2.6.3, with a small simulation time step (much less than one second) is recommended. However, it should be noted that in some cases, local Knudsen numbers may be much larger than free stream Knudsen numbers, causing greater probability of intermolecular collision (for the reasons outlined in Section 2.2.1). In such cases, the DSMC method, outlined in Section 2.6.4, should be used instead of the TPMC method.

Despite the recommendations noted above, an option has been provided to model the effects of low-speed rotation in conjunction with the simulation of reflected flow, as explained in the *Step 9: Set-Up MAC* page of the SEDAT Help System, described in Section 5.7. The option has been left in for experimental purposes, but is unlikely to yield any meaningful results for the reasons outlined previously.

### **6.5.3 Gas-Flow Modelling**

As discussed in Section 2.2.2, accurate modelling of the neutral atmospheric gas flow encountered by a spacecraft is essential for hi-fidelity aerodynamic analysis

in the free molecular flow regime. To illustrate this point, Figure 6-23 illustrates the trend lines for several macroscopic flow properties with altitude in Earth's upper atmosphere for the dominant gas species.

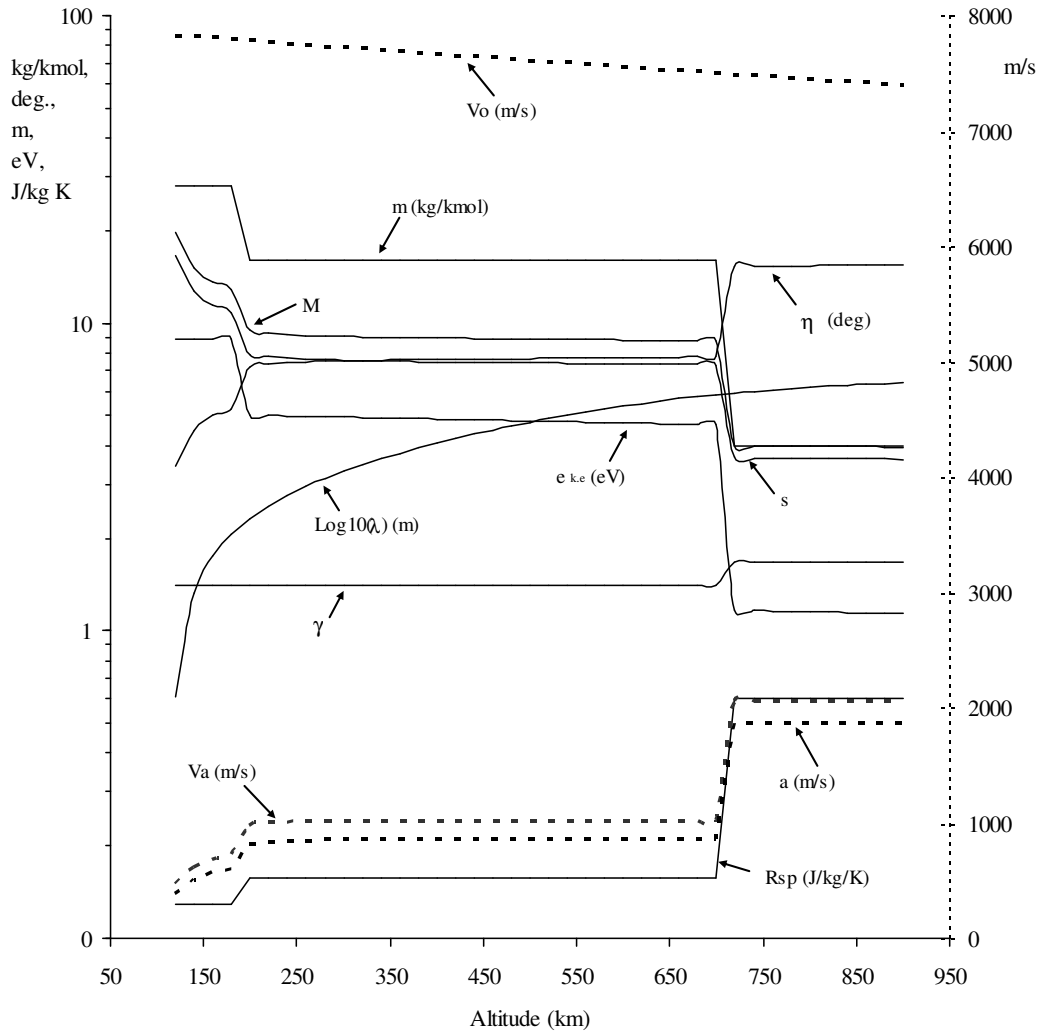


**Figure 6-23 - Selected Aerodynamic Parameters versus Altitude based on the Dominant Gas Species**

Solid trend lines relate to the left vertical axis, dashed trend lines relate to the right vertical axis. Based on Equations 2-1 to 2-3, 2-6 to 2-18 and data from the MSISE-90 Atmospheric Model [18]. Assumes mean solar conditions (as defined by [18]) and values of  $\gamma$ ,  $m$ , and  $R_{sp}$  based on the dominant constituent of the gas ( $i = i_{(n = \text{max})}$ ). Calculation of mean free path ( $\lambda$ ) assumes a molecular mean collision diameter equivalent to that for  $N_2$  ( $d_{avg} = 3.62 \times 10^{-10}$  m).

Comparing Figure 6-23 with Figure 2-11, which shows the same data based on the number density weighted average (mean) of the species, demonstrates that assumptions about the nature of the incident gas flow can introduce significant errors into results.

The graph in Figure 6-23 shows large changes in the trend lines where the dominant gas species changes with altitude. For example, the speed of sound almost doubles between 700 km and 725 km because the molar mass decreases from 16 kg kmol<sup>-1</sup> to 4 kg kmol<sup>-1</sup> as the dominant gas molecule changes from atomic oxygen to helium. Therefore, caution should be used when performing analyses using the dominant gas species, especially at altitudes where the dominant species changes.

The classes of the *Aurora.Engineering.Aerodynamics.Flow* namespace, described in Section A2.2.5 in Appendix 2, are used to represent gases and gas flows. These classes can be used to represent monomolecular gases, or gas mixtures. In addition, they provide the functionality to calculate the mean or the dominant species of a gas mixture.

Therefore, the FMF Module can perform analyses using the dominant gas species, the mean of the species, or individual gas species. This latter option provides numerous options for gas-flow modelling. For example, the molecular flux of each gas species can be compared and gas-species specific GSIM data can be used.

To make best use of the gas-flow modelling functionality, the client can access data related to multiple atmospheric models, as described in Section 6.5.5. The SEDAT Database tables that store this data are described in Section 5.5.4.

The *Step 10: Set-Up MAC Gas Flow* of the SEDAT Help System, described in Section 5.7, provides details of how to use the atmospheric model data and the gas-flow modelling functionality available via the client to full effect.

#### 6.5.4 Surface-Dependent Properties

The FMF Module provides the functionality to assign every panel of a surface mesh a different surface material. Since different GSIM data sets relate to different surface materials, mappings can be created to associate individual surface meshes and surface mesh panels to GSIM data sets. The *Step 4: Set-Up Surface Mesh Surface* page of the SEDAT Help System, described in Section 5.7, explains how to do this.

Similarly, every panel can be assigned a different surface temperature, allowing multiple temperature distributions to be created for a single surface mesh. The *Step 5: Set-Up Surface Mesh Temperature* page of the SEDAT Help System explains how to create surface mesh temperature distributions.

#### 6.5.5 Multiple Gas-Surface Interaction Models

As summarised in Section 3.6, the variety of GSIMs and the large size of their related Empirical data sets is increasing all the time. Furthermore, new Molecular Dynamics (MD) computer simulations are creating vast quantities of GSIM data. To exploit the data-handling and data-storage capabilities of the SEDAT

Database and address these issues, the FMF Module has been designed to accommodate the widest possible variety of GSIMs and GSIM data.

Chapter 1 provides details of two GSIMs that come pre-installed with the FMF Module. GSIMs must inherit from the GSIM base class described in Section A2.2.7 of Appendix 2. This guarantees that they provide a consistent interface to the rest of the FMF Module and ensures that they have access to all of the properties and methods of an impact object. The impact class provides properties that expose the incident gas flow ray object and the impacted panel object associated with an impact. The impact class is described in Section A2.2.7 and the gas flow ray and panel objects are described in Section A2.2.7.

New GSIMs can be written in a text file using any Microsoft .Net compatible language and added to the FMF Module using a few data entries. They will then be compiled at run-time during analysis processing if required. The GSIM tables and their relationships enable collections of input parameters, input bounds (that define the limits of the associated data set), and outputs (or attributes) to be defined for each GSIM.

The *Step 3: Set-Up Gas-Surface Interaction Models (GSIMs)* page of the SEDAT Help System, described in Section 5.7, provides a detailed explanation of how to add new GSIMs and insert, update, and delete GSIM data. It also provides an illustration of the GSIM tables and their relationships as well as the full code of the GSIM base class.

### 6.5.6 Multiple Atmospheric Models

The SEDAT Database has been designed to accommodate multiple atmospheric models. The tables and relationships of the SEDAT Database that are used to store the atmospheric models are described in Section 5.5.4. All of the atmospheric models can be accessed by the FMF Module and used to perform aerodynamic analyses.

The *Solar System Body* page of the SEDAT Help System, described in Section 5.7, provides a detailed explanation of how to add and update atmospheric models using the functionality of the SEDAT Client. Step 7e of the *Step 7: Set-Up Model* help page provides details of how to use an atmospheric model to perform an aerodynamic analysis using the FMF Module.

The MSISE-90 Earth atmospheric model [18] used throughout this thesis comes pre-installed with the SEDAT System.

### 6.5.7 Computing and Data Handling Capabilities

Section 5.5.3 describes how SEDAT's client-server architecture and Relational Database Management System (RDBMS) mimics a computing grid that

enables multiple distributed computers to run processes on the same data set simultaneously. This approach can be used to speed up the processing of complex analyses. Each computer must have the SEDAT Client installed and each client must be connected to the same SEDAT Database.

For example, each computer can be used to perform the analysis of a different set of spacecraft orientations. For further information about how to set up different spacecraft orientations for a single analysis run, refer to the *Step 13: Set-Up MAC Orientations* page of the SEDAT Help System, described in Section 5.7.

As discussed previously, one of the many benefits of Relational Database Management Systems (RDBMSs), such as the SEDAT Database, is that they are highly scalable. The FMF Module exploits this scalability to store all of the calculation data generated during a free molecular flow analysis. For example, this includes individual panel gas-surface interaction results.

The built-in Structured Query Language (SQL) querying capability of the SEDAT RDBMS provides numerous options for reporting on this vast amount of data. The *Step 15: View Results* page of the Help System, describes the *View Results* screen of the FMF Module client, which provides access to reports and a bespoke three-dimensional graphical results screen for displaying colour-coded surface mesh panel results. Together, these features enable highly detailed post-processing analysis to be carried out.

The preceding discussion has illustrated the various advantages of using the FMF Module client and accompanying database to perform analyses. However, the processing components of the FMF Module can also be used to perform rapid analyses of spacecraft via an appropriate interface. Depending on the computer processing power available and the complexity of the analysis, real-time simulation is achievable. An example interface is described in Section 6.4.4.

## 6.6 Summary

This chapter has described the FMF Module, which is a module within the SEDAT System described in Chapter 5. The FMF Module can be used to perform aerodynamic calculations in the free molecular flow regime of low Earth orbit spaceflight. The prototype tool that was developed as a precursor to the SEDAT System and FMF Module is also described briefly.

This chapter has explained the innovative new Hybrid method that has been developed as part of this PhD and implemented in the FMF Module. It has described the accompanying SEDAT Ray-Tracer, which is used by the FMF Module to assist with implementing the Hybrid method. It has also provided an explanation of how the FMF Module has been implemented, along with descriptions of some of the key features of the model.



As outlined in Section 6.5.5, one of the features of the FMF Module is that it enables multiple gas-surface interaction models to be used. Furthermore, as explained in Section 6.2.3, the gas-surface interaction models described in Chapter 3 require some additional functionality in order to make full use of the TPMC method that is incorporated into the Hybrid method.

Therefore, Chapter 1 provides details of two gas-surface interaction models that are pre-installed with the SEDAT System that can be used by the FMF Module to perform aerodynamic analyses using the Hybrid method. To demonstrate the features of the FMF Module and meet the objectives outlined in Section 1.4, Chapter 8 provides the results of several analyses that have been performed using the FMF Module.



## 7 PRE-INSTALLED GAS-SURFACE INTERACTION MODELS

Chapter 3 describes two of the most popular Gas-Surface Interaction Models (GSIMs) that can be used to model gas-surface interactions in the free molecular flow regime: the Newtonian model and the Schaaf and Chambre model. This chapter describes how both GSIMs are implemented in the FMF Module.

Section 7.1 describes the Newtonian model and Section 7.2 describes a new form of the Schaaf and Chambre model. The new derivation of the Schaaf and Chambre model can be used to model reflected flow using the Hybrid method described in Section 6.2. Therefore, it is referred to as the Hybrid Schaaf and Chambre (H-SC) model.

For the reasons outlined in Section 0, both GSIMs are implemented as object-orientated classes. The classes inherit from the base GSIM class described in Section A2.2.7 of Appendix 2 and are located in the *Aurora.Engineering.Aerodynamics.FMF.RayTracer.GSIM.Library* namespace. The full code for both classes is provided in a Microsoft Visual Basic.Net file named *AuroraGSIMs.vb*, which is copied to the *GSIM Library* folder in the SEDAT application folder during the installation process outlined in Section 5.9.

As discussed in Section 6.5.5, additional GSIMs can be added to the FMF Module. For more information about adding GSIMs and GSIM data to the FMF Module refer to the *Step 3: Set-Up Gas-Surface Interaction Models (GSIMs)* page of the SEDAT Help System, described in Section 5.7.

### 7.1 Newtonian Model

Section 3.1 describes the original and modified forms of the Newtonian GSIM that can be used to perform analytical calculations using the RTP method outlined in Section 2.6.2. Both forms have been implemented in the *Aurora.Engineering.Aerodynamics.FMF.RayTracer.GSIM.Library.Newton* class.

The *Newton* GSIM has one parameter, which determines whether to use the original Newtonian method to calculate  $C_p$  using Equation 3-2, or the modified Newtonian method using Equation 3-3. When set to two it does the former, when set to one it does the latter.

The *Newton* GSIM has no bounds, since it is equally as accurate (or, more precisely, inaccurate) in all regimes of free molecular flow.

It has one attribute, which is the dimensionless value of  $C_{p,max}$ . If the original Newtonian method is being used then the attribute will always return the value 2, otherwise it will return the value calculated using Equation 3-3.

Since the Newtonian GSIM does not include a scattering kernel and cannot be used to model particulate flow, it can only be used to perform analytical analysis of convex geometries. Therefore, when performing an analysis the *Type* property of the *Analysis* should be set to either “*Disable Ray Tracing And Reflections And Rotational Effects*” or “*Enable Ray Tracing But Not Reflections Or Rotational Effects*.” The *Step 9: Set-Up MAC (Model Analysis Configuration)* help file of the Help System explains how to do this if using the FMF Module’s client.

## 7.2 Hybrid Schaaf and Chambre Model

Both direct and reflected flow can be accounted for by the Hybrid method. However, in order to model reflected flow using the Schaaf and Chambre GSIM presented in Section 3.2.2 some additional functionality is required.

To model reflected molecular flux, the Hybrid method requires the GSIM to split the flow that is incident on a surface into one or more test particles, which are then reemitted. For the Hybrid Schaaf and Chambre (H-SC) GSIM, depending on the accommodation coefficients (as explained in Section 7.2.2), this means one specularly reemitted test particle and multiple diffusely reemitted test particles, as illustrated in Figure 7-1.

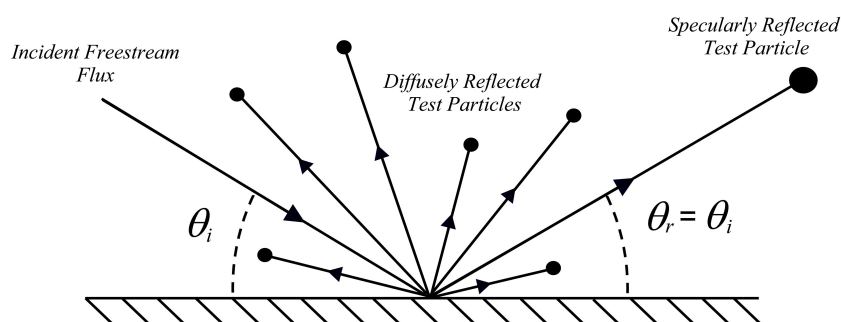


**Figure 7-1 - Hybrid Schaaf and Chambre GSIM**

The incident flow may constitute the free stream flow or it may be a test particle that has been generated during a previous gas-surface interaction.

The reemitted test particles may not necessarily be fired at further surfaces. However, if the incident flux is represented by a test particle, then the reemitted test particles can be used to help calculate the energy and momentum imparted during a gas-surface interaction.

Figure 7-2 illustrates the program flow of the H-SC GSIM. The acronym GFR refers to a Gas Flow Ray. GFRs are used to represent both free stream flow and test particles. The sections that follow describe the functionality illustrated in Figure 7-2 in more detail.

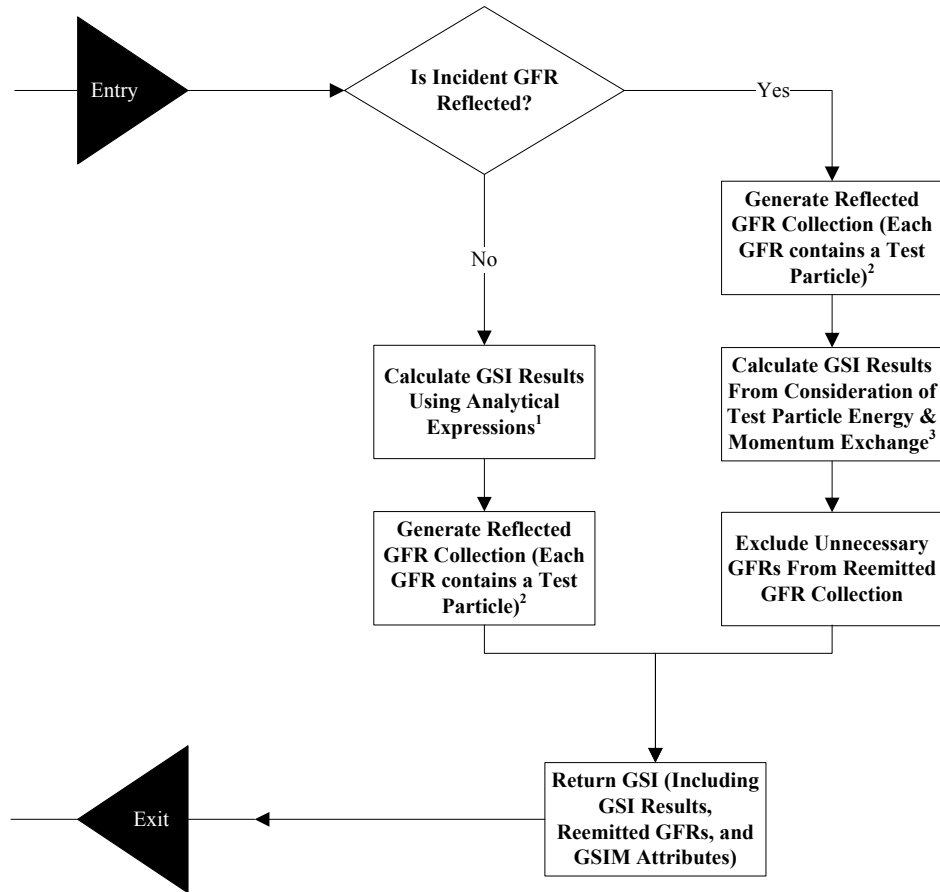


**Figure 7-2 - Hybrid Schaaf and Chambre GSIM Program Flow**

**Key:** <sup>1</sup> uses Equations 3-18, 3-19, and 3-20; <sup>2</sup> determine fractions of diffusely and specularly reflected flux using the method outlined in Section 7.2.2 and use the scattering kernel described in Section 7.2.3 to determine the reemitted test particle velocities; <sup>3</sup> uses Equations 7-8, 7-9, and 7-41.

### 7.2.1 Pressure and Shear Stress

The total pressure and shear stress on a surface due to the impact of both direct and reflected flow is given by Equations 7-1 and 7-2 respectively in terms of pressure and shear stress coefficients. All the coefficients in Equations 7-1 and 7-2 are normalised by the same quantity, the free stream dynamic pressure  $q_\infty$ , which is described by Equation 2-22.

$$C_{p_{Total}} = \frac{\Delta p_{Total}}{q_\infty} = C_p + \sum_{j=1}^J C'_{p_j} \quad 7-1$$

$$C_{\tau_{Total}} = \frac{\Delta \tau_{Total}}{q_\infty} = C_\tau + \sum_{j=1}^J C'_{\tau_j} \quad 7-2$$

The coefficients of pressure and shear stress due to the direct impact of the free stream flow,  $C_p$  and  $C_\tau$  respectively, can be calculated using Equations 3-18 and

3-19. Therefore, it is only necessary to calculate the additional pressure generated by the impact and reemission of test particles, which represent reflected flow.

The second term on the right-hand side of Equation 7-1 represents the total pressure exerted on the surface due to the impact of  $J$  test particles. Similarly, the second term on the right-hand side of Equation 7-2 represents the total shear stress exerted on the surface due to the impact of  $J$  test particles.

The terms  $C'_p$  and  $C'_\tau$  correspond to the coefficients of pressure and shear respectively due to the impact of a single test particle. In general, an apostrophe indicates that a term relates to a test particle quantity (except in the case of molecular mass  $m'$ ).

The pressure and shear stress exerted on a surface is due to the exchange of momentum between the surface and the incident and reemitted test particles. Therefore, for a given surface area  $\Delta A$ ,  $C'_p$  can be written in terms of the total momentum change at the surface along the direction of the surface's negative unit normal  $\Delta \bar{p}'|_{\rightarrow -\hat{n}}$  due to the impact and reemission of all test particles over the time period  $\Delta t$ , as given by Equation 7-3.

$$C'_p = \frac{\Delta p'}{q_\infty} = \frac{1}{q_\infty} \cdot \frac{\Delta \bar{p}'|_{\rightarrow -\hat{n}}}{\Delta t \Delta A} \quad 7-3$$

Likewise,  $C'_\tau$  can be written in terms of the total momentum change at the surface along the incident test particle's shear direction  $\Delta \bar{\tau}'|_{\rightarrow \hat{x}'}$  due to the impact and reemission of all test particles over the time period  $\Delta t$ , as given by Equation 7-4.

$$C'_\tau = \frac{\Delta \tau'}{q_\infty} = \frac{1}{q_\infty} \cdot \frac{\Delta \bar{\tau}'|_{\rightarrow \hat{x}'}}{\Delta t \Delta A} \quad 7-4$$

For the reasons given in Section 6.2.3, the simulation time period  $\Delta t$  can be set to unit time (i.e. one second).

From inspection of Figure 3-3, the momentum of an incident test particle along the negative unit normal direction ( $-\hat{n}$ ) is given by Equation 7-5.

$$\bar{p}'|_{\rightarrow -\hat{n}} = N'_i m'_i (\bar{v}'_i \cdot -\hat{n}) \quad 7-5$$

The term  $N'_i$  in Equation 7-5 is the number of real molecules, with molecular mass  $m'_i$ , represented by the incident test particle. The term  $\bar{v}'_i$  is the velocity of the incident test particle.

The total momentum imparted by a user-defined number  $M_d$  of diffusely reemitted test particles along the negative unit normal direction is given by Equation 7-6.

$$\sum_{m=1}^{M_d} \bar{p}'_{w_m} \Big|_{\rightarrow-\hat{n}} = N'_w m'_w \sum_{m=1}^{M_d} (\bar{v}'_{w_m} \cdot \hat{n}) \quad 7-6$$

The term  $N'_w$  in Equation 7-6 is the number of real molecules, with molecular mass  $m'_w$ , represented by a reemitted test particle. The velocity of the  $m^{\text{th}}$  diffusely reemitted test particle  $\bar{v}'_{w_m}$  depends upon the diffuse scattering kernel and is therefore defined by Equation 7-24 in Section 7.2.3.

For a steady state, the number of incident molecules equals the number of reflected molecules. Therefore, by analogy of Equation 7-6 with Equation 3-12 and assuming  $m'_w = m'_i$ , the number of molecules represented by a single test particle  $N'_w$  is given by Equation 7-7.

$$N'_w = \frac{N'_i}{M_d} \quad 7-7$$

By combining Equation 3-10 with Equations 7-5, 7-6, and 7-7 an expression for  $\Delta \bar{p}' \Big|_{\rightarrow-\hat{n}}$  can be derived in terms of the normal accommodation coefficient  $\sigma_N$ , as given by Equation 7-8. The use of Equation 3-10 means that the first term on the right-hand side of Equation 7-8 represents both the momentum of the incident flux and the momentum of the specularly reemitted flux, whereas the second term represents the diffusely reemitted flux.

$$\Delta \bar{p}' \Big|_{\rightarrow-\hat{n}} = (2 - \sigma_N) N'_i m'_i (\bar{v}'_i \cdot -\hat{n}) + \frac{\sigma_N N'_i m'_i}{M_d} \sum_{m=1}^{M_d} (\bar{v}'_{w_m} \cdot \hat{n}) \quad 7-8$$

With the help of Equation 3-11 and Figure 3-3, a similar analysis leads to an expression for  $\Delta \bar{\tau}' \Big|_{\rightarrow\hat{t}'}$  in terms of the tangential accommodation coefficient  $\sigma_T$  and the unit shear direction  $\hat{t}'$  of the test particle relative to the surface, as given by Equation 7-9.

$$\Delta \bar{p}' \Big|_{\rightarrow\hat{t}'} = \sigma_T N'_i m'_i (\bar{v}'_i \cdot \hat{t}') \quad 7-9$$

## 7.2.2 Accommodation Coefficients

One of the consequences of Equation 7-8 is that the normal momentum imparted to the surface by the  $m^{\text{th}}$  diffusely reemitted test particle is given by Expression 7-10.

$$\frac{\sigma_N N'_i m'_i}{M_d} \bar{v}'_{w_m} \cdot \hat{n} \quad 7-10$$

Another way of looking at Expression 7-10 is to say that the actual number of real molecules represented by a single diffusely reemitted test particle  $N'_{wActual(\sigma_N)}$  depends upon the extent of normal momentum accommodation, as defined by Equation 7-11.

$$N'_{wActual(\sigma_N)} = \frac{\sigma_N N'_i}{M_d} \quad 7-11$$

Equation 7-11 implies that the fraction  $\rho_d$  of incident molecules that are reemitted diffusely is equivalent to the normal accommodation coefficient  $\sigma_N$ . As a result, the fraction  $\rho_s$  of molecules simulated by a specularly reemitted test particle is equal to  $1 - \sigma_N$ . Given the original definition of  $\sigma_N$  by Equation 3-6 this is to be expected. For example, as  $P_w$  increases in Equation 3-6 the denominator on the right-hand side decreases and  $\sigma_N$  increases, and vice-versa.

Consistent with Schaaf and Chambre's original definition of shear stress provided by Equation 3-7,  $\sigma_N$  and hence  $\rho_d$  and  $\rho_s$  have no influence on shear stress. Shear stress is only dependent on the independent parameter  $\sigma_T$ , which determines the extent of momentum accommodation along the shear direction due to the incident flux only. However, as already discussed in Section 3.2.2, it would be physically impossible for  $\sigma_N = \rho_d = 0$  (complete specular reemission), while  $\sigma_T = 1$ .

The fractions  $\rho_d$  and  $\rho_s$  are analogous to the fractions  $\varepsilon_d$  and  $\varepsilon_s$  respectively defined by Maxwell in his original GSIM, as outlined in Section 3.2.1. However, Maxwell assumed that the diffusely reflected molecules do not leave in thermal equilibrium with the surface. Therefore, Maxwell's resulting derivations for the pressures and shear stresses take a slightly different form to those presented here, which use Schaaf and Chambre's GSIM. Nonetheless, they are relatively straightforward and have been used by many investigators. An overview of how to derive Maxwell's expressions is provided in Schaaf and Chambre's original paper for comparison [37].

It is worth cautioning that because of this small difference between the GSIMs, values of  $\varepsilon_d$  should not be used interchangeably with  $\rho_d$  ( $\sigma_N$ ).

Schaaf and Chambre's GSIM assumes that all of the incident flux is reemitted. However, in reality, a fraction  $\Omega$  of molecular flux may be adsorbed. The fractions of incident molecular flux diffusely reemitted, specularly reemitted, and adsorbed are then related by Equation 7-12 [60].

$$\rho_d + \rho_s + \Omega = 1 \quad 7-12$$

However, because it has not been possible to find a data set that includes  $\Omega$  as well as the Schaaf and Chambre accommodation coefficients, it is here assumed that  $\Omega = 0$ . Consequently, the fractions of incident molecular flux diffusely and



specularly reemitted in terms of the normal accommodation coefficient  $\sigma_N$  are defined by Equation 7-13.

$$\begin{aligned}\rho_d &= \sigma_N \\ \rho_s &= 1 - \sigma_N \quad (\Omega = 0)\end{aligned}\tag{7-13}$$

The number of real molecules carried by a specularly reflected test particle  $N'_s$  is then given by Equation 7-14.

$$N'_s = (1 - \sigma_N)N'_i\tag{7-14}$$

Since the time period  $\Delta t$  in Equations 7-3 and 7-4 can be set to unit time, the number of real molecules incident upon a surface due to the direct impact of the free stream flow  $N_i$  can be calculated directly from Equation 3-15. Therefore, the number of real molecules carried by each diffusely reemitted test particle as a result of the direct impact of the flow is then given by Equation 7-11, with  $N'_i = N_i$ . Similarly, the number of real molecules carried by a specularly reflected test particle as a result of the direct impact of the flow is given by Equation 7-14, with  $N'_i = N_i$ .

Exploring the definitions provided by Equations 7-11, 7-13, and 7-14 reveals that for complete accommodation of normal and tangential momentum, such that all incident flux is reemitted diffusely ( $\sigma_N = \rho_d = 1$ ,  $\rho_s = 0$ ,  $\sigma_T = 1$ ), Equations 7-8 and 7-9 reduce to Equations 7-15 and 7-16 respectively.

$$\Delta\bar{p}'\Big|_{\rightarrow\hat{n}} = N'_i m'_i (\bar{v}'_i \cdot -\hat{n}) + \frac{N'_i m'_i}{M_d} \sum_{m=1}^{M_d} (\bar{v}'_{w_m} \cdot \hat{n})\tag{7-15}$$

$$\Delta\bar{p}'\Big|_{\rightarrow\hat{t}} = N'_i m'_i (\bar{v}'_i \cdot \hat{t})\tag{7-16}$$

Contrastingly, for zero accommodation of normal and tangential momentum, such that all incident flux is reemitted specularly ( $\sigma_N = \rho_d = 0$ ,  $\rho_s = 1$ ,  $\sigma_T = 0$ ), Equation 7-8 reduces to Equation 7-17 and Equation 7-9 becomes zeroed.

$$\Delta\bar{p}'\Big|_{\rightarrow\hat{n}} = 2N'_i m'_i (\bar{v}'_i \cdot -\hat{n})\tag{7-17}$$

Equation 7-17 illustrates that in the specular case the momentum transferred to the surface along the negative unit normal is twice the momentum of the incident test particle in that direction. This result is to be expected since specularly reflected molecules experience a full reversal of their normal momentum, whilst their tangential momentum remains unchanged. Therefore, they impart twice their incident normal momentum to the surface because of Newton's third law.

### 7.2.3 Scattering Kernel

This section describes the so-called scattering kernel that has been implemented to determine the direction and velocity of reemitted flux in both the specular and diffuse reemission cases.

The geometry of the diffuse reemission case is illustrated in Figure 7-3. The local panel reemission coordinate system  $(R_1, R_2, R_3)$  composed of the three orthogonal directions  $\hat{r}_1$ ,  $\hat{r}_2$ , and  $\hat{r}_3$  is chosen such that  $\hat{r}_1$  represents the panel's outward unit normal direction,  $\hat{r}_2$  represents a unit vector in the direction from vertex 1 to vertex 2 of the panel, and  $\hat{r}_3$  represents the cross product of  $\hat{r}_1$  and  $\hat{r}_2$ , thus completing the right-handed set. These definitions, which are represented by Equalities 7-18, ensure that  $\hat{r}_2$  and  $\hat{r}_3$  act along the surface of the panel and are orthogonal to one another and  $\hat{r}_1$ .

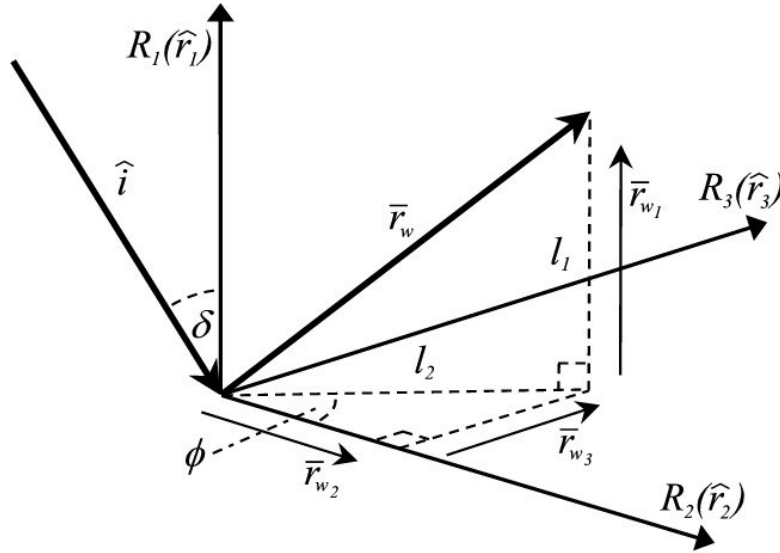


Figure 7-3 - Maxwellian Diffuse Reemission Scattering Geometry

$$\begin{aligned}
 \hat{r}_1 &\equiv \hat{n} \\
 \hat{r}_2 &\equiv \hat{v}_{12} \\
 \hat{r}_3 &\equiv \hat{n} \times \hat{v}_{12}
 \end{aligned}
 \tag{7-18}$$

The inward unit velocity vector  $\hat{i}$  acts at an angle  $\delta$  to the panel's unit normal ( $\hat{r}_1$ ). The direction of a reemitted test particle, represented by the vector  $\bar{r}_w$ , is given by Equation 7-19.

$$\bar{r}_w = r_{w1} \hat{r}_1 + r_{w2} \hat{r}_2 + r_{w3} \hat{r}_3
 \tag{7-19}$$

The lengths  $r_{w_1}$ ,  $r_{w_2}$ , and  $r_{w_3}$  can be determined from inspection of Figure 7-3 and are provided by Equation 7-20.

$$\begin{aligned} r_{w_1} &= l_1 \\ r_{w_2} &= l_2 \cos \phi \\ r_{w_3} &= l_2 \sin \phi \end{aligned} \quad 7-20$$

Combining Equations 7-18, 7-19, and 7-20 provides an expression for  $\bar{r}_w$ , which is given by Equation 7-21.

$$\bar{r}_w = l_1(\hat{n}) + l_2 \cos \phi(\hat{v}_{12}) + l_2 \sin \phi(\hat{n} \times \hat{v}_{12}) \quad 7-21$$

The values of the scalar quantities  $l_1$ ,  $l_2$ , and  $\phi$  in Equation 7-21 must be sampled for each reemitted test particle. In order to produce a random probability distribution of  $\bar{r}_w$  it is necessary to employ so-called Monte Carlo statistical sampling techniques.

The lengths  $l_1$  and  $l_2$  vary between 0 and 1. Their respective values can be sampled successively using Equation 7-22, which is derived from consideration of the normal distribution of a thermal velocity component in an equilibrium gas [27].

$$l = \sqrt{-\ln R_F} \quad 7-22$$

The term  $R_F$  in Equation 7-22 represents a random fraction between 0 and 1. Modern computing systems provide a means to generate pseudo-random numbers using mathematical algorithms that are sufficiently random for practical purposes. In Microsoft .Net, the *Random* class is used to generate random fractions as double-precision 64-bit floating-point numbers.

The azimuth angle  $\phi$  varies uniformly between 0 and  $2\pi$  radians. Values of  $\phi$  can be sampled using Equation 7-23, which is derived from consideration of the normal distribution of  $\phi$  between 0 and  $2\pi$  [27].

$$\phi = 2\pi R_F \quad 7-23$$

Diffusely reflected test particles are reemitted in thermal equilibrium with the surface. They issue from the fictitious Maxwellian gas behind the surface at a speed equal to the thermal speed  $V_w$  of the gas, which is found from Equation 2-11 by setting  $T = T_w$ . Therefore, the velocity vector of a reemitted test particle is given by Equation 7-24.

$$\bar{v}'_w = V_w \hat{r}_w = \sqrt{2R_{sp_w} T_w} \hat{r}_w \quad 7-24$$

The term  $\hat{r}_w$  is the unit reemission direction vector, which is found by normalising  $\bar{r}_w$  by its magnitude  $|\bar{r}_w|$ . The term  $R_{sp_w}$  is the specific gas constant of the molecules that are represented by the reemitted test particle.

The geometry of the specular reemission case is illustrated in Figure 7-4. The local panel coordinate system employed is the same as that used in the diffuse case and is therefore defined by Equalities 7-18.

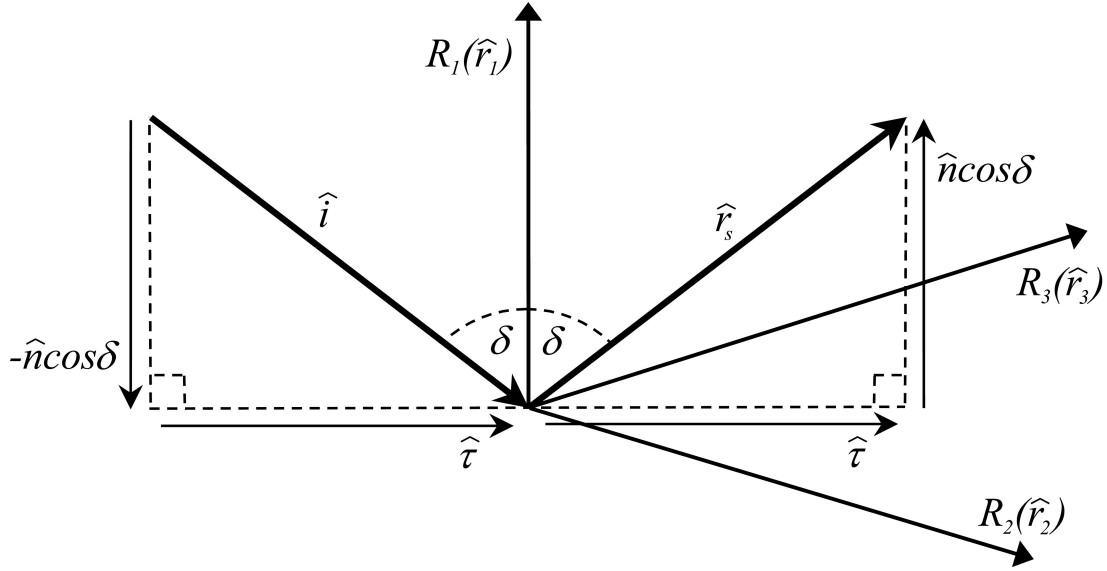


**Figure 7-4 - Specular Reemission Geometry**

The incident direction vector  $\hat{i}$ , the reemission direction vector  $\hat{r}_s$ , the shear component  $\hat{\tau}$  of the incident direction vector, and the projection of  $\hat{i}$  in the direction of the panel outward unit normal  $\hat{n}$  ( $-\hat{n} \cos \delta$ ) are coplanar. Therefore, from inspection of Figure 7-4,  $\hat{r}_s$  can be written as Equation 7-25.

$$\hat{r}_s = \hat{\tau} + \hat{n} \cos \delta \quad 7-25$$

In the case of specular reflection, the angle of incidence equals the angle of reflection. Therefore, the shear component  $\hat{\tau}$  of the incident direction vector is conserved. From inspection of Figure 7-4,  $\hat{\tau}$  can be written as Equation 7-26.

$$\hat{\tau} = \hat{i} + \hat{n} \cos \delta \quad 7-26$$

Combining Equations 7-25 and 7-26 provides an expression for  $\hat{r}_s$  in terms of  $\hat{n}$ ,  $\delta$ , and  $\hat{i}$ , which is given by Equation 7-27.

$$\hat{r}_s = 2\hat{n} \cos \delta + \hat{i} \quad 7-27$$

Specularly reflected molecular flux is reemitted at the same speed and temperature as the incident flux. Therefore, the velocity of a specularly reemitted test particle in terms of the incident speed  $V_i$  is given by Equation 7-28.

$$\vec{v}'_s = V_i \hat{r}_s \quad 7-28$$

Equation 7-28 applies whether the incident flux is due to direct flow or a test particle. If the incident flux is due to direct flow, then for specular reflection,  $V_i$  is equivalent to the bulk speed of the gas. For conservation of energy, this implies that the H-SC GSIM is strictly only valid in free stream hyperthermal conditions.

Consistent with this definition of a specularly reemitted test particle's speed and the description of a diffusely reemitted test particle's speed (given by Equation 7-24), all test particles travel at their total translational speed. Therefore, if the incident flux is due to a test particle then  $V_i$  in Equation 7-28 is simply equal to the test particle's speed.

#### 7.2.4 Heat Transfer

The total convective heat transfer to a surface due to the impact of both direct and reflected flow is given by Equation 7-29 in terms of heat transfer coefficients.

$$C_{h_{Total}} = \frac{\Delta Q_{Total}}{q_{\infty} V_{\infty} \Delta A} = C_h + \sum_{j=1}^J C'_{h_j} \quad 7-29$$

The term  $\Delta Q_{Total}$  represents the total convective heat transfer to the surface in unit time. Therefore, all the heat transfer quantities in Equation 7-29 are normalised by the same quantity  $q_{\infty} V_{\infty} \Delta A$ , where  $q_{\infty}$  is the free stream dynamic pressure given by Equation 2-22,  $V_{\infty}$  is the speed of the free stream flow, and  $\Delta A$  is the elemental surface area.

The heat transfer to the surface due to the direct impact of the free stream flow, described by the heat transfer coefficient  $C_h$ , can be calculated using Equation 3-20. The second term on the right-hand side of Equation 7-29 represents the total heat transfer to the surface due to the impact of  $J$  reflected test particles. As before, the apostrophe indicates that a term relates to a test particle quantity (except in the case of molecular mass  $m'$ ).

In order to derive an expression for the heat transfer to the surface due to the impact of the  $j^{th}$  test particle it is necessary to consider the energy balance at the surface. The amount of heat transferred to a surface per unit time is given by Equation 7-30 [37].

$$\Delta Q = \Delta E_i - \Delta E_r \quad 7-30$$

The terms  $\Delta E_i$  and  $\Delta E_r$  represent the energy fluxes carried by the incident and reflected flow respectively. With the help of Equation 3-5, Equation 7-30 can be re-written in terms of the thermal accommodation coefficient  $\sigma_a$  and the energy flux of the molecules that are reemitted diffusely  $\Delta E_w$ , as provided by Equation 7-31.

$$\Delta Q = \sigma_a (\Delta E_i - \Delta E_w) \quad 7-31$$

For a neutral gas the energy carried by a molecule can be found using Equation 7-32 [37].

$$\Delta E = \Delta E_{trans} + \Delta E_{int} \quad 7-32$$

The  $\Delta E_{trans}$  component of energy is due to the molecule's translational kinetic energy, as defined by Equation 7-33. The term  $V$  represents the molecule's speed and, as before,  $m'$  represents the molecule's mass.

$$\Delta E_{trans} = \frac{1}{2} m' V^2 \quad 7-33$$

The  $\Delta E_{int}$  component is due to the molecule's internal energy, as defined by Equation 7-34 [37].

$$\Delta E_{int} = \frac{1}{2} \vartheta k T \quad 7-34$$

The term  $T$  in Equation 7-34 represents the molecule's temperature, and  $k$  represents the Boltzmann constant ( $1.3807 \times 10^{-23}$  J K<sup>-1</sup>). The term  $\vartheta$  represents the number of internal (non-translational) degrees of freedom of the molecule (e.g. its rotation and vibration about its centre of mass). It is related to the specific heat ratio  $\gamma$  and the number of degrees of freedom  $\zeta$  of the gas by Equation 7-35 [37]. Given this definition, it should be noted that  $\vartheta = 0$  for a monatomic gas because it has three translational degrees of freedom and no internal degrees of freedom.

$$\vartheta = \frac{5 - 3\gamma}{\gamma - 1} = \zeta - 3 \quad 7-35$$

Combining Equations 7-32, 7-33, and 7-34 yields Equation 7-36.

$$\Delta E = \frac{1}{2} (m' V^2 + \vartheta k T) \quad 7-36$$

It is worthwhile comparing Equation 7-36 with Equation 2-17 defined in Section 2.2.2. It is noticeable that the translational energy of a molecule due to its thermal speed, which by the principle of equipartition is equal to  $\frac{3}{2} k T$  (due to the three translational directions in space), is included in the right-hand term containing  $\zeta$  in Equation 2-17. However, it has been absorbed into the translational kinetic energy term in Equation 7-36. This is because the speed  $V$  in Equation 7-36

represents the total speed of the molecule, which includes its translational thermal speed.

Multiplying Equation 7-36 through by the number of molecules that an incident test particle represents ( $N'_i$ ), results in an expression for the energy carried by that test particle  $\Delta E'_i$ , as given by Equation 7-37.

$$\Delta E'_i = \frac{1}{2} N'_i (m'_i V_i^2 + \vartheta_i k T_i) \quad 7-37$$

To calculate the total energy carried by  $M_d$  diffusely reemitted test particles requires the use of Equation 7-38, which is similarly derived from Equation 7-36. Equation 7-38 assumes steady state conditions such that Equation 7-7 applies, it also assumes that  $m'_w = m'_i$ .

$$\sum_{m=1}^{M_d} \Delta E'_{w_m} = \frac{N'_i}{2M_d} \sum_{m=1}^{M_d} (m'_i V_{w_m}^2 + \vartheta_{w_m} k T_w) \quad 7-38$$

Combining Equation 7-31 with Equation 7-37 and Equation 7-38, results in an expression for the heat transferred to a surface due to the impact of a test particle, as given by Equation 7-39.

$$\Delta Q' = \frac{1}{2} \sigma_a N'_i \left\{ m'_i V_i^2 + \vartheta_i k T_i - \frac{1}{M_d} \sum_{m=1}^{M_d} (m'_i V_{w_m}^2 + \vartheta_{w_m} k T_w) \right\} \quad 7-39$$

Equation 7-39 reveals some interesting characteristics that are intrinsic to the Schaaf and Chambre GSIM, and, by extension, the H-SC GSIM. It has been assumed that the number of real molecules carried by a test particle can be determined by  $N'_{w \text{ Actual}(\sigma_N)}$ , which is given by Equation 7-11. However, this assumption is strictly only valid when the thermal accommodation coefficient is equal to the normal momentum accommodation coefficient ( $\sigma_a = \sigma_N$ ). This is because Equation 7-39 includes the factor  $N'_{w \text{ Actual}(\sigma_a)}$  given by Equation 7-41, which is analogous to  $N'_{w \text{ Actual}(\sigma_N)}$ .

$$N'_{w \text{ Actual}(\sigma_a)} = \frac{\sigma_a N'_i}{M_d} \quad 7-40$$

These two independent definitions of  $N'_{w \text{ Actual}}$  are to be expected because  $\sigma_a$  and  $\sigma_N$  are by definition independent phenomenological parameters that both describe the extent of diffuse reemission.

If  $\sigma_a \neq \sigma_N$  then the question arises as to which accommodation coefficient should be used to determine the number of molecules carried by a test particle. The answer depends on whether the modelling of momentum or energy has greater priority. It is here assumed that momentum has greater priority, such that Equation

7-11 is used to calculate  $N'_{w_{Actual}}$ . If  $\sigma_a = \sigma_N$  then this assumption will have no bearing on energy results.

The number of internal degrees of freedom of each diffusely reemitted test particle  $\vartheta_{w_m}$  can be determined using Monte-Carlo statistical sampling [27]. Some additional energy would then be transferred to the surface if  $\vartheta_w$  were lower than  $\vartheta_i$  for a particular test particle. However, consistent with Schaaf and Chambre's GSIM [37], it is here assumed that  $\vartheta_w = \vartheta_i$ , such that the extent of rotational and vibrational thermal accommodation is described only by  $\sigma_a$ .

As is obvious from Figure 2-6 and Equations 2-15 and 7-35, the mean value of  $\vartheta$  in low Earth orbit is close to zero, except at lower altitudes where diatomic constituents are prevalent. Therefore, in low Earth orbit, the exchange of internal molecular energy is negligible in comparison to the exchange of translational energy during a gas-surface interaction. Consequently, the assumption that  $\vartheta_w = \vartheta_i$  will have very little bearing on energy results in low Earth orbit.

The thermal speed  $V_w$ , which can be found from Equation 2-11 by setting  $T = T_w$ , is the same for each diffusely reemitted molecule. Given this, and assuming  $\vartheta_w = \vartheta_i$ , Equation 7-39 can be reduced to Equation 7-41.

$$\Delta Q' = \frac{1}{2} \sigma_a N'_i \{ m'_i (V_i^2 - V_w^2) + \vartheta_i k (T_i - T_w) \} \quad 7-41$$

## 7.2.5 Surface Temperature

In free molecular flow, the surface temperature  $T_w$  is predominantly determined by the internal thermal environment of the spacecraft as well as external radiative heat sources (for example, the Sun and Earth) and not by aerodynamic heating. Nonetheless, aerodynamic heating can become significant in high-density high-velocity free molecular flow.

Therefore, for a more realistic simulation of the gas-surface interaction,  $T_w$  in Equation 7-3 (which uses Equations 3-18, 7-8, and 7-24) should take into account the aerodynamic heating of the surface, which can be determined from Equation 7-29. However, since each panel impact is dealt with sequentially, feeding back the temperature rise due to the total heat transferred to a panel by all gas-surface interactions is not possible during analysis.

Moreover, computation of the temperature rise that would occur to a particular surface due to aerodynamic heating must form part of a thermal equilibrium calculation. Such a calculation must account for, among other things, the surface material's specific heat capacity as well as the surface's mass, conductive paths, and radiative heat inputs and outputs. This calculation is complex even under steady-state conditions and beyond the scope of the current aerodynamic analysis



tool. Furthermore, multiple thermal analysis tools already exist that can perform this type of analysis (for example, the European Space Agency's ESATAN tool [92]).

The optimum solution would be to use an iterative approach to determine the value of  $T_w$ . An initial value of  $T_w$  could be calculated using an external thermal analysis tool, excluding the effects of aerodynamic heating. The FMF Module could then use this initial value to calculate the aerodynamic heat transfer in terms of the heat transfer coefficient  $C_h$ . The heat transfer coefficient could then be used by the external thermal analysis tool to re-calculate  $T_w$ .

The results presented in Table 8-2 of Section 8.2.4 indicate that surface temperature has very little influence on aerodynamic heating for a typical spacecraft at mid altitude in low Earth orbit. Therefore, it is unlikely that the iterative procedure would need to be continued using the new value of  $T_w$  except perhaps for a few specific analyses. For example, during a re-entry analysis or if reflected molecular flux converges upon the same region of a secondary surface over a significant period (a scenario that could occur for the drag deorbit device analysed in Section 8.4.2).

At the present time, a thermal analysis tool is not available to the author to perform a thermal analysis. Therefore, the surface temperature  $T_w$  is assumed to be dependent only on the internal thermal environment of the spacecraft and the external radiative environment.

### 7.2.6 Parameters, Bounds, and Attributes

As described Section 6.5.5, every GSIM implemented in the FMF Module can have multiple sets of input parameters and bounds defined, as well as multiple sets of output attributes.

Table 7-1 lists the nominal input parameters for this GSIM. They are based upon the Knechtel and Pitts accommodation coefficients [17], defined by Equations 3-25 and 3-26 in Section 3.3.2.

The Knechtel and Pitts curve-fit parameters listed in Table 7-1 are based on the experimental results of Knechtel and Pitts, as discussed in Section 3.3.2. The Mazanek, Kumar, Qu, and Seywald [20] curve fit parameters listed in Table 7-1 are based on the orbital observations of Mazanek et al discussed in Section 3.3.3.

For the reasons outlined in Section 7.2.4, the curve fit parameters for the thermal accommodation coefficient have been set to equal the curve fit parameters for the normal accommodation coefficient.

The number of diffuse test particles that will be generated during a gas-surface interaction ( $M_d$ ) has been set to 50. However, a statistical analysis will need to be carried out to determine the sensitivity of results to this value in each case.

**Table 7-1 - Nominal Hybrid Schaaf and Chambre GSIM Parameters**

Parameter	Index	Description	Specular	Diffuse	K & P [17]	Mazanek [20]
$A_N$	0	Curve fit parameter for the normal accommodation coefficient $\sigma_N$ .	0	1	1.0	1.0
$B_N$	1		0	0	0.9	0.9
$C_N$	2		0	0	0.28	0.28
$A_T$	3	Curve fit parameter for the tangential accommodation coefficient $\sigma_T$ .	0	1	0.9	1.67
$B_T$	4		0	0	1.2	1.67
$C_T$	5		0	0	0.147	0.147
$A_Q$	6	Curve fit parameter for the thermal accommodation coefficient $\sigma_Q$ .	0	1	1.0	1.0
$B_Q$	7		0	0	0.9	0.9
$C_Q$	8		0	0	0.28	0.28
$M_d$	9	Number of diffuse test particles to be generated.	0	50	50	50

Figure 7-5 illustrates a plot of the Knechtel and Pitts accommodation coefficients versus incidence angle  $\delta$ , for various incident molecular energies, corresponding to different Earth altitudes in mean solar conditions.

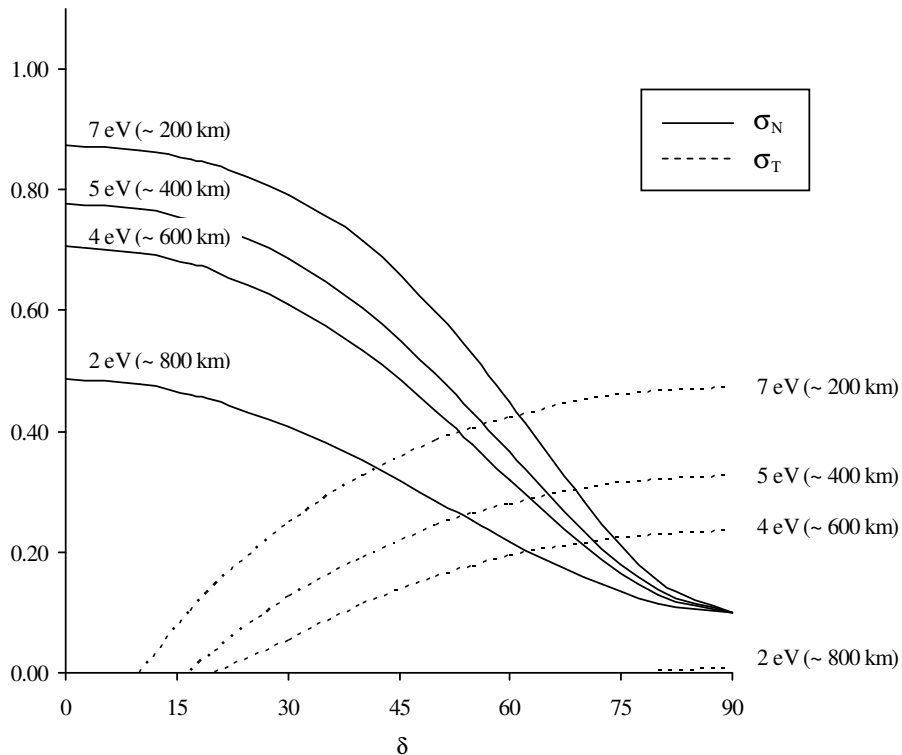


**Figure 7-5 - Accommodation Coefficients versus Incidence Angle Using the Knechtel & Pitts Curve-Fit Parameters**

Altitude approximations use mean molecular quantities and Equation 2-14 and assume mean solar conditions, using the MSISE-90 atmospheric model [18].

Figure 7-6 shows a similar plot using the Mazanek curve-fit parameters. Both figures indicate that the accommodation coefficients will predict significantly lower pressures and shear stresses with increasing altitude.

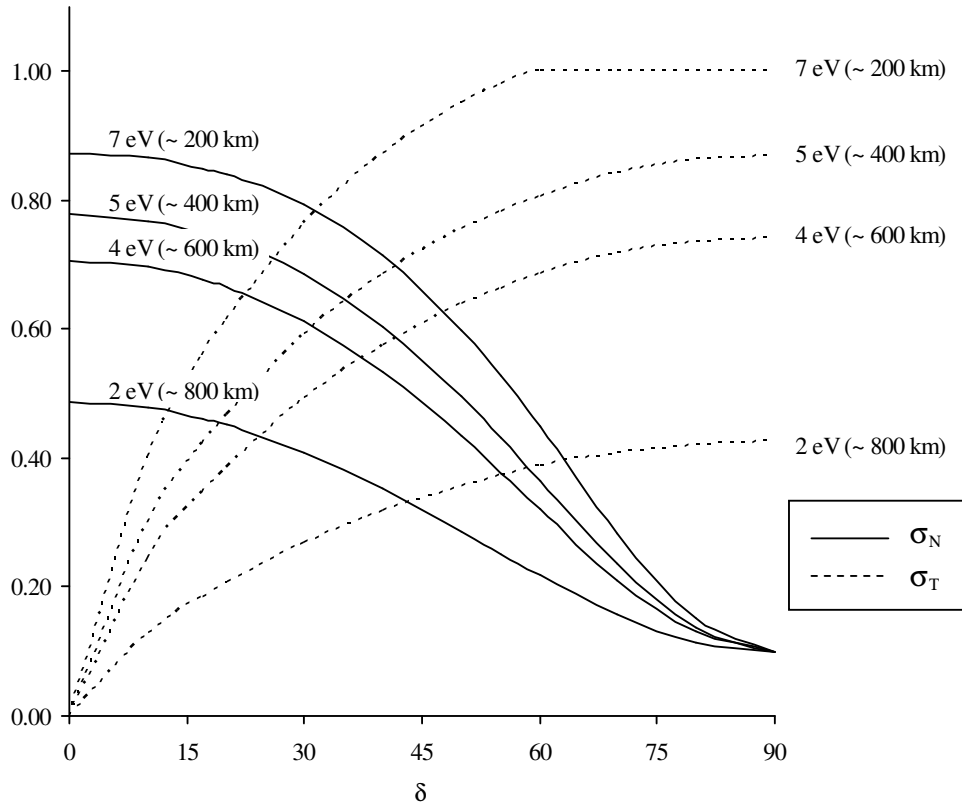


**Figure 7-6 - Accommodation Coefficients versus Incidence Angle Using the Mazanek Curve-Fit Parameters**

**Altitude approximations use mean molecular quantities and Equation 2-14 and assume mean solar conditions, using the MSISE-90 atmospheric model [18].**

As described in Sections 3.3.2 and 3.3.3, the Knechtel and Pitts and Mazanek accommodation coefficients are based upon extrapolated empirical data that relates to incident molecular kinetic energies of approximately 5 eV or more. Therefore, their predictions may be less reliable at higher altitudes, where, as illustrated in Figure 7-5 and Figure 7-6, molecular kinetic energies are lower.

Table 7-2 lists the nominal input bounds for the GSIM. Despite the caution noted in the previous paragraph, the bounds have been set very loosely in order to enable the widest possible range of inputs during testing.

Table 7-3 lists the output attributes of the GSIM. Only three have been included, although additional quantities could be outputted with very little additional coding effort.

**Table 7-2 - Hybrid Schaaf and Chambre GSIM Bounds**

Bound	Index	Description	Nominal Values
$T_w$	0	Surface temperature.	0 to 2000° K
$T_i$	1	Incident flux temperature.	0 to 2000° K
$e_{k.e}$	2	Incident flux molecular kinetic energy.	0 to 100 eV
$n_\infty$	3	Number density of the free stream flow (used if the incident Gas Flow Ray represents the free stream flow).	0 to $2 \times 10^{26} \text{ m}^{-3}$
$N'_i$	4	Number of molecules represented by an incident test particle (used if the incident Gas Flow Ray represents a test particle).	0 to $2 \times 10^{26}$

**Table 7-3 - Hybrid Schaaf and Chambre GSIM Attributes**

Attribute	Index	Description
$\sigma_N$	0	Normal accommodation coefficient.
$\sigma_T$	1	Tangential accommodation coefficient.
$\sigma_Q$	2	Heat transfer accommodation coefficient.

### 7.3 Summary

This chapter has described two Gas-Surface Interaction Models (GSIMs) that have been developed and implemented in the Free Molecular Flow (FMF) Module. The first GSIM, described in Section 7.1, is a Newtonian GSIM that cannot be used to model reflected flow. The second GSIM, described in Section 7.2 and referred to as the Hybrid Schaaf and Chambre (H-SC) GSIM, includes some new functionality that allows it to model reflected flow using the Test-Particle Monte-Carlo (TPMC) method.

This chapter has presented the derivation of the H-SC GSIM from Schaaf and Chambre's original work. It has also listed some nominal values for its phenomenological input parameters. The applicability of the H-SC GSIM and the nominal input parameters to different problems must be examined.

Chapter 8 presents the results of analyses using both the Newtonian GSIM and the H-SC GSIM.

## 8 CASE STUDIES

This chapter presents the results of several aerodynamic analyses that were performed using the FMF Module described in Chapter 6. Two Gas-Surface Interaction Models (GSIMs) have been used: the Newtonian GSIM described in Section 7.1, and the Hybrid Schaaf and Chambre (H-SC) GSIM, which is described in Section 7.2.

The case studies that are presented have been chosen to demonstrate the capabilities of the FMF Module (described in Section 6.5), validate the Hybrid method (described in Section 6.2) and the H-SC GSIM, and meet the objectives outlined in Section 1.4. Where possible the results have been compared with the results of other published studies. All the results are discussed in detail and, where appropriate, findings are stated.

The first results presented are for two simple convex shapes: a flat plate and a sphere. These results demonstrate the validity of the FMF Module and provide many interesting findings that can be used by other spacecraft aerodynamicists to compare GSIMs, accommodation coefficients, surface temperature effects, and Earth atmospheric effects.

Section 8.2.1 compares the results of multiple analyses of a flat plate using different H-SC accommodation coefficients. Section 8.2.2 provides a similar analysis for a sphere at multiple different altitudes in different atmospheric conditions.

Section 8.2.3 presents detailed surface results for the sphere analysed in Section 8.2.2. It includes print screens from the FMF Module that show surface molecular flux, pressure, shear stress, and heat distributions. Section 8.2.4 presents an additional sphere analysis, which exploits the functionality of the FMF Module to explore the effects of an asymmetric surface temperature distribution.

In order to validate the Hybrid method's approach to modelling reflected flow, Section 8.3 presents the results of an analysis of a simple configuration of two flat plates placed at right angles to one another. Section 8.3 also presents results that investigate the effect of using different accommodation coefficients with the H-SC GSIM. It explains the findings with the help of print screens from the FMF Module, which illustrate the paths of reflected test particles.

One of the objectives of this thesis is to analyse the aerodynamic performance of the drag deorbit device concept that is under development within the Space Research Centre (SRC). Section 8.4 presents the results of multiple analyses of a concept proposed by Harkness [12], including print screens from the FMF Module of the types described previously.

The studies presented in Section 8.4 include comparisons with Harkness's own analytical Newtonian calculations, comparisons of different H-SC

accommodation coefficient results, analysis of the effect of multiple molecular reflections using the Hybrid method, and analysis of the effect of aerodynamic damping torques.

Based on these analyses, several conclusions are drawn related to the aerodynamic performance of the drag deorbit device concept proposed by Harkness. In addition, some recommendations are made regarding materials selection and the structural design of the device.

In addition to the case studies described above, several other studies were planned and some were conducted. However, for the reasons outlined in the introduction to Section 8.5, just one additional study is presented. Section 8.5.1 presents the results of an aerodynamic analysis of the NASA Space Shuttle operating in the free molecular flow regime.

In order to present the results it is first necessary to describe the coordinate system and flow geometry used for the analyses. The following section, Section 8.1, provides this description.

## 8.1 Coordinate System and Flow Geometry

The aerodynamic forces and moments calculated by the FMF Module are resolved relative to the spacecraft's body-fixed coordinate system using Equations 2-24 and 2-25 respectively. However, aerodynamicists often find it convenient to resolve the forces on a body relative to the incident free stream flow direction.

The force in the direction of the incident free stream flow direction, which has been referred to multiple times throughout this thesis already, is commonly known as the drag force. The forces that act perpendicular to the drag force and each other are known, for obvious reasons, as the lift and side forces. The side force direction is defined using a right-handed coordinate system in which the lift and drag directions constitute the first and second directions respectively.

In general, since spacecraft often have unusual geometry and may rotate considerably during flight, the definitions of lift and side force in particular are not that useful to a spacecraft aerodynamicist. Furthermore, spacecraft attitude dynamics simulations usually require aerodynamic forces and torques to be resolved relative to a body-fixed coordinate system. Nonetheless, lift, drag, and side forces continue to be used by many spacecraft aerodynamicists. Therefore, in some instances it is necessary to present results in terms of lift, drag, and side force in order to compare them with the results of other authors.

The FMF Module automatically saves values of drag, lift, and side force coefficient ( $C_D$ ,  $C_L$ , and  $C_S$  respectively) for every analysis along with the body-fixed force and moment (torque) coefficients ( $C_F$  and  $C_T$  respectively) for each Cartesian direction. The following paragraphs describe the flow geometry and provide the definition of drag, lift, and side force used by the FMF Module.

Figure 8-1 provides a geometric definition of the free stream direction  $\hat{V}_\infty$  in terms of the angles of attack  $\alpha$  and sideslip  $\beta$  defined in the spacecraft's body-fixed coordinate system, which is denoted by the subscript  $s/c$ .

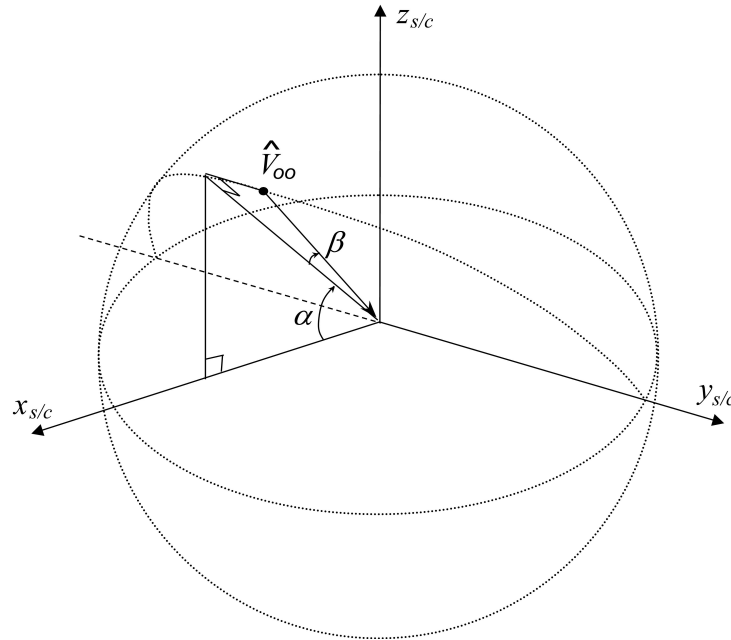


**Figure 8-1 - Definition of Angles of Attack  $\alpha$  and Sideslip  $\beta$**

The spherical coordinate system employs a  $\beta$  then  $\alpha$  projection with a radius of unit magnitude.

From inspection of Figure 8-1, it is possible to derive an expression for  $\hat{V}_\infty$  relative to the body in terms of the spherical coordinate system angles  $\alpha$  and  $\beta$ , as provided by Equation 8-1.

$$\begin{aligned}\hat{V}_{\infty_x} &= -\cos \beta \cos \alpha \\ \hat{V}_{\infty_y} &= -\sin \beta \\ \hat{V}_{\infty_z} &= -\cos \beta \sin \alpha\end{aligned}\tag{8-1}$$

Since the drag force acts in the direction of the free stream flow, Equation 8-1 also provides a definition of the drag direction vector  $\hat{D}$ .

Drag should always have a positive value. However, the sign of the lift and side force values will depend upon the spacecraft attitude and geometry as well as other aerodynamic considerations.

In general, it is assumed that the spacecraft's nominal flight direction is in the  $+x_{s/c}$  direction, such that the  $+z_{s/c}$  direction represents the spacecraft's nominal downwards direction (nadir) and the  $+y_{s/c}$  direction represents the spacecraft's nominal starboard direction, as illustrated in Figure 8-2.

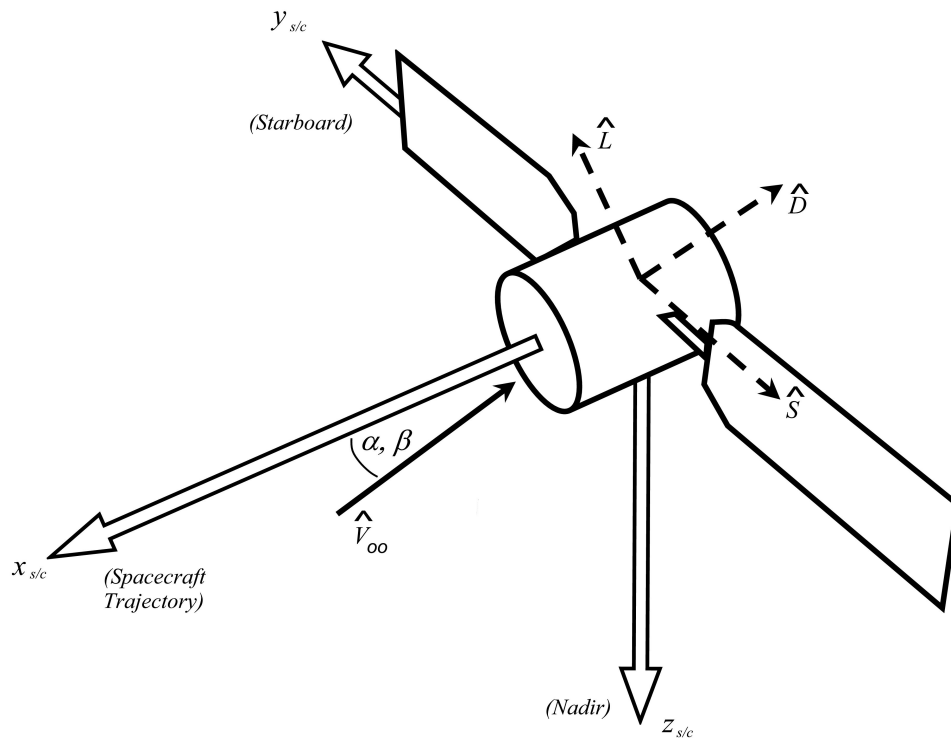


**Figure 8-2 - Nominal Spacecraft Body-Fixed Coordinate System and Lift ( $L$ ), Drag ( $D$ ), and Side ( $S$ ) Force Directions**

The system is a right-handed coordinate system. Therefore, moments (torques) about each axis use the right-handed screw rule.

To try to ensure that the lift force is positive when  $\alpha$  is positive and less than  $180^\circ$ , the lift direction vector  $\hat{L}$  is defined by Equation 8-2, where the unit direction vector  $\hat{Z}$  is equivalent to  $[0, 0, -1]^T$ . For example, to ensure positive values of lift for a flat plate for  $0^\circ < \alpha < 180^\circ$ , the flat plate should lie in the  $x$ - $y$  plane.

$$\hat{L} = (\hat{D} \times \hat{Z}) \times \hat{D} \quad 8-2$$

The side force direction  $\hat{S}$  can be found by taking the right-handed vector cross product of  $\hat{D}$  and  $\hat{L}$ , as given by Equation 8-2.

$$\hat{S} = \hat{D} \times \hat{L} \quad 8-3$$

Drag, lift, and side force can be found by projecting the body-fixed force  $\bar{F}$  in each respective direction,  $\hat{D}$ ,  $\hat{L}$ , and  $\hat{S}$  using the vector dot product.

The spacecraft configuration and body-fixed coordinate system illustrated in Figure 8-2 is used by most astrodynamics texts [13][69][107]. However, many spacecraft in low Earth orbit have their solar panels aligned parallel to the  $x$ -axis, to ensure that they face the Sun (see, for example, [35]).



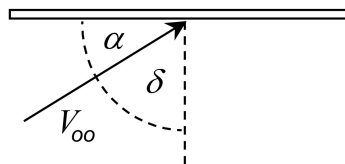
It is also possible to define  $\hat{V}_\infty$  by projecting in the  $\alpha$  direction first and then the  $\beta$  direction. The *Step 13: Set-Up MAC Orientations* page of the SEDAT Help System, described in Section 5.7, provides details of this alternative spherical coordinate system for the free stream flow vector.

## 8.2 Simple Convex Shapes

This section presents the results of analyses of some simple convex shapes that were calculated using the FMF Module. The results of these analyses are compared with the results of other authors in order to validate the FMF Module. They also provide the opportunity to present other interesting aerodynamic findings that are more easily understood using simple geometrical shapes.

### 8.2.1 Different Accommodation Coefficient Results for a Flat Plate

The simplest shape to analyse is a flat plate. The angle of attack  $\alpha$  and panel angle of incidence  $\delta$  have their usual definitions, but are illustrated in Figure 8-3 for clarity nonetheless.



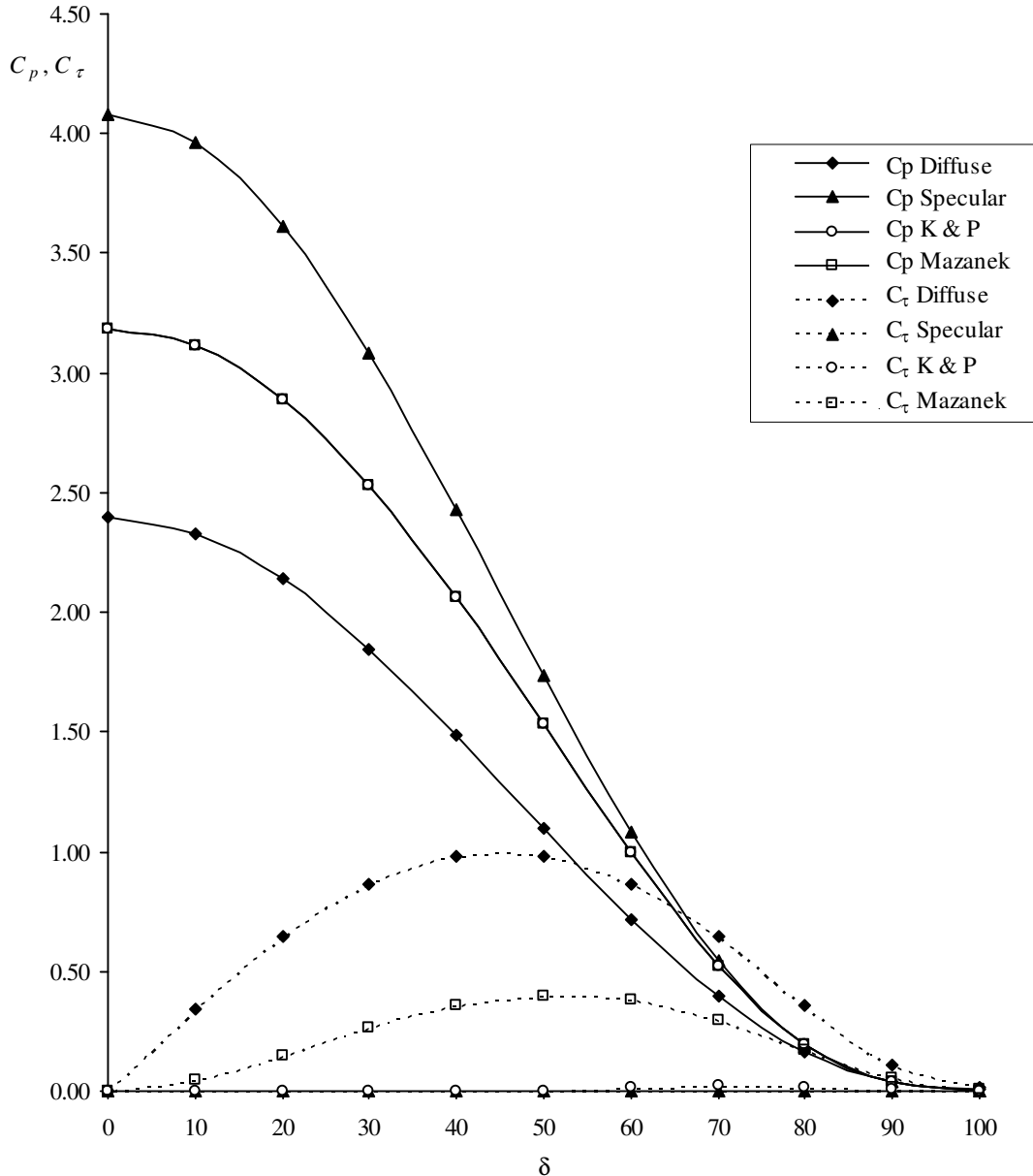
**Figure 8-3 - Flat Plate Analysis: Configuration**

Figure 8-4 compares pressures and shear stresses on a flat plate as a function of incidence angle, calculated using the FMF Module and the H-SC GSIM (with the empirically based Knechtel and Pitts [17] and Mazanek et al [20] accommodation coefficients defined using the input parameters listed in Table 7-1).

The calculations are based upon a surface to free stream temperature ratio of one and a free stream molecular speed ratio of five. The FMF Module input parameters were varied to achieve these values for  $s_\infty$  and  $T_w/T_\infty$  respectively by assuming mean atmospheric gas properties in mean solar conditions at an altitude of 400 km and free stream speed of  $5,078 \text{ ms}^{-1}$ , corresponding to a free stream molecular kinetic energy  $e_{k,e}$  of 2.3 eV. These conditions were selected to enable the results to be compared with the results of the spreadsheet analysis described in Section 3.2.3.

To enable the simulation of sub-hyperthermal conditions, the analysis was set-up to ensure the flat plate would be tested for gas-surface interactions regardless of its orientation with respect to the free stream flow (using the method described in

the *Step 9: Set-Up MAC (Model Analysis Configuration)* page of the SEDAT Help System, described in Section 5.7. Therefore, the flat plate experienced pressure and shear stresses whether forward or aft facing.



**Figure 8-4 - Flat Plate Analysis: Comparison of Pressure and Shear Stress versus Incidence for Different Accommodation Coefficients**

Assumes  $T_w/T_\infty = 1$ ,  $s_\infty = 5$ , and  $e_{k,e} = 2.3$  eV, equivalent to mean atmospheric gas properties in mean solar conditions at an altitude of 400 km and free stream speed of  $5,078 \text{ ms}^{-1}$ . The terms Specular, Diffuse, K & P, and Mazanek refer to the curve-fit parameters listed in Table 7-1.

The specular and diffuse results illustrated in Figure 8-4 correlate well with the spreadsheet results illustrated in Figure 3-6 and Figure 3-7 respectively.

The Mazanek and Knechtel and Pitts' pressure and shear stress results demonstrate the trends expected given their dependence on incidence angle and molecular kinetic energy  $e_{k,e}$ , which is illustrated in Figure 7-5 and Figure 7-6 respectively. In addition, the Knechtel and Pitts tangential accommodation coefficient predicts significantly lower shear stresses due to its lower value across all incidences at the molecular kinetic energy being considered.

The corresponding lift and drag coefficients are plotted against angle of attack in Figure 8-5.

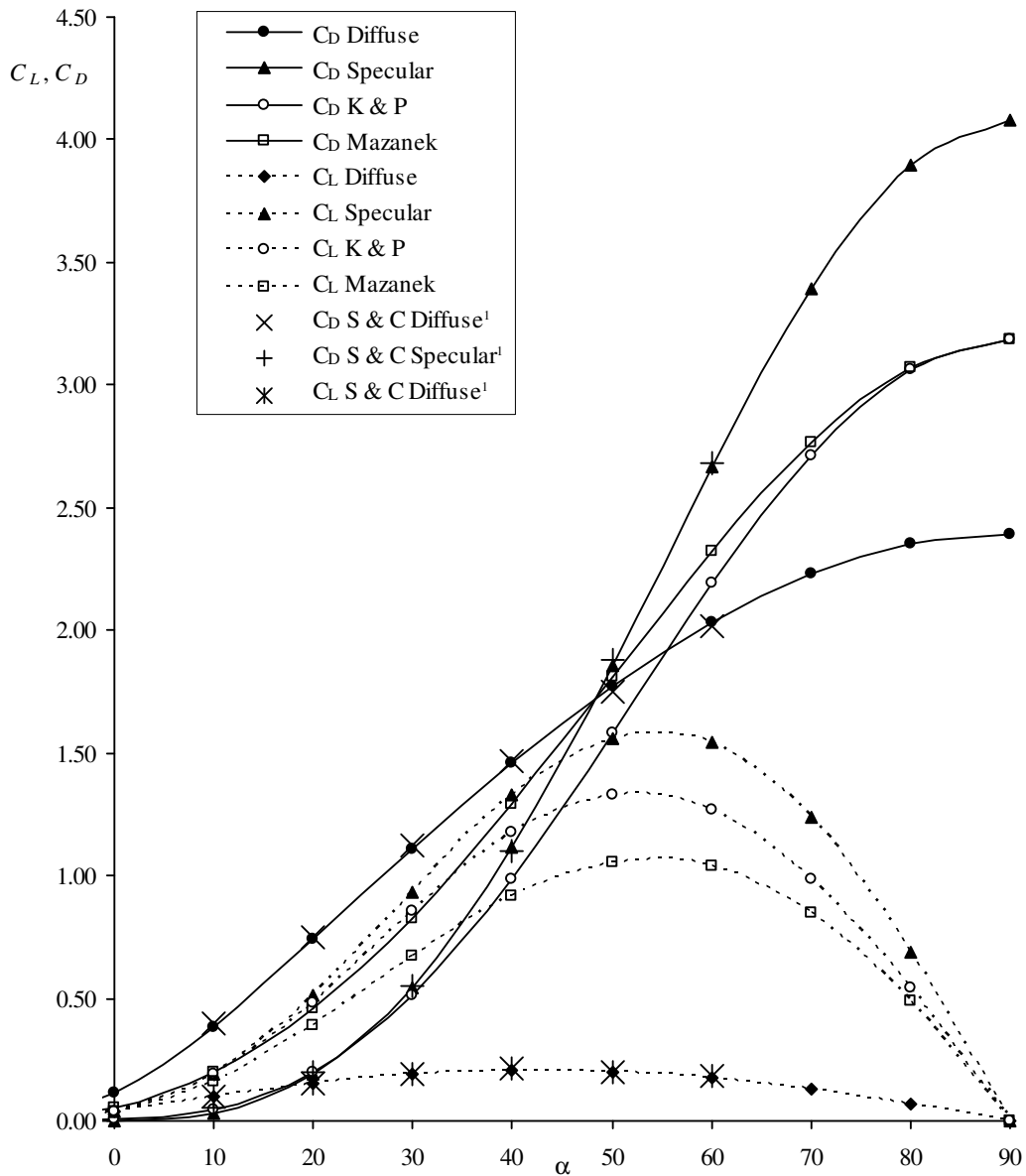


**Figure 8-5 - Flat Plate Analysis: Drag and Lift Forces versus Angle of Attack**

Assumes  $T_w/T_\infty = 1$ ,  $s_\infty = 5$ , and  $e_{k,e} = 2.3$  eV, equivalent to mean atmospheric gas properties in mean solar conditions at an altitude of 400 km and free stream speed of  $5,078$   $\text{ms}^{-1}$ . The terms Specular, Diffuse, K & P, and Mazanek refer to the curve-fit parameters listed in Table 7-1. The S & C plotted points (<sup>1</sup>) refer to values predicted by [37] (extracted from graphical data).

As illustrated in Figure 8-5, the specular and diffuse results correlate well with Schaaf and Chambre's predictions, which are also plotted. The trends shown demonstrate that the significant differences in pressure and shear stress predicted by difference accommodation coefficients can lead to considerable variations in lift and drag predictions.

### 8.2.2 Sphere Parametric Analysis

A sphere is not subject to multiple reflections or shielding, is symmetric about any plane through its centre, and can be solved for analytically. Therefore, the most convenient way to compare GSIMs, accommodation coefficient effects, and atmospheric models is to use a spherically shaped spacecraft.

Figure 8-6 illustrates a plot of drag coefficient versus altitude for a spherical satellite in low Earth orbit under low, mean, and high solar conditions assuming diffuse reemission and  $T_w/T_\infty = 1$ . The results were calculated using the H-SC GSIM (with the input parameters defined in Table 7-1 for the diffuse case), the MSISE-90 atmospheric model [18], and an unstructured triangular mesh with 850 panels.

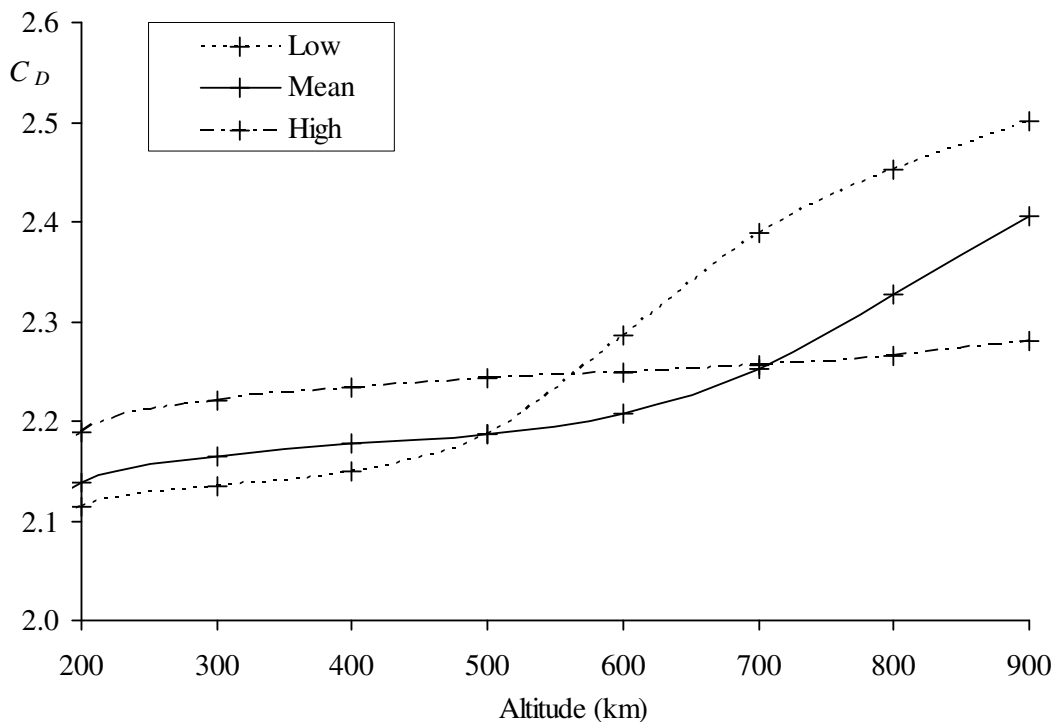


**Figure 8-6 - Drag Coefficient versus Altitude for a Spherical Satellite in Low Earth Orbit Assuming Diffuse Reemission with  $T_w/T_\infty = 1$**   
The terms Low, Mean, and High refer to solar conditions, based on the MSISE-90 atmospheric model [18].

Like the flat plate results presented in the previous section, these results correlate well with Schaaf and Chambre's own findings [37] (Schaaf and Chambre

plot drag coefficient against molecular speed ratio  $s_\infty$ , which can be found from Figure 2-11 in the case of mean solar conditions).

There is quantitative disagreement between the diffuse results illustrated in Figure 8-6 and the results presented by Moe [19], illustrated in Figure 3-9. Although not explicitly stated, Moe appears to assume  $T_w/T_\infty = 1$ , since no value of  $T_w$  is provided. However, Moe uses a different GSIM (by Sentman) and this is the most likely cause of the discrepancy. This result therefore reinforces the findings of Chapter 3 (summarised in Section 3.6), which highlights the complexity of gas-surface interaction modelling.

An analysis has been performed that takes account of actual atmospheric temperatures and a more realistic surface temperature. The inputs for the analysis are summarised in Table 8-1.

**Table 8-1 - Sphere Analysis: Summary of Inputs**

Input	Notes
GSIM	Hybrid Schaaf and Chambre (H-SC), defined in Section 7.2.
Accommodation Coefficients	As defined in Table 7-1.
Characteristic Dimensions	$A_{ref} = 12.57 \text{ m}^2$ , $L_{ref} = 4 \text{ m}$ .
Surface Temperature	All surfaces $200^\circ \text{ K}$ .
Atmospheric Model	MSISE-90 model [18], mean solar conditions.
Local Wind Vector	Directed along the spacecraft's orbital track at the spacecraft's orbital speed (assuming a circular orbit).
Body Fixed Coordinate System	$x$ -axis points in the direction of travel, $y$ -axis points towards the zenith, $z$ -axis completes the right-handed set.
Surface Mesh	Unstructured triangular mesh with 850 panels.

The analysis was performed using mean molecular properties, such that the free stream gas flow had the properties illustrated in Figure 2-11. Both forward and aft facing panels were tested for gas-surface interactions.

Figure 8-7 illustrates the analysis results for the specular and diffuse accommodation coefficients as well as the empirically based Knechtel and Pitts [17] and Mazanek et al [20] accommodation coefficients, defined using the input parameters listed in Table 7-1.

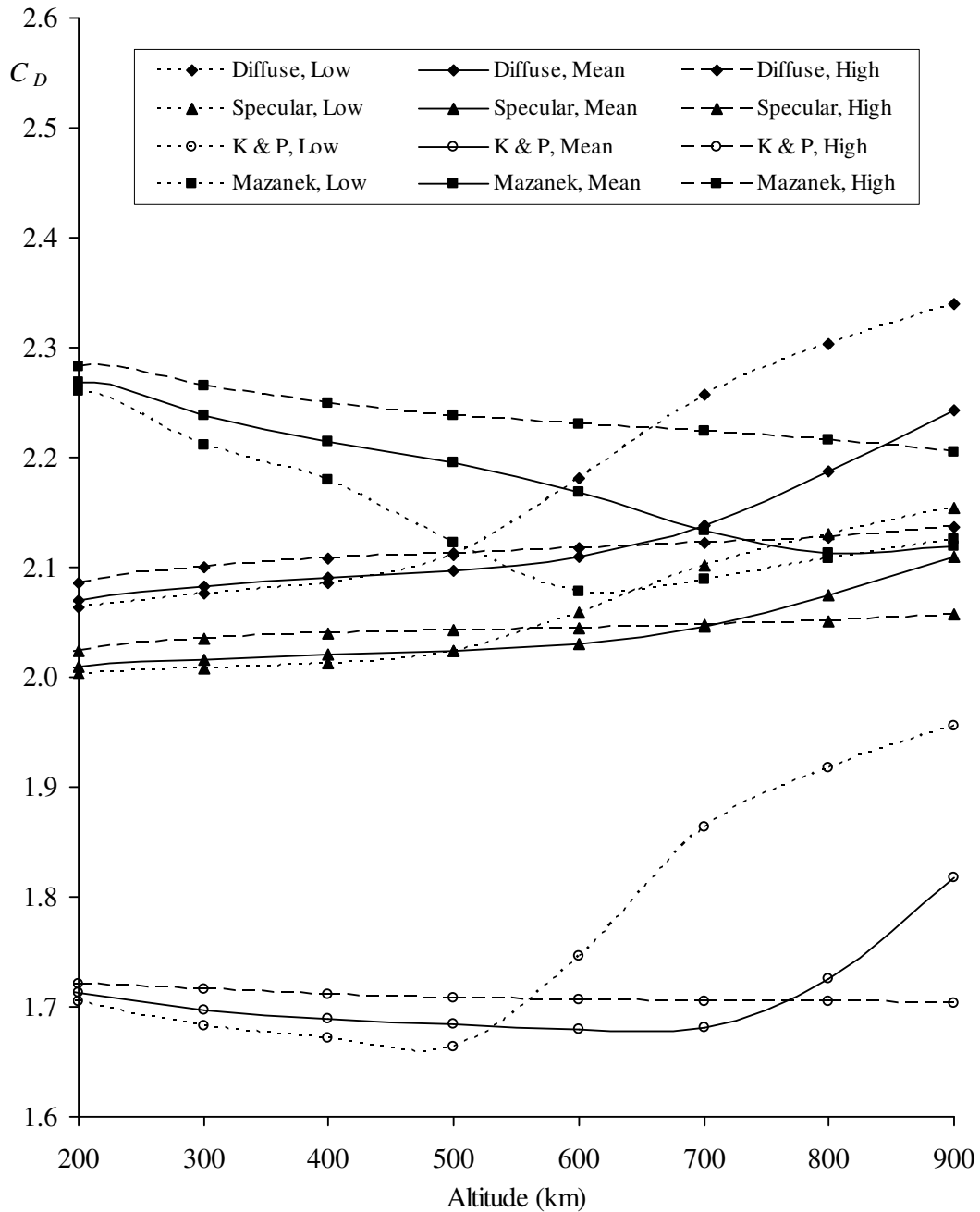


**Figure 8-7 - Comparison of Drag Coefficient versus Altitude for a Spherical Satellite in Low Earth Orbit for Different Accommodation Coefficients**

Low, Mean, and High refer to solar conditions, based on the MSISE-90 atmospheric model [18]. The terms Specular, Diffuse, K & P, and Mazanek refer to the curve-fit parameters listed in Table 7-1.

Inspection of Figure 8-7 reveals several interesting trends, which are described in the following bullet points:

1. The specular and diffuse drag curves follow the inverse trend of molecular speed ratio  $s_\infty$  with altitude, which is illustrated in Figure 2-11. This is because pressure and shear stress, described by Equations 3-18 and 3-19 respectively, are inversely proportional to  $s_\infty$ .
2. Full accommodation of normal and tangential momentum (diffuse case), results in higher drag than specular reflection because of the contribution of shear stresses (see Figure 3-6 and Figure 3-7).
3. The specular and diffuse cases are not limiting cases. Other combinations of accommodation coefficient values can produce lower and higher drag coefficients as demonstrated by the Knechtel and Pitts and Mazanek results respectively.
4. The Mazanek drag values are higher at lower and middle altitudes due to the combined effect of high average  $C_p$  and  $C_\tau$  values across a range of panel incidence angles compared to the specular and diffuse cases (refer to Figure 8-4 for evidence of this).
5. The Knechtel and Pitts tangential momentum accommodation coefficient  $\sigma_T$  is lower than the Mazanek accommodation coefficient across all incidences (see Figure 3-11). This leads to lower shear stresses over the whole surface of the sphere, which combined with a normal accommodation coefficient  $\sigma_N$  that is lower than one at higher incidences, results in the smallest drag at all altitudes.
6. In the case of low solar activity, drag increases rapidly above approximately 500 km (slightly higher for the Mazanek accommodation coefficients). In the case of mean solar activity, this increase is evident above approximately 650 km (and not at all for the Mazanek accommodation coefficients). Inspection of Figure 2-11 indicates that these rises are due to the rapid decrease in molar mass  $m$ , which proportionally increases the specific gas constant  $R_{sp}$  thereby decreasing  $s_\infty$ .
7. Noting these exceptions at higher altitudes and lower levels of solar activity, in general, the Knechtel and Pitts and Mazanek accommodation coefficients predict a decrease in drag with altitude. Figure 7-5 and Figure 7-5 indicate that this is due to the reduction in molecular kinetic energy  $e_{k.e}$  with altitude, caused by the trend of both molecular mass  $m'$  and orbital velocity  $V_o$ . For the reasons outlined in Section 7.2.6, the predictions of the Knechtel and Pitts and Mazanek accommodation coefficients should be treated with caution at higher altitudes due to this reduction in molecular kinetic energy.
8. As can be ascertained from Section 3.2.2,  $T_w = T_\infty$  is not a requirement for complete diffuse reemission (incident molecules may impart all of their momentum and energy to a surface but may not necessarily be in thermal equilibrium with it). Comparing the diffuse results of Figure 8-7 with Figure

8-6 demonstrates that using actual values of  $T_\infty$  and a more realistic estimation of  $T_w$  leads to lower predicted values of  $C_p$  and hence  $C_D$ . Therefore, it is recommended that an accurate temperature ratio should be used in all gas-surface interaction calculations involving diffuse reemission.

Mazanek calibrated their curve-fit parameter values for the tangential momentum accommodation coefficient  $\sigma_T$  to achieve  $C_D = 2.2$  for a sphere at 500 km, in mean solar conditions, using hyperthermal expressions for pressure and shear stress (Equations 3-27 and 3-28), in which they also assumed  $T_w/T_\infty = 1$ .

The nominal atmospheric density they used was  $7.0 \times 10^{-13} \text{ kg m}^{-3}$ , which approximates the value predicted by the MSISE-90 model used in this thesis ( $7.3 \times 10^{-13} \text{ kg m}^{-3}$ ). They also assumed the local wind speed to be  $7,600 \text{ ms}^{-1}$ , which approximates the circular orbital velocity at an altitude of 500 km ( $7,613 \text{ ms}^{-1}$ ).

An analysis has been performed using their expressions in these conditions. Unsurprisingly, a value of  $C_D = 2.2$  was predicted by the FMF Module. However, as illustrated in Figure 8-7, Mazanek's curve-fit parameters coincidentally produce the same result at 500 km in mean solar conditions when the hyperthermal and temperature ratio assumptions are not applied.

At 500 km in mean solar conditions  $s_\infty$  is approximately five (as illustrated by Figure 2-11), which is at the limit of what may be considered hyperthermal flow (see Section 2.2.3). However, Mazanek's derivations from Schaaf and Chambre's equations only eliminate second-order molecular speed ratio terms and therefore still include a  $s_\infty$  term. Consequently, their expressions may be considered applicable in quasi-hyperthermal flow.

Mazanek et al were criticised by a group of their peers for not accounting for a finite molecular speed ratio. They defend their approach in an afterword included with the report. However, they do not provide details of their defence, which presumably follows the reasoning outlined in the previous paragraph.

As Figure 8-7 illustrates, Mazanek's approach would require a different set of momentum accommodation coefficient curve-fit parameters at every altitude to achieve  $C_D = 2.2$  for a sphere at all altitudes.

However, as described in Section 2.1.1, the supposition that  $C_D = 2.2$ , which has been applied to observations of orbital satellites to assist with generating atmospheric models, is predicated on the questionable assumption that most low Earth orbiting satellites have a roughly spherical geometry with approximately the same surface characteristics.

Therefore, the validity of Mazanek's modification of  $\sigma_T$  to achieve  $C_D = 2.2$  for a sphere may be considered dubious. However, not enough is known by this author about the use of satellite drag measurements in atmospheric modelling to



question this aspect of their approach and time constraints do not permit further investigation into this very broad and multifarious subject area.

### 8.2.3 Detailed Surface Results for a Sphere

This section presents the detailed surface results for the spherical satellite analysed in Section 8.2.2, at an altitude of 500 km in mean solar conditions, using the inputs summarised in Table 8-1 and the Mazanek accommodation coefficients.

The incident molecular flux  $N_i$  to each surface mesh panel is illustrated in Figure 8-8, which is a print screen from the FMF Module. It and all other similar results figures provided throughout the following pages were created in the FMF Module using the *Graphical Results Display* component, using the process described in the *Step 15: View Results* page of the SEDAT Help System, described in Section 5.7.

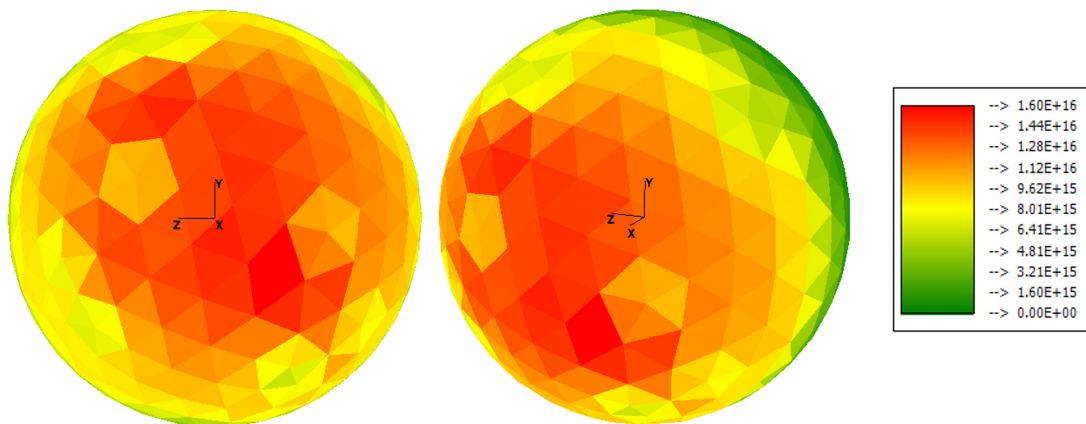


**Figure 8-8 - Molecular Number Density Flux ( $N_i$ ) on a Sphere**

Images generated using the FMF Module. Results relate to the inputs provided in Table 8-1 and correspond to an altitude of 500 km in mean solar conditions.

The uneven distribution of  $N_i$ , illustrated in Figure 8-8, indicates the quality of the surface meshing rather than any physical phenomena. This is because  $N_i$ , which is calculated using Equation 3-13, is dependent on panel area and the panels are all different sizes.

The corresponding distributions of  $C_p$ ,  $C_\tau$ , and  $C_h$  predicted by the Mazanek accommodation coefficients and illustrated in Figure 8-9, Figure 8-10, and Figure 8-11 respectively, exhibit the symmetry expected because they are not dependent on panel area.

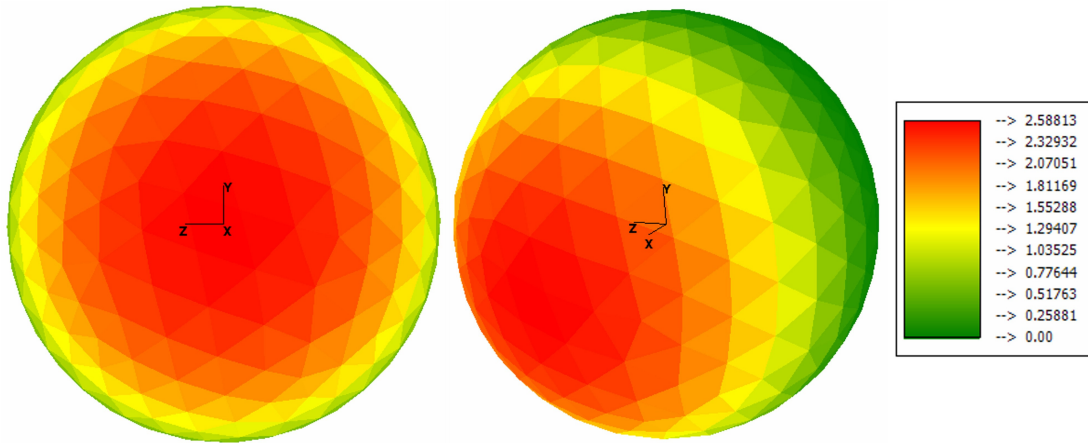


**Figure 8-9 - Pressure Distribution ( $C_p$ ) on a Sphere**

Images generated using the FMF Module. Results relate to the inputs provided in Table 8-1 using the Mazanek accommodation coefficients, corresponding to an altitude of 500 km in mean solar conditions.

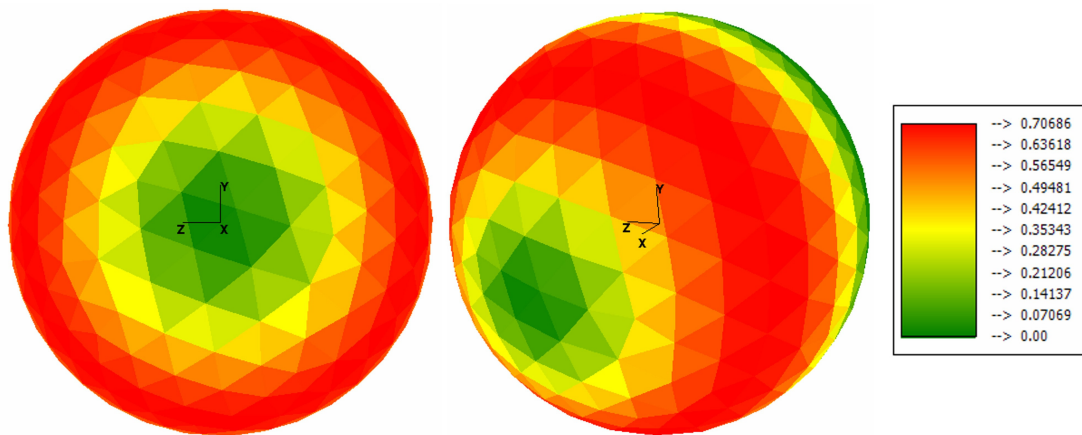


**Figure 8-10 - Shear Stress Distribution ( $C_\tau$ ) on a Sphere**

Images generated using the FMF Module. Results relate to the inputs provided in Table 8-1 using the Mazanek accommodation coefficients, corresponding to an altitude of 500 km in mean solar conditions.

The pressure and shear stress distributions shown in Figure 8-9 and Figure 8-10 illustrate the trends with incidence angle that would be expected based on the flat plate results presented in Section 8.2.1. The predicted pressures are highest for surfaces at lowest incidence ( $\delta$ ) to the free stream flow and the shear stresses are highest for surfaces at incidences of about  $45^\circ$ .

All surface mesh panels were tested for gas-surface interactions. However, due to the hyperthermal nature of the flow the very small coefficients predicted for the aft facing panels are too low to be distinguishable in the colour-coded visualisations illustrated in Figure 8-9, Figure 8-10, and Figure 8-11.

The heat transfer distribution illustrated in Figure 8-11 indicates that surface heating is highest where surface pressures are highest. This is to be expected since the curve-fit parameters for the Mazanek thermal accommodation coefficient were set to equal the parameters for the normal accommodation coefficient, as indicated in Table 7-1. In addition, the Schaaf and Chambre GSIM predicts decreasing heat transfer with increasing incidence angle for all finite thermal accommodation coefficients (refer to Equation 3-20).

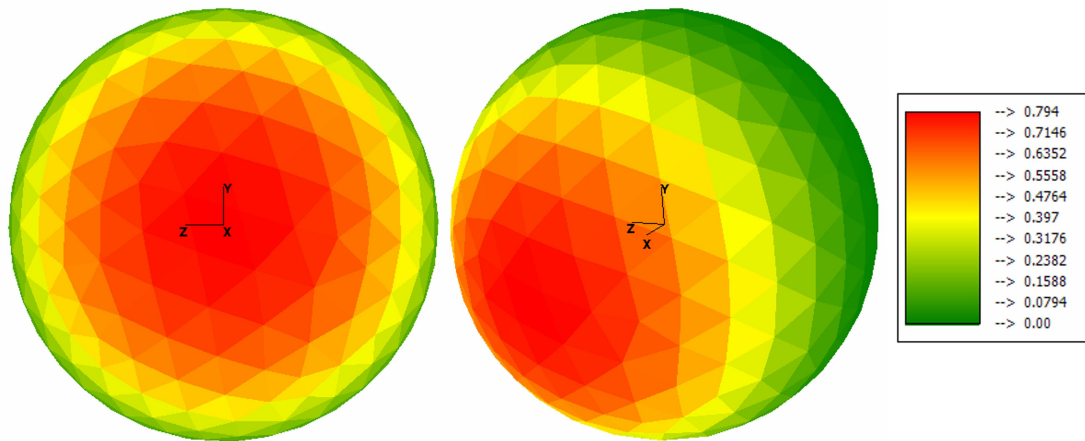


**Figure 8-11 - Heat Transfer Rate Distribution ( $C_H$ ) on a Sphere**

Images generated using the FMF Module. Results relate to the inputs provided in Table 8-1 using the Mazanek accommodation coefficients, corresponding to an altitude of 500 km in mean solar conditions.

#### 8.2.4 Affect of Surface Temperature Differences

In order to demonstrate the effect of surface temperature on the aerodynamic forces experienced by a spacecraft in low Earth orbit, this section re-examines the spherical spacecraft analysed in Section 8.2.2. This analysis is possible because the FMF Module incorporates functionality that enables surface-dependent properties to be assigned to different surface mesh panels, as described in Section 6.5.4.

The surface mesh panels on the +y side of the spacecraft are all set to 400° K. The panels on the -y side of the spacecraft are all set to 100° K. All other inputs are identical to those provided in Section 8.2.2.

Table 8-2 provides the results of the analysis. It compares the force coefficients in the x and y directions (equivalent to drag and lift force coefficients respectively for the spherical satellite) for the laterally asymmetric surface temperature distribution scenario with the coefficients for the scenario analysed in Section 8.2.2. Also shown for comparison are the maximum values of  $C_p$  and  $C_h$  in both scenarios ( $C_\tau$  is not dependent on temperature in the H-SC GSIM).

**Table 8-2 - Uniform versus Hot and Cold Temperature Distribution for a Spherical Spacecraft**

	$C_{F(x)}$	$C_{F(y)}$	$C_{p(max)}$	$C_{h(max)}$
Uniform: $T_w = 200^\circ \text{ K}$ for all surfaces (results of Section 8.2.2).	-2.195	0.000	2.588	0.794
Laterally asymmetric: $T_w = 400^\circ \text{ K}$ for +y surfaces, $T_w = 100^\circ \text{ K}$ for -y surfaces.	-2.197	-0.007	2.624	0.796

The laterally asymmetric temperature distribution causes an increase in pressure on the panels of the +y side of the spacecraft, as indicated by the higher  $C_{p(max)}$  value in Table 8-2, as well as a decrease in pressure on the panels of the -y side of the spacecraft. The reason for these pressure variations is the  $T_w/T_\infty$  term in Equation 3-18 (Section 3.2.2).

The pressure differential causes a force in the -y indicated by the  $C_{F(y)}$  value of -0.007, which, using Equation 2-19 and noting that  $q_\infty = 2.172 \times 10^{-5} \text{ N m}^{-2}$  and  $A_{ref} = 12.566 \text{ m}^2$ , equates to a force of magnitude  $1.9 \mu\text{N}$ .

A small increase in drag coefficient  $C_{F(x)}$  ( $\sim 0.002$ ) is also noticeable in the results listed in Table 8-2. It is caused by the increased pressure brought about the higher surface temperatures of the panels on the +y side.

In order to appreciate the significance of these results it is worth comparing them to another non-gravitational environmental disturbance. The force  $\bar{F}_e$  exerted on an opaque flat plate due to electromagnetic radiation pressure is given by Equation 8-4 [20].

$$\bar{F}_e = p_e \Delta A_p \left[ (\xi_a + \xi_{r_d}) \hat{s} + \left( 2\xi_{r_s} \cos \delta + \frac{2}{3} \xi_{r_d} \right) \hat{n} \right] \quad 8-4$$

The term  $P_e$  in Equation 8-4 is the electromagnetic radiation pressure in the direction of the vector  $\hat{s}$ . In Earth orbit, there are two main sources of radiation pressure: Solar Radiation Pressure (SRP) and radiation pressure caused by the reflection of solar radiation from the Earth, this secondary effect is known as the albedo effect. In low Earth orbit during mean solar conditions mean SRP is approximately  $4.5 \mu\text{N m}^{-2}$ , whilst the Earth albedo SRP can reach up to  $2 \mu\text{N m}^{-2}$  over the equator at local noon [69].

Using similar notation to that employed for the aerodynamic analysis presented throughout this thesis,  $\delta$  in Equation 8-4 is the angle of incidence between the solar radiation vector and the panel unit normal  $\hat{n}$  and  $\Delta A_p$  is the panel's projected area (given by Equation 3-22).

The terms,  $\xi_a$ ,  $\xi_{r_d}$  and  $\xi_{r_s}$  in Equation 8-4 represent the fractions of impinging photons that are absorbed, diffusely reflected, and specularly reflected respectively (since the panel is assumed to be opaque no photons are transmitted,

such that  $\xi_a + \xi_{r_d} + \xi_{r_s} = 1$ ). This treatment of reflected “particulate” flux should be familiar, since a similar method is employed by some GSIMs, see, for example Equation 7-12 in Section 7.2.2.

Using a Structured Query Language (SQL) query, an export was taken from the FMF Module database tables of the panel geometry calculated during the aerodynamic analysis. The *Step 16: View Results Data* page of the SEDAT Help System, described in Section 5.7, provides further details of the export process and how to calculate SRP forces.

The export includes data for  $\Delta A_p$ ,  $\hat{s}$ , and  $\hat{n}$ . Given the spacecraft’s spherical geometry,  $\hat{s}$  is assumed equal to the wind vector.  $\bar{F}_e$  was calculated for every panel assuming the spacecraft’s side surface to be equal parts aluminium and solar panel. Therefore, a value of  $\xi_a = 0.5$  was chosen based on an approximate intermediate value of reflectance for sandblasted aluminium and SiO-coated solar cells provided by [108]. The remaining fractions  $\xi_{r_d}$  and  $\xi_{r_s}$  were both set to the intermediate value 0.25 due to a lack of reliable data for either surface. The total force in the direction of the SRP vector was found to be 36.0  $\mu\text{N}$  in the case of direct SRP and 16.0  $\mu\text{N}$  in the case of albedo SRP.

Based on this analysis, a temperature difference of 300° K between the sides of a spherical spacecraft that are perpendicular to the local wind vector can cause a force in the direction of the cold side that is approximately 5% of the SRP force, or 12% of the Earth albedo SRP force at an altitude of 500 km in mean solar conditions.

Therefore, an asymmetric surface temperature distribution can have a small but significant perturbing effect in some scenarios. For example, a low Earth orbiting spacecraft in a sun-synchronous polar orbit, such as the now abandoned TerraSAR-L satellite [35], would experience a temperature difference similar to that employed in the analysis above because of its sun-facing photovoltaic panels and other surfaces.

One last point to note is that the maximum heat transfer rate  $C_{h(max)}$ , which relates to the hottest panels, increases only a negligible amount ( $\sim 0.002$ ) for a surface temperature increase of 200° K. This result justifies the single iteration approach proposed for accurate determination of surface temperature inputs using an external thermal analysis tool, as outlined in Section 7.2.5.

### 8.3 Modelling Reflected Flow

This section presents the results of an analysis that demonstrates the validity of the Hybrid method’s TPMC approach to modelling reflected flow and explains some of the features of the FMF Module that can be used to visualise it.

A simple geometrical configuration has been chosen to enable the reflected flow field and resultant forces to be readily estimated from first principles. The

geometry consists of two rectangular panels (both 1 m wide and 2 m long) placed perpendicular to one another and connected along their longest sides. The panels are orientated so that the free stream flow approaches at an incidence of  $45^\circ$  to both.

The analysis assumed mean solar conditions at an Earth altitude of 400 km, with a wind speed  $V_\infty$  of  $8000 \text{ m s}^{-1}$ . These conditions correspond to a free stream molecular speed ratio  $s_\infty = 8$ . Both panels were assumed to have a surface temperature  $T_w = 300^\circ \text{ K}$ .

The Hybrid Schaaf and Chambre (H-SC) GSIM was used. The GSIM input parameters used are as defined in Table 7-1. Two cases were considered, complete specular reemission and complete diffuse reemission. For this demonstration case, the number of diffusely reflected test particles generated ( $M_d$ ) was set to 50.

Figure 8-12 illustrates the pressure distribution for the two cases analysed. The visualisation functionality used to generate the images shown in Figure 8-12, is a useful feature of the SEDAT System and FMF Module. It is made possible because data related to every gas-surface interaction and test particle is stored in the SEDAT Database. One of the benefits of the functionality is that it enables detailed examination of results that are difficult to understand from raw data and graphs alone.

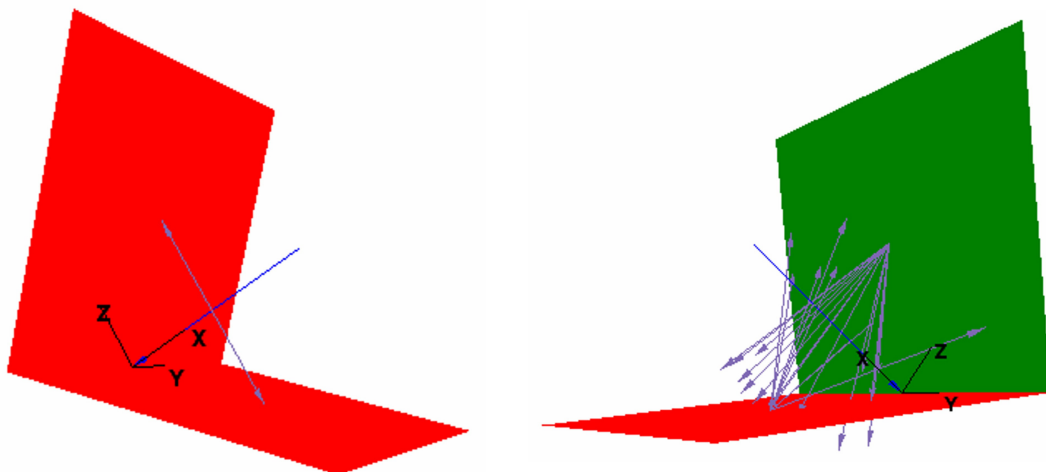


**Figure 8-12 - Corner Plate Analysis: Pressure Distribution and Reflected Test Particle Paths for Specular (left) and Diffuse (right) Accommodation Coefficients**

Images generated using the FMF Module. The free stream flow direction is indicated by the blue arrow along the negative  $x$ -axis in both cases. The purple arrows indicate the directions of reflected test particles. In the specular case (left),  $C_p = 4.03$  for both panels. In the diffuse case (right),  $C_p = 1.14$  for the red panel and  $1.12$  for the green panel.

The blue arrows illustrated in Figure 8-12 indicate the free stream flow direction and the purple arrows indicate reflected test particle directions. The test particles emanate from the centroid of their originating panel. A test particle's arrow

length is equal to the length of the vector between the test particle's origin (the emission panel's centroid) and the impacted panel's centroid. Therefore, test particle arrows may sometimes appear to stop short of the impacted surface or pass straight through it, as illustrated in the diffuse case on the right-hand side of Figure 8-12.

Table 8-3 lists the drag coefficients calculated by the FMF Module, assuming a reference area  $A_{ref} = 4 \text{ m}^2$  (the dynamic pressure  $q_\infty$  corresponding to the free stream conditions described previously is  $1.246 \times 10^{-4} \text{ N m}^{-2}$ ).

**Table 8-3 - Corner Plate Analysis: Drag Coefficient**

	No Reflections	With Reflections
Diffuse	2.10	2.12
Specular	2.03	4.03

In the specular case, all of the reflected flow from one panel is reflected and subsequently impacts the other panel. Since the free stream incident angle is  $45^\circ$ , the reflected flow also impacts the second panel at  $45^\circ$ , as illustrated in the image on the right-hand side of Figure 8-12. Consequently, both the direct free stream flow and the reflected flow exert the same pressure on each plate. Since shear stress is zero in the specular case, the drag force is approximately double that predicted when reflected flow is not simulated.

In the diffuse case, the effect of the diffusely reflected molecules impacting their neighbouring surfaces is negligible in comparison to the effect of the direct impact of the free stream flow. There are two main reasons for this. Firstly, all the diffusely reflected test particles travel at their thermal speed, which is based on the surface temperature ( $V_w = 553 \text{ m s}^{-1}$  from Equation 2-11). This speed is a fraction (approximately  $1/100$ 's) of the free stream speed. Secondly, since the test particles are emitted diffusely few of them (approximately  $1/5$ ) actually hit a neighbouring panel.

Very small lift and side forces are produced by the diffusely reflected molecules impacting their neighbouring surfaces ( $C_L = 0.012$ ,  $C_S = 0.003$ ). These are a result of the very small number of diffusely reflected test particles used ( $M_d = 50$ ). In the results presented, only 22 diffusely reflected test particles impacted a secondary panel (14 hit one panel, and 8 hit the other). This, combined with the different directions of the test particles, is the cause of the small lift and side forces.

Increasing  $M_d$  increases the number of diffusely emitted test particles and reduces these statistical errors, which are a result of the Monte-Carlo sampling technique required to generate the normal distribution of test particle directions (using Equation 7-21). For example, a single test run with  $M_d$  increased to 500 produced the same value of  $C_D$ , but reduced  $C_L$  to 0.001 and  $C_S$  to 0.000.

It should also be noted that results can also be averaged over multiple simulations to find mean values, regardless of the chosen value of  $M_d$  (so long as  $M_d$  is not set impracticably low).

In general, the results indicate that the modelling of diffusely reflected flow is sensitive to  $M_d$ , but that even low values of  $M_d$  can yield useful results, particularly if multiple analyses are run in order to calculate mean values. However, at orbital speeds, with realistic surface temperatures, the effect of diffusely reflected flow is negligible in comparison to the effect of specularly reflected flow and so this sensitivity is not always relevant.

Before leaving this section, it is worthwhile discussing the effects of the reflected flux on surface heating. Since the diffusely reemitted test particles leave the surface in thermal equilibrium with it, both surfaces are set to the same temperature, and the mean number of internal degrees of freedom of the free stream is negligible, the diffusely reflected test particles transfer very little heat to the surfaces during secondary interactions. Furthermore, the specularly reemitted test particles do not transfer any heat to the surfaces during secondary interactions, since these interactions are also specular.

A significant heat transfer due to the reflected flux would only be noticeable if the accommodation coefficients lay somewhere between the two limits of specular and diffuse reemission. In such a scenario, the specularly reemitted test particles would transfer heat to secondary surfaces due to the partially diffuse nature of the secondary interactions. For an example of this, refer to Figure 8-26 in Section 8.4.2.

## 8.4 Drag Deorbit Device

In order to fulfil objective two, outlined in Section 1.4, this section presents the results of multiple analyses of the drag deorbit device that is under development within the Space Research Centre (SRC).

As mentioned previously, Harkness [12] has developed an optimal design for such a device that has the geometry of a four-sided pyramidal cone when deployed, as illustrated in Figure 8-13.

Harkness based his aerodynamic analysis on a circular cone because it is simpler to analyse. The analyses presented here use the same cone geometry specified by Harkness. The cone's base radius  $r$  is 1.784 m and its height  $h$  is 1.147 m. This geometry corresponds to an apex half-angle  $\phi$  of 1 radian ( $57.30^\circ$ ) and a base area of  $10 \text{ m}^2$ . For the purposes of calculating aerodynamic coefficients, the reference length  $l_{ref}$  is set to the height ( $h$ ) and the reference area  $A_{ref}$  is set to the base area.

According to Harkness's definitions, drag coefficient refers to the force coefficient in the body-fixed  $-x$  direction  $C_{F(-x)}$ , lift coefficient refers to the force in



the body-fixed  $-z$  direction  $C_{F(-z)}$ , and the restoring torque coefficient refers to the torque about the body-fixed  $y$ -axis  $C_{T(y)}$  (the subscript  $s/c$  used to denote the spacecraft's body-fixed coordinate system in Figure 8-2 and elsewhere has been dropped throughout this section for clarity).

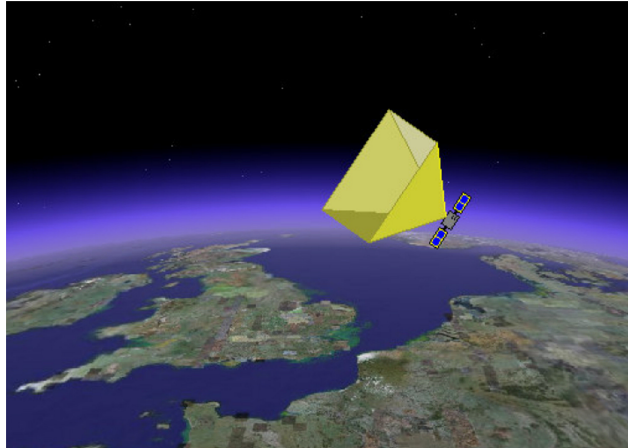


**Figure 8-13 - Drag Sail Concept**

**Image credit Harkness [12], background credit Google Earth. Image shows the fully deployed drag sail before collapse.**

These definitions are different to the actual lift and drag definitions described in Section 8.1, which are used conventionally. Therefore, for clarity, the body-fixed coordinate axes, body-fixed force and torque directions defined by Harkness, actual lift and drag directions, and geometry of the cone are illustrated in two dimensions in Figure 8-14. As before, the angle  $\alpha$  illustrated in Figure 8-14 represents the angle of attack of the free stream flow.

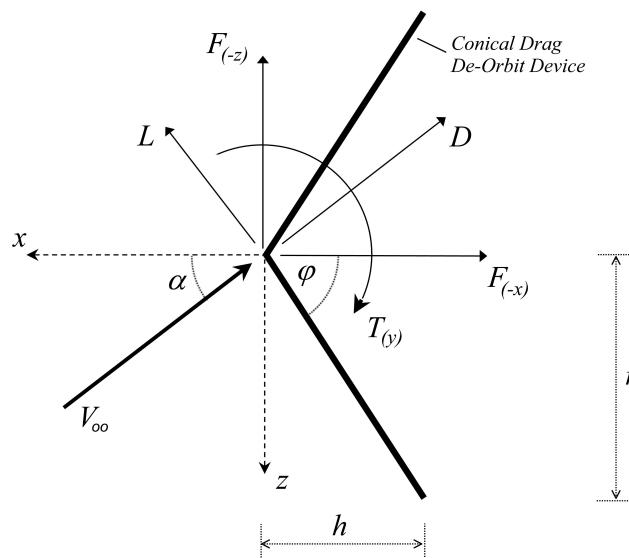


**Figure 8-14 - Drag Deorbit Device Analysis: Cone Geometry, Body-Fixed Force ( $F$ ) and Torque ( $T$ ) Definitions, and Drag ( $D$ ) and Lift ( $L$ ) Directions**

The deployed device would be connected via its apex to the parent spacecraft, as illustrated in Figure 8-13. Therefore, the centre-of-gravity of the system can be assumed represented by a point mass at the cone's apex. Consequently, the reference origin chosen for all moments is the apex.

For the material of the drag sail, Harkness proposes the use of either kapton or mylar films 5  $\mu\text{m}$  thick. However, the empirically based Knechtel and Pitts (K & P) [17] and Mazanek et al [20] accommodation coefficients, defined using the input parameters listed in Table 7-1, correspond to oxygen impacting an aluminium surface. Such data is not available for either kapton or mylar. Therefore, for the purposes of these analyses, it is necessarily assumed that the surface of the drag sail is aluminium.

A thermal analysis conducted by Harkness indicates that the deployed drag deorbit device would have a uniform surface temperature  $T_w$  of approximately 500° K. Therefore, all surface mesh panels are set to this temperature.

The trends of aerodynamic forces with increasing altitude and different solar conditions have been investigated and are presented in Section 8.2.2. Therefore, this section will only present the results of analyses at 500 km in mean solar conditions. This altitude was chosen for three reasons:

1. Harkness used the Newtonian GSIM, which is altitude-independent (calculation of pressure coefficient depends only on the incidence angle of the flow  $\delta$ ).
2. Harkness presented attitude simulation results for three selected altitudes, which are close to 500 km (450 km, 550 km, and 650 km). However, the database of atmospheric model data installed with the SEDAT System does not include data for these specific altitudes.
3. An analysis similar to that presented in Section 8.2.2, but assuming  $T_w = 500^\circ \text{ K}$ , also produces a drag coefficient of 2.2 for a sphere at 500 km, in mean solar conditions, using the Mazanek accommodation coefficients. Therefore, according to Mazanek's approach, the Mazanek accommodation coefficients are calibrated for the drag deorbit device operating at 500 km.

It is assumed that the spacecraft is operating in a circular orbit and that its incident wind speed can be approximated by its orbital speed (7,612.68  $\text{m s}^{-1}$ ). These conditions correlate to a hyperthermal molecular speed ratio  $s_\infty$  of 7.21  $\text{m s}^{-1}$ , a molecular kinetic energy  $e_{k,e}$  of 4.66 eV, and a Knudsen number  $Kn$  of approximately 36,000. Where  $Kn$  is based on  $l_{ref}$  and a mean free path  $\lambda$  that assumes a molecular mean collision diameter  $d_{avg}$  equivalent to that for  $N_2$  ( $3.62 \times 10^{-10} \text{ m}$ ).

Two surface meshes have been used to analyse the drag deorbit device concept proposed by Harkness. The first, referred to as the coarse surface mesh is

illustrated on the left of Figure 8-15. The second, referred to as the refined surface mesh is illustrated on the right of Figure 8-15.

The coarse surface mesh is a structured triangular mesh composed of 224 panels (112 forward facing panels, 112 aft facing panels). The refined surface mesh is an unstructured triangular mesh composed of 1,336 panels (668 forward facing panels, 668 aft facing panels).

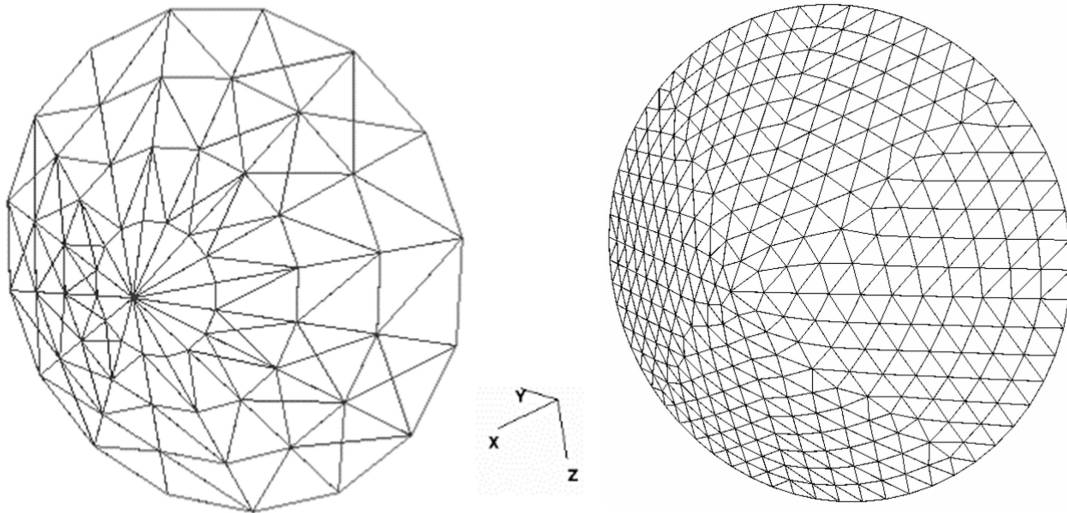


**Figure 8-15 - Drag Deorbit Device Analysis: Coarse Surface Mesh (Left), Refined Surface Mesh (Right)**  
 Images generated using the FMF Module.

#### 8.4.1 Comparison with Analytical Newtonian Results

This section compares the results of an analysis using the Newtonian GSIM described in 7.1 with Harkness's analytical Newtonian results.

Harkness derived complex analytical expressions to calculate the forces exerted on the inside surfaces of the cone, whilst accounting for the effects of surface shielding. Therefore, Harkness's results present an exact analytical solution for a cone using a Newtonian GSIM for  $0^\circ \leq \alpha \leq 180^\circ$ .

In contrast, the FMF Module used the shielding method outlined in Section 6.2.2 to determine which surface mesh panels would be shielded to the free stream flow. The initial FMF Module analysis of the cone used the coarse surface mesh illustrated on the left of Figure 8-15.

The results of Harkness's analytical analysis and the initial FMF Module analysis were compared by Harkness, as shown in Figure 8-16. The plots in the figure illustrate that using the coarse surface mesh the FMF Module predicts a slightly smaller magnitude of force in the  $-x$  direction at angles of attack close to  $0^\circ$

and  $180^\circ$ , and a slightly smaller negative torque about the y-axis at angles of attack close to  $45^\circ$  and  $135^\circ$ .

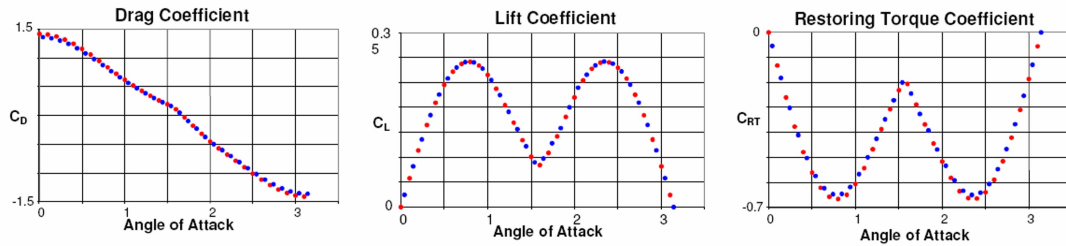


**Figure 8-16 - Drag Deorbit Device Analysis: Newtonian Results Compared with Analytical Calculations**

Image credit Harkness [12]. Drag Coefficient refers to the force coefficient in the body-fixed  $-x$  direction  $C_{F(-x)}$ , Lift Coefficient refers to the force in the body-fixed  $-z$  direction  $C_{F(-z)}$ , and the Restoring Torque Coefficient refers to the torque about the body-fixed  $-y$ -axis  $C_{T(-y)}$ . The Angle of Attack is given in radians. Harkness’s results are identified by red markers, the results of the FMF Module, which are based on the coarse surface mesh illustrated on the left of Figure 8-15, are indicated by blue markers.

Figure 8-17 illustrates a comparison between results calculated using the coarse surface mesh and results calculated during a later analysis using the refined surface mesh illustrated on the right of Figure 8-15. The convergence of the refined surface mesh results towards Harkness’s analytical results clearly indicates that these discrepancies are caused by the coarse surface mesh representation of the cone.

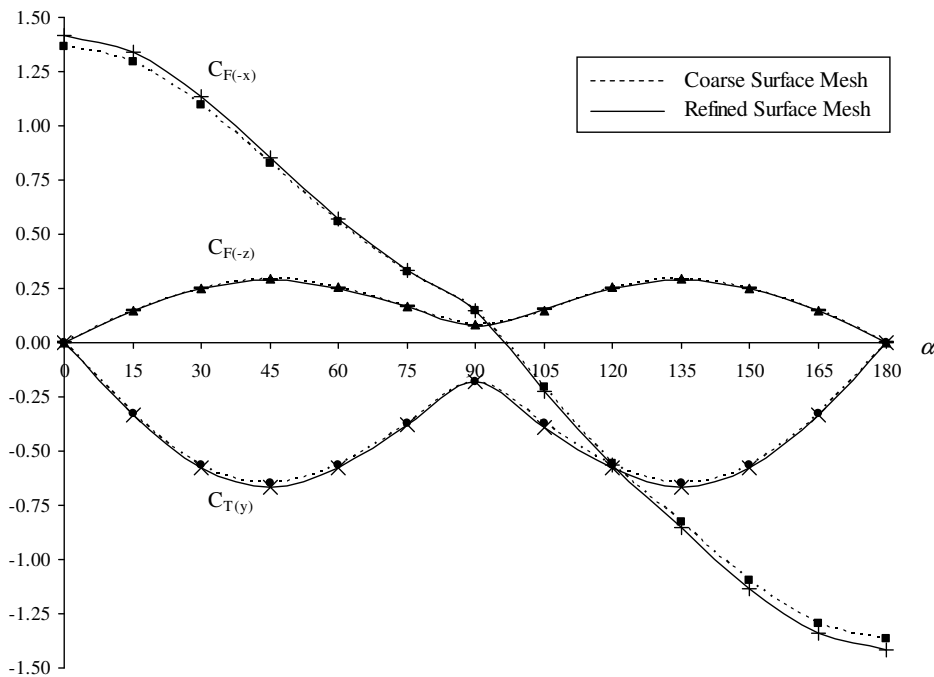


**Figure 8-17 - Drag Deorbit Device Analysis: Force and Torque versus Angle of Attack for Coarse and Refined Surface Meshes, using a Newtonian GSIM**

The close agreement between Harkness's analytical results and the results calculated for the refined surface mesh provide confidence in the FMF Module and, in particular, the shielding calculation of the SEDAT Ray-Tracer, outlined in Section 6.3. They also indicate that the accuracy provided by the refined surface mesh is sufficient for the purposes of performing shielding calculations (more refined surface meshes have been tested, but they did not provide a noticeable improvement in accuracy).

In order to demonstrate this accuracy, the refined surface mesh shielding calculated by the SEDAT Ray-Tracer during processing by the FMF Module is illustrated in Figure 8-18, for three different angles of attack.

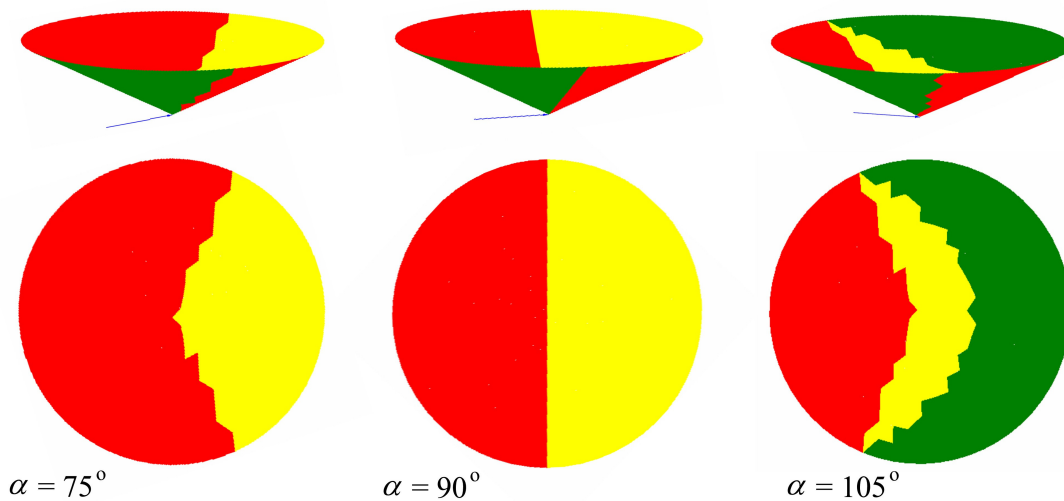


**Figure 8-18 - Drag Deorbit Device Analysis: Ray-Tracer Renderings for Angles of Attack 75°, 90°, and 180° showing Side and Rear Views**

Image generated using the FMF Module. Red panels are aft facing, yellow panels are shielded, and green panels are impacted by the free stream flow. The blue arrow indicates the free stream direction. The side views are shown along the top row and the rear views are shown along the bottom row.

#### 8.4.2 Comparison of Different Accommodation Coefficient Results

This section uses the Hybrid Schaaf and Chambre (H-SC) GSIM described in Section 7.2 to compare the effects of using different accommodation coefficients. As before, the input parameters used to calculate the accommodation coefficients are defined in Table 7-1.

As in Section 8.4.1, the shielding method outlined in Section 6.2.2 is used to determine areas of the inside surfaces of the cone that would be shielded to the free stream flow. However, this section also presents the results of analyses using the Hybrid method's TPMC approach to modelling reflected flow, which is described in

Section 6.2.3. Results are presented for both the coarse and refined surface meshes illustrated in Figure 8-15.

As has been shown in Section 8.3, the forces imparted by diffusely reemitted test particles hitting a secondary surface are negligible in the low Earth orbital conditions being considered. In contrast, the forces imparted by specularly reemitted test particles can be significant. For the cone geometry being considered, any specularly reflected test particle reemitted during the secondary interaction of a specularly reemitted test particle, will not impact subsequent panels. Therefore, in order to model reflected flow, reemitted test particles were simulated for one interaction only.

The results for the specular reemission case are illustrated in Figure 8-19. As illustrated in the figure, the coarse and refined surface mesh results both show the same trends across all angles of attack. However, like the Newtonian results illustrated in Figure 8-17, the refined surface mesh results display a slightly larger magnitude of force in the  $-x$  direction close to  $0^\circ$  and  $180^\circ$  and a slightly larger negative torque about the  $y$ -axis at angles of attack close to  $45^\circ$  and  $135^\circ$  ( $145^\circ$  in the case of reflected flow). These trends are consistent across all the accommodation coefficients analysed, as illustrated in subsequent figures.

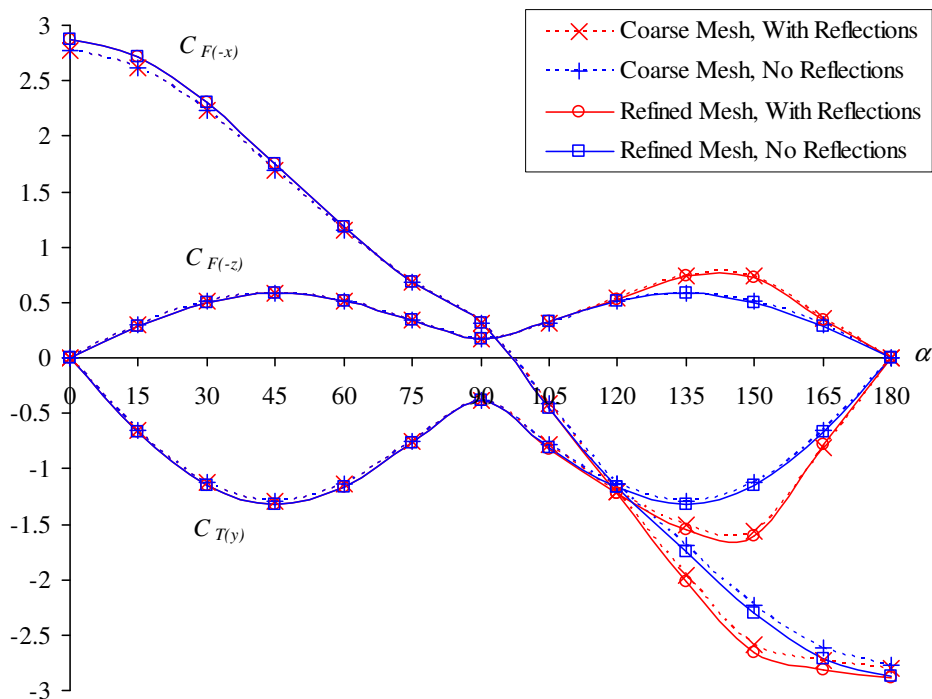


**Figure 8-19 - Drag Deorbit Device Analysis: Body-Fixed Force and Torque Coefficients versus Angle of Attack, assuming Specular Reflection**

As described in Section 8.4.1, the refined surface mesh produced results comparable with an analytical solution using a Newtonian GSIM. Since the same convergence is evident for the accommodation coefficients analysed here, it is concluded that the refined surface mesh provides a sufficient level of accuracy for the purposes of this study.

The effect of specularly reflected test particles impacting secondary surfaces is clearly illustrated in Figure 8-19. Between the angles of attack of  $90^\circ$  and  $180^\circ$ , the  $C_{F(-x)}$ ,  $C_{F(-z)}$ , and  $C_{T(y)}$  reflected results all have bigger magnitudes than the results that do not account for reflected flow, with the greatest differences occurring at approximately  $145^\circ$ .

Figure 8-20 shows several screen shots from the FMF Module, which illustrate the paths of the specularly reflected test particles that impact secondary surfaces.

It illustrates that for  $90^\circ < \alpha < 180^\circ$ , the geometry of the cone causes the specularly reflected test particles to impact the panels on the far side of the cone causing large increases in pressure in the impacted region. The consequences of this pattern of specularly reflected flow will be discussed with reference to the empirically based Mazanek accommodation coefficient results presented later.

For  $\alpha = 180^\circ$ , the  $C_{F(-x)}$  curves illustrated in Figure 8-19 for the reflected flow case converge towards the results that exclude the effects of reflected flow and approximate the values for the front surface of the cone. This seems counter-intuitive since it might be expected that  $C_{F(-x)}$  would have a greater magnitude owing to the effects of multiple reflections inside the rear surfaces of the cone.

However, inspection of Figure 8-20 reveals that in fact the cone's apex half-angle  $\phi$  is so large that at  $\alpha = 180^\circ$  very few specularly reflected test particles impact secondary surfaces. Consequently, the magnitudes of the forces and moments caused at  $\alpha = 0^\circ$  and  $\alpha = 180^\circ$  are approximately equal, assuming complete specular reflection.

It should also be noted that the small variations in pressure coefficient at  $\alpha = 180^\circ$ , related to the direct impact of the free stream flux only, which are visible in Figure 8-20, are due to the slightly different incidences of the surface mesh's panels. The  $C_p$  variations are small (approximately 0.1) and tests using a surface mesh with a higher mesh density have shown that they have a negligible effect on the spacecraft's total aerodynamic forces and moments. Use of a more sophisticated surface distribution renderer, to smooth the colour contours across multiple panels, would provide a more realistic image of the pressures.

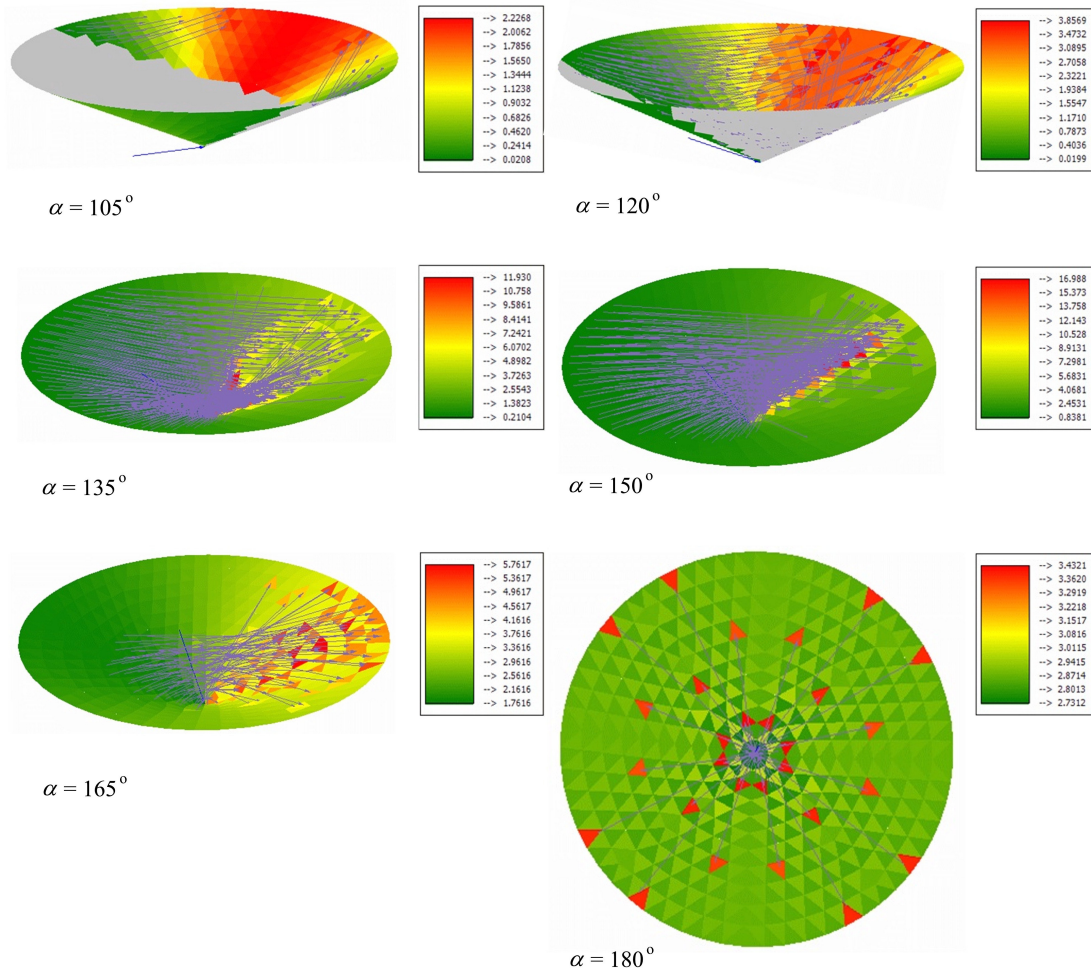


**Figure 8-20 - Drag Deorbit Device Analysis: Pressure Coefficient ( $C_p$ ) Distribution assuming Specular Reflection for Angles of Attack  $105^\circ$ ,  $120^\circ$ ,  $135^\circ$ ,  $150^\circ$ ,  $165^\circ$ , and  $180^\circ$**

Images generated using the FMF Module. The free stream flow direction is indicated by the blue arrow in all cases. The purple arrows indicate the directions of the reflected test particles. The grey surfaces indicate shielded or aft facing surfaces. To the right of each image is its corresponding pressure coefficient colour key.

The results for the diffuse reemission case are shown in Figure 8-21. The large number of diffusely reflected test particles that impact secondary surfaces is evident from the purple colouring visible in Figure 8-22, which is a screen shot from the FMF Module for  $\alpha = 180^\circ$ .



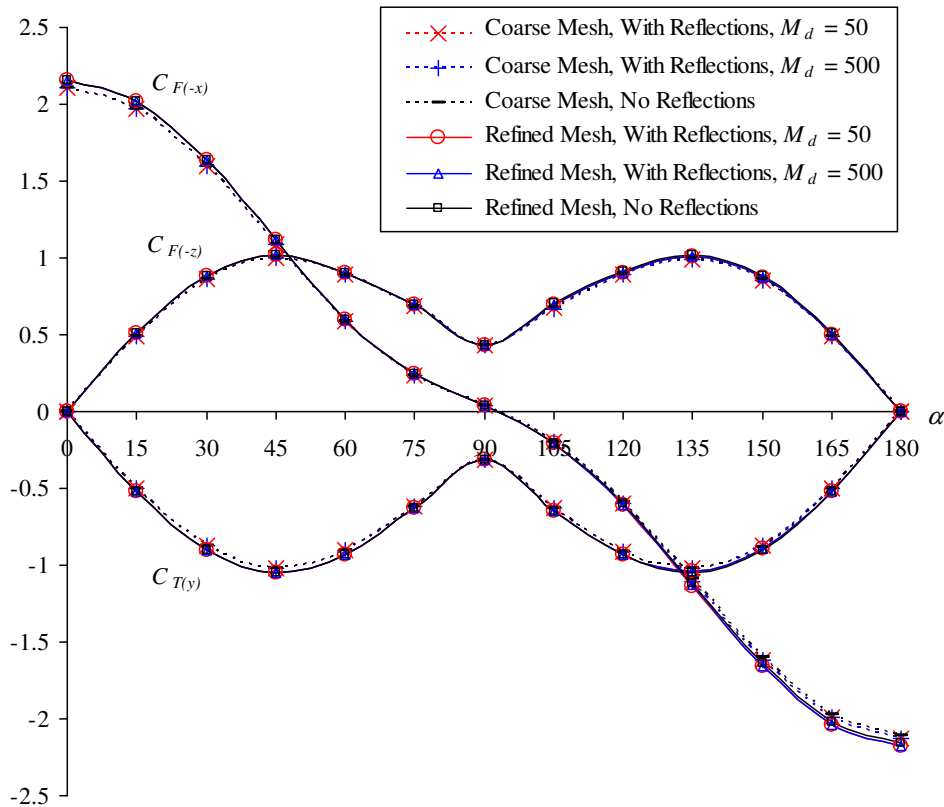


**Figure 8-21 - Drag Deorbit Device Analysis: Body-Fixed Force and Torque Coefficients versus Angle of Attack, assuming Diffuse Reflection**  
 $M_d$  refers to the user-defined number of diffusely reemitted test particles generated during a gas-surface interaction (as described in Section 7.2.1).

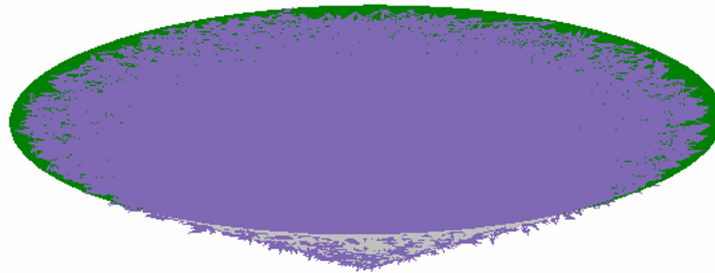


**Figure 8-22 - Drag Deorbit Device Analysis: Diffusely Reflected Test Particle Paths for Angle of Attack  $\alpha = 180^\circ$**

Image generated using the FMF Module. The purple arrows indicate the directions of the reflected test particles. The grey surfaces indicate shielded or aft facing surfaces.

As discussed previously, the momentum imparted by diffusely reflected molecules impacting secondary surfaces is negligible. Therefore, only a very small increase in the magnitude of  $C_{F(-x)}$  is evident in the reflected results illustrated in Figure 8-21 (occurring as  $\alpha$  approaches  $180^\circ$ ). Furthermore, the results illustrated in

the figure indicate that there is little sensitivity to  $M_d$  (the number of diffusely reemitted test particles generated during a gas-surface interaction).

Since the diffusely reemitted test particle directions are generated using a Monte-Carlo sampling technique a small degree of scatter between results would be expected (regardless of the value of  $M_d$ ). However, given the minimal benefit of modelling secondary interactions of diffusely reflected test particles, statistical analyses using multiple results sets to determine average values have not been conducted.

Analyses have been carried out using the empirically based Knechtel and Pitts (K & P) and Mazanek accommodation coefficients described in Section 7.2.6. For comparison, an analysis has also been performed which assumes quasi-specular reemission. In this “50-50” analysis,  $A_n$ ,  $B_t$ , and  $C_t$ , as defined in Table 7-1, are all set to 0.5 to simulate a scenario in which 50% of the flux is reemitted diffusely and the remaining 50% is reemitted specularly, such that  $\sigma_N = \sigma_T = \sigma_Q = 0.5$ .

Based on the diffuse result findings, the K & P, Mazanek, and 50-50 results illustrated in Figure 8-23, Figure 8-24, and Figure 8-25, respectively were all calculated with  $M_d = 50$ .

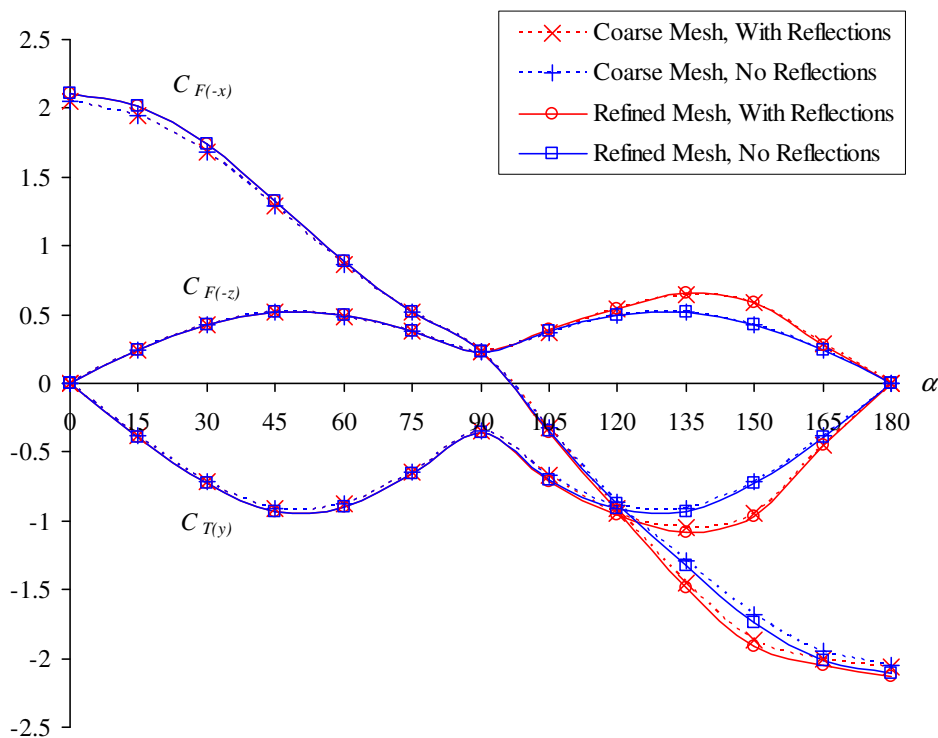


**Figure 8-23 - Drag Deorbit Device Analysis: Body-Fixed Force and Torque Coefficients versus Angle of Attack, assuming Knechtel & Pitts (K & P) Accommodation Coefficients**

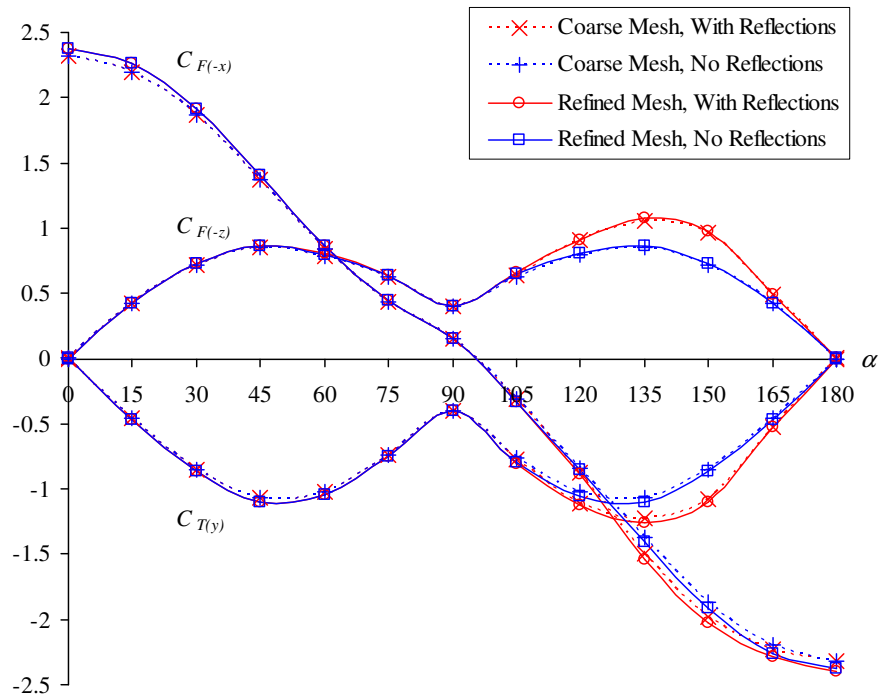


**Figure 8-24 - Drag Deorbit Device Analysis: Body-Fixed Force and Torque Coefficients versus Angle of Attack, assuming Mazanek Accommodation Coefficients**

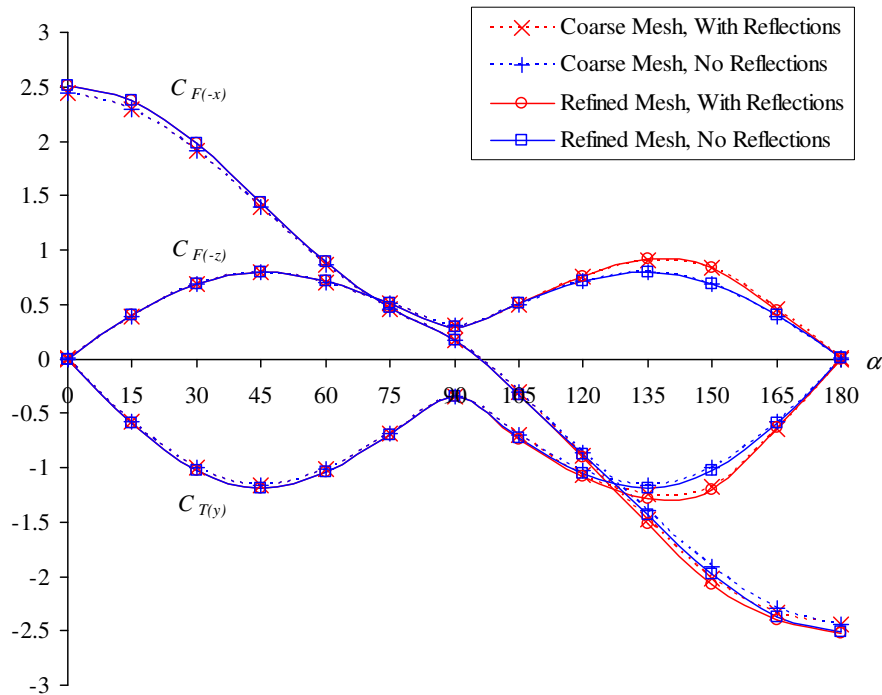


**Figure 8-25 - Drag Deorbit Device Analysis: Body-Fixed Force and Torque Coefficients versus Angle of Attack, assuming Quasi-Specular "50-50" Remission**

Figure 8-26 and Figure 8-27 show several selected screen shots from the FMF Module, which illustrate the pressure, shear stress, and heat transfer distributions over the surface for various angles of attack using the Mazanek accommodation coefficients.

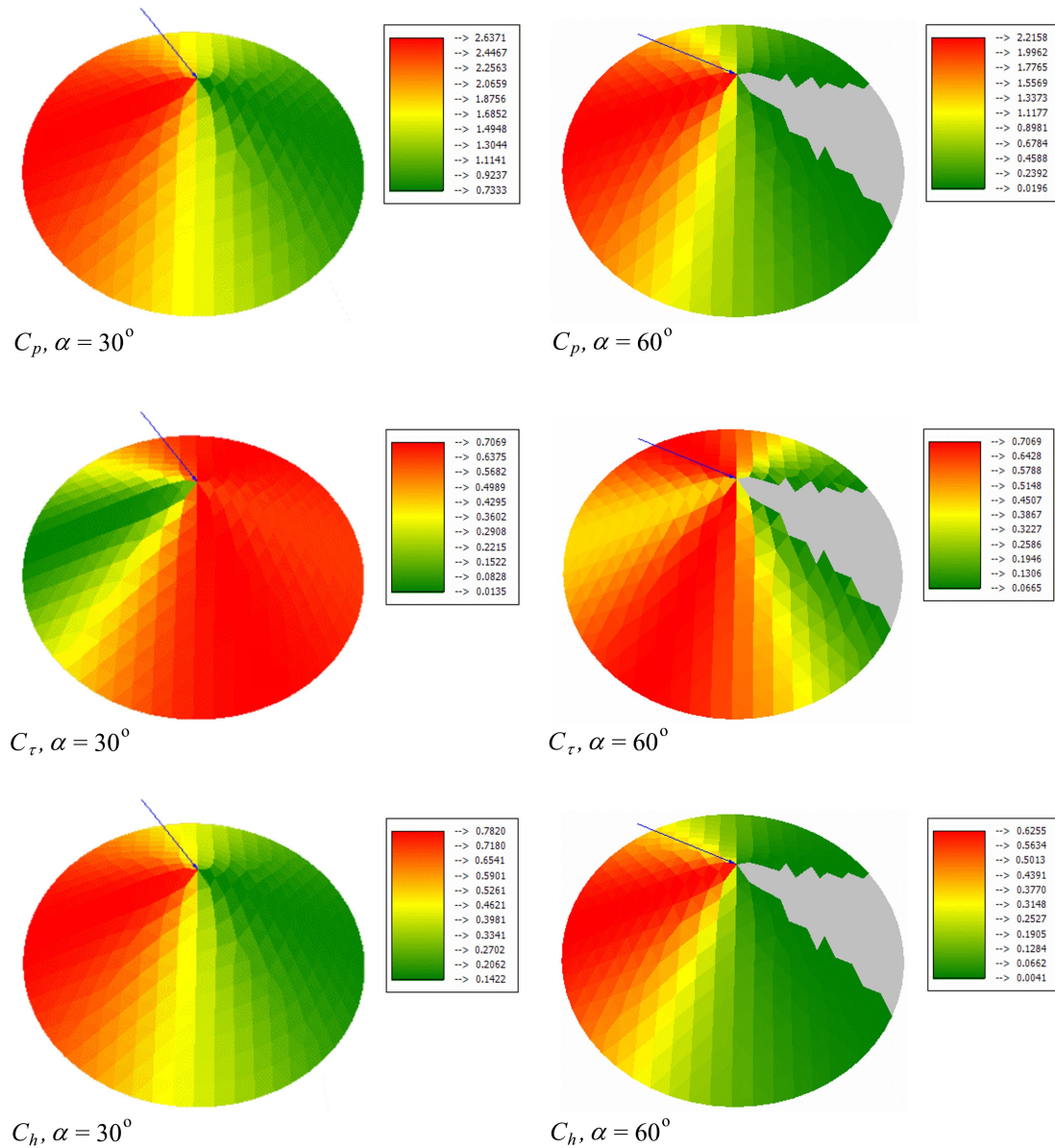


**Figure 8-26 - Drag Deorbit Device Analysis: Pressure ( $C_p$ ), Shear Stress ( $C_\tau$ ), and Heat Transfer ( $C_h$ ) Coefficient distributions assuming Mazanek Accommodation Coefficients for Angles of Attack  $30^\circ$  and  $60^\circ$**

Images generated using the FMF Module. The free stream flow direction is indicated by the blue arrow in all cases. The grey surfaces indicate shielded or aft facing surfaces. To the right of each image is its corresponding colour key.

For  $0^\circ < \alpha < 90^\circ$ , the distributions illustrated in Figure 8-26 show the trends expected, based upon the flat plate and sphere analyses presented in Section 8.2.1 and Section 8.2.3 respectively.

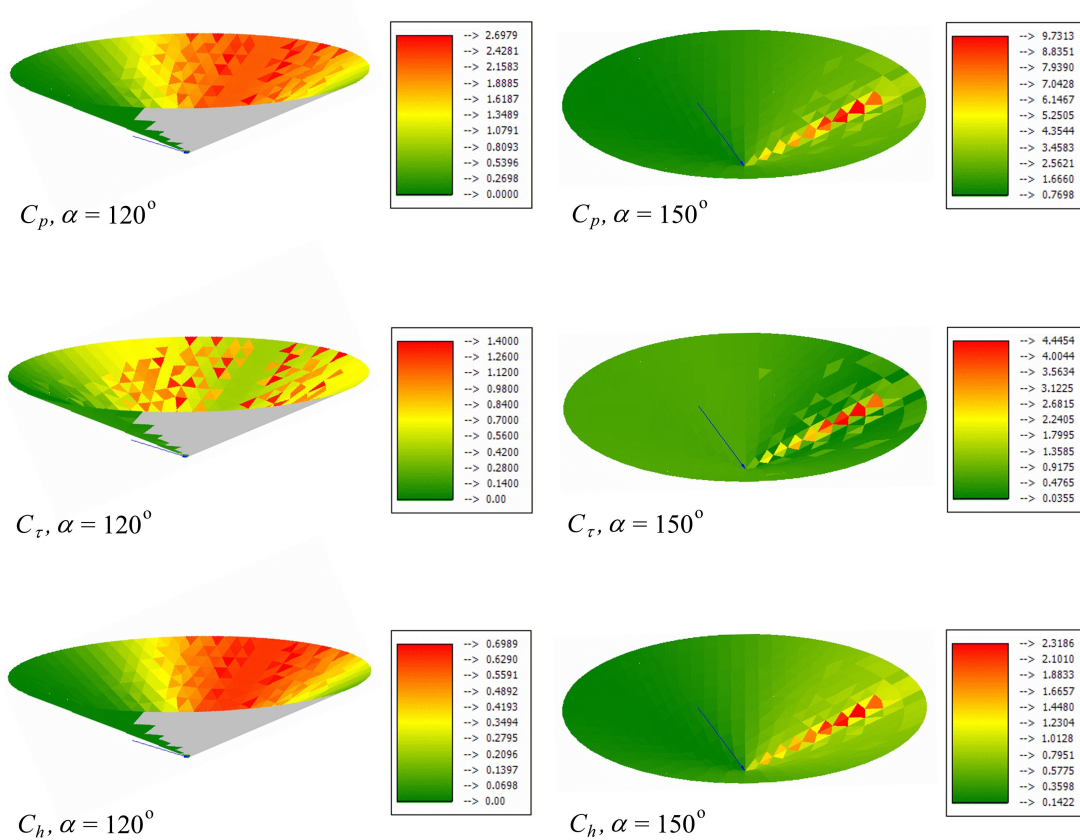


**Figure 8-27 - Drag Deorbit Device Analysis: Pressure ( $C_p$ ), Shear Stress ( $C_\tau$ ), and Heat Transfer ( $C_h$ ) Coefficient distributions assuming Mazanek Accommodation Coefficients for Angles of Attack  $120^\circ$  and  $150^\circ$**

Images generated using the FMF Module. The free stream flow direction is indicated by the blue arrow in all cases. The directions of the reflected test particles are not illustrated. The grey surfaces indicate shielded or aft facing surfaces. To the right of each image is its corresponding colour key.

For  $90^\circ < \alpha < 180^\circ$ , the distributions illustrated in Figure 8-27 show the effects of the specularly reflected flow described previously. In the case of the Mazanek accommodation coefficients, this means that the panels that are impacted by the specularly reflected test particles exhibit large increases in pressure, shear stress, and heating.

The increases are most significant at  $135^\circ < \alpha < 155^\circ$ , because at these angles of attack the specularly reflected test particles converge on the region along the centre-line of the far side of the cone, as illustrated in Figure 8-27 for  $\alpha = 150^\circ$ .

The rises in pressure, shear stress, and heating caused by the specularly reflected flux may affect the structural integrity of the drag deorbit device and hence

its shape. This change in shape would in turn affect the device's aerodynamics, creating a feedback situation that would be difficult to model due to its dynamic nature.

One of the maxims of spacecraft engineering is that if something cannot be modelled with a high degree of confidence or otherwise tested it should not be flown. Therefore, it is recommended that the drag deorbit device should be designed so that its shape is not significantly compromised under the increased aerodynamic loads caused by the specularly reflected flow. Similarly, thermal analyses should be conducted to check that the increased heating caused by the specularly reflected flow does not adversely affect structural integrity or other performance characteristics.

As per the purely specular results, at  $\alpha = 180^\circ$ , very little specularly reflected flow impacts secondary surfaces using the Mazanek accommodation coefficients. Therefore, the magnitudes of the forces and moments caused at  $\alpha = 0^\circ$  and  $\alpha = 180^\circ$  are approximately equal.

The specular, diffuse, Knechtel and Pitts, and Mazanek results that include the effects of reflections are compared in Figure 8-28. Also shown in the figure for comparison are the Newtonian results from Figure 8-17. All five results sets are based upon the refined surface mesh. The diffuse result set plotted corresponds to  $M_d = 500$ , the Knechtel and Pitts and Mazanek results sets correspond to  $M_d = 50$ .

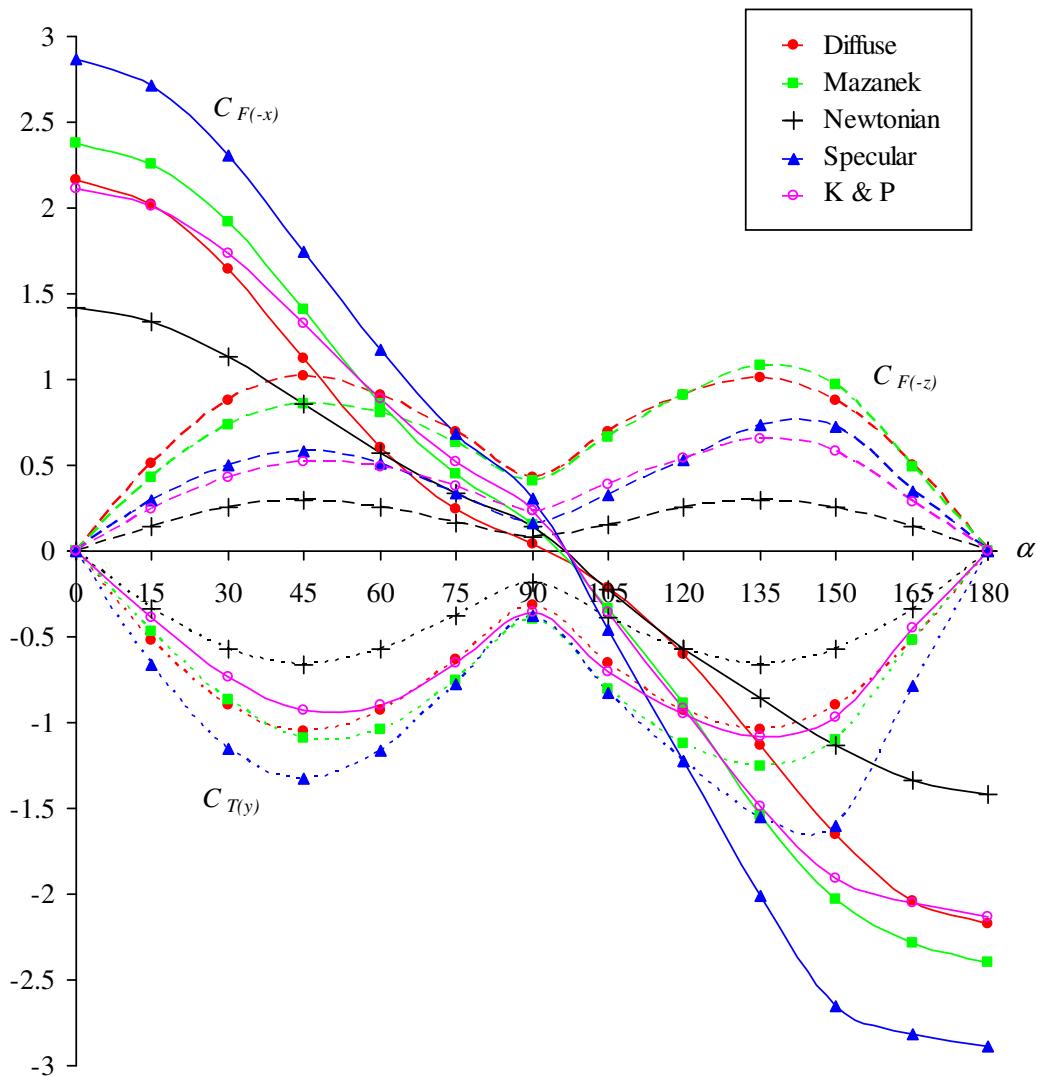


**Figure 8-28 - Drag Deorbit Device Analysis: Body-Fixed Force and Torque Coefficients versus Angle of Attack for Different GSIMs and Accommodation Coefficients**

Results calculated using the refined surface mesh illustrated in Figure 8-15. The Specular, Diffuse, Knechtel and Pitts (K & P), and Mazanek results incorporate the effects of multiple molecular reflections.

In order to help with the interpretation of these results, plots of lift and drag versus angle of attack are illustrated in Figure 8-29 for the same analyses. For consistency, the definition of lift provided in Section 8.1 has been used, which results in the lift direction illustrated in Figure 8-14. Based on this definition, a negative lift force is generated for all angles of attack.

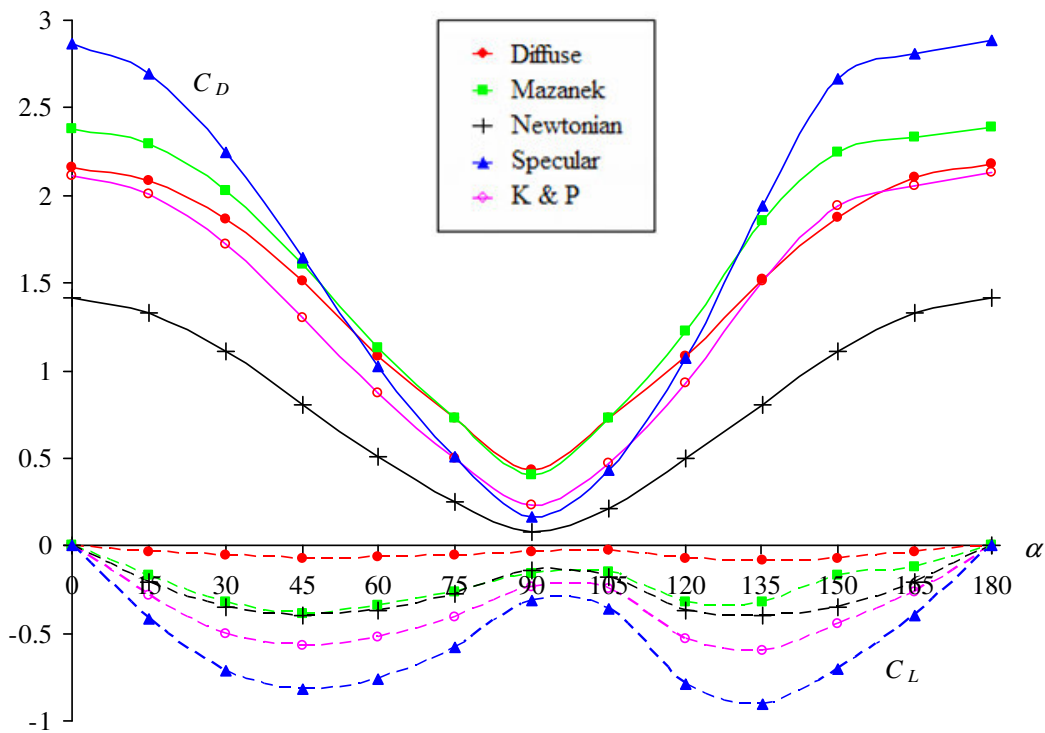


**Figure 8-29 - Drag Deorbit Device Analysis: Lift and Drag Coefficients versus Angle of Attack for Different GSIMs and Accommodation Coefficients**

Results calculated using the refined surface mesh illustrated in Figure 8-15. The Specular, Diffuse, Knechtel and Pitts (K & P), and Mazanek results incorporate the effects of multiple molecular reflections.

For optimal performance a drag deorbit device should be statically stable and produce maximum drag in its nominal flight attitude ( $\alpha \sim 0^\circ$ ). Inspection of Figure 8-28 and Figure 8-29 reveals several interesting findings related to the aerodynamic performance of the conical drag deorbit device design, which are described in the following bullet points:

1. The lowest drag and restorative torques across all angles of attack are predicted by the Newtonian GSIM. This indicates that the analytical Newtonian method used by Harkness provided a conservative estimate of the performance of the conical drag deorbit device. This finding provides further confidence in the drag deorbit device concept. However, it also indicates that the structure of the drag deorbit device may need to be reinforced to cope with the increased aerodynamic loads predicted if it is to maintain its shape within reasonable margins.
2. The H-SC GSIM results demonstrate that the geometry of the drag deorbit device determines whether specular or diffuse reemission has a greater influence on aerodynamic performance at any given angle of attack. For the



geometry analysed, drag is highest in the specular case when the device is in its optimal flight orientation. Furthermore, the restoring torque is also highest in the specular case for all angles of attack. Therefore, for the geometry analysed, the results indicate that for optimal aerodynamic performance the surface materials and surface characteristics of the drag deorbit device should be chosen to maximise the extent of specular reflection.

3. There are scenarios in which the flatter shapes and lower maximums of the drag curves caused by more diffuse reemission might confer some benefits. For example, if attitude stability cannot be achieved and the device becomes orientated sub-optimally. Alternatively, if the higher aerodynamic loads predicted in the case of specular reemission and multiple reflection cause significant deformation of the sail shape that cannot be eliminated without compromising other design requirements.
4. In general, it may be concluded that the effect of reflected flow impinging on secondary surfaces is to increase the force in both the  $+x$  and  $+z$  directions when  $90^\circ < \alpha < 180^\circ$ , thus increasing drag and restorative torque. Therefore, for the geometry analysed, the effect of multiple molecular reflections is to improve the aerodynamic performance of the drag deorbit device.

Based upon the discussion of accommodation coefficients in Section 3.3, finding 2 indicates that the drag sail surface should be as clean, smooth, and hot as possible. In addition, it should be manufactured from materials that inherently produce increased specular reemission, which are also not susceptible to atomic oxygen attack.

A recent experimental study conducted by Cook [74] analysed the angular distribution of reemitted  $H_2$ ,  $N_2$ ,  $CO$ , and  $CO_2$  flux from a variety of spacecraft surfaces at incident speeds of approximately  $4,620 \text{ m s}^{-1}$ , using a modified Nocilla GSIM. The results of the study indicate that kapton, which is one of the drag sail material options considered by Harkness, produces a higher degree of specular reemission than many other spacecraft surfaces. Furthermore,  $SiO_2$ -coated kapton, which has greater resistance to atomic oxygen attack [76], was found to have a similarly specular reemission pattern.

However, it is questionable whether Cook's findings can be extrapolated to the higher incident speeds considered here for an incident molecular flux of  $O_2$ , which is the dominant molecular constituent at 500 km in mean solar conditions.

The higher drag and restorative torque and lower negative lift predicted for the Mazanek accommodation coefficients across all angles of attack in comparison to the Knechtel and Pitts results indicates that shear stresses must be accurately accounted for to assess aerodynamic performance. The bullet points below describe

some of the detailed trends illustrated in Figure 8-28 and Figure 8-29 in relation to the Knechtel and Pitts and Mazanek predictions:

1. At angles of attack between approximately  $57^\circ$  and  $123^\circ$ , shear stresses dominate the drag response, with higher shear stresses leading to higher drag. Consequently, between these angles of attack, the diffuse and Mazanek accommodation coefficients predict the highest drag. Furthermore, across all angles of attack the diffuse and Mazanek accommodation coefficients cause the highest  $C_{F(-z)}$  values, leading to much smaller negative values of lift.
2. Between  $57^\circ < \alpha < 123^\circ$ , the lower shear stresses predicted by the Knechtel and Pitts accommodation coefficients in comparison to the Mazanek coefficients result in a larger magnitude of  $C_{F(-x)}$  (because between these angles of attack the shear stresses generated act in the  $+x$  direction). However, for all other  $\alpha$ , the higher shear stresses predicted by the Mazanek accommodation coefficients result in higher magnitudes of  $C_{F(-x)}$ .
3. The specularly reflected test particles in the Knechtel and Pitts and Mazanek cases generate significant pressures and shear stresses on the secondary surfaces they impact, causing the small reduction in negative lift and increase in drag noticeable for  $135^\circ < \alpha < 165^\circ$ . The Mazanek results exhibit more significant effects due to the increased shears predicted. However, even in the Knechtel and Pitts case, the effect of the specularly reflected test particles impacting secondary surfaces is sufficient to increase the drag force above that predicted by the diffuse case.

As described in the introduction to Section 8.4, the Mazanek accommodation coefficients are calibrated for the free stream conditions and surface temperatures being considered using the same technique as Mazanek. Therefore, it is recommended that the Mazanek force, torque, and heat transfer predictions should be used in any future attitude and orbital simulation (in equivalent free stream conditions).

### 8.4.3 Damping Torques

As described in Section 6.5.2, the FMF Module provides the functionality to calculate aerodynamic damping torques. However, as also noted in Section 6.5.2, the modelling of aerodynamic damping torques is no longer considered a vital objective of this PhD because Harkness [12] has shown that their effect on the performance of the drag deorbit device is negligible. Furthermore, the Hybrid method cannot account for the effect of reflected flux in concave regions of rotating bodies, for the reasons described in Section 6.5.2.

Nonetheless, analyses have been performed to quantify the effect of aerodynamic damping on the conical drag deorbit device analysed in the previous two sections. A one radian per second negative rotation about the  $y$ -axis was applied to the device. Only forward facing unshielded surface mesh panels were tested for gas-surface interactions and, for the reasons stated previously, reflected flow was not modelled.

Figure 8-30 presents the results of the analyses using the same H-SC GSIM accommodation coefficients and Newtonian GSIM used in Section 8.4.1 and Section 8.4.2 respectively. The refined surface mesh illustrated in Figure 8-15 was used for all analyses.

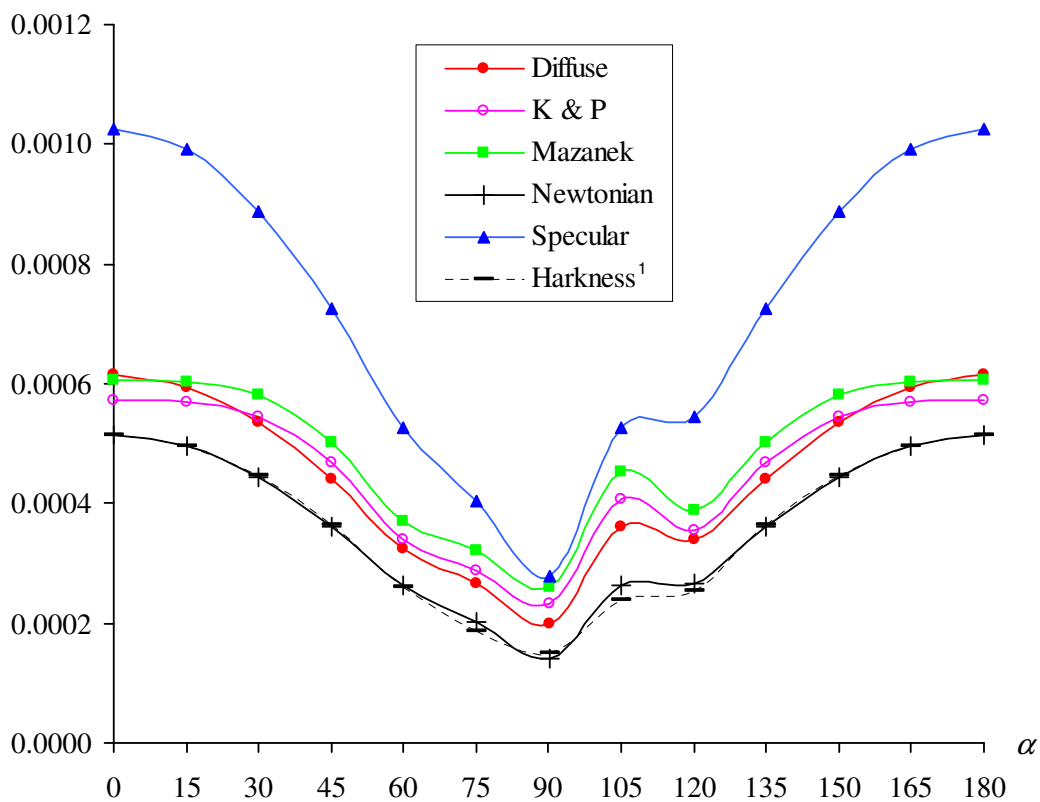


**Figure 8-30 - Drag Deorbit Device Analysis: Damping Contribution to Torque Coefficient ( $C_{T(y)}$ ) as a function of Angle of Attack for Different GSIMs and Accommodation Coefficients**

<sup>1</sup> refers to values predicted by Harkness [12] (extracted from graphical data), which were calculated for a cone with the same base radius, but a slightly larger half-apex angle  $\phi$  than the other results ( $60.16^\circ$ , instead of  $57.30^\circ$ ).

Also illustrated in Figure 8-30 are Harkness's analytical Newtonian results for a cone with the same base radius, but a slightly larger apex half-angle  $\phi$  of  $60.16^\circ$ . The values plotted were extracted from Harkness's graphical data, which includes plots for several other larger values of  $\phi$ .

In order to assist with understanding the effect of aerodynamic damping the FMF Module provides the functionality to visualise the angular velocity component ( $\bar{V}_\omega$ ) of the flow that is created by the rotation of a spacecraft. Figure 8-31 illustrates two print screens taken from the FMF Module, which show the directions of the angular velocity components for all attacking panels (panels that are rotating into the free stream flow, rather than retreating from it).

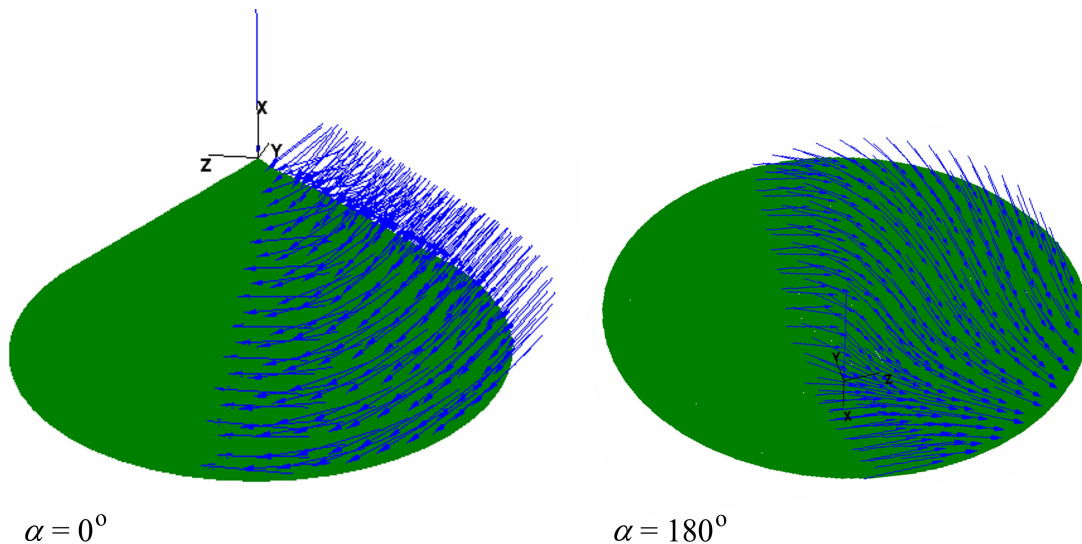


**Figure 8-31 - Drag Deorbit Device Analysis: Angular Velocity Component**  
**Directions for Attacking Panels at Angles of Attack  $0^\circ$  and  $180^\circ$**

Images generated using the FMF Module. The blue arrows directed towards the origin indicate the free stream directions. The remaining blue arrows indicate the directions of the angular velocity components of the flow for each attacking panel.

The curves illustrated in Figure 8-30 indicate that there is excellent agreement between Harkness's results and the FMF Module's Newtonian predictions. The small differences between the results are caused by the difference in half-apex angle. Furthermore, the FMF Module's Newtonian predictions follow the trends predicted by Harkness for a smaller value of  $\varphi$ .

The general trends illustrated in Figure 8-30 for the H-SC GSIM accommodation coefficients are consistent with the findings of Section 8.4.2. The damping torques predicted are highest in the specular case and lowest in the Newtonian case and the damping torques predicted by the Mazanek accommodation coefficients are higher than the values predicted by the Knechtel and Pitts coefficients.

The main feature of interest is that at  $\alpha = 0^\circ$  and  $\alpha = 180^\circ$  the damping torques predicted by the diffuse case are higher than those predicted by both the Mazanek and Knechtel and Pitts accommodation coefficients. The reason for this is that the higher shear stresses predicted by the diffuse case across all incidence angles

(see Figure 8-4 for an illustration of this) have a greater influence at these angles of attack.

In order to understand the magnitude of the very small damping torques predicted it is worthwhile looking at the forces involved. The maximum damping force occurs at  $\alpha = 0^\circ$  in the  $-z$  direction and corresponds to  $C_{F(-z)} = 0.0004$ . Given that the free stream dynamic pressure  $q_\infty$  is  $2.115 \times 10^{-5} \text{ N m}^{-2}$ , this equates to a force of  $0.08 \mu\text{N}$ . This very small force is approximately a twentieth of the size of the force that could be induced by an asymmetric surface temperature distribution, as described in Section 8.2.4.

## 8.5 Other Demonstration Studies

Several other demonstration studies were planned and a small number were executed. However, due to external factors, and the need for brevity, this section only presents the results of a single study of the NASA Space Shuttle, currently scheduled for decommission in 2010.

The space shuttle was chosen because it presents a large and complex geometry for which a surface mesh was available. In addition, the space shuttle is still operational and a large amount of published data exists for it that could be used by subsequent investigators to continue this work.

It is worth noting here that one of the planned demonstration studies was an analysis of the TerraSAR-L satellite illustrated in Figure 6-1, which was scheduled for launch in 2011. An analysis of it was performed using the prototype tool, as described in Section 6.1. However, since this analysis ESA has abandoned the mission. Furthermore, permission to use the results of an aerodynamic study of TerraSAR-L commissioned by ESA [35] has not been obtained. Therefore, the motivation for a further analysis of TerraSAR-L using the FMF Module no longer exists.

### 8.5.1 Space Shuttle

The Space Shuttle is presently being used to construct the International Space Station (ISS), which is planned for completion in 2010 and orbits at about 340 km. This section presents the results of a free molecular flow analysis of the Space Shuttle operating at this altitude, during the solar minima predicted for 2008 by the International Space Environment Service (ISES) [109]. Figure 8-32 shows an image of the Space Shuttle Endeavour docked with the ISS.

Conveniently, at 340 km in low solar conditions, the Mazanek accommodation coefficients predict a drag coefficient of 2.2 for a sphere, assuming a surface temperature of  $300^\circ \text{ K}$ . Therefore, this section presents the results of an

analysis based upon the nominal Mazanek [20] accommodation coefficients defined in Table 7-1.



**Figure 8-32 - The Space Shuttle Endeavour Docked to the Destiny Laboratory of the International Space Station**

**Image credit NASA.**

Obtaining accurate surface meshes of different spacecraft has proved to be very difficult. As mentioned in the introduction to this section, one of the reasons that the Space Shuttle analysis was performed is that a surface mesh of the Space Shuttle was available. The Space Shuttle surface mesh used for the analysis was obtained from a commercial website specialising in three-dimensional Computer Aided Design (CAD) models for computer games [110]. It is an unstructured triangular mesh containing 27,492 panels and is illustrated in Figure 8-33.

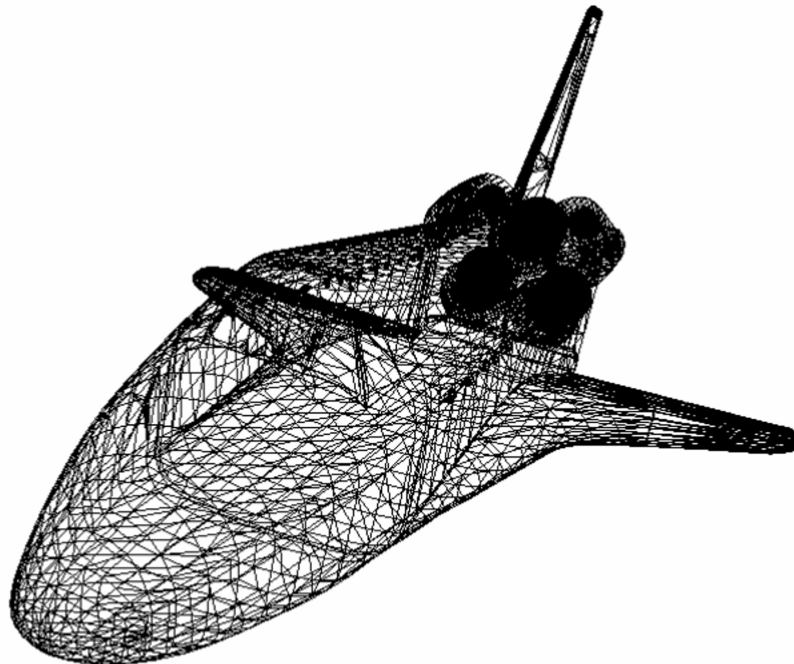


**Figure 8-33 - Space Shuttle Analysis: Surface Mesh**

**Image generated using the FMF Module.**

The wingspan and length of the surface mesh correspond to the Space Shuttle's actual dimensions (to within 0.01 m) and, in general, the geometry appears to be accurate. However, its detailed surface topology could not be guaranteed by the commercial provider. Therefore, any analysis based upon it cannot be relied upon. For this reason, the quantitative findings that are presented have not been compared to other published sources and are provided merely to demonstrate the capability of the FMF Module and SEDAT System to handle very large and complex surface geometries.

The ISS is in a near-circular orbit (it has an eccentricity of 0.0008250). Therefore, the wind speed is assumed to be equal to the circular orbital speed at 340 km ( $7,703 \text{ m s}^{-1}$ ), which corresponds to a molecular speed ratio  $s_{\infty} = 9$ , a molecular kinetic energy  $e_{k.e} = 5$ , and a free stream dynamic pressure of  $7.413 \times 10^{-5} \text{ N m}^{-2}$ .

The reference area  $A_{ref}$  is set equal to the wing planform area ( $47.31 \text{ m}^2$ ) and the reference length  $l_{ref}$  is set equal to the wingspan (23.76 m). The Knudsen number that corresponds to this characteristic length is 774, based on the mean collision diameter of dinitrogen ( $\text{N}_2$ ).

The results presented correspond to just one orientation of the Space Shuttle in which the angles of attack  $\alpha$  and sideslip  $\beta$  are both zero. In this orientation, the forward facing surfaces of the Space Shuttle have an essentially convex geometry. Therefore, reflections did not need to be simulated. However, the ray-tracing functionality of the Hybrid method was employed to determine areas of the surface that are shielded to the free stream flow, as illustrated in Figure 8-34.

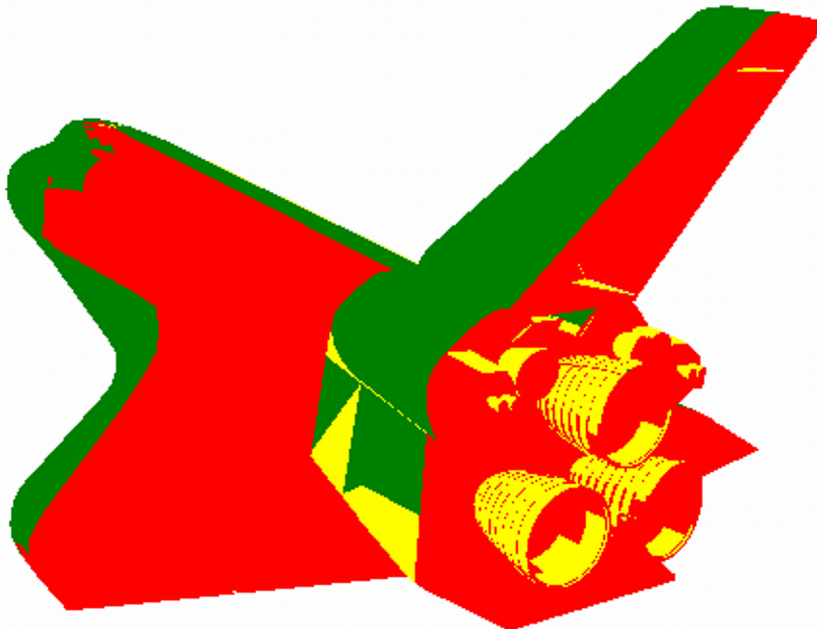


**Figure 8-34 - Space Shuttle Analysis: Ray-Tracer Rendering (rear view)**  
Image generated using the FMF Module. Red panels are aft facing, yellow panels are shielded, and green panels are impacted by the free stream flow.

The rear view of the FMF Module's ray-traced rendering of the Space Shuttle, illustrated in Figure 8-34, clearly shows the three main engines above the body trailing edge flap and the Orbital Manoeuvring System (OMS) to the left and right of the top main engine. This detailed rendering visibly demonstrates the accuracy of the SEDAT Ray-Tracer.

The pressure, shear stress, and heat transfer distributions over the Space Shuttle surface predicted by the FMF Module are illustrated in Figure 8-35, Figure 8-36, and Figure 8-37 respectively. The distributions show the trends expected, based upon the flat plate and sphere analyses presented in Section 8.2.1 and Section 8.2.3 respectively.

The pressure and shear stress distributions correspond to a drag coefficient ( $C_D$ ) of 3.130 and a lift coefficient ( $C_L$ ) of 0.176.

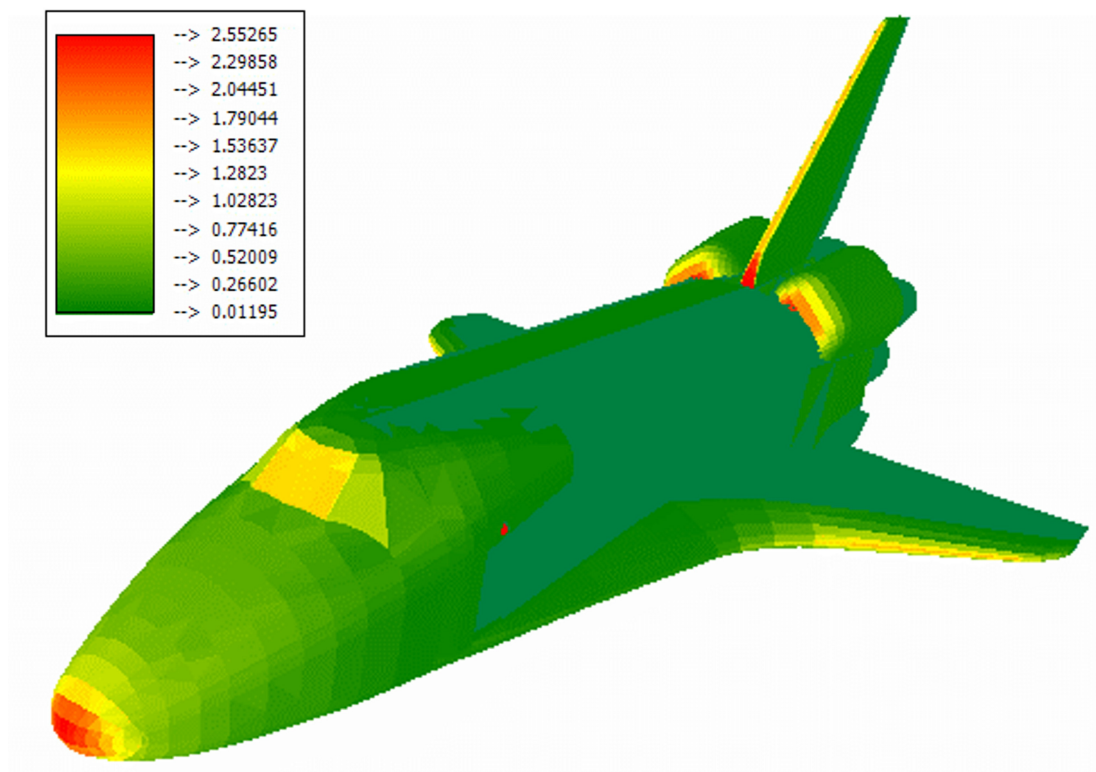


**Figure 8-35 - Space Shuttle Analysis: Pressure ( $C_p$ ) Distribution**

**Image generated using the FMF Module.**

The small patch of high pressure just aft of the cockpit window is caused by a protrusion in the surface mesh that is present on both sides of the fuselage. The protrusions can also be seen in subsequent figures. The Space Shuttle does not have protrusions at these locations in normal operation and it is not clear what they are supposed to represent. However, they are small enough to be ignored for the purposes of this qualitative discussion.



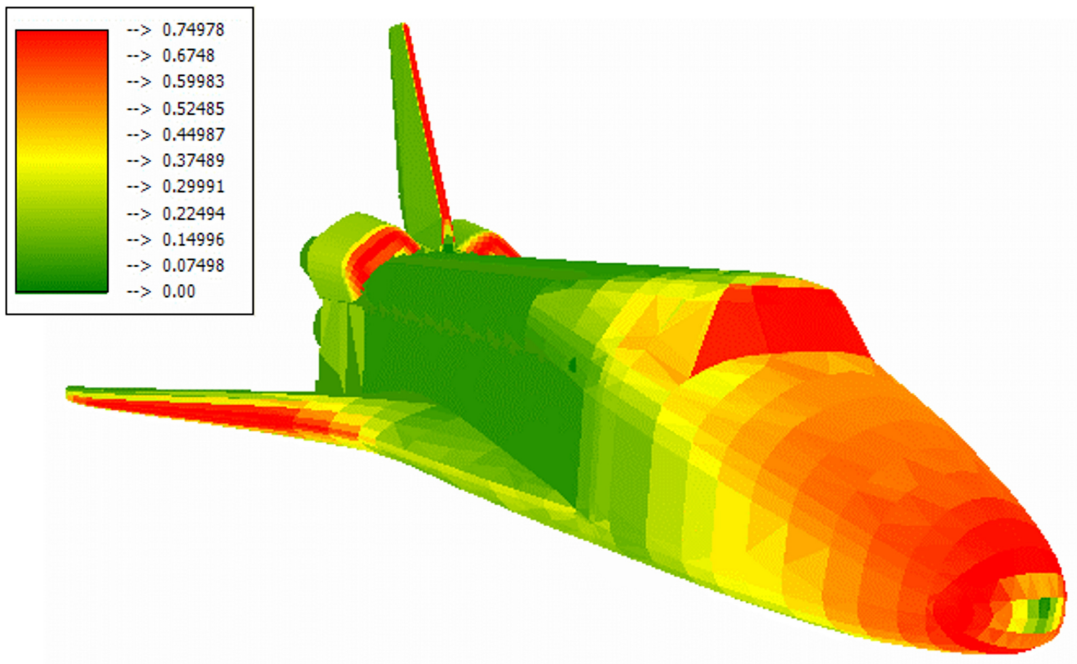


**Figure 8-36 - Space Shuttle Analysis: Shear Stress ( $C_\tau$ ) Distribution**  
 Image generated using the FMF Module.

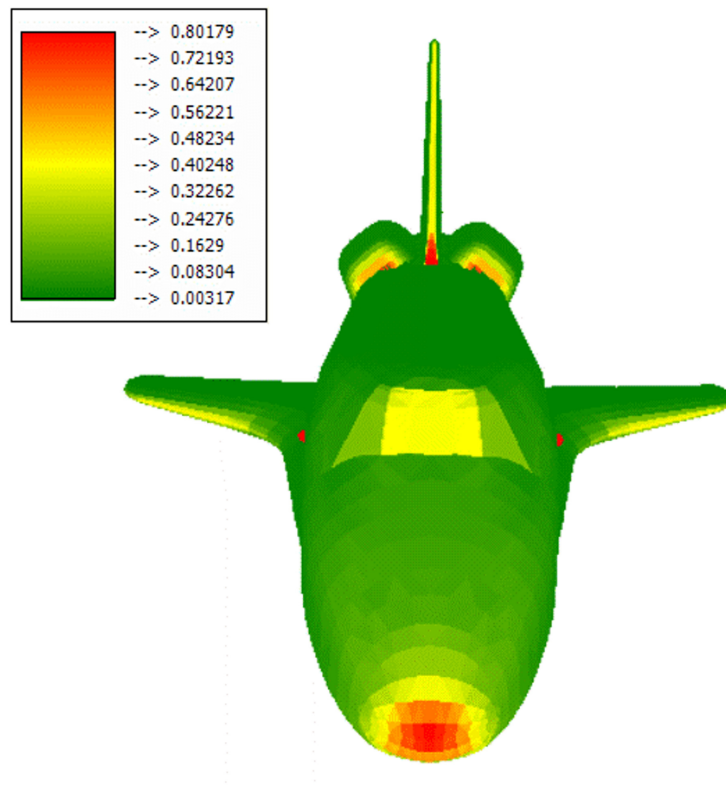


**Figure 8-37 - Space Shuttle Analysis: Heat Transfer ( $C_h$ ) Distribution**  
 Image generated using the FMF Module.

## 8.6 Summary

This chapter has presented the results of several case studies that verify the aerodynamic calculation methods of the FMF Module, Hybrid method, and H-SC GSIM via detailed analysis and, where possible, comparison with published results.

The analysis of a flat plate presented in Section 8.2.1 provided a useful means to compare and verify the predictions of different GSIMs and accommodation coefficients. It also highlighted that the significant differences in pressure and shear stress predicted by different accommodation coefficients can lead to considerable variations in lift and drag predictions at different angles of attack.

Sections 8.2.2 and 8.2.3 presented the results of analyses of a spherical satellite. These analyses took advantage of the functionality of the FMF Module to compare the predictions of different accommodation coefficients at multiple altitudes in different solar conditions. Significant variations were found between the predictions, demonstrating the importance of understanding the relationship between atmospheric conditions and gas-surface interaction modelling when performing aerodynamic analyses of spacecraft.

Section 8.2.2 also investigated the effect of using a realistic surface temperature  $T_w$  and actual free stream temperature  $T_\infty$ , instead of assuming a uniform temperature ratio (for example,  $T_w/T_\infty = 1$ ). The results indicated that using an accurate temperature ratio could have a significant effect on aerodynamic predictions that are based upon a diffuse reemission model. Given this finding, it is recommended that an accurate temperature ratio should be used in all gas-surface interaction calculations involving diffuse reemission.

Section 8.2.4 continued the analysis of the spherical satellite and investigated the effects of an asymmetric surface temperature distribution. The results presented indicated that a 300° K difference between the sides of a spherical satellite can induce an aerodynamic force in the direction of the cold side equivalent to approximately 5% of the Solar Radiation Pressure (SRP) force at an altitude of 500 km in mean solar conditions.

Section 8.3 presented an analysis of a simple configuration of two flat plates placed at right angles to one another. This configuration provided a useful means to investigate and validate the Hybrid method's TPMC approach to modelling the effects of multiple molecular reflections. It was found that at orbital speeds in low Earth orbit the effect of diffusely reflected molecular flux impacting secondary surfaces is negligible in comparison to the effect of specularly reflected flux.

In order to fulfil objective 2, described in Section 1.4, Section 8.4 presented the detailed results of multiple aerodynamic analyses of the drag deorbit device concept developed by Harkness [12] within the Space Research Centre. These analyses used the FMF Module to investigate the aerodynamics of a conical drag

deorbit device at all orientations, whilst accounting for the effects of surface shielding.

Section 8.4.1 compared the results of analyses using the Newtonian GSIM described in Section 7.1 with the analytical Newtonian results of Harkness. Excellent agreement was found between the results using a moderately high-density surface mesh representation of the drag deorbit device. This demonstrated the accuracy of the SEDAT Ray-Tracer, which was used by the FMF Module to perform the shielding calculation.

Section 8.4.2 presented the results of analyses using the Hybrid method and Hybrid H-SC GSIM to compare the effects of using different accommodation coefficients and investigate the effects of multiple molecular reflections. Based on these results, several findings were stated in relation to the aerodynamic performance of the drag deorbit device. These findings are summarised below:

- The lowest drag and restoring torque were predicted by the Newtonian GSIM. Therefore, the structure proposed by Harkness may need reinforcing to cope with the higher aerodynamic loads predicted. However, the aerodynamic performance of the device is significantly better than that predicted by Harkness, increasing confidence in the concept.
- The highest drag and restorative torques were predicted in the case of specular reemission. Therefore, surface materials should be selected that produce a more specular angular distribution of reemission. A preliminary literature survey indicates SiO<sub>2</sub>-coated kapton may be a suitable candidate material.
- The effect of specularly reflected flow impinging on secondary surfaces is to increase significantly both drag and restorative torque. At certain angles of attack, the specularly reflected flux converges upon the panels on the far side of the cone causing large increases in pressure, shear stress, and heat transfer in the impacted region, which should be accounted for in the structural design.
- The effect of diffusely reflected flow impinging on secondary surfaces is negligible.
- The structure of the drag sail should be designed to cope with the aerodynamic loads predicted without significant deformation to its shape. This is because any change in shape would alter the aerodynamics of the situation and the resulting feedback scenario may be difficult to model with any confidence.
- More diffuse reemission may be desirable if aerodynamic loads are too high or the device has unrecoverable attitude instability when deployed (leading to sub-optimal orientation).

- The Mazanek accommodation coefficients were shown to be calibrated for the free stream conditions and surface temperatures being considered using the same technique as Mazanek. Therefore, it is recommended that the Mazanek force, torque, and heat transfer predictions that have been presented should be used in any future attitude and orbital simulation (in equivalent atmospheric and orbital conditions).

Section 8.4.3 presents the results of additional analyses of the drag deorbit device that were conducted to determine the magnitude of aerodynamic damping torques that would be induced by its rotation. The results of a Newtonian analysis demonstrated excellent agreement with the analytical Newtonian results of Harkness. The results of analyses using the H-SC GSIM also showed the trends expected. However, all the torques calculated were negligible in comparison to the static restoring torque and other possible sources of perturbation.

Section 8.5 presented the results of an analysis of the NASA Space Shuttle, which used a surface mesh containing over 25,000 panels. It demonstrated the capability of the FMF Module, SEDAT Ray-Tracer, and SEDAT System to handle very large and complex geometries.

In general, the results presented and the findings stated in this chapter illustrate the point made in Chapter 3 that there is continued uncertainty surrounding the modelling of gas-surface interactions in rarefied flow. Furthermore, the limited amount of empirical data available for the Schaaf and Chambre GSIM further illustrates the need to be able to utilise multiple GSIMs in order to be able to model the maximum number of surfaces and free stream conditions.

The success of the FMF Module and SEDAT System for performing the analyses presented in this chapter is discussed in Chapter 9, with particular emphasis placed on how well concurrent engineering principles were utilised and facilitated.

## **9 DISCUSSION AND CONCLUSIONS**

This chapter discusses the work presented in the thesis and presents its main conclusions. In order to connect the many different topics of the thesis, a summary of the work completed is incorporated into the conclusions, given in Section 9.2.

However, prior to presenting the conclusions it is necessary to assess the SEDAT Concept, described in Chapter 5, as well as the SEDAT System and accompanying FMF Module, described in Chapter 6, that have been developed to demonstrate it. Section 9.1 provides this assessment.

To assist with understanding the various overlapping topics of the thesis and its numerous conclusions, a summary of its contributions to scientific and engineering knowledge is presented in Section 9.3.

Finally, for the benefit of future investigators, Section 9.4 lists several suggestions for further work.

### **9.1 Assessment of the SEDAT Concept**

The SEDAT Concept described in Chapter 5 is a very ambitious attempt to apply concurrent engineering principles beyond Phase A of the spacecraft development process. It is based upon the enterprise application software model used by businesses and large organisations.

The idea behind SEDAT is that all of the computer tools used on a spacecraft development project should be incorporated into one system as separate modules. All of the modules should be presented via a single GUI and connected to a single centralised Relational Database Management System (RDBMS), which contains all project data.

A practical realisation of the SEDAT Concept has been developed within the framework of this PhD research project. Section 9.1.1 provides an assessment of it. Section 9.1.2 assesses the accompanying FMF Module that has been developed and integrated into the SEDAT System. Based on these assessments, Section 9.1.3 evaluates the future prospects of the SEDAT Concept.

#### **9.1.1 The SEDAT System**

The SEDAT System that has been developed provides a useful demonstration of the SEDAT Concept because it implements the client-server architecture, centralised RDBMS, integrated Graphical User Interface (GUI), and modular approach proposed by the concept.

Furthermore, both the database and the client are fully scalable and their components are object-orientated. Therefore, the SEDAT System also provides a

reasonable starting point for future testing and development within university-scale satellite development and demonstration programmes.

In October 2006, the author attended the Concurrent Engineering for space applications Workshop (CEW 2006), at ESA's ESTEC facility in Noordwijk, the Netherlands. The workshop was hosted by Massimo Bandecchi, Head of the ESA Concurrent Design Facility (CDF).

A presentation by Miró [111], Head of the Software Systems Division, within the Technical and Quality Management Directorate within ESA, stated, for the first time, that an integrated and centralised systems engineering database must form part of the solution for implementing concurrent engineering beyond Phase A. This statement provides confidence in the SEDAT Concept and indicates its proposal was also timely.

Discussions that took place at the conference indicated that any type of integrated concurrent engineering system based upon a centralised database would require a stepwise approach to development. Within ESA, it would most likely start with the CDF's next generation concurrent engineering software for Phase A studies, based around the new Open Concurrent Design Server (OCDS) concept, which incorporates a centralised RDBMS [112].

A paper describing the SEDAT Concept titled "*An Integrated Information Systems Approach to Spacecraft Engineering*" was presented at the workshop by the author [113].

As a result of the presentation and subsequent discussions, engineers working at ESA's CDF expressed an interest in incorporating parts of the SEDAT System into the OCDS. For example, the object-orientated processing components of the FMF Module and the plug-and-play functionality that enables modules to be integrated into the Graphical User Interface (GUI) using a few database table entries.

### **9.1.2 The FMF Module**

The FMF Module has proven to be a suitable platform for demonstrating the SEDAT Concept because the calculations it performs utilise many inputs from multiple disciplines and affect core mission design considerations such as attitude, orbit, and lifetime. In addition, it utilises large amounts of empirical data, in the form of GSIM and atmospheric data. It also creates large amounts of results data.

Given the emphasis of many papers at CEW 2006 on data modelling and data exchange, it is unsurprising that the greatest challenge of the development was modelling the analysis data structures and designing an appropriate RDBMS schema for them. In order to model the data structures the aerodynamic analysis process and related engineering data sources needed to be fully understood.

At every stage of the database design, a trade-off was needed between the functional requirements of the FMF Module, the ideal of normalised RDBMS design

(which is an inherent requirement of the SEDAT Concept), usability, and complexity.

Once designed, the RDBMS conferred many benefits. It was ideal for handling the large and complex datasets involved. In addition, the functionality it provided to write ad-hoc Structured Query Language (SQL) queries to perform pre- and post-processing of analysis data proved to be a useful feature.

However, the large and complex datasets involved in the analysis process created significant challenges for the presentation, manipulation, and processing of data by the client. They required numerous generic processing, reporting, three-dimensional modelling, and user-interface components to be developed.

Once developed these components could be re-used elsewhere within the SEDAT System with very little additional effort because of the object-orientated programming techniques employed. However, many of the components addressed information technology challenges that are not unique to the field of spacecraft engineering.

### 9.1.3 Future Prospects

As described in Section 4.3, enterprise applications already address many of the information technology challenges of implementing concurrent engineering. Furthermore, they incorporate features such as integrated document management, CAD drawing management, and system configuration control.

The two largest enterprise applications, SAP<sup>1</sup> and Oracle Business Suite, also incorporate features such as Product Lifecycle Management (PLM) that facilitate real-time collaboration and viewing of information related to selected engineering parts.

Therefore, a concept as ambitious and all encompassing as SEDAT is most likely to be developed by an existing enterprise application provider in collaboration with spacecraft manufacturers and organisations such as ESA and NASA. Within this collaborative framework, the spacecraft manufacturers and organisations would benefit the most from focussing resources on developing modules for those aspects of engineering that are unique to spacecraft.

Regardless of the approach taken, many challenges remain for commercial implementation of the SEDAT Concept. Fortunately, concurrent engineering advocates such as Miró [111] are tackling these challenges as a by-product of addressing the practical issues that need to be overcome to implement concurrent engineering in the short term.

These issues, which, as discussed in Section 9.1.2, represented significant challenges during the development of the FMF Module, include developing a fuller

---

<sup>1</sup> Software providers are listed in Section III.iii.

understanding of the systems engineering data model and corresponding standards for the exchange of data.

## 9.2 Conclusions

This research was originally motivated by the need to perform an accurate aerodynamic analysis of the drag deorbit device concept currently under development within the Space Research Centre (SRC), at Cranfield University. The purpose of the device is to deorbit satellites from low Earth orbit at the end of their useful lives in order to help reduce the growing problem of space debris.

This thesis has presented a contemporary review of the aerodynamics of spaceflight in the Free Molecular Flow (FMF) regime of low Earth orbit, in which Gas-Surface Interactions (GSIs) dominate the flow. This review has shown that there are continued uncertainties surrounding our knowledge of GSIs and demonstrated that no single Gas-Surface Interaction Model (GSIM) hitherto developed is accompanied by enough proven data to be sufficiently accurate for all scenarios of interest.

Numerous free molecular flow analysis tools were found to exist for performing the required aerodynamic analysis. However, none of them were designed to make use of the maximum variety of GSIMs and their associated data. Nor were they explicitly designed to facilitate Concurrent Engineering (CE).

This thesis has shown that the development of any new spacecraft analysis tool must be designed with CE in mind from the outset. However, investigation into the use of CE principles in the space industry revealed that very little progress has been made in implementing CE beyond Phase A studies.

This thesis has shown that the challenge of implementing CE beyond Phase A is predominantly an information technology one, which is manifested in two main ways: the increasing number of computer tools used and the related problem of maintaining data continuity among these tools.

Enterprise applications, used by businesses and large organisations, provide a model for integrating these disparate tools and facilitating concurrent engineering. They incorporate multiple modules, for handling different processes, which can be accessed via a single user interface that is connected to a centralised Relational Database Management System (RDBMS).

This approach has been applied to spacecraft engineering in the form of the Spacecraft Engineering, Design, and Analysis Tools (SEDAT) concept. The idea behind SEDAT is that all of the computer tools used on a spacecraft development project should be incorporated into one system as separate modules. All of the modules should be presented via a single Graphical User Interface (GUI) and connected to a single centralised RDBMS, which contains all project data.



Papers presented at ESA's Concurrent Engineering Workshop (CEW) in 2006 indicate that the proposal of the SEDAT Concept is timely because many CE proponents now recognise that a centralised RDBMS is essential for the implementation of CE beyond Phase A.

In order to test the concept it was recognised that a working SEDAT System and accompanying module must be developed. This requirement combined with the need for a FMF analysis tool that could incorporate multiple GSIMs and handle large amounts of data whilst also facilitating CE, lead to the development of the SEDAT System and FMF Module.

It has been shown that the SEDAT System provides a useful demonstration of the SEDAT Concept because it implements the client-server architecture, centralised RDBMS, integrated GUI, and modular approach proposed by the concept. Furthermore, both the database and the client are fully scalable and their components are object-orientated. Therefore, it also provides a reasonable starting point for future testing and development within university-scale satellite development and demonstration programmes.

A paper about the SEDAT Concept, which was presented by the author at the CEW, generated several enquiries from members of ESA's Concurrent Design Facility (CDF). They were particularly interested in using some of the modularisation functionality and FMF analysis components of the SEDAT System and FMF Module in their next generation CE software, which will incorporate a centralised RDBMS.

Development of the FMF Module demonstrated that the use of a single client promoted the re-use of components. This is because the object-orientated components of the FMF Module could be re-used by other modules within SEDAT with very little additional development effort.

Use of the FMF Module has shown that RDBMSs are ideal for storing, connecting, and manipulating the large and complex datasets used by engineering analyses that affect multiple disciplines. In addition, the capability to write ad-hoc queries to perform pre- and post-processing tasks has demonstrated the value of using a RDBMS to store engineering analysis data.

Development of the FMF Module and SEDAT System has shown that many of the challenges that must be overcome to realise the SEDAT Concept can and have been successfully tackled by enterprise applications.

Therefore, a concept as ambitious and all encompassing as SEDAT is most likely to be developed by an existing enterprise application provider in collaboration with spacecraft manufacturers and organisations such as ESA and NASA. Within this collaborative framework, the spacecraft manufacturers and organisations would benefit the most from focussing resources on developing modules for those aspects of engineering that are unique to spacecraft.

Development of the FMF Module and discussions that took place at the CEW have shown that the main challenges that must be overcome for commercial realisation of the SEDAT Concept are to develop a fuller understanding of the systems engineering data model and corresponding standards for the exchange of data between tools. Fortunately, these challenges are already being addressed by CE advocates.

The FMF Module that has been developed uniquely combines a number of features that are common to other spacecraft aerodynamic analysis tools. For example, it supports the use of multiple atmospheric models, it supports the use of surface-dependent properties, it can be used to calculate forces and torques due to aerodynamic damping, it provides a number of options for modelling gas flow, it includes a 3D graphical results display screen, and its installed Dynamic Link Library (DLL) files can be used by third party applications to perform real-time simulations.

In addition, unlike the other tools, it can incorporate any GSIM with any currently available amount of associated data because all its data is stored in a RDBMS. Therefore, it directly addresses the problem identified earlier, which is the growing number of GSIMs and their associated data, thereby enabling analysis of the maximum number of gas-surface interactions.

The FMF Module also incorporates some other innovative features. For example, in order to facilitate efficient analysis of a wide range of spacecraft operating in different scenarios, a new method of performing spacecraft aerodynamic analysis has been developed and implemented in the FMF Module. This method is a hybrid between the analytical Ray-Tracing Panel (RTP) method, and the Test-Particle Monte-Carlo (TPMC) method.

In the Hybrid method, the spacecraft is represented by a surface mesh. The RTP method is used to determine which surface mesh panels are shielded to the free stream flow. Analytical calculations are then performed to determine the molecular flux, pressure, shear stress, and heat transfer to the panels due to the direct impact of the free stream flow.

The incident free stream molecular flux to each panel is then split into a representative number of test particles, which each simulate a finite number of reemitted (reflected) molecules. A scattering kernel, which uses Monte-Carlo statistical sampling techniques, can be used to determine the directions of any diffusely reflected test particles. The paths of the reflected test-particles are traced and the pressure, shear stress, and heat transfer caused by their interactions with any other panels is recorded.

The TPMC results are integrated over a unit time step and then added to the analytical calculations related to the free stream gas-surface interactions. The

resulting pressures and shear stresses on each panel can be used to calculate the forces and moments on the spacecraft.

The Hybrid method can be used to analyse spacecraft in all regimes of free molecular flow. However, the analysis of complex spacecraft geometries in orientations that are prone to shielding is strictly only accurate in hyperthermal free stream conditions (typically encountered at low Earth altitudes). This is because the free stream flow is assumed to be a collimated beam of molecules.

Therefore, although the Hybrid method is not as versatile as the pure TPMC method, it is appropriate for modelling the aerodynamics of the majority of low Earth orbit spaceflight scenarios in which aerodynamic disturbances may be considered significant. The advantage of the Hybrid method over the TPMC method is that it is slightly simpler to set-up and requires less computation time. This is because the Hybrid method does not require a simulation control volume to be placed around the spacecraft and it uses the TPMC method to model the reflected flow only.

To accompany the Hybrid method a Hybrid Schaaf and Chambre (H-SC) GSIM has been developed from Schaaf and Chambre's original work. Expressions for the pressure, shear stress, and heat transfer to a surface due to the interaction of a test particle have been derived and explained.

The ray-tracer used by the FMF Module to perform shielding calculations and determine the paths of reflected test particles was developed as part of this PhD. Methods for calculating ray-panel intersection positions were derived and compared with published methods used by graphics programmers. The published methods were found to be faster and were used instead. To reduce further the ray-tracing computation time, surface mesh bounding-boxes, also used by graphics programmers, were employed.

The SEDAT System and FMF Module have been used to conduct numerous case studies. Some of these analyses took advantage of the functionality of the FMF Module to compare the results predicted for some simple convex shapes. These analyses employed a variety of accommodation coefficients at multiple altitudes in different solar conditions with various surface temperature distributions.

Significant variations were found between the results predicted, demonstrating the importance of understanding the relationship between free stream conditions, surface characteristics, and accommodation coefficients when performing aerodynamic analyses of spacecraft.

Several case studies of the drag deorbit device concept using the FMF Module have been presented. One of these compared the results of analyses using the Newtonian GSIM with the analytical Newtonian results of Harkness [12]. Excellent agreement was found between both static and damping results using a moderately high-density surface mesh representation of the drag deorbit device. The same

surface mesh was used for subsequent analyses and found to have the required accuracy.

Other analyses of the drag deorbit device employed the Hybrid method and H-SC GSIM to compare the effects of using different accommodation coefficients and investigate the consequences of multiple molecular reflections. Among the accommodation coefficients used were the empirically calibrated coefficients recently proposed by Mazanek [20]. The results of the analyses lead to a number of significant findings, which are summarised below:

- The lowest drag and restoring torque were predicted by the Newtonian GSIM. Therefore, the structure proposed by Harkness may need reinforcing to cope with the higher aerodynamic loads predicted by the H-SC GSIM. However, the aerodynamic performance of the device is significantly better than that predicted by Harkness, increasing confidence in the concept.
- The highest drag and restorative torques were predicted in the case of specular reemission. Therefore, surface materials should be selected that produce a more specular angular distribution of reemission. A preliminary literature survey indicates SiO<sub>2</sub>-coated kapton may be a suitable candidate material.
- The effect of specularly reflected flow impinging on secondary surfaces is to increase significantly both drag and restorative torque. At certain angles of attack, the specularly reflected flux converges upon the surfaces on the far side of the cone causing large increases in pressure, shear stress, and heat transfer in the impacted region, which should be accounted for in the structural design.
- The effect of diffusely reflected flow impinging on secondary surfaces is negligible.
- The structure of the drag sail should be designed to cope with the aerodynamic loads predicted without significant deformation to its shape. This is because any change in shape would alter the aerodynamics of the situation and the resulting feedback scenario may be difficult to model with any confidence.
- More diffuse reemission may be desirable if aerodynamic loads exceed tolerable structural limits or the device has unrecoverable attitude instability when deployed (leading to sub-optimal orientation).
- The effect of aerodynamic damping is negligible.
- The Mazanek accommodation coefficients were shown to be calibrated for the free stream conditions and surface temperatures being considered. Therefore, it is recommended that the Mazanek force, torque, and heat transfer predictions that have been presented should be used in any future

attitude and orbital simulation (in equivalent atmospheric and orbital conditions).

An analysis of the NASA Space Shuttle has also been presented, which used a surface mesh containing over 25,000 panels. It demonstrated the capability of the FMF Module, SEDAT Ray-Tracer, and SEDAT System to handle very large and complex geometries

In general, the results of the case studies indicate that there is continued uncertainty surrounding the modelling of gas-surface interactions in rarefied flow. Furthermore, the limited amount of empirical data available for the Schaaf and Chambre GSIM further illustrates the need to be able to utilise multiple GSIMs in order to be able to model the maximum number of surfaces and free stream conditions.

In summary, the objectives of this thesis, which are described in Section 1.4, have been met.

### **9.3 Summary of Contributions**

Based on the conclusions presented in Section 9.2, it is considered that this thesis makes three main contributions to scientific and engineering knowledge:

1. A new concept to address the challenge of implementing concurrent engineering, particularly beyond Phase A (preliminary design): the Spacecraft Engineering, Design, and Analysis Tools (SEDAT) Concept.
  - a. Inspired by the approach employed by enterprise applications, the SEDAT Concept proposes that all the computer tools used on a spacecraft project should be incorporated into one system as separate modules, presented via a single client, and connected to a centralised Relational Database Management System (RDBMS).
  - b. To demonstrate the concept a SEDAT System and accompanying Free Molecular Flow (FMF) analysis module have been developed. They have shown that a RDBMS is ideal for storing, manipulating, and connecting large and complex datasets used by multiple disciplines in order to facilitate concurrent engineering. Furthermore, object-orientated software design principles should be employed to enable maximum re-use of components amongst modules.
  - c. It has been shown that the concept is most likely to be developed by an enterprise application provider in collaboration with members of the space industry. To assist with this development it is recommended that these members address the challenges specific to the space

industry. In particular, development of a comprehensive engineering data model for the entire spacecraft development process.

2. A new spacecraft aerodynamic analysis tool: the FMF Module.
  - a. Unlike other spacecraft aerodynamic tools, the FMF Module is explicitly designed to facilitate concurrent engineering and make use of the maximum variety of GSIMs and their associated data. It also uniquely combines many features of existing tools.
  - b. It incorporates a new Hybrid method of FMF analysis that combines the Ray-Tracing Panel (RTP) and Test-Particle Monte Carlo (TPMC) methods, enabling it to analyse complex geometries that are subject to surface shielding and multiple molecular reflections.
  - c. To accompany the FMF Module a new Hybrid version of the Schaaf and Chambre GSIM has been derived (the H-SC GSIM).
  
3. A thorough state-of-the-art aerodynamic analysis of the drag deorbit device concept:
  - a. The analysis used the Hybrid method and H-SC GSIM to model reflected flow.
  - b. The analysis used a range of accommodation coefficients, including the latest empirically based incidence-dependent coefficients.
  - c. Based on the analysis, recommendations were made regarding material selection and structural design.

## 9.4 Suggestions for Further Work

This section lists suggestions for further work, which are based upon the topics discussed throughout this thesis and, in particular, its conclusions. For clarity, the suggestions are grouped into subject areas and summarised in the following bullet points.

1. Development of the SEDAT Concept:
  - a. Investigate how the SEDAT Concept could be developed for commercial purposes in collaboration with an enterprise application provider and a spacecraft manufacturer. For example, by implementing a trial system within a spacecraft manufacturing company that already uses an enterprise application.

- b. Collaborate with the ESA CDF to assist with developing their next generation CE software and help them to develop a strategy for implementing CE beyond Phase A.
  - c. Further investigate advanced engineering methodologies that a fully-implemented SEDAT system would enable, such as distributed grid computing, workflow, Knowledge Based Engineering (KBE), and Multidisciplinary Design Optimisation (MDO).
  - d. Further investigate the use of an Object (orientated) Database Management System (ODBMS) as an alternative to a Relational Database Management System (RDBMS).
2. Development of the existing SEDAT System:
  - a. Develop additional modules that specifically tackle the challenges that are unique to spacecraft systems engineering. For example, a Solar Radiation Pressure (SRP) analysis module using the SEDAT Ray-Tracer. Alternatively, a spacecraft re-entry analysis module that uses components of the FMF Module combined with the bridging methods described in Section 2.6.5.
  - b. Implement ESA information technology standards (for example, for database design, data exchange, 3D graphics, and programming).
3. FMF Module Enhancements:
  - a. Investigate methods to optimise the SEDAT Ray-Tracer (see section 6.3.3)
  - b. Add a Hybrid GSIM that more realistically simulates reflected flow by combining the specular and diffuse components of reemitted flux into a user-defined number of test-particles.
  - c. Add full TPMC analysis capability to the FMF Module.
4. Gas-Surface Interactions:
  - a. Design a satellite experiment to gather empirical gas-surface interaction data for multiple surface types at different incidence angles in various free stream conditions.
5. Additional Drag Deorbit Device Case Studies:

- a. Apply the Mazanek et al [20] approach to determine calibrated accommodation coefficient curve-fit parameters using satellite observations at different low Earth orbit altitudes. Conduct analyses of the drag deorbit device at these altitudes.
- b. Gather GSIM data related to the drag deorbit device's likely surface material (kapton or mylar). If necessary, implement a new Hybrid GSIM to utilise this data. For example, Cook [74] provides data for O<sub>2</sub> impacting kapton at sub-orbital speeds (using a modified Nocilla GSIM), which could be extrapolated.

6. Other Case Studies:

- a. Analyse the GRACE satellite's orbital and attitude data and compare it with Mazanek et al's predictions (refer to Section 3.3.3 for details of the GRACE satellite and Mazanek et al's aerodynamic analysis). For example, using the Precise Orbital Analysis (POA) method of Harrison and Swinerd [31].
- b. Perform an aerodynamic analysis of ESA's Gravity field and steady state Ocean Circulation Explorer (GOCE) spacecraft, which is due for launch in 2008. GOCE will study the Earth's geoid from an altitude of approximately 250 km, posing some significant aerodynamic challenges.

7. Drag Deorbit Device Design:

- a. Analyse additional drag deorbit device geometries to help optimise the design.
- b. Investigate the potential for combining the drag deorbit device with an aerodynamic front-fairing device, to create a single bolt-on aerodynamics package, as illustrated in Figure 9-1.

The fairing would use similar technology to the drag deorbit device, but would be deployed during the satellite's operational mission phase to reduce its drag and extend its lifetime. The fairing would be constructed from a similar thin film material as the drag deorbit device, such as kapton film, and folded and stowed during the pre-operational mission phases.

A tension rod, extended at the beginning of the satellite's operational phase, would hold the sail in tension. Tilting or bending the tension rod would enable the fairing to be used as a forward rudder to alter the satellite's attitude. At the end of the operational phase, the fairing and



the tension rod could be jettisoned and the drag deorbit device deployed.

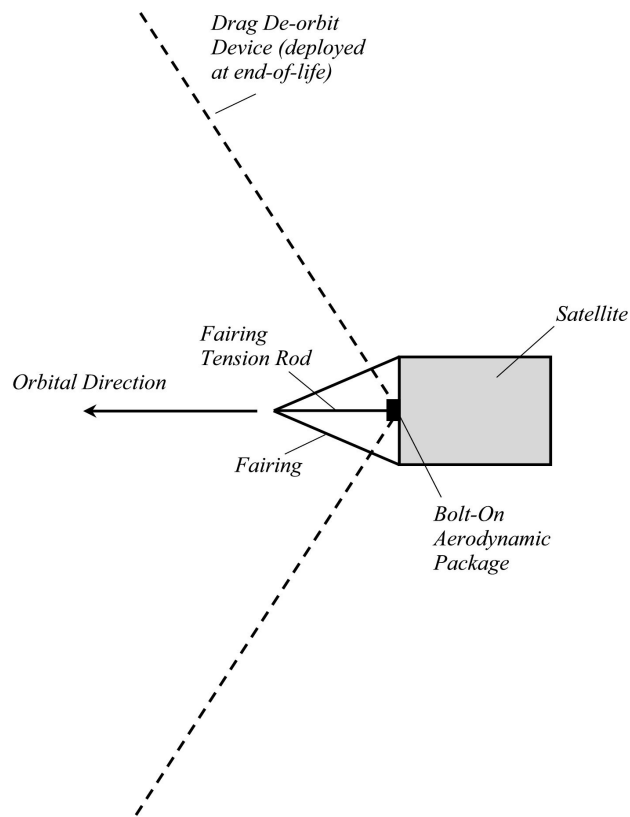


**Figure 9-1 - Bolt-On Aerodynamics Package for Low Earth Orbit**



## 10 REFERENCES

All references are provided in the following format: *Author(s), Title, Publisher, Publisher Code, Notes, ISBN, Library Code, Hyperlink, Publication Date.*

- [1] "Technical Report on Space Debris", United Nations, A/AC.105/720, New York, 92-1-100813-1, 1999
- [2] "Inter-Agency Space Debris Coordination Committee (IADC) Space Debris Mitigation Guidelines", IADC, IADC-02-01, <http://www.iadc-online.org>, 15/10/2002
- [3] Klinkrad, H., Walker, R., Martin, C., Stokes, H., Wilkinson, J., Sdunnus, H., Hauptmann, S. and Beltrami, P., "Update of the ESA Space Debris Mitigation Handbook", QinetiQ, ESA Contract 14471/00/D/HK, 7/2002
- [4] Roberts, P. C. E., et al, "Deorbit Device Demonstrator (D3), MSc in Astronautics and Space Engineering - Group Design Project", unpublished internal report of the Space Research Centre, Cranfield University, 8/10/2002
- [5] "Union of Concerned Scientists (UCS): Satellite Database", [http://www.ucsusa.org/global\\_security/space\\_weapons/satellite\\_database.html](http://www.ucsusa.org/global_security/space_weapons/satellite_database.html)
- [6] Ali, A., "Mustang: EOL De-Orbit Device Dynamics", MSc Thesis, Space Research Centre, Cranfield University, 4/2002
- [7] Chutha, J., "De-Orbit and Atmospheric Entry of Nanosatellites", MSc Thesis, Space Research Centre, Cranfield University, 9/2001
- [8] Roberts, P. C. E., Bowling, T. and Hobbs, S. E., "MUSTANG: A Technology Demonstrator for Formation Flying and Distributed Systems Technologies in Space", Space Research Centre, Cranfield University, 2002
- [9] Andringa, J. M. and Hastings, D. E., "A Systems Study of How to Dispose of Fleets of Small Satellites", AIAA, AIAA-2001-4741, AIAA Space 2001 - Conference and Exposition, Albuquerque, NM, MIT Presentation, 8/2001
- [10] Meyer, K. W. and Chao, C. C., "Atmospheric Reentry Disposal for Low-Altitude Spacecraft", AIAA, Journal of Spacecraft and Rockets, Vol. 37, No. 5, 16/3/2000
- [11] Bousquet, P. W., "Deorbitation of Small CNES Satellites", International Academy of Astronautics (IAA), 56th International Astronautical Congress 2005, Fukuoka, Japan, 17/10/2005

- [12] Harkness, P. G., "An Aerostable Drag-Sail Device for the Deorbit of Sub-Tonne, Low Earth Orbit Spacecraft", PhD thesis, Space Research Centre, Cranfield University, 10/2006
- [13] Fortescue, P. and Stark, J., "Spacecraft Systems Engineering", Wiley, 0-471-95220-6, 1995
- [14] King-Hele, D. G., "Satellite Orbits in an Atmosphere: Theory and Application", Glasgow: Blackie, 1987, cited in: 'Spacecraft Systems Engineering', Second Edition, by Peter Fortescue and John Stark, Published by Wiley, 1995, 0216922526, 629.783 KIN, 1987
- [15] Bruinsma, S., Tamagnan, D. and Biancale, R., "Atmospheric Densities Derived from CHAMP/STAR Accelerometer Observations", Elsevier, Planetary and Space Science 52 (2004) 297 – 312, 21/10/2003
- [16] Cook, G. E., "Satellite Drag Coefficients", Pergamon, Planet. Space Sci, Vol. 13, pp. 929-946, 27/5/1965
- [17] Knechtel, E. D. and Pitts, W. C., "Normal and Tangential Momentum Accommodation for Earth Satellite Conditions, Astronautica Acta, Vol. 18, pp. 171-184", Pergamon Press, 1973
- [18] "Space engineering: Space environment", ESA Publications Division, ECSS-E-10-04, <http://www.spacelab.dti.supsi.ch/Tecnica/ECSS-E-10-04ASpaceEnvironment1.pdf>, 21/1/2000
- [19] Moe, K. and Moe, M. M., "Gas-Surface Interactions and Satellite Drag Coefficients", Elsevier, Planetary and Space Science 52 (2005) 793-801, 18/3/2005
- [20] Mazanek, D. D. and Kumar, R. R., "Aerothermal Analysis and Design of the Gravity Recovery and Climate Experiment (GRACE) Spacecraft", NASA, TM-2000-210095, 1/4/2000
- [21] Doornbos, E. and Klinkrad, H., "Modelling of Space Weather Effects on Satellite Drag", Elsevier, Advances in Space Research 37 (2006) 1229–1239, 21/4/2005
- [22] Walterscheid, R. L., "Solar Cycle Effects on the Upper Atmosphere: Implications for Satellite Drag", AIAA, Journal of Spacecraft, Vol. 26, NO. 6, pp. 439-444, 31/3/1989
- [23] Klinkrad, H. and Fritsche, B., "Orbit and Attitude Perturbations due to Aerodynamics and Radiation Pressure", ESA, ESA Workshop on Space Weather, 11-13 November 1998 ESTEC, Noordwijk, the Netherlands, 13/11/1998

- [24] Knowles, S. H., Picone, J. M., Thonnard, S. E. and Nicholas, A. C., "The Effect of Atmospheric Drag on Satellite Orbits During the Bastille Day Event", Kluwer Academic Publishers, *Solar Physics* 204: 387–397, 2001
- [25] Ruskin, J., "Of The Open Sky", *Modern Painters I, Part II, Section III*, [http://www.cloudappreciationsociety.org/a/of-interest/of\\_open\\_sky.html](http://www.cloudappreciationsociety.org/a/of-interest/of_open_sky.html), 1860
- [26] Laštovička, J., Akmaev, R. A., Beig, G., Bremer, J. and Emmert, J. T., "Global Change in the Upper Atmosphere", AAAS, 1135134, *Science*, Vol. 314, pp. 1253 - 1254, 24/11/2006
- [27] Bird, G. A., "Molecular Gas Dynamics and the Direct Simulation of Gas Flows", Oxford University Press, 0-19-856195-4, 5/5/1994
- [28] Glass, C. E. and Moss, J. N., "Aerothermodynamic Characteristics in the Hypersonic Continuum-Rarefied Transitional Regime", AIAA, 2001-2962, 35th AIAA Thermophysics Conference, Anaheim, CA, 14/6/2001
- [29] Regan, F. J., and Anandakrishnan, S. M., "Dynamics of Atmospheric Re-Entry", AIAA, 533.655 REG, 1993
- [30] Dubisch, R., "On the Averaging of Ratios of Specific Heats in a Multicomponent Planetary Atmosphere", Elsevier Science, *Icarus*, v 22, n 4, p 474-5, 8/1974
- [31] Harrison, I. K. and Swinerd, G. G., "Analysis of Satellite Laser Ranging Data To Investigate Satellite Aerodynamics", Pergamon, *Planet. Space Sci.*, Vol. 43, No. 8, pp. 1023-1033, 9/1/1995
- [32] Fishbane, P. M., Gasiorowicz, S. and Thornton, S. T., "Physics for Scientists and Engineers", Prentice hall, Second Edition, Extended, 0-13-231176-3, 1996
- [33] Crowther, R. and Stark, J., "The Determination of the Gas-Surface Interaction from Satellite Orbit Analysis as applied to ANS-1 (1975-70A)", Pergamon Press Limited, *Planet. Space Sci.*, Vol. 39, No. 5, pp. 729-736, 1991
- [34] Kuyper, D. C., "Modelling of the Aerodynamic Forces for the Earth Remote Sensing Satellite ERS-1", Delft University of Technology, 3/1991
- [35] Tarabini, L. and Gil-Fernandez, J., "Aerodynamic Analysis of TerraSAR-L. Drag Coefficient Computation Report.", an unpublished ESA commissioned study conducted by GMV ([www.GMV.es](http://www.GMV.es)) provided by Dave Simpson of EADS Astrium, UK ([www.astrium.eads.net](http://www.astrium.eads.net)), 5/2005
- [36] Pike, J., "Forces on Convex Bodies in Free Molecular Flow", AIAA Journal, Vol. 13, No 11, pg 1454-1459, Royal Aircraft Establishment, Farnborough, Hants, UK, 11/1975

- [37] Schaaf, S. A. and Chambré, P. L., edited by Emmons, H.W., "Flow of Rarefied Gases, Fundamentals of Gas Dynamics", Princeton University Press, p. 687-708, 1958
- [38] Storch, J. A., "Aerodynamic Disturbances on Spacecraft in Free-Molecular Flow", The Aerospace Corporation, TR-2003(3397)-1, 2/5/2003
- [39] Klinkrad, H., Koppenwallner, G., Johannsmeier, D., Ivanov, M. and Kashkovsky, A., "Free Molecular and Transitional Aerodynamics of Spacecraft", Pergamon, 0273-1 177(95)00414, Adv. Space Res. Vol. 16. No. 12. pp. (12)33+(12)36, 1995
- [40] Davis, D. H., "Monte Carlo Calculation of Molecular Flow Rates Through a Cylindrical Elbow and Pipes of Other Shapes", J. Appl. Phys. 31, 1169-1176. cited in Bird, G. A., 'Molecular Gas Dynamics and the Direct Simulation of Gas Flows', Oxford University Press, 0-19-856195-4, 5/5/1994, 1961
- [41] Crowther, R., "Re-Entry Aerodynamics Derived from Space Debris Trajectory Analysis", Pergamon Press Limited, Planet. Space Sci., Vol. 40, No. 5, pp. 641-646, 1991
- [42] Bird, G. A., "Direct Simulation Monte Carlo Method: Visual Programs at GAB Consulting", Help Document, <http://www.gab.com.au/>
- [43] Bird, G. A., edited by Bartel, T. J. and Gallis, M. A., "Forty Years of DSMC, and Now?", American Institute of Physics, Rarefied Gas Dynamics: 22nd International Symposium, 22/7/2000
- [44] Moss, J. N., Wilmoth, R. G. and Price, J. M., "DSMC Simulations of Blunt Body Flows for Mars Entries: Mars Pathfinder and Mars Microprobe Capsules", AIAA, 97-2508, 1997
- [45] Takashima, N. and Wilmoth, R. G., edited by Ketsdever, A. D. and Muntz, E. P., "Rarefied Aerothermodynamics of Mars Odyssey", AIAA, Rarefied Gas Dynamics: 23rd International Symposium, 7/2002
- [46] Lips, T. and Fritsche, B., "A Comparison of Commonly Used Re-Entry Analysis Tools", Pergamon, Acta Astronautica 57 (2005) 312 – 323, 21/4/2005
- [47] Fritsche, B., Roberts, T., Romay, M., Ivanov, M., Grinberg, E. and Klinkrad, H., "Spacecraft Disintegration during Uncontrolled Atmospheric Re-Entry", Hyperschall Technologie Göttingen, ESA SP-393, Second European Conference on Space Debris, <http://www.htg-hst.de>, 3/1997
- [48] Klinkrad, H., Fritsche, B. and Kashkovsky, A., "Prediction of Spacecraft Destruction during Uncontrolled Re-Entries", ESA, Sp-468, Proc. of the European Conf. on Spacecraft Structures, Materials, and Testing,

- Noordwijk, the Netherlands, 29/11/2000-01/12/2000
- [49] Wilmoth, R. G., Blanchard, R. C. and Moss, J. N., "Rarefied Transitional Bridging of Blunt Body Aerodynamics", American Institute of Physics (AIP), 21st International Symposium on Rarefied Gas Dynamics, Marseille, France, 26/7/1998 - 31/7/1998
- [50] Koppenwallner, G., Fritsche, B. and Lips, T., "Multidisciplinary Analysis Tools for Orbit and Re-entry", 3rd International Workshop on Astrodynamics Tools and Techniques, 10/2006
- [51] Zheng, Y. S., Reese, J. M. and Struchtrup, H., "Comparing Macroscopic Continuum Models for Rarefied Gas Dynamics: A New Test Method", Elsevier Science Ltd, Journal of Computational Physics, Vol. 218, Issue 2, pp 748-769, 0021-9991, 1/11/2006
- [52] "MOLFLUX: Molecular Flux Program",  
<http://www.openchannelfoundation.org/projects/molflux>  
<http://www.openchannelfoundation.org/projects/molflux>
- [53] "Astrium Spacecraft Systems Engineering Tools",  
<http://www.astrium.eads.net/corp/prod/>
- [54] "PLUME, a Thruster Plume Impingement Modelling Tool", Developed by EADS Astrium, <http://www.astrium.eads.net/corp/prod/00000994.htm>
- [55] Provost, S., Theroude, C., Tonu, T. and Viel-Inguimbert, V., "Onera Ion Erosion and Contamination Tests and their Application to Astrium PPS Modelling Tool", ESA, SP-540, Proc., of the 9th Int. Symp. On Materials in a Space Env., Noordwijk, the Netherlands, 20/6/2003
- [56] Ivanov, M., "RAMSES: Rarefied Aerodynamics Modelling System for Earth Satellites", Hyperschall Technologie Göttingen, <http://www.htg-hst.de/>
- [57] "ESABASE: An Engineering Tool Supporting the Harmonisation /Standardisation of Spacecraft Analysis Modelling and Space-Related Analysis", [http://www.estec.esa.nl/wmwww/wma/R\\_and\\_D/esabase-1.html](http://www.estec.esa.nl/wmwww/wma/R_and_D/esabase-1.html)
- [58] Borde, J., Renard, P., De Sabbathier, G. and Drolshagen, G., "Improved Analysis Tool for the Computation of Spacecraft Surface Erosion Due to Atomic Oxygen", ESA, SP-368, Proceedings of the Sixth International Symposium on Materials in Space Environment, ESTEC, Noordwijk, 92-9092-314-8, 11/1994
- [59] Boulton, W. J., "The Determination and Analysis of the Orbit of NIMBUS 1 Rocket 1964-52B Variations in Orbital Inclination (Parts 1 and 2)", Pergamon Press Limited, Planet. Space Sci., Vol. 33, No. 8, pp. 965-982, 14/2/1985

- [60] Moore, P. and Ehlers, S., "Preliminary Study of Differential Force Modelling on ERS-1 and ERS-2", Elsevier Science Limited, Adv. Space Res Vol. 19, No. 11, pp. 1655-1659, 1997
- [61] Hedahl, M. O. and Wilmoth, R. G., "Comparisons of the Maxwell and CLL Gas/Surface Interaction Models using DSMC", NASA Langley Research Centre, TM-110205, 12/1995
- [62] Borisov, S. F., "Progress in Gas-Surface Interaction Study", 24th International Symposium on Rarefied Gas Dynamics, Bari, 10/7/2004
- [63] Cercignani, C., "Rarefied Gas Dynamics from Basic Concepts to Actual Calculations", Cambridge University Press, 0-521-65992-2, 2000
- [64] Newton, I., "Philosophiae Naturalis Principia Mathematica", The Royal Society, London, 1687
- [65] Anderson, J. D. (JR), "Introduction to Flight, Third Edition", McGraw-Hill International Editions, 0-07-100496-3, 1989
- [66] Wadsworth, D. C., VanGilder, D. B., and Dogra, V. K., edited by Ketsdever A. D. and Muntz, E. P., "Gas-Surface Interaction Model Evaluation for DSMC Applications", American Institute of Physics (AIP), Rarefied Gas Dynamics 23rd International Symposium, Whistler, British Columbia, Canada, 0-7354-0124-1, 20/7/2002-25/7/2002
- [67] Mazanek, D. D., Kumar, R. R., Seywald, H. and Qu, M., "GRACE Mission Design: Impact of Uncertainties in Disturbance Environment and Satellite Force Models", AIAA, AAS-00-163, <http://www.csr.utexas.edu/grace>, 26/1/2002
- [68] Henry, M. W. and Mazanek, D. D., "Spacecraft and Sensors Branch Application Guide for FREEMOL Software", AMA Report No. 95-5, NASA Contract NAS1-18935, 4/1996
- [69] Hughes, P. C., "Spacecraft Attitude Dynamics", AIAA, 0-471-81842-9, 1986
- [70] Emmons, H. W., "Fundamentals of Gas Dynamics", Princeton University Press, Vol. III, High Speed Aerodynamics And Jet Propulsion, 533.6 EMM, 1958
- [71] Patterson, G. N., "Molecular Flow of Gases", John Wiley & Sons, 533.6.011.8 PAT, 1956
- [72] Smoluchowski, M. V., "Wied. Ann 64, 101 (1898)", cited in Flow of Rarefied Gases, Fundamentals of Gas Dynamics, by Schaaf, S.A. and Chambré, P.L., edited by Emmons, H.W., p. 687-708, Princeton University Press, 1958



- [73] Bird, G. A., "Aerodynamic Effects on Atmospheric Composition Measurements from Rocket Vehicle in the Atmosphere", Pergamon, Planet. Space Sci., Vol. 36, No 9, pp 921-926, 15/4/1988
- [74] Cook, S. R. and Hoffbauer, M. A., "Measurement of Momentum Transfer Coefficients for H<sub>2</sub>, N<sub>2</sub>, and CO<sub>2</sub> Incident upon Spacecraft Surfaces", NASA, Technical Paper 3701, 11/1997
- [75] Tennyson, R. C., "Atomic Oxygen and its Effect on Materials in Space", AIAA, Rarefied Gas Dynamics: Space Science and Engineering, Vol. 160, pp.461-477, edited by Shizgal, B. D. and Weaver, D. P., Eighteenth International Symposium on Rarefied Gas Dynamics, Vancouver, Canada, 31/7/1992
- [76] Tribble, A. C., "The Space Environment Implications for Spacecraft Design", Princeton University Press, revised and expanded edition, 0691102996, 629.78 TRI, 7/2003
- [77] Hurlbut, F. C., "Particle Surface Interaction in the Orbital Context: A Survey", AIAA, Rarefied Gas Dynamics: Space-Related Studies, Vol. 116, pp.419-450, edited by Muntz, E. P., Weaver, D. P. and Campbell, D. H., Sixteenth International Symposium on Rarefied Gas Dynamics, Pasedena, California, 0-930403-53-3, 1989
- [78] Moser, H. O. and Schempp, A., edited by Muntz, E. P., Weaver, D. P. and Campbell, D. H., "Options for Generating Greater Than 5-eV Atmospheric Species", AIAA, Rarefied Gas Dynamics Vol. 116, pp. 171-186, 0-930403-53-3, 1989
- [79] Crowther, R. and Stark, J., "Determination of Momentum Accommodation from Satellite Orbits: An Alternative Set of Coefficients", AIAA, Rarefied Gas Dynamics: Space-Related Studies, Vol. 116, pp.463-475, edited by Muntz, E. P., Weaver, D. P. and Campbell, D. H., Sixteenth International Symposium on Rarefied Gas Dynamics, Pasedena, California, 16/7/1998
- [80] "2006 Commercial Space Transportation Forecasts", United States Federal Aviation Authority, [http://www.faa.gov/about/office\\_org/headquarters\\_offices/ast/media/2006\\_Forecast\\_GSO\\_NGSO\\_May\\_24.pdf](http://www.faa.gov/about/office_org/headquarters_offices/ast/media/2006_Forecast_GSO_NGSO_May_24.pdf), 2006
- [81] Harrison, I. K. and Swinerd, G. G., "A Free Molecular Aerodynamic Investigation Using Multiple Satellite Analysis", Pergamon, Planet Space Science, Vol. 44, No. 2, pp. 178-180, 22/5/1995
- [82] Brown, C. D., "Elements of Spacecraft Design", AIAA, J. S. Przemieniecki Series Editor-in-Chief, 1-56347-524-3, 2002

- [83] Wertz, J. R., edited by Wiley, L. J., "Space Mission Analysis and Design", Kluwer, 1991
- [84] "ESA Concurrent Design Facility Concurrent Engineering Definition", [http://www.esa.int/SPECIALS/CDF/SEM1OF1P4HD\\_0.html](http://www.esa.int/SPECIALS/CDF/SEM1OF1P4HD_0.html)
- [85] "The ESA Concurrent Design Facility (CDF)", ESA, [http://www.esa.int/SPECIALS/CDF/SEMLU49YFDD\\_0.html](http://www.esa.int/SPECIALS/CDF/SEMLU49YFDD_0.html)
- [86] Matthysen, A. and Henderson, R., "The CDF IDM Core Template to support European partners' CE initiatives", ESA, 1st Concurrent Engineering for Space Applications Workshop (CEW 2004), Noordwijk, the Netherlands, 30/9/2004
- [87] DeFlori, P. "JPL Facilities and Software for Collaborative Design", ESA, 1st Concurrent Engineering for Space Applications Workshop (CEW 2004), Noordwijk, the Netherlands, 30/9/2004
- [88] Hartmann, R., Scheuble, M., Paus, S., Waugh, L., Fritz, S., Mussat, P., and Koeck, C., "The Satellite Design Office: An Industrial Concurrent Design Centre Application", ESA, 1st International Workshop on Concurrent Engineering for Space Applications (CEW 2004), 30 September – 01 October 2004, ESA/ESTEC, Noordwijk, the Netherlands, 30/9/2004
- [89] Paccagnini, C., Zoppo, G. P. and Piantieri, G., "CODE: the COncurrent Development Environment", ESA, 1st International Workshop on Concurrent Engineering for Space Applications (CEW 2004), 30 September – 01 October 2004, ESA/ESTEC, Noordwijk, the Netherlands, 30/9/2004
- [90] Hartman, R., "The Collaborative Engineering Environment (CEE)", ESA, 1st ESA Space System Design, Verification & AIT Workshop, Noordwijk, the Netherlands, 13/6/2002
- [91] "Selected Quotations from the 1st Concurrent Engineering for Space Applications Workshop (CEW 2004)", ESA, Noordwijk, the Netherlands, [http://www.esa.int/SPECIALS/CDF/SEM0Z2NKPZD\\_0.html](http://www.esa.int/SPECIALS/CDF/SEM0Z2NKPZD_0.html), 1/10/2004
- [92] "ESATAN", <http://mechanical-engineering.esa.int/thermal/tools>
- [93] Schrage, D., Beltracchi, T., Berke, L., Dodd, A., Niedling, L. and Sobieski, J., "AIAA Technical Committee on Multidisciplinary Design Optimization (MDO) White Paper on Current State of the Art", AIAA, [http://endo.sandia.gov/AIAA\\_MDOTC/sponsored/aiaa\\_paper.html](http://endo.sandia.gov/AIAA_MDOTC/sponsored/aiaa_paper.html), 15/1/1991
- [94] De Koning, H. P., "Data Exchange Standardisation – Experiences and Outlook", ESA, 1st Concurrent Engineering for Space Applications Workshop, Noordwijk, the Netherlands, 30/9/2004

- [95] Stephenson, A. G., et al, "Report on Project Management in NASA by the Mars Climate Orbiter Mishap Investigation Board", NASA, [ftp://ftp.hq.nasa.gov/pub/pao/reports/2000/MCO\\_MIB\\_Report.pdf](ftp://ftp.hq.nasa.gov/pub/pao/reports/2000/MCO_MIB_Report.pdf)
- [96] "Object (orientated) Database Management System (ODBMS) Organisation", <http://odbms.org>
- [97] Mosher, T., "Applicability of Selected Multidisciplinary Design Optimisation Methods To Conceptual Spacecraft Design", AIAA, 96-4052, 1996
- [98] "International Standards Organisation (ISO)", <http://www.iso.org>
- [99] "ESA Software Engineering Standards", [http://www.esa.int/TEC/Software\\_engineering\\_and\\_standardisation](http://www.esa.int/TEC/Software_engineering_and_standardisation)
- [100] Lin, R. and Afjeh, A. A., "An Extensible, Interchangeable and Sharable Database Model for Improving Multidisciplinary Aircraft Design", AIAA, 2002-5613, 2002
- [101] "Database Normalisation Basics", Microsoft, <http://support.microsoft.com/kb/100139>
- [102] Hoxley, J., "DirectX Online Tutorials", Jack.Hoxley@DirectX4VB.com, <http://www.DirectX4VB.com>, 21/12/2002
- [103] Watt, A., "Fundamentals of Three-Dimensional Computer Graphics", Addison-Wesley Publishing Company, 0201154420, 681.327.1 WAT, 1989
- [104] Heiny, L., "Advanced Graphics Programming using C/C++", Wiley, 681.327.1 HEI, 1993
- [105] Foley, J. D., Van Dam, A., Feiner, S. K. and Huges, J. F., "Computer Graphics Principles and Practice", Addison Wesley, 0-201-12110-7, 681.327.1 FOL, 1990
- [106] Rennie, M., Fernandex, V. and Caramagno, A., "Integrated Model-based Simulation, Autocoding and Real-Time Onboard Software Validation and Verification", ESA, 8th International Workshop for European Space Programmes (SESP 2004), ESTEC, Noordwijk, the Netherlands, 21/10/2004
- [107] Wertz, J. R. and Larson, W. J., "Space Mission Analysis and Design", Microcosm Press and Kluwer Academic Publishers, 1-881883-10-8, 1999
- [108] Harris, M. and Lyle, R., "Spacecraft Radiation Torques", NASA, SP-8027, 1969
- [109] "The latest International Space Environment Service (ISES) Solar Cycle Predictions", NOAA/Space Environment Centre, <http://www.sec.noaa.gov/SolarCycle/>

- [110] "Space Shuttle Surface Mesh", 3D CAD Browser,  
<http://www.3dcadbrowser.com/>
- [111] Miró, J., "Evolution of Concurrent Engineering in Phases B/C/D", ESA,  
2nd Concurrent Engineering for space applications Workshop (CEW 2006),  
at ESTEC, Noordwijk, the Netherlands, 20/10/2006
- [112] Bandecchi, M., Gunner, J. and Matthyssen, A., "iCDF and OCDS  
Distribution and sharing of ESA CDF Models, Tools and Methodologies",  
ESA, 2nd Concurrent Engineering for space applications Workshop (CEW  
2006), at ESTEC, Noordwijk, the Netherlands, 20/10/2006
- [113] Graziano, B. P. and Roberts, P. C. E., "An Integrated Information Systems  
Approach to Spacecraft Engineering", ESA, 2nd Concurrent Engineering  
for space applications Workshop (CEW 2006), at ESTEC, Noordwijk, the  
Netherlands, 20/10/2006

## 11 BIBLIOGRAPHY

This section lists the main reference books used. They are recommended reading for anyone wishing to follow-up this work. The format of the references is consistent with the format used in Chapter 10.

- Tribble, A. C., "The Space Environment Implications for Spacecraft Design", Princeton University Press, revised and expanded edition, 0691102996, 629.78 TRI, 7/2003
- Watt, A., "Fundamentals of Three-Dimensional Computer Graphics", Addison-Wesley Publishing Company, 0201154420, 681.327.1 WAT, 1989
- Bird, G. A., "Molecular Gas Dynamics and the Direct Simulation of Gas Flows", Oxford University Press, 0-19-856195-4, 5/5/1994
- Cercignani, C., "Rarefied Gas Dynamics From Basic Concepts to Actual Calculations", Cambridge University Press, 0-521-65992-2, 2000
- Fortescue, P. and Stark, J., "Spacecraft Systems Engineering", Wiley, 0-471-95220-6, 1995
- Hughes, P. C., "Spacecraft Attitude Dynamics", AIAA, 0-471-81842-9, 1986
- Foley, J. D., Van Dam, A., Feiner, S. K. and Hughes, J. F., "Computer Graphics Principles and Practice", Addison Wesley, 0-201-12110-7, 1990
- Wertz, J. R., edited by Wiley, L. J., "Space Mission Analysis and Design", Kluwer, 1991
- Anderson, J. D. (JR), "Fundamentals of Aerodynamics", McGraw-Hill International Editions, Second Edition, 0-07-100767-9, 1991
- Anderson, J. D. (JR), "Introduction to Flight, Third Edition", McGraw-Hill International Editions, 0-07-100496-3, 1989
- Stoecker M. A. with Microsoft Corporation, "Developing Windows-Based Applications with Microsoft Visual Basic .Net and Visual C#.Net", Microsoft Press, Second Edition, 0-7356-1926-3, 2003



## **A1 APPENDIX 1 - DIGITAL INFORMATION**

The accompanying Compact Disc (CD) provides a digital copy of the SEDAT Database Schema (described in Section 5.5) and the SEDAT Help System (described in Section 5.7), which constitute Appendix 1. It also includes a digital copy of the thesis (including Appendices 2 and 3). Its full contents are:

- *Database Schema\SEDAT\_v1\_7.html* (Appendix 1)
- *Help\Help.chm* (Appendix 1)
- *Thesis.pdf* (includes Appendix 2 and Appendix 3)





## A2 APPENDIX 2 - FMF MODULE TECHNICAL IMPLEMENTATION

This appendix provides details of the FMF Module's technical implementation. Section A2.1 provides a list of the SEDAT Database tables, with descriptions. Section A2.2 provides details of the SEDAT Client object model.

### A2.1 Database Tables

The database tables of the FMF Module are referred to throughout the thesis and accompanying appendices where contextually relevant. To assist with navigating around these various references, Table A2-1 lists all 52 tables of the FMF Module with a high-level description.

**Table A2-1 - The Database Tables of the FMF Module**

Table	Description
<i>ZFRT_FlowSource</i>	Stores information related to a gas flow source.
<i>ZFRT_FlowVector</i>	Stores information related to a gas flow vector.
<i>ZFRT_GasFlowRay</i>	Stores information related to a gas flow ray.
<i>ZFRT_GSIM</i>	Stores information related to a GSIM.
<i>ZFRT_GSIMAttribute</i>	Stores information related to a GSIM's attributes.
<i>ZFRT_GSIMBound</i>	Stores information related to a GSIM's bounds.
<i>ZFRT_GSIMLibrary</i>	Stores information related to a GSIM library.
<i>ZFRT_GSIMParameter</i>	Stores information related to a GSIM's parameter.
<i>ZFRT_MAC</i>	Stores information related to a Model Analysis Configuration (MAC).
<i>ZFRT_MACCalcGeom</i>	Stores information related to the calculated geometry of a MAC.
<i>ZFRT_MACCalcGeomSmesh</i>	Stores information related to the calculated geometry of a MAC's surface mesh.
<i>ZFRT_MACCalcGeomSmeshPanel</i>	Stores information related to the calculated geometry of a MAC's surface mesh's panels.
<i>ZFRT_MACCalcGeomSmeshPanelVector</i>	Stores information related to the calculated geometry of a MAC's surface mesh's panel's vertices.
<i>ZFRT_MACCalcGeomSmeshPanelVertex</i>	Stores information related to the calculated geometry of a MAC's surface mesh's panel's vectors.
<i>ZFRT_MACGasFlow</i>	Stores information related to the gas flow associated with a MAC.

## Appendix 2 - FMF Module Technical Implementation

<i>ZFRT_MACGasFlowMolecule</i>	Stores information related to the gas flow molecules associated with a MAC.
<i>ZFRT_MACGSI</i>	Stores information related to the GSIs associated with a MAC.
<i>ZFRT_MACOrientation</i>	Stores information related to the spacecraft orientations and angular velocities associated with a MAC.
<i>ZFRT_MACR</i>	Stores information related to the results associated with a MAC.
<i>ZFRT_MACRCoefficient</i>	Stores information related to the results coefficients associated with a MAC.
<i>ZFRT_MACRSmesh</i>	Stores information related to the results associated with a MAC's surface mesh.
<i>ZFRT_MACRSmeshPanel</i>	Stores information related to the results associated with a MAC's surface mesh's panels.
<i>ZFRT_MACRSmeshPanelGSI</i>	Stores information related to the results associated with a MAC's surface mesh's panel's GSIs.
<i>ZFRT_MACRSmeshPanelGSIAttribute</i>	Stores information related to the results associated with a MAC's surface mesh's panel's GSI's attributes.
<i>ZFRT_MACSmesh</i>	Stores information related to surface meshes associated with a MAC.
<i>ZFRT_Model</i>	Stores information related to a model.
<i>ZFRT_ModelAnalysis</i>	Stores information related to a model analysis.
<i>ZFRT_ModelAnalysisRotation</i>	Stores information related to the rotations associated with a model analysis.
<i>ZFRT_ModelAnalysisSmesh</i>	Stores information related to the surface meshes associated with a model analysis.
<i>ZFRT_ModelAnalysisSmeshRotation</i>	Stores information related to the surface mesh rotations associated with a model analysis.
<i>ZFRT_ModelCoordinateSystem</i>	Stores information related to the coordinate systems associated with a model.
<i>ZFRT_ModelGasFlow</i>	Stores information related to the gas flow associated with a model.
<i>ZFRT_ModelNozzlePlume</i>	Stores information related to the nozzle plumes associated with a model.
<i>ZFRT_ModelSmesh</i>	Stores information related to the surface meshes associated with a model.
<i>ZFRT_Nozzle</i>	Stores information related to a nozzle.
<i>ZFRT_NozzleParameter</i>	Stores information related to a nozzle's parameters.
<i>ZFRT_NozzlePlume</i>	Stores information related to a nozzle plume.
<i>ZFRT_NozzlePlumeParameter</i>	Stores information related to a nozzle plume's parameters.
<i>ZFRT_ReflectedFlow</i>	Stores information related to reflected gas flow.

<i>ZFRT_SimulatedGas</i>	Stores information related to simulated gas molecules.
<i>ZFRT_SmeshSurface</i>	Stores information related to a surface mesh's surface.
<i>ZFRT_SmeshSurfaceMap</i>	Stores information related to the GSIMs associated with a surface mesh's surface.
<i>ZFRT_SmeshTemperature</i>	Stores information related to a surface mesh's temperature.
<i>ZFRT_SmeshTemperaturePanel</i>	Stores information related to a surface mesh's panel's temperature.
<i>ZFRT_SurfaceGSIM</i>	Stores information related to the surface associated with a GSIM.
<i>ZFRT_SurfaceGSIMInt</i>	Stores information related to a gas-surface interaction associated with a GSIM.
<i>ZFRT_SurfaceGSIMIntData</i>	Stores information related to the gas-surface interaction data associated with a GSIM.
<i>ZFRT_SurfaceGSIMIntDataBound</i>	Stores information related to the gas-surface interaction data's bounds associated with a GSIM.
<i>ZFRT_SurfaceGSIMIntDataParameter</i>	Stores information related to the gas-surface interaction data's parameters associated with a GSIM.
<i>ZFRT_WindVector</i>	Stores information related to a wind vector.
<i>ZFRT_WindVectorAutomatic</i>	Stores information related to an automatic wind vector.
<i>ZFRT_WindVectorExplicit</i>	Stores information related to an explicit wind vector.

## A2.2 Client Object Model

This section of the appendix describes some of the programming objects that were developed to meet the specific requirements of the FMF Module, but which, as explained in Section 6.4.2, could be used by other modules. The headings in the following sub-sections refer to the namespaces that contain the objects. The root namespace for all code in the SEDAT solution is *Aurora*.

Throughout the sub-sections, reference is made to the two client layers of SEDAT's client-server architecture (illustrated in Figure 5-2). The two client layers are the Data Access Layer (DAL) and the Processing, Presentation, and Reporting Layer (PPRL).

### A2.2.1 Aurora.Engineering.ThreeD.VectorSpace

The classes of the *Aurora.Engineering.ThreeD.VectorSpace* namespace represent processing components within the PPRL. Table A2-2 provides descriptions of some of the main classes of the namespace.

**Table A2-2 - The Main Aurora.Engineering.ThreeD.VectorSpace Classes**

Class	Description
<i>AngularVelocity</i>	Represents angular velocity objects, defined using a right-handed coordinate system.
<i>Axis</i>	Represents axis objects, defined by two points ( <i>Aurora.Engineering.ThreeD.Vector's</i> ).
<i>Quaternion</i>	Used to represent quaternion objects. Implements the <i>ILockable</i> interface, which prevents the eigenvector components and eigenvalue of the quaternion object from being changed when locked.
<i>QuaternionCollection</i>	Represents a collection of <i>Aurora.Engineering.ThreeD.Quaternion</i> objects.
<i>RotationMatrix</i>	Represents rotation matrix objects. Can be used to rotate vectors in three-dimensional space. Can be instantiated using Euler parameters or matrix elements.
<i>TransformationMatrix</i>	Represents transformation matrix objects. Can be used to rotate, translate, and scale vectors in three-dimensional space. Can be instantiated using Euler parameters or matrix elements.
<i>UnitQuaternion</i>	Represents unit quaternion objects (quaternions that have been normalised by their magnitude). Inherits from the <i>Aurora.Engineering.ThreeD.Quaternion</i> class.
<i>UnitQuaternionCollection</i>	Represents a collection of <i>Aurora.Engineering.ThreeD.UnitQuaternion</i> objects.
<i>UnitVector</i>	Represents unit vector objects (vectors that have been normalised by their magnitude). Inherits from the <i>Aurora.Engineering.ThreeD.Vector</i> class.
<i>UnitVectorCollection</i>	Represents a collection of <i>Aurora.Engineering.ThreeD.UnitVector</i> objects.
<i>Vector</i>	Used to represent vector objects. Implements the <i>ILockable</i> interface, which prevents the Cartesian components of the vector object from being changed when locked. Also implements the <i>IRotatable</i> interface, which enables the vector to be rotated in three dimensional space using a variety of methods (Euler rotations, axis and angle method, quaternions, or matrices).
<i>VectorCollection</i>	Represents a collection of <i>Aurora.Engineering.ThreeD.Vector</i> objects.

The structure of the *Vector* class is illustrated in Figure A2-1, to provide an example of the size and complexity of the classes in the *Aurora.Engineering.ThreeD.VectorSpace* namespace.

```

+Lock()
+Unlock()
+IsLocked(): Boolean
+Accuracy(): Double
+NormalisedAccuracy(): Double
+Zero(): Vector
+GeometryChanged(in sender : Object, in e : VectorGeometryChangedEventArgs)
#OnGeometryChanged(in sender : Object, in e : VectorGeometryChangedEventArgs)
+New()
+New(in pX : Double, in pY : Double, in pZ : Double)
+New(in pColumn(): Double)
+New(in pVector3 : Vector3)
+X(): Double
+Y(): Double
+Z(): Double
+Component(in pVectorComponent : VectorComponent) : Double
+Component(in pVectorComponent : VectorComponent) : Double
+Component(in pVectorComponent : VectorComponent) : Double
+Column(): Double
+Magnitude(): Double
+L(): Double
+M(): Double
+N(): Double
+DirectionCosine(in pDirectionCosine : DirectionCosines) : Double
+DirectionCosine(in pDirectionCosine : DirectionCosines) : Double
+DirectionCosine(in pDirectionCosine : DirectionCosines) : Double
+GetUnitVector(): UnitVector
+GetQuaternion(): Quaternion
+Clone(): Object
+CompareTo(in pObject : Object) : ComparisonResult
+ToString(): String
+ToString(in pFormat : String) : String
+Equals(in pObject : Object) : Boolean
+Equals(in pObject : Object, in pAccuracy : Double) : Boolean
+GetHashCode(): Integer
+GetVector3(): Vector3
+Dot(in pVector : Vector) : Double
+ProjectedOnto(in pVector : Vector) : Double
+Plus(in pVectors(): Vector) : Vector
+Minus(in pVectors(): Vector) : Vector
+Times(in pScalar : Double) : Vector
+Scale(in pScale : Vector) : Vector
+Over(in pScalar : Double) : Vector
+Cross(in pVector : Vector) : Vector
+Rotate(in pPoint1 : Vector, in pPoint2 : Vector, in pAngle : Double) : Vector
+Rotate(in pAxis : UnitVector, in pAngle : Double) : Vector
+Rotate(in pPhi : Double, in pTheta : Double, in pPsi : Double, in pEulerRotation : EulerRotation, in pUseQuaternions : Boolean = True) : Vector
+Rotate(in pUnitQuaternion : UnitQuaternion) : Vector
+Rotate(in pUnitQuaternions(): UnitQuaternion) : Vector
+Rotate(in pRotationMatrices() : RotationMatrix) : Vector
+Rotate(in pRotationMatrix : RotationMatrix) : Vector
+Transform(in pTransformationMatrices() : TransformationMatrix) : Vector
+Transform(in pTransformationMatrix : TransformationMatrix) : Vector
+Rotate(in pVector : Vector, in pPoint1 : Vector, in pPoint2 : Vector, in pAngle : Double) : Vector
+Rotate(in pVector : Vector, in pAxis : UnitVector, in pAngle : Double) : Vector
+Rotate(in pVector : Vector, in pPhi : Double, in pTheta : Double, in pPsi : Double, in pEulerRotation : EulerRotation) : Vector
+Rotate(in pVector : Vector, in pUnitQuaternion() : UnitQuaternion) : Vector
+Rotate(in pVector : Vector, in pRotationMatrix : RotationMatrix) : Vector
+Rotate(in pVector : Vector, in pRotationMatrices() : RotationMatrix) : Vector
+Transform(in pVector : Vector, in pTransformationMatrix : TransformationMatrix) : Vector
+Transform(in pVector : Vector, in pTransformationMatrices() : TransformationMatrix) : Vector
+Equals(in pObjectA : Object, in pObjectB : Object) : Boolean
+Equals(in pObjectA : Object, in pObjectB : Object, in pAccuracy : Double) : Boolean
+Project(in pVectorA : Vector, in pVectorB : Vector) : Double
+Multiply(in pVector : Vector, in pScalar : Double) : Vector
+Divide(in pVector : Vector, in pScalar : Double) : Vector
+Subtract(in pVectorTo : Vector, in pVectorFrom : Vector) : Vector
+Sum(in pVectors() : Vector) : Vector
+Cross(in pVector1 : Vector, in pVector2 : Vector) : Vector
+Dot(in pVector1 : Vector, in pVector2 : Vector) : Double
+TripleProduct(in pVector1 : Vector, in pVector2 : Vector, in pVector3 : Vector) : Double
+AngleBetween(in pVector1 : Vector, in pVector2 : Vector, in pAngleBetweenVectorsDefinitionType : AngleBetweenVectorsDefinitionType = AngleBetweenVectorsDefinitionType.AngleTendsToZeroIfVectorsTendTowardsOppositeDirections) : Double
+CosOfAngleBetween(in pVector1 : Vector, in pVector2 : Vector, in pAngleBetweenVectorsDefinitionType : AngleBetweenVectorsDefinitionType = AngleBetweenVectorsDefinitionType.AngleTendsToZeroIfVectorsTendTowardsOppositeDirections) : Double
+AngleBetween(in pUnitVector1 : UnitVector, in pUnitVector2 : UnitVector, in pAngleBetweenVectorsDefinitionType : AngleBetweenVectorsDefinitionType = AngleBetweenVectorsDefinitionType.AngleTendsToZeroIfVectorsTendTowardsOppositeDirections) : Double
+CosOfAngleBetween(in pUnitVector1 : UnitVector, in pUnitVector2 : UnitVector, in pAngleBetweenVectorsDefinitionType : AngleBetweenVectorsDefinitionType = AngleBetweenVectorsDefinitionType.AngleTendsToZeroIfVectorsTendTowardsOppositeDirections) : Double
+AreParallel(in pVector1 : Vector, in pVector2 : Vector) : Boolean
+AreAntiParallel(in pVector1 : Vector, in pVector2 : Vector) : Boolean
+AreOrthogonal(in pVector1 : Vector, in pVector2 : Vector) : Boolean
+GetAreaBetween(in pVector1 : Vector, in pVector2 : Vector) : Double
+Parse(in pVector : String) : Vector
+Determinant(in pVector1 : Vector, in pVector2 : Vector, in pVector3 : Vector) : Double
+RandomVector() : Vector

```

Figure A2-1 - Vector Class Structure

### A2.2.2 Aurora.Engineering.ThreeD.WorkSpace

The classes of the *Aurora.Engineering.ThreeD.WorkSpace* namespace represent processing components within the PPRL. Table A2-3 provides descriptions of some of the main classes of the namespace.

**Table A2-3 - The Main Aurora.Engineering.ThreeD.WorkSpace Classes**

Class	Description
<i>Entity</i>	Represents an entity in three-dimensional space. It must be inherited (it cannot be instantiated). It is the base class for all other classes that represent three-dimensional objects in the <i>Aurora.Engineering.ThreeD.WorkSpace</i> namespace.
<i>Mesh</i>	Represents a mesh object. It inherits from the <i>Aurora.Engineering.ThreeD.WorkSpace.MeshEntity</i> class. It must be inherited (it cannot be instantiated).
<i>MeshEntity</i>	Represents a mesh entity object. It inherits from the <i>Aurora.Engineering.ThreeD.WorkSpace.Entity</i> class. It must be inherited (it cannot be instantiated).
<i>MeshPrimitive</i>	Represents a primitive mesh object, such as a panel (a surface mesh element) or a cell (a volume mesh element). It must be inherited (it cannot be instantiated). It inherits from the <i>Aurora.Engineering.ThreeD.WorkSpace.MeshEntity</i> class.
<i>Model</i>	Represents a model object, which contains a <i>Aurora.Engineering.ThreeD.WorkSpace.SurfaceMeshCollection</i> . It inherits from the <i>Aurora.Engineering.ThreeD.WorkSpace.Entity</i> class.
<i>Panel</i>	Represents a panel object, which contains a collection of vertices. It inherits from the <i>Aurora.Engineering.ThreeD.WorkSpace.MeshPrimitive</i> class. It must be inherited (it cannot be instantiated).
<i>PanelCollection</i>	Represents a collection of <i>Aurora.Engineering.ThreeD.WorkSpace.Panel</i> objects as a set of key-value pairs, in which the key is an integer representing the panel's position.
<i>QuadrilateralPanel</i>	Represents a quadrilateral panel object with four vertices. It inherits from the <i>Aurora.Engineering.ThreeD.WorkSpace.Panel</i> class.
<i>SurfaceMesh</i>	Represents a surface mesh object, which contains a <i>Aurora.Engineering.ThreeD.WorkSpace.PanelCollection</i> . It inherits from the <i>Aurora.Engineering.ThreeD.WorkSpace.Mesh</i> class.
<i>SurfaceMeshCollection</i>	Represents a collection of <i>Aurora.Engineering.ThreeD.WorkSpace.SurfaceMesh</i> objects.
<i>TriangularPanel</i>	Represents a triangular panel object with three vertices. It inherits from the <i>Aurora.Engineering.ThreeD.WorkSpace.Panel</i> class.
<i>Vertex</i>	Represents vertex objects. It inherits from the <i>Aurora.Engineering.ThreeD.VectorSpace.Vector</i> class described in Section A2.2.1.

<i>VertexCollection</i>	Represents a collection of <i>Aurora.Engineering.ThreeD.WorkSpace.Vertex</i> objects as a set of key-value pairs, in which the key is an integer representing the vertex's position.
-------------------------	--

Many of the classes of the *Aurora.Engineering.ThreeD.WorkSpace* namespace inherit from one another. One of the benefits of using inheritance is that the inherited classes can use the functionality of the parent class as well exposing additional specialised functionality. The inheritance hierarchy of the classes in the *Aurora.Engineering.ThreeD.WorkSpace* namespace is illustrated in Figure A2-2.

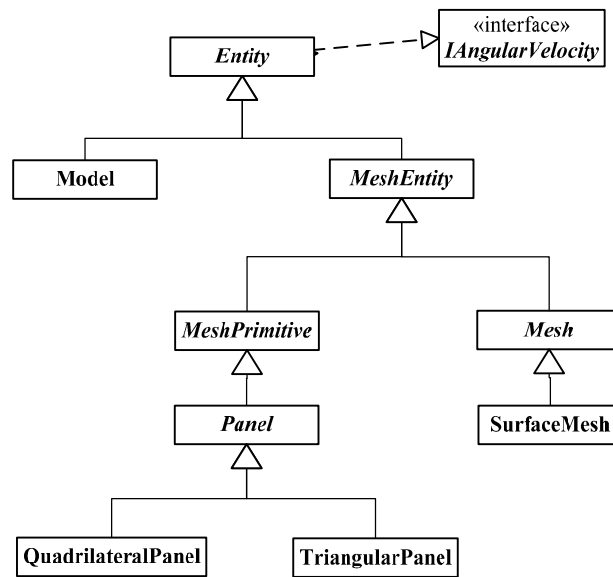


**Figure A2-2 - *Aurora.Engineering.ThreeD.WorkSpace* Inheritance Hierarchy**

### A2.2.3 *Aurora.Engineering.ThreeD.WorkSpace.RayTracer*

The classes of the *Aurora.Engineering.ThreeD.WorkSpace.RayTracer* namespace represent processing components within the PPRL. The classes represent the programmatic implementation of the SEDAT Ray-Tracer, which is described in Section 6.3.

Many of the classes of the *Aurora.Engineering.ThreeD.WorkSpace.RayTracer* namespace inherit from classes of the *Aurora.Engineering.ThreeD.WorkSpace.RayTracer* namespace described in the previous section. Table A2-4 provides descriptions of some of the main classes of the *Aurora.Engineering.ThreeD.WorkSpace.RayTracer* namespace.

**Table A2-4 - The Main *Aurora.Engineering.ThreeD.WorkSpace.RayTracer* Classes**

Class	Description
<i>Model</i>	Represents a model object, which contains an <i>Aurora.Engineering.ThreeD.WorkSpace.SurfaceMeshCollection</i> . Inherits from the <i>Aurora.Engineering.ThreeD.WorkSpace.Model</i> class.
<i>PanelCollection</i>	Represents a collection of <i>Aurora.Engineering.ThreeD.WorkSpace.RayTracer.TriangularPanel</i> or <i>Aurora.Engineering.ThreeD.WorkSpace.RayTracer.QuadrilateralPanel</i> objects.
<i>QuadrilateralPanel</i>	Inherits from the <i>Aurora.Engineering.ThreeD.WorkSpace.QuadrilateralPanel</i> class. Implements the <i>Aurora.Engineering.ThreeD.WorkSpace.RayTracer.IPanel</i> interface, which exposes a number of ray-tracing methods (for example to calculate ray-panel intersection parameters, as outlined in Section 6.3.2).
<i>Ray</i>	Represents a ray-tracing ray object, as described in Section 6.3.2. Its two main properties are its <i>Origin</i> and <i>Direction</i> , represented by <i>Aurora.Engineering.ThreeD.WorkSpace.Vector</i> and <i>Aurora.Engineering.ThreeD.WorkSpace.UnitVector</i> objects respectively.
<i>RayCollection</i>	Represents a collection of <i>Aurora.Engineering.ThreeD.WorkSpace.RayTracer.Ray</i> objects.
<i>RenderState</i>	Used by <i>Aurora.Engineering.ThreeD.WorkSpace.RayTracer.TriangularPanel</i> and <i>Aurora.Engineering.ThreeD.WorkSpace.RayTracer.QuadrilateralPanel</i> objects to store information related to the panel's render state (e.g. whether or not the panel is forward facing, or shadowed).
<i>RenderStateCollection</i>	Represents a collection of <i>Aurora.Engineering.ThreeD.WorkSpace.RayTracer.RenderState</i> objects.
<i>SurfaceMesh</i>	Represents a surface mesh object, which contains a <i>Aurora.Engineering.ThreeD.WorkSpace.RayTracer.PanelCollection</i> . Inherits from <i>Aurora.Engineering.ThreeD.WorkSpace.SurfaceMesh</i> .
<i>SurfaceMeshCollection</i>	Inherits from <i>Aurora.Engineering.ThreeD.WorkSpace.SurfaceMeshCollection</i> . Represents a collection of <i>Aurora.Engineering.ThreeD.WorkSpace.RayTracer.SurfaceMesh</i> objects.
<i>TriangularPanel</i>	Inherits from the <i>Aurora.Engineering.ThreeD.WorkSpace.TriangularPanel</i> class. Implements the <i>Aurora.Engineering.ThreeD.WorkSpace.RayTracer.IPanel</i> interface, which exposes a number of ray-tracing methods (for example to calculate ray-panel intersection parameters, as outlined in Section 6.3.2).

The classes of the *Aurora.Engineering.ThreeD.WorkSpace.RayTracer* namespace can be used to perform any type of ray-tracing. For example, they can be



used to simulate light or other forms of electromagnetic radiation, or, as demonstrated in this thesis, to simulate the paths of gas molecules. However, in most cases some additional functionality is required.

As described previously, the best way to create several specialised classes that share common functionality is to use inheritance. Section A2.2.6 describes the *Aurora.Engineering.Aerodynamics.FMF.RayTracer*, which contains classes that inherit from the classes of the *Aurora.Engineering.ThreeD.WorkSpace.RayTracer* namespace and expose additional functionality specifically for free molecular flow analysis.

#### A2.2.4 Aurora.Engineering.Aerodynamics

The classes of the *Aurora.Engineering.Aerodynamics* namespace represent processing components within the PPRL and are comprised of over 150 lines of bespoke code.

There are two main classes in the *Aurora.Engineering.Aerodynamics* namespace: the *Coefficient* class, which is used to represent aerodynamic coefficients (described in Section 2.3); and the *CoefficientCollection* class, which represents a collection of *Coefficient* objects. Both classes are used by the classes of the *Aurora.Engineering.Aerodynamics.FMF.RayTracer* namespace, described in Section A2.2.6.

#### A2.2.5 Aurora.Engineering.Aerodynamics.Flow

The classes of the *Aurora.Engineering.Aerodynamics.Flow* namespace represent processing components within the PPRL. The classes are used to represent gases and gas flows and are used by the classes of the *Aurora.Engineering.Aerodynamics.FMF.RayTracer* namespace, described in Section A2.2.6.

Table A2-5 provides descriptions of some of the main classes of the *Aurora.Engineering.Aerodynamics.Flow* namespace.

**Table A2-5 - The Main Aurora.Engineering.Aerodynamics.Flow Classes**

Class	Description
<i>Gas</i>	Represents a gas. It must be inherited (it cannot be instantiated). It is the base class for the <i>MonomolecularGas</i> and <i>GasMixture</i> classes. It exposes a <i>Temperature</i> property of type <i>Double</i> (double precision)
<i>GasFlow</i>	Represents a gas flow. It exposes two main properties: a <i>Speed</i> of type <i>Double</i> (double precision) and a <i>Gas</i> of type <i>Aurora.Engineering.Aerodynamics.Flow.Gas</i> .
<i>GasFlowRay</i>	Represents a gas flow with a direction and, optionally, an origin. It inherits from the <i>Aurora.Engineering.ThreeD</i> .

	<i>WorkSpace.RayTracer.Ray</i> class and exposes a <i>GasFlow</i> property of type <i>Aurora.Engineering.Aerodynamics.Flow.GasFlow</i> .
<i>GasFlowRayCollection</i>	Represents a collection of <i>Aurora.Engineering.Aerodynamics.Flow.GasFlowRay</i> objects.
<i>GasMixture</i>	Represents a gas mixture. Inherits from the <i>Aurora.Engineering.Aerodynamics.Flow.Gas</i> class. It exposes a <i>GasSpecies</i> property of type <i>Aurora.Engineering.Aerodynamics.Flow.GasSpeciesCollection</i> .
<i>GasMolecule</i>	Represents a gas molecule. Exposes several properties, representing different physical characteristics of a gas molecule.
<i>GasSpecies</i>	Represents a gas species. Exposes a <i>NumberDensity</i> property of type <i>Double</i> (double precision) and a <i>GasMolecule</i> property of type <i>Aurora.Engineering.Aerodynamics.Flow.GasMolecule</i> .
<i>GasSpeciesCollection</i>	Represents a collection of <i>Aurora.Engineering.Aerodynamics.Flow.GasSpecies</i> objects.
<i>MonomolecularGas</i>	Represents a gas mixture. Inherits from the <i>Aurora.Engineering.Aerodynamics.Flow.Gas</i> class. It exposes a <i>GasMolecule</i> property of type <i>Aurora.Engineering.Aerodynamics.Flow.GasMolecule</i> .

The inheritance hierarchy for the *Gas* class of the *Aurora.Engineering.Aerodynamics.Flow* namespace is illustrated in Figure A2-5.

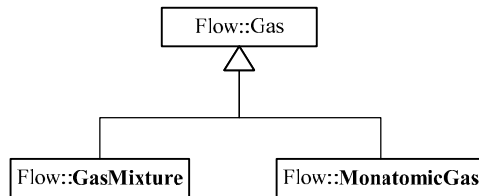


**Figure A2-3 - Gas Class Inheritance Hierarchy of the *Aurora.Engineering.Aerodynamics.Flow* Namespace**

### A2.2.6 *Aurora.Engineering.Aerodynamics.FMF.RayTracer*

The classes of the *Aurora.Engineering.Aerodynamics.FMF.RayTracer* namespace represent processing components within the PPRL and are comprised of over 2,600 lines of bespoke code. The classes are used to perform spacecraft aerodynamic analyses using the Hybrid method described in Section 6.2. Many of the classes inherit from the classes of the *Aurora.Engineering.ThreeD.WorkSpace.RayTracer* namespace described in Section A2.2.3.

Table A2-6 provides descriptions of some of the main classes of the *Aurora.Engineering.Aerodynamics.FMF.RayTracer* namespace.

**Table A2-6 - The Main Aurora.Engineering.Aerodynamics.FMF.RayTracer Classes**

Class	Description
<i>Analysis</i>	Represents an analysis object that can be used to perform analyses of spacecraft in the free molecular flow regime using the Hybrid method described in Section 6.2. Contains multiple properties related to the set-up of an analysis, including a Model property of type <i>Aurora.Engineering.Aerodynamics.FMF.RayTracer.Model</i> .
<i>GasFlowRay</i>	Inherits from the <i>Aurora.Engineering.Aerodynamics.Flow.GasFlowRay</i> class. It can be used to represent multiple different types of gas flow ray object. It can also be used to represent test particles for the simulation of reflected flow using the Hybrid method described in Section 6.2.
<i>GasFlowRayCollection</i>	Represents a collection of <i>Aurora.Engineering.Aerodynamics.FMF.RayTracer.GasFlowRay</i> objects.
<i>Model</i>	Represents a model object, which contains an <i>Aurora.Engineering.Aerodynamics.FMF.RayTracer.SurfaceMeshCollection</i> . It inherits from the <i>Aurora.Engineering.ThreeD.WorkSpace.RayTracer.Model</i> class. It exposes several methods for calculating aerodynamic coefficients, using the <i>Coefficient</i> class described in Section A2.2.4. Implements the <i>Aurora.Engineering.ThreeD.WorkSpace.RayTracer.Impactable</i> interface.
<i>PanelCollection</i>	Represents a collection of <i>Aurora.Engineering.Aerodynamics.FMF.RayTracer.TriangularPanel</i> or <i>Aurora.Engineering.Aerodynamics.FMF.RayTracer.QuadrilateralPanel</i> objects. Implements the <i>Aurora.Engineering.ThreeD.WorkSpace.RayTracer.Impactable</i> interface.
<i>QuadrilateralPanel</i>	Inherits from the <i>Aurora.Engineering.ThreeD.WorkSpace.RayTracer.QuadrilateralPanel</i> class. Implements the <i>Aurora.Engineering.ThreeD.WorkSpace.RayTracer.IPanel</i> interface.
<i>SurfaceMesh</i>	Inherits from the <i>Aurora.Engineering.ThreeD.WorkSpace.RayTracer.SurfaceMesh</i> class. Implements the <i>Aurora.Engineering.ThreeD.WorkSpace.RayTracer.Impactable</i> interface.
<i>SurfaceMeshCollection</i>	Represents a collection of <i>Aurora.Engineering.Aerodynamics.FMF.RayTracer.SurfaceMesh</i> objects. Implements the <i>Aurora.Engineering.ThreeD.WorkSpace.RayTracer.Impactable</i> interface.
<i>TriangularPanel</i>	Inherits from the <i>Aurora.Engineering.ThreeD.WorkSpace.RayTracer.TriangularPanel</i> class. Implements the <i>Aurora.Engineering.ThreeD.WorkSpace.RayTracer.IPanel</i> interface.

The *Impactable* interface implemented by multiple classes in the *Aurora.Engineering.Aerodynamics.FMF.RayTracer* namespace exposes a number of methods to generate and handle impact and gas-surface interaction events. The

impacts and gas-surface interactions are represented by classes in the *Aurora.Engineering.Aerodynamics.FMF.RayTracer.GSI* namespace, described in Section A2.2.7.

The *IPanel* interface implemented by the *TriangularPanel* and *QuadrilateralPanel* classes in the *Aurora.Engineering.Aerodynamics.FMF.RayTracer* namespace inherits from the *IImpactable* interface. It exposes additional functionality to store impacts and gas-surface interactions for a panel. It also exposes a *Temperature* property to store the temperature of the panel and a *GasSurfaceInteractionModels* property to store gas-surface interaction models. The gas-surface interaction models are represented by classes in the *Aurora.Engineering.Aerodynamics.FMF.RayTracer.GSI* namespace, described in Section A2.2.7.

The interface inheritance hierarchy and implementation structure for the *Aurora.Engineering.Aerodynamics.FMF.RayTracer* namespace is illustrated in Figure A2-4.

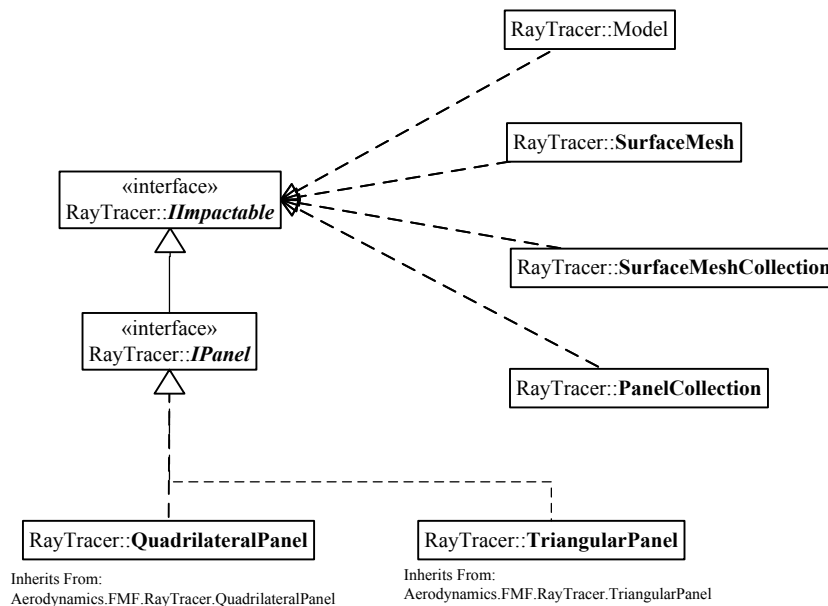


**Figure A2-4 - Inheritance Hierarchy and Implementation Structure for the *Aurora.Engineering.Aerodynamics.FMF.RayTracer* Namespace**

The inheritance hierarchy of the panel classes is shown in Figure A2-5. The figure illustrates the end-to-end line of inheritance from the panel classes of the *Aurora.Engineering.ThreeD.WorkSpace* namespace to the panel classes of the *Aurora.Engineering.Aerodynamics.FMF.RayTracer*.

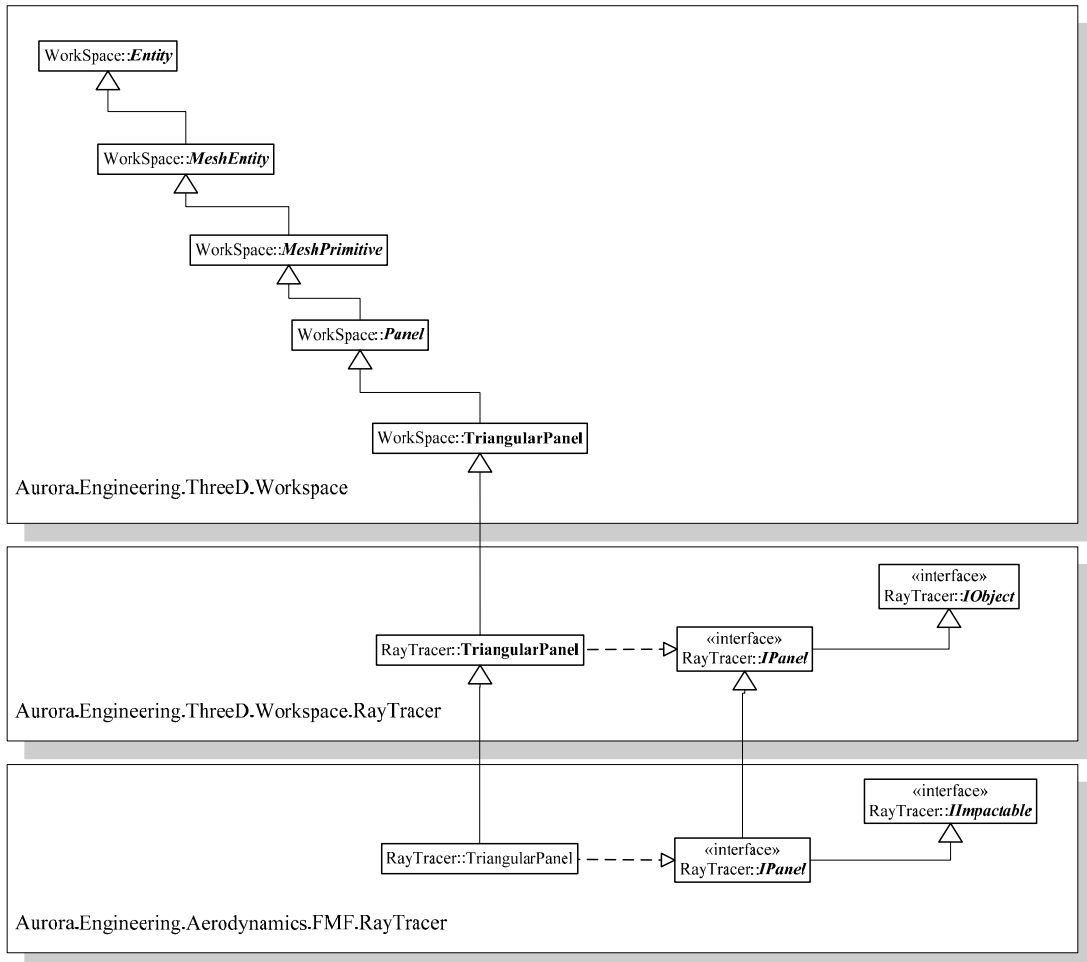


**Figure A2-5 - End-to-End Line of Inheritance for the Panel Classes**

### A2.2.7 Aurora.Engineering.Aerodynamics.FMF.RayTracer.GSI

The classes of the *Aurora.Engineering.Aerodynamics.FMF.RayTracer.GSI* namespace represent processing components within the PPRL. The classes are used to represent Gas-Surface Interactions (GSIs) and Gas-Surface Interaction Models (GSIMs) and their related objects. Both GSIs and GSIMs are described in Chapter 3. The GSIMs that are pre-installed in the FMF Module are described in Chapter 1.

Table A2-7 provides descriptions of some of the main classes of the *Aurora.Engineering.Aerodynamics.FMF.RayTracer.GSI* namespace.

**Table A2-7 - The Main Aurora.Engineering.Aerodynamics.FMF.RayTracer.GSI Classes**

Class	Description
<i>Attribute</i>	Represents a calculated property of a gas-surface interaction.
<i>AttributeCollection</i>	Represents a collection of <i>Aurora.Engineering.</i>

## Appendix 2 - FMF Module Technical Implementation

	<i>Aerodynamics.FMF.RayTracer.GSI.Attribute</i> objects.
<i>Bound</i>	Represents a bound of a GSIM.
<i>BoundCollection</i>	Represents a collection of <i>Aurora.Engineering.Aerodynamics.FMF.RayTracer.GSI.Bound</i> objects.
<i>GasSurfaceInteraction</i>	Represents the calculated results of a gas-surface interaction. Exposes several read-only properties that return aerodynamic coefficient values as well as a collection of calculated attributes, represented by an <i>Aurora.Engineering.Aerodynamics.FMF.RayTracer.GSI.AttributeCollection</i> object and a <i>ReflectedGasFlowRays</i> property that returns an <i>Aurora.Engineering.Aerodynamics.FMF.RayTracer.GasFlowRayCollection</i> (described in Section A2.2.6) that can be used to store any reflected gas flow rays.
<i>GasSurfaceInteractionCollection</i>	Represents a collection of <i>Aurora.Engineering.Aerodynamics.FMF.RayTracer.GSI.GasSurfaceInteraction</i> objects.
<i>GSIM</i>	<p>Represents a Gas-Surface Interaction Model (GSIM). It must be inherited (it cannot be instantiated). It contains two main functions:</p> <ol style="list-style-type: none"> <li>1. The <i>IsGasSurfaceInteractionWithinBounds</i> function should be overridden by the inheriting class. It is used to check whether or not the gas-surface impact, represented by an <i>Aurora.Engineering.Aerodynamics.FMF.RayTracer.GSI.Impact</i> object, can be modelled using the GSIM, based upon the GSIM bounds.</li> <li>2. The <i>GetGasSurfaceInteraction</i> function calculates and returns the results of a gas-surface interaction as an <i>Aurora.Engineering.Aerodynamics.FMF.RayTracer.GSI.GasSurfaceInteraction</i> object, based upon the gas-surface impact, represented by an <i>Aurora.Engineering.Aerodynamics.FMF.RayTracer.GSI.Impact</i> object and the GSIM parameters.</li> </ol> <p>The bounds and parameters of the GSIM are exposed as properties of type <i>Aurora.Engineering.Aerodynamics.FMF.RayTracer.GSI.BoundCollection</i> and <i>Aurora.Engineering.Aerodynamics.FMF.RayTracer.GSI.ParameterCollection</i> respectively.</p>
<i>GSIMCollection</i>	Represents a collection of <i>Aurora.Engineering.Aerodynamics.FMF.RayTracer.GSI.GSIM</i> objects.
<i>Impact</i>	Represents an impact between a gas flow ray, represented by an <i>Aurora.Engineering.Aerodynamics.FMF.RayTracer.GasFlowRay</i> object, and a panel, represented by an <i>Aurora.Engineering.Aerodynamics.FMF.RayTracer.IPanel</i> object. Both objects are described in Section A2.2.6.
<i>ImpactCollection</i>	Represents a collection of <i>Aurora.Engineering.Aerodynamics.FMF.RayTracer.GSI.Impact</i> objects.
<i>Parameter</i>	Represents a parameter of a GSIM.
<i>ParameterCollection</i>	Represents a collection of <i>Aurora.Engineering.Aerodynamics.FMF.RayTracer.GSI.Parameter</i> objects.

In keeping with the rest of the SEDAT System, the structure of the classes in the *Aurora.Engineering.Aerodynamics.FMF.RayTracer.GSI* namespace closely resembles the arrangement of the corresponding tables in the SEDAT Database. The GSIM table relationships are illustrated in Figure A2-6 for comparison.

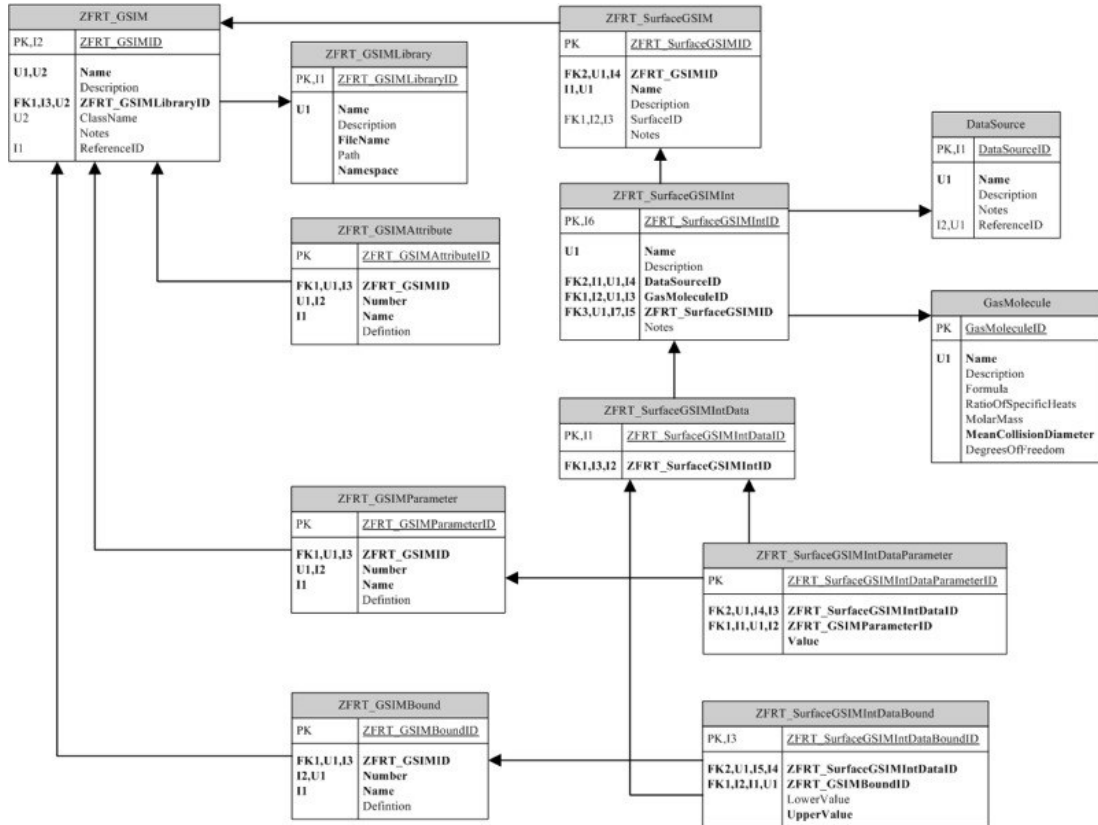


**Figure A2-6 - SEDAT Database Relationships: Gas-Surface Interaction Model (GSIM) Tables**

Note that only relationships between displayed tables are shown. Bold field names indicate that the field is part of one the table’s unique keys (e.g. *UI*) or foreign keys (e.g. *FKI*). Primary keys (PKs) are in all cases named *<Table Name>ID*. Arrows indicate the direction of the one-to-many relationship (the arrow points to the “one” side of the relationship).

The SEDAT Help System, described in Section 5.7, provides detailed information about how to set-up a GSIM, including how to set-up the parameters and bounds of a GSIM, and the attributes of a GSI.

### A2.2.8 Aurora.SEDAT.Data

The *Aurora.SEDAT.Data* namespace contains all of the components of the FMF Module’s Data Access Layer (DAL). The components of the DAL are listed in Table A2-8.

**Table A2-8 - FMF Module's Data Access Layer**

Component	Description
XML Schemas	Twelve XML schemas contain over 4,500 lines of bespoke XML and are used to represent different tables, queries, and relationships of the SEDAT Database.
Disconnected Datasets	The disconnected datasets provide localised representations of the SEDAT Database, based upon the XML schemas.
Data Processing Components	The data processing components contain over 5,500 lines of bespoke code. They provide a data transfer interface between the disconnected datasets and the SEDAT Database. They also provide the interface between the disconnected datasets and the processing components of the PPRL (described in the previous sections).

Ideally, all of the components of the FMF Module's DAL should be removed and from the *Aurora.SEDAT.Data* namespace and recreated in a separate namespace (for example, *Aurora.SEDAT.FMF.Data*). However, this has not been possible due to time constraints.



## A3 APPENDIX 3 - FMF MODULE ANALYSIS SET-UP VIA AN INTERFACE

This appendix provides details of how to set-up an interface to the FMF Module in order to run aerodynamic analyses using Microsoft Excel<sup>1</sup>.

The Microsoft .Net Dynamic Link Library (DLL) files that contain the classes of the FMF Module (listed in Section A2.2) can be used directly by any Microsoft .Net compile-able code, written in any Microsoft .Net compatible language (for example, Visual Basic, C#, C++, Fortran etc). However, to use them in Microsoft Excel, they must first be wrapped in a Component Object Model (COM) callable class that is registered for COM interoperation (Interop).

Figure A3-1, provides an example COM callable wrapper, written in Visual Basic.Net (VB.Net) code, that can be used to perform a simple aerodynamic analysis using the classes of the FMF Module.

```
Imports System.Runtime.InteropServices
Imports Aero = Aurora.Engineering.Aerodynamics
Imports AeroFlow = Aurora.Engineering.Aerodynamics.Flow
Imports FMFRT = Aurora.Engineering.Aerodynamics.FMF.RayTracer
Imports VS = Aurora.Engineering.ThreeD.VectorSpace
Imports WS = Aurora.Engineering.ThreeD.WorkSpace
<ClassInterface(ClassInterfaceType.None)>Public Class FMFAnalysis
    ' This Class Interface is required by the COM wrapper to enable
    ' intellisense for Microsoft VBA (to provide drop-downs when typing VBA code).
    Public Class FMFAnalysis
        ' Define a function that returns a force coefficient
        Public Function GetForceCoefficient(ByVal SurfaceMeshPath As String, _
            ByVal SurfaceTemperature As Double, ByVal GasMolarMass As Double, _
            ByVal GasRatioOfSpecificHeats As Double, _
            ByVal GasNumberOfDegreesOfFreedom As Double, _
            ByVal GasTemperature As Double, ByVal GasNumberDensity As Double, _
            ByVal GasFlowSpeed As Double, ByVal GasFlowDirection_X As Double, _
            ByVal GasFlowDirection_Y As Double, _
            ByVal GasFlowDirection_Z As Double, _
            ByVal ReferenceArea As Double, ByVal ReferenceLength As Double, _
            ByVal ReferenceOrigin_X As Double, _
            ByVal ReferenceOrigin_Y As Double, _
            ByVal ReferenceOrigin_Z As Double) As Double
            ' Declare local variables
            Dim myGasMolecule As AeroFlow.GasMolecule
            Dim myAtmosphericGas As AeroFlow.MonomolecularGas
            Dim myAtmosphericGasFlow As AeroFlow.GasFlow
            Dim myFreestream As FMFRT.GasFlowRay, myAnalysis As FMFRT.Analysis
            Dim myModel As FMFRT.Model, mySmesh As FMFRT.SurfaceMesh
            Dim mySmeshes As FMFRT.SurfaceMeshCollection
            Dim myGSIM As FMFRT.GSIM.Library.Maxwell
            Dim myCoefs As Aero.CoefficientCollection
            ' -> Go to Figure A3-2 to view the function's executable code.
        End Function
    End Class
End Class
```

**Figure A3-1 - Example COM Callable Interface to Perform a FMF Analysis in Microsoft Excel**

---

<sup>1</sup> Software providers are listed in Section III.iii

The executable code for the *GetForceCoefficient* function shown in Figure A3-1, which returns the force on the body in its body-fixed *x* direction, is provided in Figure A3-2.

```

' Set-Up the GSIM
myGSIM = New FMFRT.GSIM.Library.Maxwell
' Add the GSIM parameters
myGSIM.Parameters = New FMFRT.GSI.ParameterCollection( _
    1, 0.9, 0.28, 1.67, 1.67, 0.147, 1, 0.9, 0.28, 0)
' Add the GSIM bounds
myGSIM.Bounds = New FMFRT.GSI.BoundCollection( _
    0, 20000, 0, 20000, 0, 100, 0, 2.0E+26, 0, 2.0E+26)
' Import & set-up the surface mesh
mySmesh = FMFRT.SurfaceMesh.GetSurfaceMesh( _
    WS.SurfaceMesh.FromSTLFile(SurfaceMeshPath), _
    myGSIM, SurfaceTemperature)
' Set-Up the model
mySmeshes = New FMFRT.SurfaceMeshCollection
mySmeshes.Add(mySmesh)
myModel = New FMFRT.Model(mySmeshes)
' Set-Up the free stream gas flow
myGasMolecule = New AeroFlow.GasMolecule(GasMolarMass,
    RatioOfSpecificHeats, 0, GasNumberOfDegreesOfFreedom)
myAtmosphericGas = New AeroFlow.MonomolecularGas("Free Stream Gas",
    "Free Stream Gas", GasTemperature, _
    myGasMolecule, GasNumberDensity)
myAtmosphericGasFlow = New AeroFlow.GasFlow(myAtmosphericGas,
    GasFlowSpeed)
' Set-up the free stream gas flow ray
myFreestream = New FMFRT.GasFlowRay(FMFRT.GasFlowRayType.Freestream)
myFreestream.Direction = New VS.UnitVector(GasFlowDirection_X, _
    GasFlowDirection_Y, GasFlowDirection_Z)
myFreestream.GasFlow = myAtmosphericGasFlow
' Set-Up the analysis
myAnalysis = New FMFRT.Analysis(FMFRT.GasFlowType.Freestream)
myAnalysis.Type = FMFRT.AnalysisType. _
    DisableRayTracingAndReflectionsAndRotationalEffects
myAnalysis.Model = myModel
myAnalysis.Freestream = myFreestream
myAnalysis.Model.RefreshGeometryDependentProperties()
' Perform the analysis
myAnalysis.Analyse()
' Calculate the coefficients
myAnalysis.Model.ReferenceArea = ReferenceArea
myAnalysis.Model.ReferenceLength = ReferenceLength
myAnalysis.Model.ReferenceOrigin = New VS.Vector(ReferenceOrigin_X, _
    ReferenceOrigin_Y, ReferenceOrigin_Z)
myCoefs = myAnalysis.Model.GetCoefficients( _
    FMFRT.GasFlowRayType.Freestream)
' Return result
Return myCoefs.GetCoefficient(Aero.CoefficientType.Force, _
    Aero.CoefficientInteractionType.All).Value.X

```

**Figure A3-2 - *GetForceCoefficient* Function Executable Code**

The namespaces that contain the classes that are used by the code illustrated in Figure A3-1 and Figure A3-2 are explained in Section A2.2, which describes the FMF Module's client object model. The DLL files that contain the namespaces, which are imported in the first few lines of Figure A3-1, are listed in Table A3-1.

**Table A3-1 - Example COM Callable Interface: Required References**

Reference	Description	Dynamic Link Library (DLL) File
Aerodynamics	Contains the classes of the <i>Aurora.Engineering.Aerodynamics</i> namespace, described in Section A2.2.4.	ASAero.dll
FMFRT	Contains the classes of the <i>Aurora.Engineering.Aerodynamics.FMF.RayTracer</i> namespace, described in Section A2.2.6.	ASFMFRT.dll
FMFRTGSIMLibrary	Contains the classes of the <i>Aurora.Engineering.Aerodynamics.FMF.RayTracer.GSI</i> namespace, described in Section A2.2.7.	ASFMFRTGSIMLibrary.dll
ThreeD	Contains the classes of the <i>Aurora.Engineering.ThreeD</i> namespace, described in Sections A2.2.1, A2.2.2, and A2.2.3.	ASThreeD.dll

Compiling the example code in Microsoft .Net and registering the code for COM Interop produces a Type Library (.tlb) file. This file can be added as a reference to a Microsoft Excel Visual Basic for Applications (VBA) project. Once the reference has been added, the *FMFAnalysis* class can be instantiated and its single *GetForceCoefficient* function can be called from within a VBA subroutine.

Figure A3-3, illustrates an example of some simple VBA code that calls the *GetForceCoefficient* and returns a drag coefficient value in a pop-up message box.

```
Public Sub TestFMFAnalysis()
    ' Instantiate a new instance of the COM Analysis class
    Dim a As New ExampleCode.FMFAnalysis
    ' Run the analysis and display the result
    MsgBox CStr(a.GetForceCoefficient("C:\MySurfaceMesh.stl", _
                                     200, 16, 1.4, 3, 1012, 2860000000000#, _
                                     7540, -1, 0, 0, 2.8, 11.324, 0, 0, 0))
End Sub
```

**Figure A3-3 - Example Code to Perform a Simple FMF Analysis in Microsoft Excel using the Example COM Callable Interface**

The Microsoft Excel example subroutine listed in Figure A3-3, performs a FMF analysis of the spacecraft geometry represented by the stereolithography file *C:\MySurfaceMesh.stl*.

The surface mesh is given a default temperature of 200° K. The free stream atmospheric gas flow is defined as a monatomic flow of atomic oxygen, with a number density equivalent to an altitude of 640 km in mean solar conditions, which corresponds to a temperature of 1012° K [18]. The spacecraft is assumed to be

travelling in a circular orbit, corresponding to an approximate local wind speed of  $7540 \text{ m s}^{-1}$ .

The spacecraft is assumed to be travelling in the direction of the positive x-axis of analysis space, resulting in a free stream flow vector that acts along the negative x-axis of analysis space (-1, 0, 0). The reference area and reference length are  $2.8 \text{ m}^2$  and  $11.324 \text{ m}$  respectively. The reference origin is set to zero (0, 0, 0).

The executable code of the *GetForceCoefficient* function listed in Figure A3-2 uses the Hybrid Schaaf and Chambre GSIM described in Section 7.2, with the Mazanek input parameters and bounds defined in Section 3.3.3.

No rotations, translations, or angular velocities are applied to the model or the surface mesh. Reflections and rotational effects are disabled to reduce processing time for the purposes of testing the interface (this means that the example code should only be used for simple convex spacecraft geometries).

The example VBA code illustrated in Figure A3-3 is provided in a Microsoft Excel spreadsheet named *Excel Interface Example.xls*, which is copied to the *Excel Interface Example* folder in the SEDAT application folder during the installation process outlined in Section 5.9.

Also installed to this folder is a Visual Basic .Net file (*ExampleCode.vb*) containing the source code illustrated in Figure A3-1 and Figure A3-2, the corresponding compiled and COM-registered .tlb file (*ExampleCode.tlb*), and a sample surface mesh (*MySurfaceMesh.stl*), which represents the geometry of the TerraSAR-L spacecraft, referred to in Sections 6.1 and 8.5. The *Instructions* sheet of the Microsoft Excel spreadsheet contains instructions describing how to use the example VBA code.